

Reproducing estuarine processes with direct numerical simulations in horizontally periodic domains

Citation for published version (APA):

Kaptein, S. J. (2021). *Reproducing estuarine processes with direct numerical simulations in horizontally periodic domains*. Eindhoven University of Technology.

Document status and date:

Published: 11/11/2021

Document Version:

Publisher's PDF, also known as Version of Record (includes final page, issue and volume numbers)

Please check the document version of this publication:

- A submitted manuscript is the version of the article upon submission and before peer-review. There can be important differences between the submitted version and the official published version of record. People interested in the research are advised to contact the author for the final version of the publication, or visit the DOI to the publisher's website.
- The final author version and the galley proof are versions of the publication after peer review.
- The final published version features the final layout of the paper including the volume, issue and page numbers.

[Link to publication](#)

General rights

Copyright and moral rights for the publications made accessible in the public portal are retained by the authors and/or other copyright owners and it is a condition of accessing publications that users recognise and abide by the legal requirements associated with these rights.

- Users may download and print one copy of any publication from the public portal for the purpose of private study or research.
- You may not further distribute the material or use it for any profit-making activity or commercial gain
- You may freely distribute the URL identifying the publication in the public portal.

If the publication is distributed under the terms of Article 25fa of the Dutch Copyright Act, indicated by the "Taverne" license above, please follow below link for the End User Agreement:

www.tue.nl/taverne

Take down policy

If you believe that this document breaches copyright please contact us at:

openaccess@tue.nl

providing details and we will investigate your claim.

Reproducing estuarine processes
with direct numerical simulations
in horizontally periodic domains

PROEFSCHRIFT

ter verkrijging van de graad van doctor aan de Technische Universiteit
Eindhoven, op gezag van de rector magnificus prof.dr.ir. F.P.T. Baaijens,
voor een commissie aangewezen door het College voor Promoties, in het
openbaar te verdedigen op donderdag 11 november 2021 om 16:00 uur

door

Steven Jeroen Kaptein

geboren te Haarlem

Dit proefschrift is goedgekeurd door de promotoren en de samenstelling van de promotiecommissie is als volgt:

voorzitter: prof.dr.ir. G.M.W. Kroesen
1^e promotor: prof.dr. H.J.H. Clercx
2^e promotor: prof.dr. V.I. Armenio (Università degli Studi di Trieste)
copromotor(en): dr. M. Duran Matute
leden: prof.dr. H. Burchard (Leibniz Institute for Baltic Sea Research)
prof.dr. L.R.M. Maas (IMAU)
prof.dr.ir. N.G. Deen
adviseur(s): dr.ir. R.E. Uittenbogaard (Deltares)

Het onderzoek of ontwerp dat in dit proefschrift wordt beschreven is uitgevoerd in overeenstemming met de TU/e Gedragscode Wetenschapsbeoefening.

*To my family...
... to my friends...
... and to Karen*

A catalogue record is available from the Eindhoven University of Technology Library
ISBN: 978-90-386-53792

Cover pictures: stratified density field with a wavy interface separating two turbulent layers (front); stratified turbulent density field (back). The pictures are from a numerical simulation by S.J. Kaptein.
Printed by: Gildeprint

Contents

List of Figures	v
List of Tables	xiii
1 Introduction	1
1.1 Motivation and outline	1
1.2 Historical importance of estuaries	2
1.3 Hydrodynamics of the Rhine ROFI	4
1.3.1 General description	4
1.3.2 Tidal currents and stratification: coupled processes with dis- tinctive time scales	9
1.4 Numerical simulations for ROFI studies	16
1.4.1 Traditional research tools	16
1.4.2 State of the art DNS configuration	18
1.4.3 Research question	20
2 Numerical methods and flow configurations	23
2.1 Direct numerical and Large-eddy simulations	23
2.2 Governing equations	25
2.3 Subgrid-scale stress model	26
2.4 Main algorithm of LES-Coast	28
2.5 Simulation dependent settings	30
2.5.1 Oscillatory flow configuration: regime transitions	30
2.5.2 Oscillatory flow configuration: numerical settings	31
2.5.3 Exchange flow configuration: regime transitions	33
2.5.4 Exchange flow configuration: numerical settings	34
3 Effect of the water depth on oscillatory flows over a flat plate: from the intermittent towards the fully turbulent regime	37
3.1 Introduction	37
3.2 Laminar solution	39
3.3 Numerical set-up	41
3.4 Results	41
3.4.1 Validation against experimental data	41
3.4.2 Velocity profiles and turbulent boundary layer thickness	43
3.4.3 Surface velocity and turbulent wall shear stress	44
3.4.4 Turbulent kinetic energy	45
3.4.5 Amplitude and phases of the velocities and wall shear stresses	47
3.5 Discussion	49
3.6 Conclusion	51

4	Existence and properties of the logarithmic layer in oscillating flows	53
4.1	Introduction	53
4.2	Problem formulation	55
4.3	Results	56
4.3.1	Identification of the logarithmic layer	56
4.3.2	Von Kármán constant and intercept.	61
4.3.3	Spatial and temporal extent of the logarithmic layer	63
4.3.4	Reynolds number based on the friction velocity.	65
4.4	Discussion and conclusions.	68
5	Analysis of one-dimensional models for exchange flows under strong stratification	71
5.1	Introduction.	71
5.2	Two-dimensional asymptotic model for exchange flows.	73
5.2.1	Numerical set-up	73
5.2.2	Salinity distribution in the channel: flow regime identification.	76
5.3	Proposals for one-dimensional models	79
5.3.1	Mathematical formulation	80
5.3.2	Limiting cases.	81
5.3.3	Numerical results: model comparison	83
5.3.4	Extension to flows with a no-stress top boundary condition	88
5.4	Discussion.	90
5.5	Conclusion	93
6	Regime transitions in stratified shear flows: the link between horizontal and inclined ducts	95
6.1	Introduction.	95
6.2	Description of the system and background	96
6.3	Analytical model	98
6.3.1	Horizontal ducts	98
6.3.2	Extension to inclined ducts	100
6.4	Experimental data	101
6.5	Comparison with experiments	102
6.6	Conclusions	103
7	Turbulent flow driven by a horizontal density gradient	105
7.1	Introduction.	105
7.2	Numerical model	106
7.2.1	Computational domain.	106
7.2.2	Modification of the governing equations.	106
7.2.3	Parametrization of the horizontal density gradient	114
7.2.4	Non-dimensionalisation.	115
7.3	Application: illustration the stage transitions in a density driven flow initially at rest.	115
7.3.1	Temporal, evolution of the density distribution and mean velocity profiles	116

7.3.2	The path to turbulence	118
7.4	Discussion	125
7.4.1	Results in perspective of previous results	125
7.5	Conclusion	127
8	Conclusion	129
8.1	Summary of results	129
8.2	Implications for the Rhine	130
8.2.1	Oscillatory boundary layer	130
8.2.2	Exchange flows	131
8.3	Outlook	132
8.3.1	Estuarine circulation	133
8.3.2	Tidal Straining	133
8.3.3	Tidal mixing and spring-neap tidal cycle	133
8.3.4	Free surface	134
8.3.5	Tidal ellipses	134
A	Analytical solution for the tidal ellipses	135
B	Analytical solution for the finite depth Stokes boundary layer	137
C	Log-layer diagnostic function in normal scaling	139
D	One-dimensional models	141
D.1	Determination of the barotropic pressure gradient	141
D.2	Maximum velocities and density differences	142
D.3	Open-channel flow in the diffusion-dominated regime	143
	References	145

List of Figures

1.1	(a) Map of the North Sea with the location of the Rhine mouth. (b) Close-up on the Rhine mouth with the indication of the two main channels of the Rhine estuary: the Rotterdam Waterway (Nieuwe Waterweg) and the Haringvliet. A frame of reference (x, y) aligned with the coast is introduced. The letter A represent the emplacement of a mooring and the letter N a transect orthogonal to Noordwijk. These locations were used for the measurements reported by Simpson et al. (1993).	5
1.2	Density distribution in a cross-shore plane (y, z) for a well-mixed water column. The horizontal density gradient generates a typical exchange flow, the estuarine circulation, shown in red.	8
1.3	Tidal ellipses in the Rhine ROFI sketched by de Boer (2009) in a well-mixed situation (top left) and a stratified situation (bottom left). The paths described by the tidal velocity vector are enlarged on the right hand side and known as tidal ellipses. The velocity vector is explicitly shown at high-water (HW), low-water (LW) and slack tide.	9
1.4	Periodic stratification identified through the lines of equal density (pycnoclines) measured during a survey along transect N (see Fig. 1.1b). a) Post spring tide survey (9 October 1990) and b) post neap tide survey (15 October 1990).	10
1.5	Time series of current velocity and mean stratification of the water column. The semi-diurnal oscillation and spring-neap cycle are clearly observed in the current velocity. These time series were recorded at mooring A (see Fig.1.1) and show: (a) the east-west tidal velocity 4m above the sea bed and (b) the salinity difference between 1 and 16m below the surface. This figure was taken from in (Simpson et al., 1993).	11
1.6	Conceptual sketch from Visser, Souza, Hessner, and Simpson (1994) showing the evolution over the depth of vertical structure of the magnitude of the cyclonic $ U+ = \ \mathbf{R}_1\ $ and anticyclonic $ U- = \ \mathbf{R}_2\ $ rotary components of the tide for (a): well-mixed, (vertically uniform ν_T) and (b): stratified (ν_T reduced in the vicinity of the pycnocline) conditions. For the definitions of $\ \mathbf{R}_1\ $ and $\ \mathbf{R}_2\ $, the reader is referred to App. A.	13
1.7	The tidal straining mechanism in a configuration in which the main tidal currents are aligned with the main horizontal density gradient, as sketched by de Boer (2009).	14

1.8	The tidal straining mechanism in the Rhine ROFI configuration as sketched by de Boer (2009). During neap tide, the upper and lower layer in the water column are uncoupled. Strong cross-shore currents can exist and stratify the water column during flood and destratify the water column during ebb. This process is accompanied by upwelling (UW) and downwelling (DW).	15
1.9	Idealization of the Rhine mouth, with the two branches (Haringvliet and Rotterdam Waterway) and the river plume deflected to the right, due to Coriolis force. The location of a DNS/LES computational domain is depicted by the white bounded area. Note that this area is only a sketch and is not too scale (the actual would be much smaller).	18
1.10	Sketch of the model domain of vertical size h , with the direction of the tide and the density gradient. The initial density distribution goes from sea-water density, ρ_{sea} (left) to river-water density, ρ_{river} (right). Horizontal boundary conditions are periodic. A no-slip condition is applied at the bottom ($z = 0$) and a no-stress boundary condition at the top ($z = h$)	19
2.1	Schematized one-dimensional energy spectrum in logarithmic scale. . .	24
2.2	Standard computational domain for the three-dimensional DNS/LES used in this thesis. The domain is not on scale and the horizontal sizes of the domain, L_x, L_y , can vary depending on the flow configuration. . .	25
3.1	Phase shift (<i>a</i>) and the amplitude (<i>b</i>) of the surface velocities and the wall shear stress with respect to U_∞ . Note that Φ_∞ and A_∞ are function of z/δ while $\Phi_{h,f}$, Φ_τ , $A_{h,f}$ and A_τ are function of h/δ	40
3.2	Comparison between the results of the numerical simulations and the data from the experimental results of Jensen et al. (Jensen, Sumer, & Fredsøe, 1989). On the left hand side (a) the numerically computed, plane and phase averaged wall shear stress is displayed for the three values of the Reynolds numbers in the largest depth configuration (i.e. $h/\delta_s = 70$). On the right hand side (b), the plane and phase-averaged velocity profiles for $\text{Re}_\delta = 3460$ and $h/\delta_s = 70$ are shown for $\omega t = \{\pi/4, \pi/2, 3\pi/4, \pi\}$. Wall shear stress data for $\text{Re}_\delta = 990$ was not available.	42
3.3	Velocity profiles for $h/\delta_s = 70$ every $\Delta\omega t = \pi/12$ in the acceleration phase and for three different Reynolds number values.	43
3.4	Plane and phase averaged velocity profiles at $\omega t = \pi/2$ (left column, i.e. (a), (c) and (e)) and wall shear stress series (right column, i.e. (b), (d) and (f)) for $\text{Re}_\delta = 990$ (top, i.e (a) and (b)), $\text{Re}_\delta = 1790$ (middle, i.e. (c) and (d)) and $\text{Re}_\delta = 3460$ (bottom, i.e. (e) and (f)). The laminar analytical solutions are also displayed and the subscript 5 refers to $h/\delta_s = 5$	44
3.5	Resolved turbulent kinetic energy integrated over $0 \leq z \leq 5\delta_s$, $E_{k,5\delta_s}$ for $\text{Re}_\delta = 990$ (a), $\text{Re}_\delta = 1790$ (b) and $\text{Re}_\delta = 3460$ (c).	46

3.6 Phase shift (a) and the amplitude (b) of the surface velocity with respect to the free-stream velocity, for $Re_\delta = 990, Re_\delta = 1790$ or $Re_\delta = 3460$. Note that Φ_∞ and A_∞ are functions of z/δ while $\Phi_{h,f}$ and $A_{h,f}$ are functions of h/δ . For turbulent flows enough data points are available to present Φ_∞ and A_∞ as line but one point per simulation is available for $\Phi_{h,f}$ and $A_{h,f}$ and they are presented as symbols. The subscript 'an' refers to the laminar analytical solution while the subscript 'num' refers to the numerical solution. 48

3.7 Phase shift Φ_τ (a) and the amplitude A_τ (b) of the wall shear stress, for $Re_\delta = 990, Re_\delta = 1790$ or $Re_\delta = 3460$. The subscript 'an' refers to the laminar analytical solution while the subscript 'num' refers to the numerical solution. 49

4.1 Resolved TKE within a $5\delta_s$ thick layer adjacent to the bottom boundary layer for ten successive half cycles. The two curves represent simulations with different values of the Reynolds number and the h/δ_s ratio. The symbols mark the TKE values at specific phases. 57

4.2 Profiles of the plane-averaged, streamwise non-dimensional velocity u^+ in semi-logarithmic scale for three different value combination of $Re_\delta, h/\delta_s$ and ωt . (a) $Re_\delta = 1790, h/\delta_s = 70$ and $\omega t = \pi/12$, (b) $Re_\delta = 990, h/\delta_s = 10$ and $\omega t = \pi/2$, and (c) $Re_\delta = 1790, h/\delta_s = 70$ and $\omega t = 2\pi/3$. The theoretical solution has been obtained for $k = 0.41$ and $B = 5.5$. . . 57

4.3 (a) Reproduction of the profiles of Fig. 4.2 while differentiating the profiles having a log-layer (red-dashed) from the ones that did not have a log-layer (gray-solid) and the ones for which the presence of the log-layer is uncertain (black-solid) and (b) their associated log-layer diagnostic function Ξ for $Re_\delta = 990, h/\delta_s = 10$ and $\omega t = \pi/2$. The absence of a plateau at $1/k$ for Ξ might be difficult detect in logarithmic scale. Therefore, this figure has been reproduced in normal scaling in the Appendix, Fig. C.1 59

4.4 Points of coordinates $(\ln(z_{vs}^+); \overline{u}(z_{vs}^+)/U_0)$, i.e. the height of the viscous sub-layer and its associated velocity. Each point corresponds to a specific value of the phase ωt , a specific period and a specific value of h/δ_s . (a) $Re_\delta = 990$ and (b) $Re_\delta = 3460$. The plane-averaged velocity \bar{u} has been made non-dimensional with the outer scale U_0 instead of the inner scale u_τ because in this way the difference between the laminar points and the turbulent points is emphasized. The points of the laminar solution are obtained by taking the first maximum of $z^+ \partial u_\infty / \partial z$, where u_∞ is the analytical solution under infinite depth assumption (Kaptein, Duran-Matute, Roman, Armenio, & Clercx, 2019). The start of the oscillating cycle $\omega t = 0$ is marked by the blue circle. . . 60

4.5 Sketch of (a) a velocity profile in logarithmic scale with its corresponding log-layer diagnostic function for $Re_\delta = 990, h/\delta_s = 10$ and $\omega t = \pi/2$ and (b) a velocity profile for $Re_\delta = 3460, h/\delta_s = 70$ and $\omega t = \pi/2$. The thickness of the viscous sub-layer $z_{\min} \equiv z_{vs}^+$ and z_c are sketched on (a) while z_{\max}^+ is sketched on (b). 62

- 4.6 Evolution of the von Kármán constant (a) and the intercept B (b) as a function of the phase ωt . The influence of the Reynolds number has been highlighted by using different coloured symbols for the data points corresponding to simulations with different values of Re_δ . All values of h/δ_s are considered. Different dotted lines are also displayed in order to indicate specific values of k and B 63
- 4.7 Value of the von Kármán constant (a) and the intercept B (b) as a function of the phase ωt , for $\text{Re}_\delta = 3460$ and $h/\delta_s = 40$. Two different ways of computing k and B are tested. One is based on the minimum of the log-layer diagnostic function Ξ (blue dots) and the other is based on fitting a function through an interval depending on the relative error Err of the velocity profile with respect to the log-law (red triangles and green diamonds). 64
- 4.8 Spatial extent and existence interval of the log-layer, depending on Re_δ and h/δ_s : $\text{Re}_\delta = 990$ (a), $\text{Re}_\delta = 1790$ (b) and $\text{Re}_\delta = 3460$ (c). The open symbols and dashed line mark the start for the logarithmic region and the filled symbols and solid line mark its end. 64
- 4.9 Start and end of the log-layer depending on the maximum error ϵ for $\text{Re}_\delta = 3460$, $h/\delta_s = 40$. Each green line or red line marks a different value of the phase ωt 66
- 4.10 Velocity profiles every $\Delta\omega t = \pi/12$ starting at $\omega t = -5\pi/12$ (most left profile) ending at $\omega t = \pi/2$ (most right profile) for $\text{Re}_\delta = 3460$. The thickness of the wall-dominated layer d , defined as the height above the bottom at which the velocity profile has its first maximum is depicted by the black dotted line. A distinction is made between the deep water solution (a) and the shallow water solution (b). 67
- 4.11 Link between the log-layer existence and the plane and phase averaged value of R_τ . The threshold for which the log-layer has been identified in the plane channel flow of Kim, Moin, and Moser (1987), i.e. $\text{R}_\tau = 180$, is also displayed. 68
- 5.1 Side-view of the 2D computational domain, with the initial distribution of salt. This sketch is not to scale as $L \gg h$ and we assume very large salt reservoirs. The salt concentration in the left reservoir is denoted by the salinity s_1 and will be kept constant (as we assume an infinitely large reservoir). Similarly, the salt concentration in the right reservoir is denoted $s_2 > s_1$ (and also kept constant). The acceleration of the gravity g is in the negative z -direction. Note that this configuration is mirrored with respect to the ROFI configuration of Chapter 1 and the configuration of Chapter 6. 74

- 5.2 The density distribution in the channel (not to scale as $h \ll L$) for four simulations in the four different regimes: (a) the diffusion-dominated regime (here with $\text{Re}_g = 50$, $\text{Sc} = 300$ and $\Gamma = 1/60$), (b) the transition regime ($\text{Re}_g = 200$, $\text{Sc} = 300$ and $\Gamma = 1/60$), (c) the high-advection/high-diffusion regime ($\text{Re}_g = 5000$, $\text{Sc} = 1$ and $\Gamma = 1/60$) and (d) the high-advection/low-diffusion regime ($\text{Re}_g = 1000$, $\text{Sc} = 300$ and $\Gamma = 1/60$). Note that $\rho_{\text{var}}/\Delta\rho = s^* - s_{\text{av}}^*$. With $s_1 = 0$ this implies $s_{\text{av}}^* = \frac{1}{2}$ and $0 \leq s^* \leq 1$ and thus $-0.5 \leq \rho_{\text{var}}/\Delta\rho \leq 0.5$ 77
- 5.3 The profiles at $y = 0$ of (a) the resolved density, (b) the horizontal density gradient, and (c) the mean horizontal velocity in the steady state for the same four simulations used to describe the four regimes in Fig.5.2. The solid black line represents the initial condition. 78
- 5.4 Shear at mid-depth as a function of $\text{Re}_g\Gamma$ spanning all different flow regimes, from the diffusion dominated to the high-advection/low-diffusion. Low Schmidt number values correspond to $\text{Sc} = 1$, and high Schmidt number values correspond to $\text{Sc} = 50, 300, 1000$ 83
- 5.5 Magnitude of the steady-state stratification (a) and the steady-state exchange flow scaled with $\text{Sc}^{1/2}$ (b) as a function of $\text{Re}_g\Gamma\text{Sc}^{1/2}$ as obtained from the 2D simulations. Different Schmidt number values are displayed with different colors. The gray solid line represents the analytical solution in the diffusion-dominated regime [i.e. the solution to Eqs. (5.24b)–(5.24a)], and the gray dashed line represents the analytical solution for the high-advection/low-diffusion regime [i.e. the solution to Eqs. (5.27)–(5.28)]. Both of these solutions are derived in Appendix D.2. The black vertical dashed line at $\text{Re}_g\Gamma\text{Sc}^{1/2} = 12\sqrt{5}$ represents the transition at which the two analytical solutions for $\Delta\rho_{\text{var}}/\Delta\rho$ intersect. 84
- 5.6 The magnitude of the steady-state stratification for the different models for high Sc values (a) and for $\text{Sc} = 1$ (c), and the corresponding errors between the 2D model and the 1D models for high Sc values (b) and for $\text{Sc} = 1$ (d). The gray solid line represents the analytical solution in the diffusion-dominated regime [i.e. the solution to Eqs. (5.24b)–(5.24a)], and the gray dashed line represents the analytical solution for the high-advection/low-diffusion regime [i.e. the solution to Eqs. (5.27)–(5.28)]. Both of these solutions are derived in Appendix D.2. The black vertical dashed line at $\text{Re}_g\Gamma\text{Sc}^{1/2} = 12\sqrt{5}$ represents the transition at which the two analytical solutions intersect; see panels (a) and (c). 86
- 5.7 Magnitude of the steady-state exchange flow for the different models for high Sc in (a) and $\text{Sc} = 1$ in (c), and the corresponding errors between the 2D model and the 1D models in (b) for high Sc and in (d) for $\text{Sc} = 1$. The gray solid and dashed lines display the trends resulting from the analytical solutions for $\Delta v/U_g$, based on Eqs. (5.24a) and (5.28), and explicitly written in Appendix D.2. The black vertical dashed line represents the transition point at $\text{Re}_g\Gamma\text{Sc}^{1/2} = 12\sqrt{5}$ 87

- 5.8 Magnitude of the steady-state stratification for the different models in the open-channel configuration for high Sc values (a) and $Sc = 1$ (c). The corresponding errors between the 2D model and the 1D models are also shown for high Sc values (b) and for $Sc = 1$ (d). The gray solid and dashed lines display the trends resulting from the analytical solutions for $\Delta\rho_{\text{var}}/\Delta\rho$, based on Eqs. (D.18) and (5.27) for the diffusion dominated and high-advection/low-diffusion flows, respectively, and explicitly written in Appendix D.3. The black vertical dashed line represents the transition where the two analytical solutions intersect at $Re_g \Gamma Sc^{1/2} = 8\sqrt{5}$ 89
- 5.9 Magnitude of the steady-state exchange flow velocities for the different models in the open-channel configuration for high Sc values (a) and for $Sc = 1$ (c). The corresponding errors between the 2D model and the 1D models are given for high Sc values (b) and for $Sc = 1$ (d). The gray solid lines in panels (a) and (c) represent the trend resulting from the analytical solution for $\Delta v/U_g$, based on Eq. (D.15) for the diffusion-dominated flows and derived in Appendix D.3. The black vertical dashed line represents the critical value $Re_g \Gamma Sc^{1/2} = 8\sqrt{5}$ for transition between the diffusion and advection-dominated regimes. 90
- 5.10 Vertical profiles of the horizontal density gradient for the four cases representative of the four regimes. The cases correspond to the those in Fig. 5.2. (a) Diffusion-dominated regime ($Re_g = 50$, $Sc = 300$), (b) Transition regime ($Re_g = 200$, $Sc = 300$), (c) high-advection/high-diffusion regime ($Re_g = 5000$, $Sc = 1$), and (d) high-advection/low-diffusion regime ($Re_g = 1000$, $Sc = 300$). $\Gamma = 60$ for all four cases. 92
- 6.1 Schematic representation of the side view of a stratified inclined duct (SID) experimental setup. In the center: the duct of length L and height h inclined an angle θ with respect to the horizontal. The duct connects two large tanks: one with water with density $\rho = \rho_{\text{ref}} + \Delta\rho/2$ and the other with density $\rho = \rho_{\text{ref}} - \Delta\rho/2$. The internal angle of the duct is $\alpha = \arctan(h/L)$. The along-duct coordinate is y_θ and the coordinate perpendicular to the bottom and the top of the duct is z_θ . The origin O of the coordinate system is located at the center of the duct. Note that this set-up is mirrored with respect to Chapter 5 and Chapter 7, but in agreement with the Rhine ROFI of Chapter 1. . . . 96
- 6.2 Location of the different regimes in the $(Re-\theta)$ plane for the four different setups: mSID, tSID, LSID, and HSID. The different symbols represent the different regimes laminar (L), Holmboe waves (H), other waves (W), intermittently turbulent (I) and turbulent (T). The solid lines represent curves of constant Ψ_θ with the value indicated along the line. The dashed line represents $\theta = \alpha$. The dotted line represents the continuation of the transition between the intermittently turbulent and fully turbulent regimes for *forced* flows given by θRe equal to a constant as proposed by Lefauve, Partridge, and Linden (2019a). For the tSID setup Re is multiplied by the aspect ratio $B = 1/4$ to account for the increased momentum diffusion in the across-channel direction. 103

7.1	Sketch of the two-dimensional numerical simulation set-up used in Chapter 5 (not to scale). Two reservoirs containing water at a different salinity are connected by a horizontal channel of length L . A section of the channel with length L_y that could be simulated with a direct numerical simulation set-up is depicted by a dashed square. Note that this configuration is mirrored with respect to the ROFI configuration of Chapter 1 and the configuration of Chapter 6. It is in agreement with the configuration of Chapter 5.	107
7.2	Computational domain, and coordinate system. The horizontal density gradient is in the y direction, and the z direction represents the vertical coordinate.	108
7.3	(a-d): Density field at different stages of the transient regime (respectively convective overturning and undisturbed interface, wavy interface, turbulent interface). (e): Corresponding velocity profiles and (f) corresponding density profiles. The analytical solutions, given by Eqs (7.33), (7.34) are also displayed. The analytical velocity profile was rescaled in order to fit on the graph.	117
7.4	Contours of the density in a (y, z) slice of the computational domain at four different times.	119
7.5	Temporal evolution of (a) the fluctuating kinetic energy, (b) the interface thickness, (c) the interface thickness with focus on the thin-interface stage, and (d) the gradient Richardson number. The different stages: laminar (L), convective overturning (CO), flat-interface turbulent (FIT), Holmboe (H), and intermittent turbulence (IT) are indicated on the graph, as well as the moments in time displayed in the previous figures.	122
7.6	Root mean square velocities during (a) the event of convective overturning; (b) undisturbed interface; (c) Holmboe waves; (d) turbulent interface.	124
7.7	Simulation and analytical profiles of (a): the velocity and (b): the density.	126
7.8	Ratio between the vertical density gradient and the velocity shear at the center of the channel and over time. The black dotted lines represent critical values of $R_\rho = 1$ and $R_\rho = \sqrt{8}$	127
C.1	Reproduction of the profiles of Fig. 4.3. (a) logarithmic layer and (b) their associated log-layer diagnostic Ξ function in normal scaling for $Re_\delta = 990$, $h/\delta_s = 10$ and $\omega t = \pi/2$	139

List of Tables

2.1	Numerical settings for each simulation. The symbols n_x , n_y and n_z are the number of grid cells in the streamwise, spanwise and vertical. The symbols L_x and L_y are the domain size in the streamwise and spanwise direction. The water depth is given by h , the thickness of the Stokes boundary layer by δ_s and the Reynolds number based on the Stokes boundary layer thickness by Re_δ	33
3.1	Recapitulation of the turbulent tidal boundary layer thickness in the Rhine estuary for spring tide and neap tide. The results are obtained for a tidal period $T_{M2} = 12.42$ h (Zimmerman, 1986), a tidal angular frequency $\omega = 1.41 \cdot 10^{-4}$ s $^{-1}$, a kinematic viscosity $\nu = 1.14 \cdot 10^{-6}$ m s $^{-1}$, a non-dimensional boundary layer thickness $\delta\omega/U_0 \sim 5 \cdot 10^{-3}$ (Jensen et al., 1989) a depth $h = 20$ m, and the velocity measurements of van der Giessen, de Ruijter, and Borst (1990) to estimate U_0	38
3.2	Turbulent boundary layer thickness for the three different Reynolds numbers in sufficiently large domains, i.e. $h/\delta_s = 70$, (left) and the corresponding h/δ ratio for the 15 different ($\text{Re}_\delta, h/\delta_s$) couples. The cells colored in gray represent simulations for which the h/δ ratio is comparable with the h/δ ratio estimated for the Rhine estuary.	43
4.1	Overview of the phases characterized by intermittency. These phases are defined as the <u>profiles</u> for which, at identical value of Re_δ , h/δ_s and ωt , the $(\ln(z_{vs}^+); \overline{u(z_{vs}^+)}/U_0)$ points are located simultaneously on the logarithmic branch and significantly off the logarithmic edge.	61
6.1	Characteristics of the experiments used in this paper. Four duct geometries [abbreviated mSID (m for mini), tSID (t for tall), LSID (L for large), HSID (H for half)] are used (Lefauve & Linden, 2020a). We list the values of the dimensionless numbers describing each duct geometry (Γ and B), the value of Sc for salt in water, and the ranges of θ and Re explored.	102
8.1	Tide related parameters for the Rhine ROFI and the relevant simulations	131
8.2	Overview of the estimation of parameter values and non-dimensional umbers for different exchange flows, for $g = 9.91$ m s $^{-2}$, $\beta = 7.7 \times 10^{-4}$ (Geyer & MacCready, 2014) and $\nu = 1 \times 10^{-6}$ m 2 s $^{-1}$	132

1

Introduction

1.1. Motivation and outline

The research presented in this thesis was motivated by the hydrodynamics in the Rhine estuary. In estuaries, these hydrodynamics are created by the interplay of several physical actors and influence the distribution of sediment, other suspended particles, contaminants, marine species, etc. Near the mouth of the Rhine, a key role is played by the competition between buoyancy input and mixing, which generates significant fluctuations in the stratification of the water column (Simpson et al., 1993). Although, the most important physical forcing mechanisms are large scale processes such as the river outflow, the tide and the Coriolis force, smaller scale processes play a determinant role. Indeed, most of the mixing occurs at these small scales due to turbulent eddies, while gradients can also be large, implying significant changes in density over limited length scales. Unfortunately, it is difficult to observe these small-scale processes in field measurements. In addition, the small scales are not resolved in three-dimensional numerical simulations based on Reynolds averaged Navier-Stokes (RANS) equations, commonly used to model estuaries and shallow-seas. Accordingly, modeling estuarine physics with high resolution numerical simulations could shed light into turbulent processes. However, using high resolution numerical simulations requires the incorporation of all the relevant physical processes at once in a direct numerical simulation (DNS) model, which is particularly challenging. In this thesis, two of these processes are isolated and investigate separately.

First, the turbulent flow generated by an oscillatory pressure gradient, as a model for the tide is studied. The aim is to elucidate the role of the water depth on the flow, a process relevant for the Rhine estuary but not described in the (DNS) literature. Second, we analyze the effect of the water depth and the oscillatory flow on the validity and properties of the logarithmic velocity profile assumption. This velocity profile is often used in RANS models as an approximated boundary condition, but it is in part based on the assumption of steadiness of the flow.

Additionally, we develop a new parametrization for horizontal density gradients so that strongly stratified exchange flows driven by horizontal density gradients can

be modeled accurately with one-dimensional vertical (1DV) models. These flows are a characteristic feature of estuaries. However, until now, their investigation with 1DV models was limited to configurations with a weak horizontal density gradient since, otherwise, the phenomenon of runaway stratification occurs. After validation of the one-dimensional parametrization, we extend it to a three-dimensional DNS model and are able to simulate a strongly stratified, turbulent shear flow, equally driven by a horizontal density gradient. It is the first time that density-driven exchange flows are simulated with this approach.

1.2. Historical importance of estuaries

The Rhine is the second largest river in Europe after the Danube and is playing a major role in Europe's economy and infrastructure since Roman times. In the Antiquity, it was a section of the *limes Germanicus*, i.e. the northern border of the Roman Empire (Hisgen & Laane, 2008, p. 46, 48). Today, it is the primary entry gate for goods in Western Europe (Hisgen & Laane, 2008, p. 46, 84), being part of the main transport axis linking the industrial Ruhr area, in Germany, to the North Sea. Furthermore, the Rhine basin is one of the most densely populated regions of the world.

The population density and the economic importance are features the Rhine basin shares with many other estuaries. In general, people seem to have always had a preference for settling near river deltas. The earliest civilizations appeared more than 5000 years ago along some of the world's most famous rivers: the Nile in Egypt, the Tigris and the Euphrates in modern day Iraq, the Indus between Pakistan and India and the Yangtze and Yellow rivers in China (Könemann, Stefánik, Gurnák, Hartstein, & Hanula, 2016, p.22). This settling preference is not coincidental. Rivers offer very advantageous living conditions, such as fertile soil for agriculture, a proximate source of food (e.g. fish) and excellent trading opportunities. Today, rivers and seas are still the most favored route for the exchange of goods. Transport over water is cheaper than transport through the air, and geopolitically less complex than transport over land. As an illustration, 469.4 million tons of goods transited through the port of Rotterdam in 2019 (Port of Rotterdam-Press release, 2020), compared to 1.83 million tons through the Dutch airports (Schiphol and Maastricht) in 2018 (Centraal Bureau voor de statistiek (CBS), 2018) and 34 million tons of goods coming from, or going to the Netherlands by rail in 2018 (CBS, 2019a). Furthermore, 361 million tons of goods were transported via inland navigation (CBS, 2019b). This preference is not a recent development. Indeed, although the silk road (a land route) is maybe one of the most famous ancient trade routes, intensive maritime trade is probably much older. For example, maritime trade relying on the monsoon winds between Sumer (nowadays southern Iraq) and the Indus valley dates back to the 2nd and 3rd millennium before common era (BCE), while the Phoenicians used maritime trade routes from Lebanon up to the Atlantic coast of North Africa in the 7th century BCE.

Nevertheless, living in the proximity of a dynamic water body has always come with many challenges. There is the risk of inundations, as testify the yearly Nile floods caused by heavy monsoon rains, the more occasional floods threatening Baghdad (Marozzi, 2014, p. 80), and the exceptional floods in the Netherlands like in 1953

(Hisgen & Laane, 2008, p. 57). There is also the need for infrastructure. Modern engineering projects like the extension of the port of Rotterdam with Maasvlakte 2 (Port of Rotterdam) and the construction of the Deurganckdok (Port of Antwerp) can be named in one breath with ancient achievements such as the canal of the Pharaoh's (6th century BCE) or the tidal dock of Lothal (20th century BCE).

With the investments in the infrastructure comes the concern of its maintenance. Inhabitants of the Indus valley civilization were already conscious about this challenge. They constructed the harbor of Lothal some distance from the main river channel to reduce sedimentation. The disastrous effects of sedimentation can be illustrated by several examples. The famous antique city of Ephesus (modern day Turkey) was once located on the shore of the Aegean Sea, while it is now located several kilometers inland due to the sedimentation of the Cayster River. In Western Europe, the city of Bruges could flourish between the 12th and the 15th century when storms created a tidal inlet, the 'Zwin', connecting the city to the North Sea. However, sedimentation of this tidal inlet over the centuries hindered the port activities (Hisgen & Laane, 2008, p. 12), and the most important port of Flanders eventually became Antwerp. In both cases, sedimentation ultimately lead to the decline and even to the abandonment, of the city in the case of Ephesus. A last example illustrating the effect of sedimentation can be found in the Rhine itself. Its course was located nearby Utrecht during Roman times, while its main distributary branch today is the Waal, about 40 km southwards. The port of Rotterdam was threatened by sedimentation of the Brielse Maas in the 19th century, at that time the principal channel linking the port to the sea. This threat ultimately lead to the construction of the 'Nieuwe Waterweg' (or Rotterdam Water Way) in 1872, which is still the main channel of the Rhine-Meuse estuary today (Hisgen & Laane, 2008, p. 82).

Naturally, the management bodies governing the important trading axis face the same issues nowadays. Fortunately, modern dredging techniques allow for the maintenance of the waterways such that sedimentation does not lead to the inaccessibility of ports. Nevertheless, these operations are extremely expensive. For example, maintenance dredging in the Scheldt for the accessibility of the port of Antwerp costs about 200M€ yearly (Rekenhof, 2016). As a result, new methods or constructions are investigated in order to try to reduce sedimentation and thus dredging costs. These investigations begin with an in-depth knowledge of the physical processes governing the estuary, starting with the hydrodynamics. Although the world's estuaries share their economical importance, they are unique in the natural conditions that determine their dynamic evolution. The Rhine is no exception.

1.3. Hydrodynamics of the Rhine Region of Freshwater Influence

1.3.1. General description

Freshwater input

Important aspects determining the hydrodynamics of estuaries are usually the bathymetry, the river discharge, the tide, the Coriolis force (due to the rotation of the Earth) and meteorological conditions such as wind and heating processes. Their relative importance makes each estuary unique. The Rhine is, with an average discharge of $2200 \text{ m}^3 \text{ s}^{-1}$, the second largest river in Europe, after the Danube (Simpson et al., 1993). This discharge is mainly divided over the Rotterdam Waterway ($1500 \text{ m}^3 \text{ s}^{-1}$) and the Haringvliet (de Kok, 1996). River water flows into the North Sea at Maasvlakte 2, located on the Dutch coast (see Fig. 1.1). The huge input of freshwater creates a salinity deficit area called Region Of Freshwater Influence (ROFI). This term was first coined by J.H. Simpson as the "region between the shelf sea regime and the estuary where the local input of freshwater buoyancy from the coastal source is comparable with, or exceeds the seasonal input of buoyancy as heat which occurs all over the shelf" (Simpson, 1997).

To gain insight in the relative magnitude of the buoyancy input through the river discharge, it is necessary to compare it to the buoyancy input caused by the heating and cooling of the sea surface. In the Rhine ROFI, the buoyancy input rate of the lateral river alone is about $5.4 \times 10^5 \text{ N s}^{-1}$ (based on the river discharge and an average density difference of 25 kg m^{-3}), which is equivalent to a peak summer heating over an area of 10^4 km^2 (Simpson et al., 1993). This feature means that the system can be stratified even when the rest of the shelf is completely mixed. Therefore, the seasonal stratification/mixing pattern usually occurring in the shelf-sea is supplemented by alternative time scales of stratification variation within the water column related to tidal mixing and tidal straining (this phenomenon is described below).

The spreading of the river water in the North Sea has a well-defined shape. The bulge of freshwater resulting from the Rhine river extends 20 to 25 km offshore and about 100 km alongshore. Rhine water can even be traced until 60 km offshore and stratification may be observed at 40 km from the coast in case of favorable winds (de Kok, 1996). The bulge turns to the right under the influence of the Coriolis force (on the Northern Hemisphere) and creates a baroclinic circulation. As a result, three different regions may be distinguished: a source, a plume region and a coastal current (Münchow & Garvine, 1993). The plume has two favorite spreading modes. In the first mode, it reattaches to the coast and forms a narrow coastal jet, northeastwards, within 10 km from the coast. In the second mode, it separates from the coast and flows to the North. The occurrence of one or the other mode is believed to depend on the wind direction and magnitude (de Ruijter, van der Giessen, & Groenendijk, 1992).

Although the high inflow of buoyancy from the river is a distinctive feature of the Rhine, it is not the only important physical actor. A competition between river runoff (stratifying forces), wind, waves and tides (stirring forces), eventually coupled by the Coriolis force, leads to alternations between vertically well-mixed and stratified conditions. The tidal currents along the Dutch coast are of order of magnitude 1 m s^{-1} ,

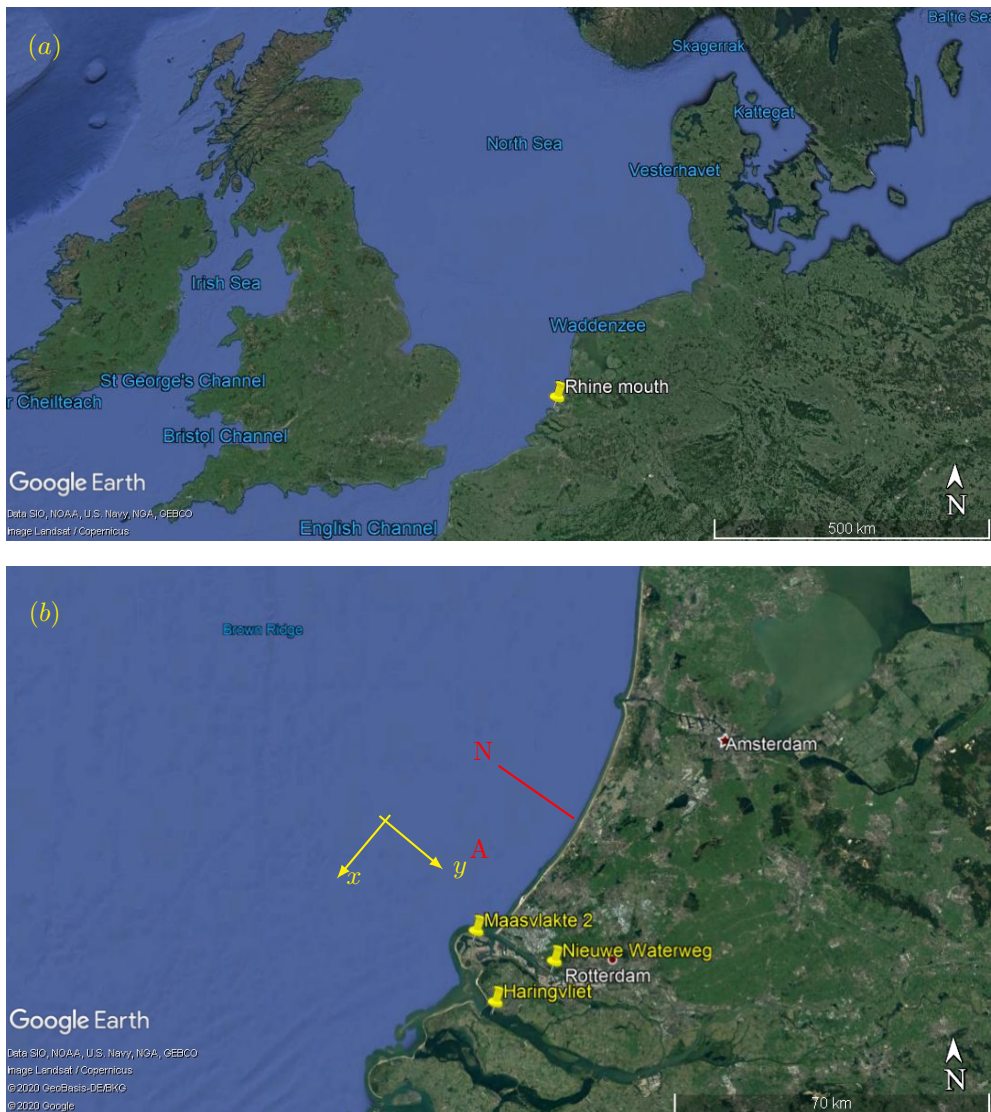


Figure 1.1: (a) Map of the North Sea with the location of the Rhine mouth. (b) Close-up on the Rhine mouth with the indication of the two main channels of the Rhine estuary: the Rotterdam Waterway (Nieuwe Waterweg) and the Haringvliet. A frame of reference (x, y) aligned with the coast is introduced. The letter A represent the emplacement of a mooring and the letter N a transect orthogonal to Noordwijk. These locations were used for the measurements reported by Simpson et al. (1993).

while the latitude of 52°N is responsible for significant Coriolis effects. Finally, the average water depth of the North Sea around the Dutch coast is about 20 m (de Boer, 2009, p.96). It is the mutual interaction of all these elements which makes the particular case of the Rhine unique and leads to very specific hydrodynamic conditions.

Residual alongshore currents

The residual surface current in the Rhine ROFI is aligned parallel to the coast. Its direction is towards the Northeast (de Ruijter, Postma, & De Kok, 1987). There are three main contributors to this residual flow: the interaction between the river outflow and the Coriolis force, the tide and the wind.

The Coriolis force constrains the discharge of river water into a flow parallel to the coast, with the land on its right in the Northern Hemisphere (Simpson, 1997). The nature of this flow is geostrophic which means that the pressure gradient balances the Coriolis force due to Earth rotation according to

$$fv = \frac{1}{\rho} \frac{\partial p}{\partial x}, \quad (1.1)$$

$$fu = -\frac{1}{\rho} \frac{\partial p}{\partial y}, \quad (1.2)$$

where u , v are the flow velocities in the alongshore direction x and in the cross-shore direction y (see Fig.1.1b for a frame of reference), respectively. The Coriolis parameter is represented by f and is equal to 1.25×10^{-3} at 52°N, while the pressure gradients $\partial p/\partial x$ and $\partial p/\partial y$ are caused by density gradients. The alongshore flow is then a classical coastal current (Münchow & Garvine, 1993) in which the buoyant-layer depth is of the same order as the water depth due to the shallowness of the continental shelf.

In the North Sea, the tide takes the form of a cyclonic Kelvin wave. The tidal wave enters the North Sea close to Scotland and travels southwards with the coast on its right. When approaching the Channel, it turns to the Northeast, following the coast. Here the North Sea tidal current is met by a secondary tidal current coming from the Channel. This property implies that the tidal currents oscillate back-and-forth, parallel to the coast (de Boer, 2009). Around the mouth of the Rhine, the dominant tidal constituents are semi-diurnal, such that the period of oscillation is also semi-diurnal. Due to changes in the bathymetry, the amplitude U_0 of tidal velocities can vary with the alongshore coordinate x (see Fig.1.1b for a frame of reference). As a result of these amplitude variations, a mean current is generated aligned with the flow oscillations. To prove this statement, we first assume that the depth-averaged alongshore velocity $\langle u \rangle_z$ evolves according to

$$\langle u \rangle_z(x, t) = U_0(x) \cos \left(\frac{2\pi}{T_{M2}} t - \frac{2\pi}{\lambda_{M2}} x \right), \quad (1.3)$$

with T_{M2} and λ_{M2} the period and the wave length of the main tidal constituent (M2) respectively, and t the time. If we insert this expression in the alongshore advection

term of the Navier-Stokes equations, we obtain

$$\underbrace{\langle u \rangle_z \frac{\partial \langle u \rangle_z}{\partial x}}_{\substack{\text{alongshore} \\ \text{advection}}} = \frac{1}{2} U_0 \frac{\partial U_0}{\partial x} \left(\cos \left(\frac{4\pi}{T_{M2}} t - \frac{4\pi}{\lambda_{M2}} x \right) + 1 \right) + \frac{1}{2} U_0^2 \frac{4\pi}{\lambda_{M2}} \left(\sin \left(\frac{4\pi}{T_{M2}} t - \frac{4\pi}{\lambda_{M2}} x \right) \right). \quad (1.4)$$

Averaging this expression over a tidal period T_{M2} gives

$$\frac{1}{T_{M2}} \int_0^{T_{M2}} \underbrace{\langle u \rangle_z \frac{\partial \langle u \rangle_z}{\partial x}}_{\substack{\text{alongshore} \\ \text{advection}}} dt = \underbrace{\frac{1}{2} U_0 \frac{\partial U_0}{\partial x}}_{\substack{\text{residual} \\ \text{flow}}} \quad (1.5)$$

In the Rhine ROFI, this tidally-induced mean residual current is mainly directed parallel to the coastline in the Northeast direction, generally following the isobaths (Simpson et al., 1993).

The average predominant southwesterly winds also drive a northeastward directed flow, reinforcing the tidally-induced residual flow. However, wind conditions are highly variable and may create deviations in the mean flow pattern. Unfavorable wind directions can even cause a complete reversal of the residual flow direction (De Ruijter, Huber, & Backhaus, 1987).

Tidally-averaged density gradients

The Rhine discharges into the shallow Southern Bight of the North Sea. Consequently, considerable amounts of fresh water, interact with the saltier sea water. It is mainly the difference in salinity that leads to density differences. However, temperature differences between the Rhine waters and the Channel waters may also results in small-scale density differences. Globally, the isotherms follow the same pattern as the isohalines (de Kok, 1996) and the density differences generate a three-dimensional flow and density structure.

The density gradients are directed normal to the coast with isohalines and isotherms parallel to it. When the water column is well-mixed, the isohalines are vertical. This situation is sketched in Fig. 1.2. More generally, sharp fronts, eddy development, growing internal waves and a discontinuous vertical density profile are observed (de Kok, 1996). The density increases from relatively fresh water near the shore to more saline water further offshore. This horizontal gradient in density leads to a horizontal pressure gradient which drives a typical exchange flow. In this exchange flow, low density water is advected in the offshore direction at the surface which is compensated by higher density water moving in the onshore direction at the bottom: an estuarine circulation.

This type of circulation is characteristic of estuaries or coastal waters (van der Giessen et al., 1990) and it tends to induce (vertical) stratification, particularly in the absence of stirring mechanisms (Simpson, 1997). During times of large river runoff (>

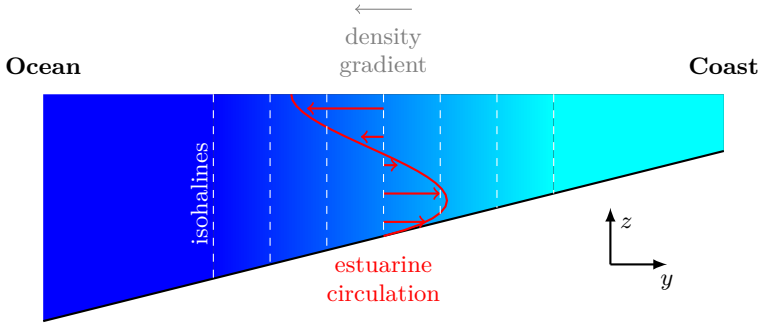


Figure 1.2: Density distribution in a cross-shore plane (y, z) for a well-mixed water column. The horizontal density gradient generates a typical exchange flow, the estuarine circulation, shown in red.

$1500 \text{ m}^3 \text{ s}^{-1}$) stratification is noticed 15 km away from the outflow points Haringvliet and Rotterdam Water Way. Two distinctive layers with a sharp interface are then formed.

The hydrodynamics are further strongly influenced by the wind conditions. Wind can inhibit stratification, by stirring the water column or by counteracting the estuarine circulation. In case of favorable direction, it can also increase stratification, on the basis of two mechanisms. First, the quicker response to anomalous wind forcing of the top layers in comparison to the lower layers leads to a more pronounced vertical structure (van der Giessen et al., 1990). The wind increases the magnitude of the flow in surface layers to a larger degree than in the bottom layers, so that fresh river water is advected faster offshore. Second, the proximity of the coast (Simpson, 1997) implies that no net flow in the cross-shore direction can take place, such that any wind-driven offshore flow of fresh water in the top layer has to be compensated by an onshore flow of saltwater in the bottom layer. As a result, strong upwelling wind, with a speed higher than 7 m s^{-1} (Münchow & Garvine, 1993) enhances stratification causing the buoyant water plume to move offshore near the surface and denser shelf waters to move onshore. As a result, stratification can be observed from the mouth of the Scheldt (30 km southwest of the Haringvliet) to even north of the Wadden Sea (de Kok, 1996).

Finally, the tidal flow has a global stirring effect (Simpson, 1997), which is mainly periodic. It influences the dynamics and dispersion of river water. The tidal streams depend usually on the topography and the shape of the coastline. They show a double periodicity: the semi-diurnal ebb-flood periodicity and the fortnightly spring-neap cycle. Depending on their magnitude, the strong tidal streams might mix up the plume completely. However, the longer the periods between stirring events, the more time stratification has to re-establish (Simpson, 1997).

1.3.2. Tidal currents and stratification: coupled processes with distinctive time scales

Observations of tidal velocities

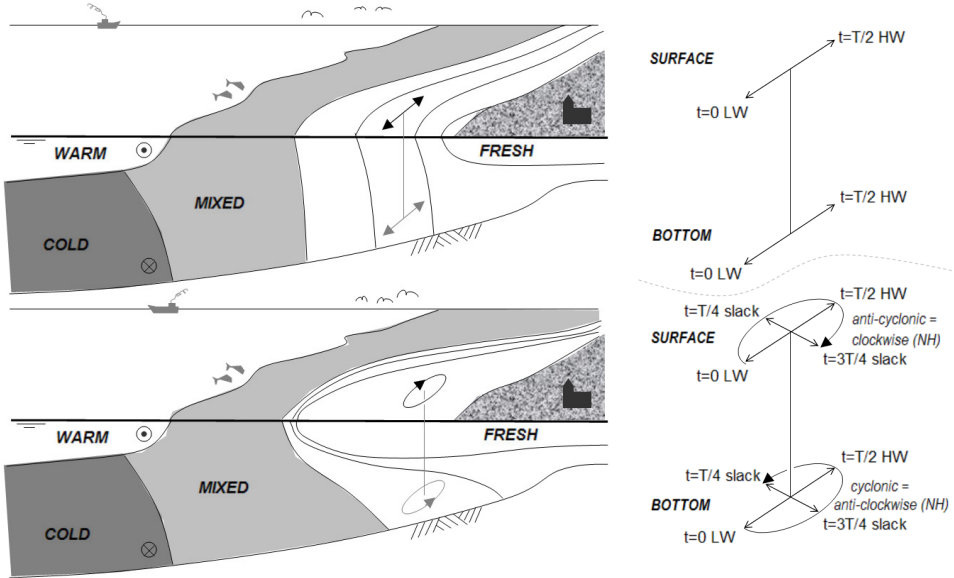


Figure 1.3: Tidal ellipses in the Rhine ROFI sketched by de Boer (2009) in a well-mixed situation (top left) and a stratified situation (bottom left). The paths described by the tidal velocity vector are enlarged on the right hand side and known as tidal ellipses. The velocity vector is explicitly shown at high-water (HW), low-water (LW) and slack tide.

As mentioned previously, the main tidal components in the Rhine ROFI are semi-diurnal. According to the Kelvin wave theory, water particles are expected to move back-and-forth along the Dutch coast. However, measurements revealed that the velocity vector of the tidal currents describes, in fact, an ellipse, which we call the tidal ellipse. The ellipticity of these ellipses changes both over depth and with the mixing ratio (i.e. homogeneous or stratified) of the water column (Visser et al., 1994). This process is illustrated in Fig. 1.3. The ellipticity is defined as the ratio between the semi-minor axis and the semi-major axis, such that the ellipticity of a circle is 1 and of a straight line is 0 (Visser et al., 1994).

In well-mixed conditions, the ellipses are degenerate (i.e. the ellipticity is very small) and the tidal currents are indeed almost rectilinear, parallel to the coast. A cross-shore component is observed, but it is very weak. The vertical variation between the ellipses in a water layer close to the bottom, and the ellipses in a water layer close to the surface is very small; the tidal ellipses are oriented in the same direction within 5° (Souza & Simpson, 1996; Visser et al., 1994).

In contrast, during stratified conditions, a significant cross-shore component of the tidal currents was observed. This cross-shore component leads to a strong elliptical path described by the vector of the tidal velocity. Furthermore, the alongshore

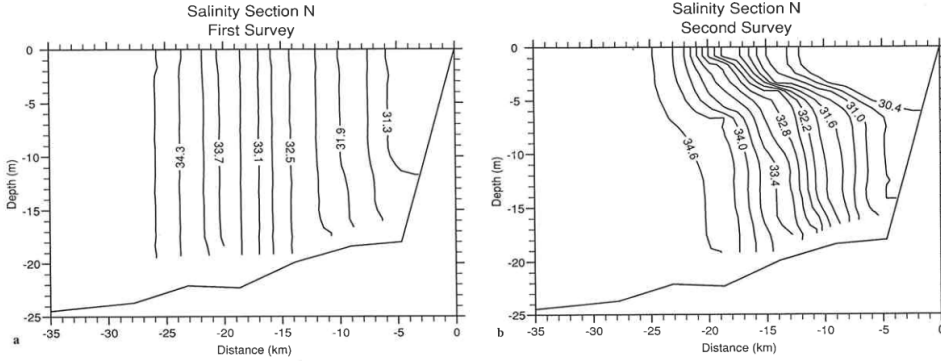


Figure 1.4: Periodic stratification identified through the lines of equal density (pycnoclines) measured during a survey along transect N (see Fig. 1.1b). a) Post spring tide survey (9 October 1990) and b) post neap tide survey (15 October 1990).

component of the top and bottom layer are out of phase by 180° . Additionally, the relative orientation of the tidal ellipses in the two layers also changes, and there is a bottom-surface orientation difference up to 15° or 20° (Souza & Simpson, 1996; Visser et al., 1994). The motion of the surface ellipses is strongly anti-cyclonic (clockwise in the Northern Hemisphere), whereas in the bottom layer, the motion becomes more cyclonic (anti-clockwise in the Northern Hemisphere).

Observations of stratification

Measurements of the mixing rate of the water column show strong variations which seem to be correlated with the tidal currents. As discussed previously, the large input of freshwater into the salty North Sea leads to stratification, which is modulated by stirring mechanisms such as tides and waves. As a result, the ROFI does not experience a seasonal periodicity of stratification due to heating-stirring competition, but more daily and weekly alternations due to the variability of river run-off, wind and wave stirring. In particular, the tidal cycle seems to impose two time scales during which the stratification pattern exhibits more structure (Simpson et al., 1993), a fortnightly time scale and a semi-diurnal time scale.

On a fortnightly time scale, mean stratification over a longer period is followed by complete vertical mixing. This process is illustrated by the surveys taken along N, a cross-section of the Rhine ROFI orthogonal to Noordwijk (see Fig. 1.1b). Figure 1.4a (taken from Simpson et al. (1993)) shows a well-mixed water column during the survey just after spring tide, while 1.4b shows a stratified water column during the survey just after neap tide.

The time series recorded at location A (see Fig. 1.1b) and reported by Simpson et al. (1993) show that changes in the mean stratification are correlated with the magnitude of the tidal velocity related to the spring-neap tidal cycle. This phenomenon can be explained by taking into account tidal stirring. The loss of energy E over time

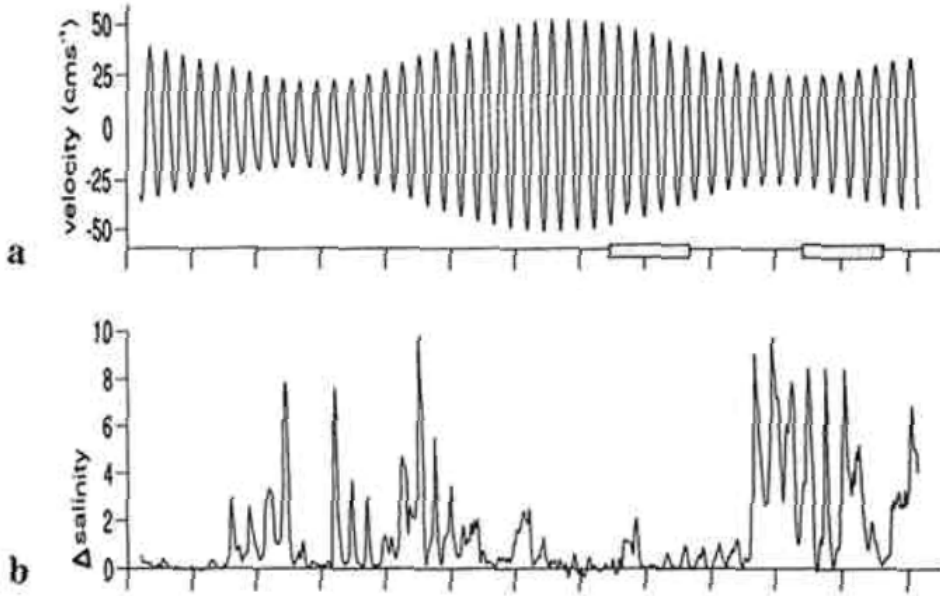


Figure 1.5: Time series of current velocity and mean stratification of the water column. The semi-diurnal oscillation and spring-neap cycle are clearly observed in the current velocity. These time series were recorded at mooring A (see Fig.1.1) and show: (a) the east-west tidal velocity 4m above the sea bed and (b) the salinity difference between 1 and 16m below the surface. This figure was taken from in (Simpson et al., 1993).

due to bottom friction can be written as

$$\frac{\partial E}{\partial t} = \overline{\tau_w u_w}, \quad (1.6)$$

where τ_w is the near-bottom friction (wall shear-stress), u_w the near-bottom velocity and $\bar{\cdot}$ denotes an ensemble average (Simpson & Hunter, 1974). Using a quadratic friction law for the velocity leads to $\partial E/\partial t \sim |\overline{u_w}|^3$, i.e. the tidal stirring power is proportional to the cubic power of the tidal velocity. As a result, changes in the magnitude of the tidal velocity, lead to more stirring, thus more mixing of the water column. As can be seen on Fig. 1.5, minimum velocities occur around neaps and the stability of the water column is observed to increase from well-mixed to maximum stratification several days later. As the stirring increases thereafter, stratification declines until complete vertical mixing around spring tide. Nevertheless, the reduction of mixing must reach a critical level in comparison to the buoyancy input in order to allow the onset of stratification (Simpson, Brown, Matthews, & Allen, 1990; Simpson, 1997).

Surprisingly, even during periods of large time-averaged stratification, the instantaneous stratification rate was observed to oscillate with a semi-diurnal frequency between very strong stratification and conditions of nearly full vertical mixing (Simpson & Souza, 1995; Simpson, 1997). These oscillations are very clear in Fig. 1.5a with minimum stratification occurring at the time of local low water (Simpson & Souza, 1995; Simpson, 1997). The amplitude of the oscillations in instantaneous stratification are in some cases of the same order as the time-averaged stratification, so that the water column is completely vertically mixed once per tide. The periods of mean and semi-diurnal stratification seem to be inextricably linked. Indeed, in the absence of time-averaged stratification there is no semi-diurnal cycle in instantaneous stratification (Simpson & Souza, 1995; Simpson, 1997).

The relation between changes in tidal currents and stratification.

In an open ocean, far from the coast and without stratification, tidal ellipses can be very well explained by Ekman theory. To this purpose, Prandle (1982a, 1982b) defined a complex number \mathbf{R} based on the two horizontal components of the velocity vector (u and v), following $\mathbf{R} = u + iv$, with i the imaginary unit. In a configuration of a flow forced by the tide and the Coriolis force, \mathbf{R} can be expressed as

$$\begin{aligned} \mathbf{R}(z, t) = & \left(R_{11} \exp\left(-i + 1\right) \frac{z}{\delta_+} \right) + R_{12} \exp\left(\left(i + 1\right) \frac{z}{\delta_+} \right) - \frac{i \|\mathbf{G}_1\|}{f + \omega} \Big) e^{i\omega t} \\ & + \left(R_{21} \exp\left(-i + 1\right) \frac{z}{\delta_-} \right) + R_{22} \exp\left(\left(i + 1\right) \frac{z}{\delta_-} \right) - \frac{i \|\mathbf{G}_2\|}{f - \omega} \Big) e^{-i\omega t}, \end{aligned} \quad (1.7)$$

i.e. the sum of an anti-clockwise rotating component and a clockwise rotating component (Gonella, 1972). In this solution, z is the vertical coordinate, R_{11} , R_{12} , R_{21} and R_{22} are integration constants and $\omega = 2\pi/T_{M2}$ is the tidal frequency. The quantities \mathbf{G}_1 and \mathbf{G}_2 are related to the surface elevation (i.e. the tidal forcing). Similarly to the velocity \mathbf{R} , Prandle (1982a, 1982b) defined a complex number \mathbf{G} being the sum of surface elevation gradient along x and i times the surface elevation gradient along y . The terms $\|\mathbf{G}_1\|$ and $\|\mathbf{G}_2\|$ are then the magnitudes of the counterclockwise and clockwise components of \mathbf{G} (for more details see Prandle (1982a) and App. A). Quite remarkable is the appearance of two different boundary layer thicknesses $\delta_+ = \sqrt{2\nu_T/(f + \omega)}$ and $\delta_- = \sqrt{2\nu_T/(f - \omega)}$ in Eq. (1.7). These boundary layer thicknesses are associated to the anti-clockwise and clockwise rotating components of the solution and depend on the eddy-viscosity ν_T (for more details, again see Prandle (1982a) and App. A). Prandle found that, over the depth of a water column, the clockwise component was more reduced due to frictional effects than the anti-clockwise one and that this reduction is maximum at the bed, explaining the differences in rotation direction between the top and the bottom ellipse.

However, this theory does not hold in the Rhine ROFI (see Fig. 1.3). During spring tide, the along-shore tidal motion is the strongest. As a result, according to the Ekman theory, strong cross-shore currents generating tidal ellipses, are expected. However, during spring tide, the tidal ellipses degenerate into a rectilinear motion. Therefore, a different explanation for the tidal tidal ellipses is required.

In the Rhine ROFI, the presence of the coast plays a determinant role, by preventing strong cross-shore currents. The coast implies that the tidally and vertically

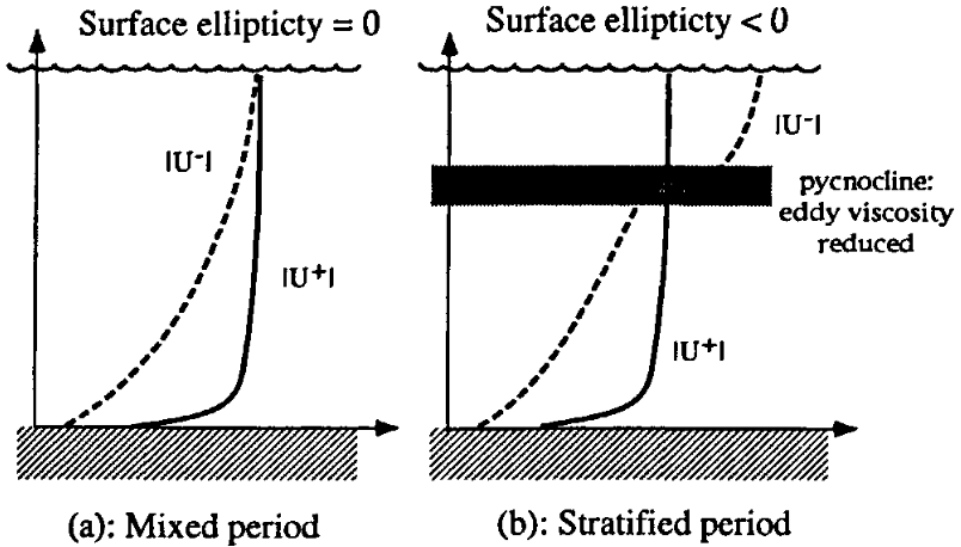


Figure 1.6: Conceptual sketch from Visser et al. (1994) showing the evolution over the depth of vertical structure of the magnitude of the cyclonic $|U^+| = \|\mathbf{R}_1\|$ and anticyclonic $|U^-| = \|\mathbf{R}_2\|$ rotary components of the tide for (a): well-mixed, (vertically uniform ν_T) and (b): stratified (ν_T reduced in the vicinity of the pycnocline) conditions. For the definitions of $\|\mathbf{R}_1\|$ and $\|\mathbf{R}_2\|$, the reader is referred to App. A.

averaged velocity in the cross-shore direction should be zero. However, Prandle's model ignores the presence of a coast. In fact, the presence of a coast should significantly reduce the cross-shore currents all the time, even during neap tide. The reason why the cross-shore currents related to the tidal ellipses occur during neap tide is explained by a second omission of Prandle's model: vertical variation in the eddy viscosity. Indeed, Prandle used a constant eddy viscosity model, which is a good approximation for a well-mixed water column, but a very poor approximation for a stratified water column. Visser et al. (1994) shows that the response of a two-layer model to a semi-diurnal tidal forcing depends to a large extent on the viscous coupling between the two layers. When the viscosity in the pycnocline is reduced, significant cross-shore velocities can occur in the upper layer, leading to clockwise tidal ellipses. Due to the proximity of the coast, a net zero flow is required in the cross-shore direction. As a result, the bottom current becomes strongly anti-clockwise to compensate for the clockwise motion of the surface current. This mechanism is sketched in Fig. 1.6. The model results are very consistent with what has been observed in the Rhine ROFI (Visser et al., 1994). During periods of stratification, vertical motions within the pycnocline are suppressed and so are the vertical eddies, inhibiting momentum transfer (Maas & van Haren, 1987). This reduced momentum transfer results in a reduction of the eddy viscosity.

Tidal straining

In the previous section, it is shown that the tidal ellipses in the Rhine ROFI are caused by the onset of stratification in the water column. However, a feedback mechanism, of the tidal ellipses on the stratification also exists. This feedback mechanism leads to the semi-diurnal oscillations of the stratification through the effect of differential advection on the horizontal density gradient. This process is called tidal straining, and is accompanied by the generation of strong fronts (Simpson et al., 1993; Simpson & Souza, 1995).

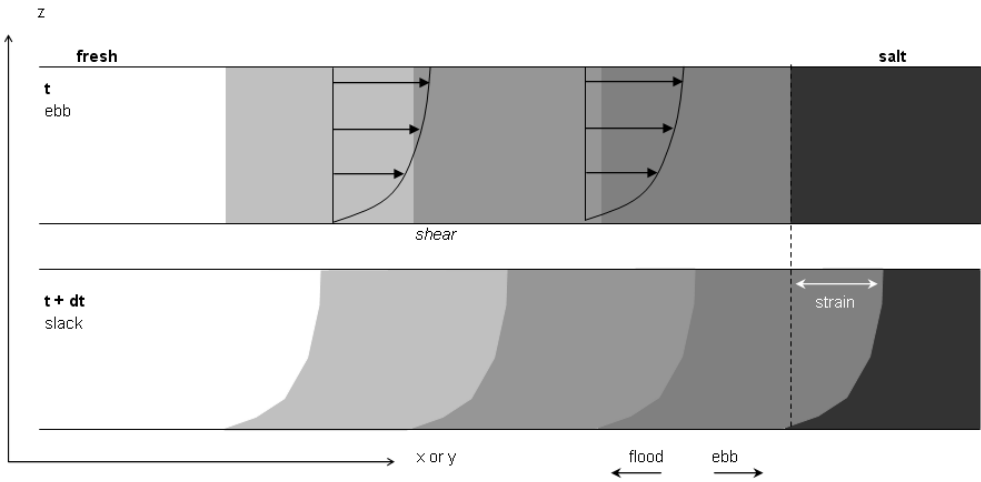


Figure 1.7: The tidal straining mechanism in a configuration in which the main tidal currents are aligned with the main horizontal density gradient, as sketched by de Boer (2009).

This mechanism of tidal straining can easily be understood if the main tidal currents are aligned with the horizontal density gradient. This situation is represented in Fig. 1.7. Initially, the water column is well-mixed. During ebb, the currents are directed offshore, but the velocity near the surface is larger than near the bottom. As a result, fresh-water is transported further offshore at the surface than at the bottom generating stratification by straining the density field. During flood, this process is reversed and freshwater is brought back onshore. In the case that the flood velocities are larger than the ebb velocities, unstable stratification might be generated, but would be immediately suppressed by convective overturning.

In the Rhine ROFI, the situation is more complex since the main tidal currents are orthogonal to the main horizontal density gradient. However, due to the tidal ellipses, significant cross-shore currents are present and the mechanism of tidal straining can be understood by combining the field observation of Simpson et al. (1993) and Simpson and Souza (1995), the model formulation of de Ruijter (1983) and the experimental results of Linden and Simpson (1986, 1988) and Simpson and Linden (1989). Under the influence of significant turbulent activity, even strong stratification can be destroyed as shown by the experiments of Linden and Simpson (1986, 1988). In such

a case, the effect of the river on the buoyancy distribution is restricted to the presence of a horizontal density gradient which corresponds to spring tide in the Rhine ROFI. When turbulence decays, the experiments Linden and Simpson (1986, 1988) show that isobars relax under gravity, accompanied by the generation of fronts in the form of an exchange flow. In a later experiment, Simpson and Linden (1989) used a configuration in which the shape and the magnitude of the horizontal density gradient was better controlled. They studied gravity currents generated by an initial horizontal density gradient. They investigated two different configurations. The first configuration had an initial constant horizontal density gradient. The second configuration had an initial piecewise constant horizontal density gradient. In the latter configuration the initial value of the density would increase at a certain constant rate along the streamwise horizontal coordinate, before abruptly increasing with a different constant rate. Simpson and Linden (1989) showed that only the second configuration would lead to the formation of fronts.

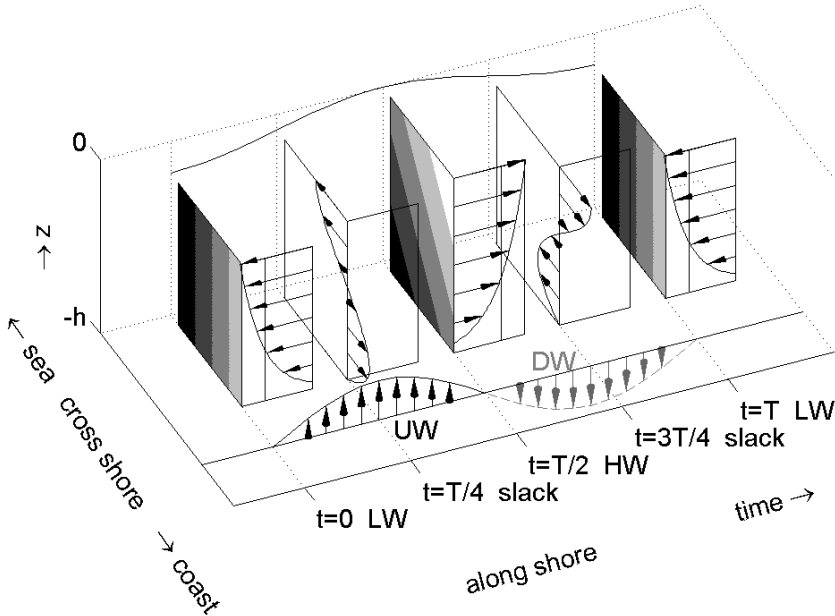


Figure 1.8: The tidal straining mechanism in the Rhine ROFI configuration as sketched by de Boer (2009). During neap tide, the upper and lower layer in the water column are uncoupled. Strong cross-shore currents can exist and stratify the water column during flood and destratify the water column during ebb. This process is accompanied by upwelling (UW) and downwelling (DW).

In the Rhine ROFI, the tidal ellipses are responsible for the shear that is necessary to generate the fronts (Simpson & Souza, 1995). The exchange flow relative to the tidal ellipses is stabilizing during flood and destabilizing during ebb. During flood, the flow in the top layer is oriented offshore, and the flow in the bottom layer is oriented onshore. The action of the shear generated by this exchange flow on the horizontal

density gradients generates stratification accompanied by fronts. The stratification is strained, potential energy is consumed, or mixed, and mechanical energy is created (Linden & Simpson, 1988; de Ruijter, 1983). During ebb, the situation is reversed. The flow in the top layer is directed onshore, and the flow in the bottom layer is directed offshore. The stratification is destroyed, not because of turbulent mixing, but because of differential advection. Mechanical energy is consumed and potential energy created. The semi-diurnal oscillations in the stratification rate of the water column are called strain induced periodic stratification (SIPS) and is shown in Fig. 1.8. It is accompanied by periods of upwelling and downwelling, as shown in sea surface temperature images (de Boer, Pietrzak, & Winterwerp, 2009).

1.4. Numerical simulations for ROFI studies

1.4.1. Traditional research tools

The literature involved in the description of the ROFI shows that field measurements are a primary source of information for the understanding of estuarine physics. Observations of physical processes (e.g. variations in the mixing rate of the water column, characteristics of tidal currents) during field measurements have led to the development of several theories (e.g. tidal straining, tidal ellipses) which were backed up by relatively simple conceptual models (Simpson & Souza, 1995; Visser et al., 1994). Nevertheless, while field measurements reflect processes that occur in the Rhine ROFI, there are two reasons for which additional knowledge is required. First, field measurements are often limited to a small number of discrete locations, which makes it sometimes difficult to link local observations to large-scale events. Second, field measurements offer no control of the system, so that recurrent manifestations such as SIPS can be obscured by sudden events such as changes in wind direction (Visser et al., 1994).

Recent studies of the ROFI's and other river plumes are still extensively based on measurement campaigns (Nash & Moum, 2005; Nash, Kilcher, & Moum, 2009; Flores, Rijnsburger, Horner-Devine, Souza, & Pietrzak, 2017; Flores et al., 2020; Horner-Devine et al., 2017; Rijnsburger et al., 2016; Rijnsburger, Flores, Pietrzak, Horner-Devine, & Souza, 2018). However, studies based on numerical model results are more and more common (de Boer, Pietrzak, & Winterwerp, 2006; Flores et al., 2018; Fischer, Burchard, & Hetland, 2009; MacCready, Banas, Hickey, Dever, & Liu, 2009; Vlasenko, Stashchuk, & McEwan, 2013). The amount and accuracy of the output data of simulations can be directly controlled by refining the computational domain. Subsequently, time series of quantities such as velocity or density can in theory be obtained at any desired location of this computational domain. Furthermore, physical processes (such as SIPS) can be isolated by switching off disturbing processes (such as wind or variable river discharge). A drawback of numerical simulations is that the data output is not related to events that 'really' happened. As a result, numerical models need to be calibrated on, or at least compared to, data from field measurements, so that they are considered trustworthy. Overall, numerical models and measurements should be considered as complementary to each other.

Besides being used in fundamental research, numerical models are also extensively used in engineering for their ability to forecast. For example, they can be employed to

predict the effect of changes in bathymetry (dredging activity) or boundary conditions (river runoff, sea-level rise) on the hydrodynamics and sedimentation processes. For this task, it is common practice to use large scale three-dimensional models covering an area much vaster than the actual region of interest. This approach was also utilized by de Boer et al. (2006), in which Delft3D (Delft3D-FLOW User Manual, 2003) was used, and by Flores et al. (2018), in which ROMS (Regional Ocean Model System) was used.

There are several reasons behind this choice for numerical modeling. First of all, these large regions allow to incorporate all the relevant physical processes. This factor is important since previous studies have shown that these processes are linked and interplay. Second, undesired boundary effects are believed to not influence the results as long as these boundaries are located sufficiently far away from the region of interest.

In contrast, an inconvenience of this approach is that it is computationally very expensive. As a result, several methods to reduce the computation time are applied. For example, the equations of motion governing the flow are transformed from three-dimensional Navier-Stokes equations to the shallow water equations. This transformation has the advantage of reducing the computational time, due to a different solving procedure in the vertical direction. However, due to this solving procedure, the set-up becomes quasi-two-dimensional at the cost of vertical resolution. Additionally, a Reynolds averaging approach can be used. In this approach, the Reynolds averaged Navier-Stokes equations (RANS) are solved for the mean value of the variables. Fluctuations related to turbulence are not resolved, but their contribution to the large-scale velocity field is parametrized. Accordingly, much coarser grid resolutions are possible at the price of loss of accuracy and detail.

A point of attention is that turbulence plays a determining role in the competition between mixing and stratification, as shown by the experiments of Linden and Simpson (1986, 1988). Accordingly, turbulence directly affects sediment transport, and water quality. Consequently, the reliability of the output of RANS simulations depends on the quality of the turbulence closures. The RANS approach can be described as seeking an approximate solution to an exact problem. The ‘problem’, i.e. the bathymetry and physics governing the flow are exact, but the ‘solution’, i.e. the average velocity field is approximate. A different procedure would be to seek an (almost) exact solution to an approximate problem. The uncertainty of the turbulence models is then bypassed by using a type of numerical model in which all the scales of turbulence, or at least the most important scales responsible for mixing, are resolved.

Numerical simulation methods in which only the large scales of turbulence are resolved are named Large-eddy Simulations (LES), while numerical simulations in which all the scales of turbulence are resolved are called Direct Numerical Simulations (DNS). The price to pay is again expressed in computational time, particularly for DNS. A way to overcome the computational time without sacrificing resolution is to model only a restricted region of the estuary, or in our study the ROFI, in which the important physical mechanisms subject of this study are represented.

A computational domain as depicted in the white bounded area in Fig. 1.9 (not to scale) would fulfill these requirements. It is located slightly offshore and slightly downstream of the river plume. This location is comparable with the location at which the transect near Noordwijk (the N survey) documented in Simpson et al.

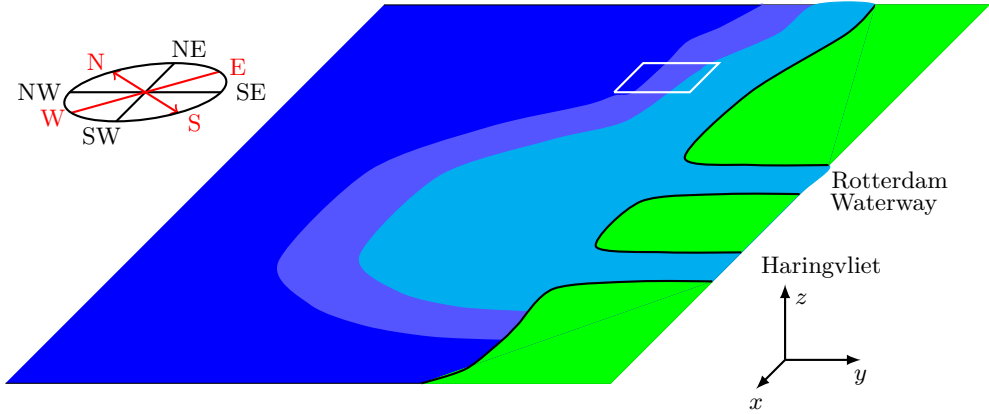


Figure 1.9: Idealization of the Rhine mouth, with the two branches (Haringvliet and Rotterdam Waterway) and the river plume deflected to the right, due to Coriolis force. The location of a DNS/LES computational domain is depicted by the white bounded area. Note that this area is only a sketch and is not too scale (the actual would be much smaller).

(1993) took place (also see Fig. 1.1b), at which observation data from a well-mixed post-spring water column, and a stratified post-neap water column were reported. A major challenge is to incorporate the necessary physical mechanisms in such a domain. These mechanisms should be idealized, such that the problem is ‘approximated’ but that the solution is ‘exact’ in DNS configuration, or ‘almost exact’ in case of the LES configuration.

1.4.2. State of the art DNS configuration

To investigate the competition between mixing and stratification in the Rhine ROFI, DNS/LES simulations should be able to reproduce the fortnightly and semi-diurnal oscillations in the stratification rate of the water column. Accordingly, the DNS/LES set-up requires all the necessary and sufficient ingredients governing this switching. Based on the literature study above, these ingredients are

- alongshore oscillations of the semi-diurnal ebb-flood tidal cycle;
- a turbulent boundary layer spanning the entire water column to provide sufficient turbulent mixing;
- fortnightly modulation of the turbulent mixing due to the spring-neap tidal cycle;
- horizontal momentum transfer between the alongshore and the cross-shore direction due to Coriolis force;
- horizontal, cross-shore density gradients driving cross-shore exchange flows, in turn generating stratification;

- the presence of a coast, forcing a zero depth integral of the cross-shore velocity profile.

Several other physical mechanisms influence the stratification pattern but are believed to be rather irrelevant for reproducing the periodic stratification events. These mechanisms include changes in water level, variations of the bathymetry, stirring effects of wind and waves, as well as residual currents driven by the Stokes drift of the Kelvin wave, the geostrophic balance or the average wind pattern over the North Sea.

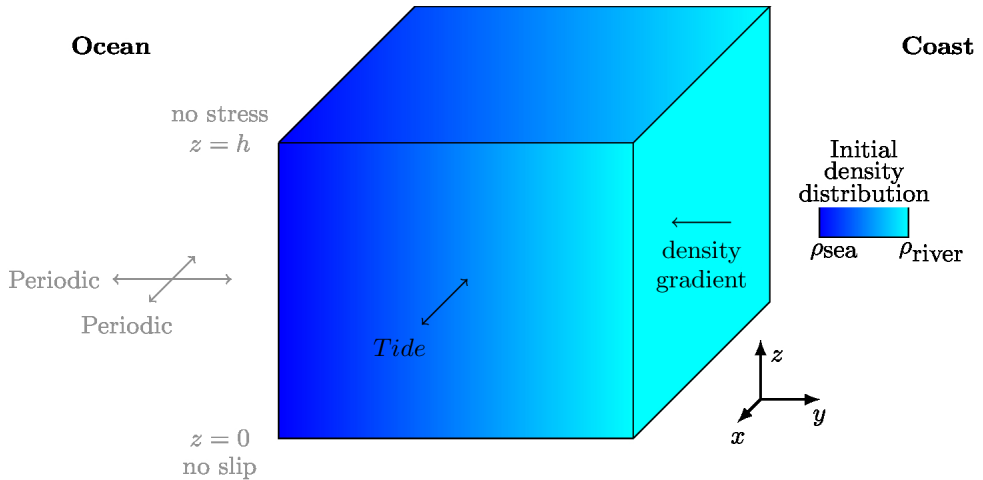


Figure 1.10: Sketch of the model domain of vertical size h , with the direction of the tide and the density gradient. The initial density distribution goes from sea-water density, ρ_{sea} (left) to river-water density, ρ_{river} (right). Horizontal boundary conditions are periodic. A no-slip condition is applied at the bottom ($z = 0$) and a no-stress boundary condition at the top ($z = h$)

As we will see below, several of the physical ROFI mechanisms governing SIPS in the North Sea have never been investigated using a schematized DNS/LES approach, or at least not in a satisfactory way. For example, the study of Li, Radhakrishnan, Piomelli, and Geyer (2010) suffered from an increase in stratification over the duration of the simulations. Therefore, substantial efforts to include these elements are necessary and it appears that fitting all the important physical ROFI components in the DNS/LES configuration is a giant leap. Unfortunately, giant leaps usually come with numerous challenges. These challenges are difficult to identify in advance, especially if they are not isolated nor considered individually. As a result, taking the leap at once makes the identification non-trivial and the subsequent implementation of the relevant processes very laborious. A better approach is to divide the giant leap into several smaller steps, that are taken and validated independently. The number and the direction of the steps is guided by the state of the art literature about the use of DNS/LES in modeling river outflow. The process starts by defining a suitable model for the main mechanism driving mixing (the tidal driven turbulence) and the main mechanism driving stratification (the river outflow).

In a Kelvin wave, which is the model for the tidal currents in the North Sea, the

tidal currents are directed alongshore, with the coast on their right (in the Northern Hemisphere). A flow driven by a homogeneous oscillating pressure gradient is an excellent model for this type of flow. Although this set-up does not take into account changes in the surface elevation, it reproduces the back-and-forth motion of the alongshore tidal currents in the Rhine ROFI. It has been used intensively in DNS/LES configurations (see among others Salon, Armenio, and Crise (2007); Radhakrishnan and Piomelli (2008), and a more detailed literature review in Chapters 2, 3 and 4). This type of oscillatory-flow set-up was also investigated under the influence of rotation (see among others Salon, Armenio, and Crise (2009); Salon and Armenio (2011); Momen and Bou-Zeid (2017); Sakamoto and Akitomo (2006, 2008)). Tidal ellipses were reproduced, particularly in the studies of Salon et al. (2009); Salon and Armenio (2011). However, in these studies, the set-up did not include the effects of stratification, and/or the presence of the coast. Accordingly, the observed tidal ellipses are related to Ekman boundary layer effects (Prandle, 1982a, 1982b), rather than to the exchange flows occurring under stratified conditions with reduced vertical motion in the pycnocline identified by Visser et al. (1994). In other studies, the oscillatory-flow set-up was combined with stratification (Gayen, Sarkar, & Taylor, 2010) and eventually with both stratification and rotation (Sakamoto & Akitomo, 2009). Nevertheless, these studies generally focused on scaling characteristics and scaling properties of the turbulent boundary layer. Accordingly, the water depth was chosen much larger than the thickness of the turbulent boundary layer and the simulation set-up was never in the Rhine ROFI parameter regime.

River outflows always generate horizontal density gradients in the cross-shore direction caused by the large input of fresh-water in a salty environment. This property is a major issue since the simplest set-up for DNS/LES simulations is a cubic computational domain with periodic horizontal boundary conditions, such as displayed in Fig. 1.10. A method to by-pass this issue, is to assume the horizontal density gradient constant and incorporate its effect as a body force in the momentum equations and a source term in the density equation. This approach was used by Li, Trowbridge, and Geyer (2008); Li et al. (2010), but the inconvenience is that it only works with significant turbulent mixing that is sufficient to destroy strong stratification. For weak turbulence, this approach fails, and the phenomenon of runaway stratification occurs (Blaise & Deleersnijder, 2008). As a result, the constant horizontal density gradient method cannot be used under its currents form for strongly stratified flows such as occurring in the Rhine ROFI.

1.4.3. Research question

The current advances in modeling estuarine physics with DNS/LES simulations imply that a complete DNS/LES model is too much of a giant leap. Instead, we will focus on two major ingredients of the mixing stratification competition and study them separately. The first question concerns the mixing process: what is the importance of the water depth on the structure of the turbulent boundary layer and its subsequent modeling? The second question involves the stratification process: how to improve the existing one-dimensional and three-dimensional models for exchange flows, so that they can handle the strongly stratified, and eventually turbulent regime?

In Chapter 3, we define an oscillating flow model that is closer to the Rhine ROFI,

by considering a configuration in which the turbulent boundary layer extends over the entire water depth. In particular, we first use a set-up in which the vertical dimension is large enough to contain the full turbulent boundary layer. Subsequently, we perform simulations with a smaller water depth than the previously defined boundary layer thickness. Accordingly, we investigate the effect of the reduced water depth on the turbulent boundary layer. In Chapter 4, we study the implication of this limited water depth on the validity of the boundary conditions usually applied in RANS type of models. More precisely, we thoroughly test the existence and properties of the logarithmic velocity profile.

In Chapter 5, we draw our attention to the stratifying processes by developing a new set of one-dimensional parametrizations for the horizontal density gradients. These new parametrizations are meant to overcome the problem of runaway stratification and to be able to simulate laminar exchange flows under strong stratification. In Chapter 6, the newly developed one-dimensional model is used to derive a velocity scale for density driven flows in inclined ducts, that converges towards the velocity scale for density driven flows in horizontal ducts, in the limit of small inclination angles. The velocity scale is eventually validated against experimental data. In Chapter 7, we implement and extend the one-dimensional parametrizations to three-dimensional flows. We simulate a strongly stratified exchange flow driven by a horizontal density gradient, characteristic of the Rhine ROFI.

The results show that the water depth plays a crucial role in turbulent oscillatory flows. A small water depth affects the balance between the oscillatory pressure gradient driving the flow, the viscous dissipation and the acceleration/deceleration term. As a result, it can change the amplitude and the phase lag of the velocity profile, and even lead to relaminarization. The logarithmic velocity profile is found to be present during large time-intervals in the oscillatory cycle. However, the duration of these intervals appear to be dependent on the value of the Reynolds number and on the ratio between the water depth and the boundary layer thickness. Additionally, the properties of the logarithmic layer are found to depend on these parameters, and on the phase. The new one-dimensional parametrizations for the exchange flow outperform the classic parametrization of the horizontal density gradient in which the latter is assumed constant. One-dimensional models reproduce well the velocity and density profiles from two-dimensional exchange flows, for a wide set of parameters. Finally, the implementation of the new parametrizations in three-dimensional models with periodic boundary conditions was successful. The simulated turbulent exchange flow was found to undergo several stages also reported in the literature. These stages include a stage in which Holmboe waves are observed and a stage in which turbulence is observed.

2

Numerical methods and flow configurations

To perform the high-resolution numerical simulations of inhomogeneous turbulent flows mentioned in the introduction, an adequate numerical software package is required. The software package used in this thesis, if not specified otherwise, is LES-Coast. LES-Coast is developed by the University of Trieste, and successfully used in several academic studies (Salon et al., 2007, 2009; Salon & Armenio, 2011; Roman, Stipcich, Armenio, Inghilesi, & Corsini, 2010; Galea et al., 2014; Lefauve, Partridge, & Linden, 2019b; Santo, Toffolon, Zanier, Giovannini, & Armenio, 2017). It is based on a combination of adequate numerical techniques and appropriate algorithms that are described hereafter. Additionally, suitable domain sizes and sufficient resolution are discussed for each of the two flow configurations, the oscillating flow and the density-driven flow, separately. Correct choices for these parameters strongly depend on the properties of the flow and geometry of the flow domain. LES-Coast offers the possibilities to solve the Navier-Stokes and continuity equation using two different techniques: (i) direct numerical simulations (DNS), and (ii) large-eddy simulations (LES). The difference between these two techniques is their approach for dealing with the smaller scales of the motion. Therefore, a brief description of fluid motion in turbulent flow is first given, to understand these differences, .

2.1. Direct numerical and Large-eddy simulations

A turbulent flow is characterized by the presence of numerous eddies of various sizes. The largest eddies belong to the macrostructure and scale directly with the characteristic length scales of the flow domain. This scale is denoted by \mathcal{L} . These eddies are generated by instabilities of the flow, and their dynamics are dominated by non-linear processes. They contain the most energy; they are responsible for mixing, and they are barely affected by viscosity. The large eddies successively break up into smaller eddies due to higher order instabilities. This process continues until the eddies are small enough for viscosity to play a significant role and dissipate the energy. The

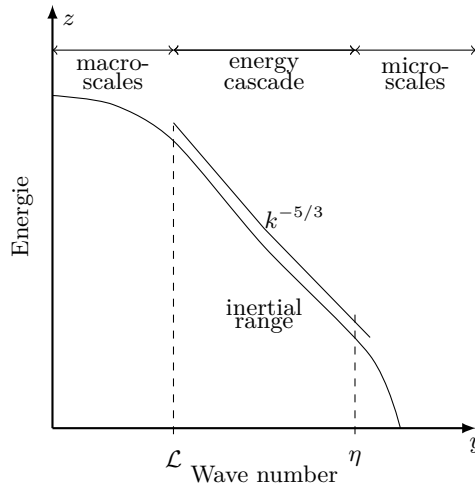


Figure 2.1: Schematized one-dimensional energy spectrum in logarithmic scale.

smallest eddies belong to the microstructure, to which we can associate a length scale η called the Kolmogorov scale, equal to $(\nu^3/\varepsilon)^{1/4}$, with ν the kinematic viscosity and ε the dissipation.

If we characterize the different eddies by their wave number, instead of by their length scale, we can sketch the energy $E(k)$ contained in each wave number range, between k and $k + dk$. The scaling of the energy as function of the wave number is given in Fig. 2.1. In this figure, the wave numbers belonging to the macroscale (small wave numbers) contain the most energy, while the wave numbers belonging to the microscale (large wave numbers) contain the smallest amount of energy and the energy is rapidly dissipated at the Kolmogorov scale. In between, in the inertial range, the energy decreases algebraically, according to $E(k) \propto k^{-5/3}$, in a process called the energy cascade. As stated previously, the key difference between DNS and LES is their way of dealing with the large wave numbers. In DNS, all the scales are resolved, theoretically up to the Kolmogorov scale. In LES, the scales until a certain wave number belonging to the energy cascade will be included. The smallest (and here discarded) scales are represented by the means of the subgrid-scale model. The excess of energy is then dissipated at sub-grid level using this subgrid-scale model.

Accordingly, on the one hand, the strength of DNS resides in the fact that all scales of motion are resolved, and that no extra model is used. The inconvenience is that, since the ratio of L/η is proportional to the Reynolds number value to the power $3/4$, the required resolution increases exponentially fast with the Reynolds number. As a result, high Reynolds number simulations are unfeasible with the current computational resources. On the other hand, LES resolves the largest scales of motion such that mixing processes are accurately reproduced and can be studied. The use of subgrid scale models allows for not resolving the smallest scales and can be used to save computation time. For more general details about turbulence, DNS

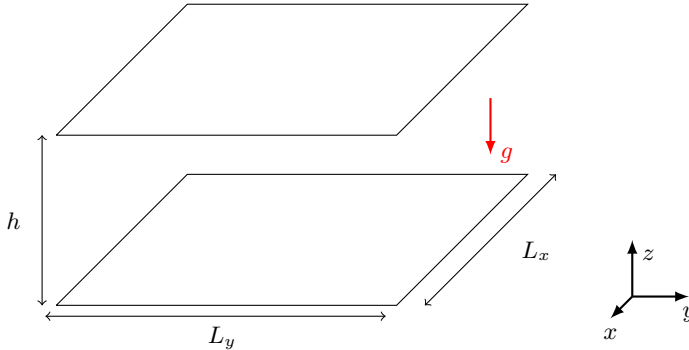


Figure 2.2: Standard computational domain for the three-dimensional DNS/LES used in this thesis. The domain is not on scale and the horizontal sizes of the domain, L_x, L_y , can vary depending on the flow configuration.

and LES techniques, the reader is referred to Nieuwstadt, Westerweel, and Boersma (2016); Sagaut (2006); Pope (2001); Geurts (2003).

2.2. Governing equations

The fluid motion is governed by the continuity equation for an incompressible fluid and the Navier-Stokes equations for conservation of momentum under the Boussinesq approximation (i.e. any variations in the density are small with respect to the average density and the density differences affect the flow through the buoyancy term only). In the $x_i = (x, y, z)$ reference frame, with z along the vertical, depicted in Fig. 2.2 they read

$$\frac{\partial u_i}{\partial x_i} = 0, \quad (2.1a)$$

$$\frac{\partial u_i}{\partial t} + \frac{\partial u_i u_j}{\partial x_j} = -\frac{1}{\rho_{\text{ref}}} \frac{\partial p}{\partial x_i} + \nu \frac{\partial^2 u_i}{\partial x_j^2} - \frac{\rho}{\rho_{\text{ref}}} g \delta_{i3} + F_i^{\text{b}}, \quad (2.1b)$$

in which t denotes time, $u_i = (u, v, w)$ the velocity in the x_i direction, p the pressure, ρ_{ref} the reference density, ρ the density variable, g the gravitational acceleration and F_i^{b} the different body forces (other than buoyancy) applied on the fluid. The symbol δ_{i3} represents the Kronecker delta (also represented thereafter as δ_{ij} , δ_{i1} or δ_{i2}) and Einstein's summation convention has been adopted for repeated indices. The exact expression of the body forces depends on the flow configuration and is detailed in Sec. 2.5.

The variations of the density ρ are described by an additional equation of state and one equation for transport of salinity. For convenience, a linear equation of state linking the density to salinity, and the equation of transport for salinity are combined in one equation describing transport of density

$$\frac{\partial \rho}{\partial t} + \frac{\partial \rho u_j}{\partial x_j} = \kappa \frac{\partial^2 \rho}{\partial x_j^2} + S^{\text{s}}, \quad (2.2)$$

in which κ is the kinematic diffusivity of salt and S^s represents the additional sources or sinks of density. Note that the equation of transport is only used in the density-driven flow configuration. In the oscillating flow configuration, the density is uniform and constant. The above set of equations, i.e. Eqs (2.1, 2.2), are used in the DNS configuration, implying that all scales of motion are resolved. However, some simulations are run in LES configuration obtained by applying a filtering operation to Eqs (2.1, 2.2). This filtering operator \tilde{G} is defined as

$$\tilde{f}(x) = \int f(\check{x})\tilde{G}(x, \check{x})d\check{x}, \quad (2.3)$$

where the integral is extended to the entire computational domain. The application of this filter to the governing equations leads to (Sagaut, 2006; Germano, Piomelli, Moin, & Cabot, 1991)

$$\frac{\partial \tilde{u}_i}{\partial x_i} = 0, \quad (2.4a)$$

$$\frac{\partial \tilde{u}_i}{\partial t} + \frac{\partial \tilde{u}_i \tilde{u}_j}{\partial x_j} = -\frac{1}{\rho_{\text{ref}}} \frac{\partial \tilde{p}}{\partial x_i} + \nu \frac{\partial^2 \tilde{u}_i}{\partial x_j^2} + F_i^b - \frac{\partial \tau_{ij}}{\partial x_j}, \quad (2.4b)$$

for the continuity and Navier-Stokes equations and

$$\frac{\partial \tilde{\rho}}{\partial t} + \frac{\partial \tilde{\rho} \tilde{u}_j}{\partial x_j} = \kappa \frac{\partial^2 \tilde{\rho}}{\partial x_j^2} + S^s - \frac{\partial \lambda_j}{\partial x_j}, \quad (2.5)$$

for the density equation. In these equations, $\tilde{\cdot}$ denotes a filtering operation. Accordingly, \tilde{u}_i ($\tilde{u}, \tilde{v}, \tilde{w}$) is the filtered velocity, \tilde{p} the filtered pressure and $\tilde{\rho}$ the filtered density. The subgrid scale (SGS) stresses for momentum and density are denoted by τ_{ij} and λ_j and verify (Germano et al., 1991)

$$\tau_{ij} = \widetilde{u_i u_j} - \tilde{u}_i \tilde{u}_j, \quad (2.6a)$$

$$\lambda_j = \widetilde{\rho u_j} - \tilde{\rho} \tilde{u}_j. \quad (2.6b)$$

2.3. Subgrid-scale stress model

In Section 2.2, the equation for the filtered variables are derived and the SGS τ_{ij} as well as the density flux λ_j are introduced. While running LES-Coast in DNS configuration, both τ_{ij} and λ_j equal zero and no other filtering other than the grid coarseness is applied. When run in LES-mode, several subgrid-scale models exist in literature for τ_{ij} and λ_j (Smagorinsky, 1963; Germano et al., 1991; Sagaut, 2006; Armenio & Piomelli, 2000; Lilly, 1992; Bardina, Ferziger, & Reynolds, 1980). We will focus here on the one that have been used in our simulations: the dynamic Smagorinsky model (Germano et al., 1991; Lilly, 1992).

The procedure to determine the parametrization of τ_{ij} and λ_j involves several steps which we detail below for the Navier-Stokes equation, following Germano et al. (1991). First, we define a second filter \hat{G} , called *test* filter as

$$\hat{f}(x) = \int f(\check{x})\hat{G}(x, \check{x})d\check{x}. \quad (2.7)$$

The width of filter \widehat{G} is assumed to be larger than the width of filter \widetilde{G} . Applying this new filter to Eqs (2.4) gives

$$\frac{\partial \widehat{u}_i}{\partial x_i} = 0, \quad (2.8a)$$

$$\frac{\partial \widehat{u}_i}{\partial t} + \frac{\partial \widehat{u}_i \widehat{u}_j}{\partial x_j} = -\frac{1}{\rho_{\text{ref}}} \frac{\partial \widehat{p}}{\partial x_i} + \nu \frac{\partial^2 \widehat{u}_i}{\partial x_j^2} + F_i^b - \frac{\partial T_{ij}}{\partial x_j}, \quad (2.8b)$$

with

$$T_{ij} = \widehat{u}_i \widehat{u}_j - \widetilde{u}_i \widetilde{u}_j, \quad (2.9)$$

the SGS stresses of the test filter. Subsequently, we define the resolved turbulent stresses as \mathcal{L}_{ij} as

$$\mathcal{L}_{ij} = \widetilde{u}_i \widetilde{u}_j - \widehat{u}_i \widehat{u}_j, \quad (2.10)$$

and consequently verifying

$$\mathcal{L}_{ij} = T_{ij} - \widehat{\tau}_{ij}. \quad (2.11)$$

If we assume that both T_{ij} and τ_{ij} can be parametrized using the same form, i.e.

$$\tau_{ij} - \tau_{kk} \frac{\delta_{ij}}{3} \approx -2C \widetilde{\Delta}^2 |\widetilde{S}| \widetilde{S}_{ij}, \quad (2.12a)$$

$$T_{ij} - T_{kk} \frac{\delta_{ij}}{3} \approx -2C \widehat{\Delta}^2 |\widehat{S}| \widehat{S}_{ij}, \quad (2.12b)$$

where C is a Smagorinsky like constant, and $\widetilde{\Delta}$ and $\widehat{\Delta}$ are the filter widths associated to \widetilde{G} and \widehat{G} . The quantities \widetilde{S} and \widehat{S} are the strain rate tensors corresponding to the filtered velocities

$$\widetilde{S}_{ij} = \frac{1}{2} \left(\frac{\partial \widetilde{u}_i}{\partial x_j} + \frac{\partial \widetilde{u}_j}{\partial x_i} \right), \quad (2.13a)$$

$$\widehat{S}_{ij} = \frac{1}{2} \left(\frac{\partial \widehat{u}_i}{\partial x_j} + \frac{\partial \widehat{u}_j}{\partial x_i} \right). \quad (2.13b)$$

The respective magnitudes of the strain rate tensors are

$$|\widetilde{S}| = \sqrt{2\widetilde{S}_{ij}\widetilde{S}_{ij}}, \quad (2.14a)$$

$$|\widehat{S}| = \sqrt{2\widehat{S}_{ij}\widehat{S}_{ij}}. \quad (2.14b)$$

Using Eqs (2.12a) and (2.12b) into Eq. (2.11), and applying plane averaging along x and y leads to an expression for the constant C (Germano et al., 1991; Lilly, 1992)

$$C(z, t) = -\frac{1}{2} \frac{\langle \mathcal{L}_{kl} \widetilde{S}_{kl} \rangle}{\widehat{\Delta}^2 \langle |\widetilde{S}| \widetilde{S}_{mn} \widetilde{S}_{mn} \rangle - \widetilde{\Delta}^2 \langle |\widehat{S}| \widehat{S}_{pq} \widehat{S}_{pq} \rangle}. \quad (2.15)$$

Finally, the subgrid-scale stresses can be expressed as

$$\tau_{ij} - \tau_{kk} \frac{\delta_{ij}}{3} \approx \frac{\langle \mathcal{L}_{kl} \tilde{S}_{kl} \rangle}{\widehat{\Delta}^2 / \widetilde{\Delta}^2 \langle |\widehat{S}| \widehat{S}_{mn} \widetilde{S}_{mn} \rangle - \langle |\widehat{S}| \widehat{S}_{pq} \widetilde{S}_{pq} \rangle} |\widetilde{S}| \widetilde{S}_{ij}. \quad (2.16)$$

2.4. Main algorithm of LES-Coast

The main algorithm of LES-Coast is based upon the algorithm described in Zang, Street, and Koseff (1994). Hereunder we briefly describe its important elements; the software package was already used and validated extensively (Salon et al., 2007, 2009; Salon & Armenio, 2011; Roman et al., 2010; Galea et al., 2014; Lefauve et al., 2019b; Santo et al., 2017). For extended details, the reader is referred to Zang et al. (1994).

The governing equations are discretized on a computational domain meshed by a non-staggered grid following Rhie and Chow (1983). The use of this type of grid implies that, in the computational space, the velocity variables \tilde{u}_i , the pressure variable \tilde{p} and the density variable $\tilde{\rho}$ are defined at the cell center. At the same time, the volume fluxes are defined at the mid-point of the corresponding cell faces (Rhie & Chow, 1983, see). This technique combines the benefits of a non-staggered grid, i.e. less equations to solve with respect to a staggered grid (Rhie & Chow, 1983), while not being affected by the decoupling between the pressure field and the velocity field (see Harlow and Welch (1965); Rubin and Harris (1975)). Equations (2.4, 2.5) are solved in curvilinear coordinates, such that the grid properties are absorbed in a Jacobian matrix (for the first order derivatives) and a ‘mesh skewness tensor’ (for the second order derivatives). For more details about the variable transformation, see Fletcher (1988); Zang et al. (1994). For the simulations carried out in the framework of this thesis, the grid is Cartesian, i.e. orthogonal and only stretched in the z direction. This means that all the metric tensors are reduced to diagonal tensors, which decreases the effective number of operation during each timestep.

Equations (2.4) are discretized using the finite-difference scheme with a second-order-explicit Adams-Bashforth method for the convective terms (respectively the advection terms in the density equation) and a second-order-implicit Crank-Nicolson method for the viscous terms (respectively the diffusive terms in the density equation), following Kim and Moin (1984). The body force term in the momentum equations is evaluated explicitly, while the source term in the density equation is evaluated using the same Adams-Bashforth discretization as the advection term. The stability limit of the viscous and diffusive terms is much more restrictive than the Courant-Friedrichs-Lewy (CFL) condition for the non-viscous terms. As a result the (semi)-implicit treatment of the viscous and the diffusive terms via the Crank-Nicolson scheme is imperative.

Mass conservation is ensured by integrating of the discretized system of equations using the fractional step method (Kim & Moin, 1984; Zang et al., 1994). In the fractional step method, an intermediate velocity \tilde{u}^* is introduced in the momentum equation. This procedure allows to split the original momentum equation into two equations. The first equation, the predictor equation, links the intermediate velocity \tilde{u}^* , to the terms depending on the velocities evaluated at time steps n and $n - 1$ (i.e.

\tilde{u}^n and \tilde{u}^{n-1}). It can be put under the form

$$M(\tilde{u}_i^* - \tilde{u}_i^n) = f_{rhs}(\tilde{u}^n, \tilde{u}^{n-1}), \quad (2.17)$$

where M is a tridiagonal matrix and f_{rhs} regroups the right hand side terms of the equation. It depends on $\tilde{u}^n, \tilde{u}^{n-1}$ but not on the pressure. This equation is solved by using the approximated factorization technique (see Kim and Moin (1984); Zang et al. (1994)): the tri-diagonal matrix M is written as the product of three diagonal matrices. The inversion of three diagonal matrices is computationally much cheaper than the inversion of a tri-diagonal matrix, while the error made by the approximation is of order $O(\Delta t)^3$.

The second equation, the corrector equation, ensures the conservation of mass. It links the intermediate velocity to the velocity u^{n+1} at the next time step $n + 1$ and the discretized pressure term. In contrast with the predictor equation, the corrector equation is rewritten at the cell face and can be put under the form

$$\tilde{U}_m^{n+1} = \tilde{U}_m^* - g_{rhs}(p^{n+1}). \quad (2.18)$$

where \tilde{U}_m^{n+1} and \tilde{U}_m^* are the volume fluxes defined at the cell faces, by linear interpolation of the velocity defined at the cell center. The function g_{rhs} represents the right hand side terms of the equation. It depends on the pressure. Continuity (i.e. mass conservation) is enforced by applying the requirement that the divergence of \tilde{U}_m^{n+1} to be zero.

Taking the divergence of Eq. (2.18) leads to an equation in which the only unknown variable is the pressure. The equation is then solved using a multi-grid successive over relaxation (SOR) method. Additionally, the code is parallelized in the spanwise direction using the Message Passing Interface (MPI) technique. Recently, the pressure solver (i.e. the bottleneck in terms of computational requirements) has also been parallelized in a second direction. This has made the algorithm roughly one order of magnitude faster according to our own tests.

Except when specified, the spatial discretization of all terms consists of centered differences, which are second order accurate in space. However, the convective and advective terms are susceptible to generate overshoots when discretized using standard centered differences. These overshoots have the potential to seriously alter the results. Accordingly, the implementation of a different advection scheme leading to significantly less overshoots was necessary: the SHARP scheme (see Leonard (1988); Choi, Nam, and Cho (1995); Zhu (1992)).

2.5. Simulation dependent settings

Two types of flow configurations are simulated in this thesis: the flow driven by an homogeneous oscillatory pressure gradient, and the flow driven by a homogeneous horizontal density gradient. The correct simulation of these two flows requires specific numerical settings according to the expected behavior and regime transition in each flow. Hereunder, we briefly present any important features of each flow as they are described in the literature. Based on these feature, we introduce the subsequently chosen numerical settings.

2.5.1. Oscillatory flow configuration: regime transitions

Oscillatory flows have been investigated intensively in the past, both experimentally (Jensen et al., 1989; Carstensen, Sumer, & Fredsøe, 2010; Chen, Chen, Tang, Stansby, & Li, 2007; Hino, Kashiwayanagi, Nakayama, & Hara, 1983) and numerically (Radhakrishnan & Piomelli, 2008; Salon et al., 2007; Costamagna, Vittori, & Blondeaux, 2003; Li, Sanford, & Chao, 2005; Spalart & Baldwin, 1989). For a long time, the focus of these studies was to establish the different regimes undergone by the flow, and to determine the Reynolds number at which these regimes changed (Hino et al., 1983; Jensen et al., 1989; Blondeaux & Vittori, 1994). Four different regimes were observed: the laminar regime (L), the disturbed laminar regime (DL), the intermittent turbulent regime (IT) and the turbulent regime (T) (Hino et al., 1983; Jensen et al., 1989; Costamagna et al., 2003; Salon et al., 2007). The exact threshold value of the Reynolds number governing the regime transition is difficult to determine with high accuracy (Hino, Sawamoto, & Takasu, 1976; Vittori & Verzicco, 1998). Discrepancies between the different studies were observed, and they could be related to the unsteady character of the flow, as well as to the symmetric properties of the oscillation cycle. For example, during the transition from the L to the DL regime, small disturbances appear due to shear instability (Hino et al., 1983). However, these disturbances cannot grow and are suppressed by the accelerating pressure gradient (Hino et al., 1983). In contrast, the transition from the DL regime to the IT regime is characterized by turbulence bursts at the beginning of the deceleration cycle (Hino et al., 1983). Nevertheless, during the subsequent acceleration cycle the flow may still be subject to relaminarization (Hino et al., 1983).

These features are fundamentally different from steady wall bounded flow. For steady flows, turbulence needs to be generated initially, but once present, it persists as long as the forcing remains unchanged. The mechanisms generating turbulence in oscillatory set-ups need to be adequately reproduced in numerical simulations: the spark generating the low-Reynolds number turbulent bursts needs to be sufficiently strong to overcome eventual damping effect of the pressure gradient. Accordingly, Blondeaux and Vittori (1994); Verzicco and Vittori (1996) showed that the presence of small wall imperfections could explain the transition from the L to the DL regime. The transition from the DL to the IT regime is less well understood. However, according to Vittori and Verzicco (1998); Akhavan, Kamm, and Shapiro (1991), the growth of three-dimensional perturbations is linked to the presence of large two-dimensional waves.

These events of turbulent burst and relaminarization (also referred to as ‘intermit-

tency’) put some serious requirements on the grid properties and eventual subgrid-scale stresses. Indeed, if the grid is too coarse or the subgrid scale stresses are too dissipative, it might delay the transition to turbulence or overestimate the relaminarization. On the other hand, if no mechanisms generating instabilities are included, the flow might remain laminar longer than necessary.

2.5.2. Oscillatory flow configuration: numerical settings

According to the available literature (Jensen et al., 1989; Hino et al., 1983; Vittori & Verzicco, 1998; Salon et al., 2007), regime transitions in oscillatory flows are governed by the Reynolds number Re_δ based on the Stokes boundary layer δ_s . This Reynolds number is defined by:

$$\text{Re}_\delta = \frac{U_0 \delta_s}{\nu}, \quad (2.19)$$

where

$$\delta_s = \sqrt{\frac{2\nu}{\omega}}. \quad (2.20)$$

The experimental and numerical set-ups of these studies were in a configuration in which the water depth was much larger than the thickness of the (turbulent) boundary layer. In contrast, this configuration is very different from the Rhine ROFI, in which the boundary extends over the entire water column. Unfortunately, there are very few studies (in fact, only Li et al. (2005) to our knowledge), that studied the effect of a reduced water depth on the flow driven by an oscillatory pressure gradient over a flat plate.

However, for a closely related configuration, the oscillatory pipe flow with a circular cross-section, an analogous effect was studied: the effect of the radius of the pipe on the flow. This effect is governed by the Womersley parameter (also referred to as Stokes parameter), which is defined as the ratio between the pipe radius and the Stokes boundary layer. Pipe flow studies indicated that the Womersley parameter affects the Reynolds number at which transition to turbulence occurs (Hino et al., 1976; Tuzi & Blondeaux, 2008; Lodahl, Sumer, & Fredsøe, 1998; Eckmann & Grotberg, 1991).

Although similar, the Womersley parameter is not exactly the same as the ratio between the water depth and the thickness of the Stokes boundary layer. The Womersley parameter is defined for a pipe flow of circular cross-section. As result, it is not only a measure for the distance between the ‘bottom’ and the ‘top’ of the flow section, but also of the curvature of the boundary normal to the flow direction. Therefore, it measures an additional effect (the curvature), which is absent in flows over flat plates.

Nevertheless, oscillatory flows over flat plates could experience the same delays in transition to turbulence as oscillatory flows in pipes, if the wall-normal dimension is reduced. Therefore, we conducted numerical simulations for three different values of the Reynolds number, and five different values of the ratio between the water-depth and the thickness of the Stokes boundary layer, h/δ_s . We choose $\text{Re}_\delta = 990, 1790$ and 3460 , and $h/\delta_s = 5, 10, 25, 40$ and 70 . These values are based on the available computational resources and the available experimental data needed for validation. In total 15 different parameter combination were studied (see Section 2.1).

From a mathematical point of view, the oscillatory motion of the flow can be obtained by a large-scale oscillatory pressure gradient along the x -coordinate. The

previously mentioned body force F_i^b is expressed as

$$F_i^b = \rho_{\text{ref}} U_0 \cos(\omega t) \delta_{i1}, \quad (2.21)$$

where U_0 and ω are the amplitude and the frequency of the free-stream oscillations, respectively, and δ_{i1} the Kronecker delta. In this flow configuration, Eqs (2.4), can be made non-dimensional by scaling x_i with the vertical length scale h , the velocity variables \tilde{u}_i with U_0 , the time t with h/U_0 , the pressure \tilde{p} with $\rho_{\text{ref}} U_0^2$ and the subgrid scale stresses τ_{ij} with U_0^2 . The resulting non-dimensional equations are

$$\frac{\partial \tilde{u}_i}{\partial x_i} = 0, \quad (2.22a)$$

$$\frac{\partial \tilde{u}_i}{\partial t} + \tilde{u}_i \frac{\partial \tilde{u}_j}{\partial x_j} = -\frac{\partial \tilde{p}}{\partial x_i} + \frac{1}{\text{Re}_\delta} \frac{\delta_s}{h} \frac{\partial^2 \tilde{u}_i}{\partial x_j^2} + \frac{2}{\text{Re}_\delta} \frac{h}{\delta_s} \cos\left(\frac{2}{\text{Re}_\delta} \frac{h}{\delta_s} t\right) \delta_{i1} - \frac{\partial \tau_{ij}}{\partial x_j}. \quad (2.22b)$$

Note that for conciseness, no differentiation in the notation was made between a dimensional variable and its non-dimensional counterpart. The size of the computational domain and the grid resolution was chosen based on previous studies (Costamagna et al., 2003; Salon et al., 2007). In most of the simulations, the computational domain was chosen with horizontal size of $65\delta_s$ in the streamwise direction (x) and $32\delta_s$ in the spanwise direction (y). Only for $\text{Re}_\delta = 1790$ or $\text{Re}_\delta = 990$ and $h/\delta_s = 5$ (i.e. simulations characterized by high intermittency), the domain was doubled in both horizontal directions, keeping the grid-spacing constant. The boundary conditions are periodic in the horizontal directions, a no-slip condition is applied at the bottom and a rigid-lid no-stress condition at the top. This means that dynamic vertical variations in the water level were neglected.

For the simulations with $\text{Re}_\delta = 1790$ or $\text{Re}_\delta = 990$ and $h/\delta_s = 5$ wall imperfections in the spirit of Blondeaux and Vittori (1994) are applied to favor retransition to turbulence after previous relaminarization. In order to resolve the wall-structures, the horizontal resolution in wall units, defined in dimensional form by $x_i^+ = x_i \nu / u_\tau$ (with $u_\tau = \sqrt{\tau_w / \rho_{\text{ref}}}$ the friction velocity and τ_w the wall shear stress and $x_i = (x, y, z)$), was chosen such that Δx^+ (streamwise) was less than $45z^+$ for the LES simulations and $12z^+$ for the DNS simulations (Piomelli & Balaras, 2002). The spanwise grid spacing Δy^+ was chosen to be at most $22y^+$ for the LES simulations and $14y^+$ for the DNS simulations. To have higher resolution close to the walls, the grid cells are stretched in the vertical direction with their size increasing with distance from the wall. The relative size difference between two adjacent cells was kept lower than 3%. This limit was set because a higher stretching would reduce the accuracy of the numerical algorithm. As a result, the cell size in the vertical direction increases from $\Delta z^+ = 2z^+$ to $\Delta z^+ = 22z^+$ (to $\Delta z^+ = 14z^+$ for the DNS simulations). Once the maximum grid spacing was reached, the grid spacing was kept constant in the remaining part of the domain. These criteria have been based on the estimated size of turbulence structures (Piomelli & Balaras, 2002; Pope, 2001) and results from previous studies (Costamagna et al., 2003; Salon et al., 2007).

For simulations characterized by a low h/δ_s ratio, time step convergence has been checked by decreasing the Courant number. This number is defined as $\max(u_i \Delta t / \Delta x_i)$,

with Δt the time step. It was found that the Courant number value of 0.6 gave converged results for all the simulations except for $\text{Re}_\delta = 1790$, $h/\delta_s = 5$ (i.e. simulations characterized by high intermittency) for which convergence was achieved for a Courant number equal to 0.3. Additionally, it has to be mentioned that the results for the simulations with $\text{Re}_\delta = 990$ and $h/\delta_s = 5$ were still highly grid dependent, probably because the flow relaminarizes through the whole cycle. Initial turbulence was generated by interpolating the velocity field from a converged turbulence simulation (either a plane channel flow or an oscillatory flow at lower resolution) for which the mean velocity was removed. The transient of the simulations takes several periods. Therefore, we started to average from period six to skip the transient regime (first five periods). The velocity profiles and other statistical quantities have been obtained by averaging over horizontal planes as well as by performing phase averaging. An overview of the simulation settings is given in Table 2.1.

Table 2.1: Numerical settings for each simulation. The symbols n_x , n_y and n_z are the number of grid cells in the streamwise, spanwise and vertical. The symbols L_x and L_y are the domain size in the streamwise and spanwise direction. The water depth is given by h , the thickness of the Stokes boundary layer by δ_s and the Reynolds number based on the Stokes boundary layer thickness by Re_δ .

Re_δ	h/δ_s	n_x	n_z	n_y	L_x/δ_s	L_y/δ_s	technique
990	5	512	64	512	130	64	DNS
990	10	256	80	256	65	32	DNS
990	25	256	144	256	65	32	DNS
990	40	256	208	256	65	32	DNS
990	70	256	352	256	65	32	DNS
1790	5	256	80	256	130	64	LES
1790	10	128	112	128	65	32	LES
1790	25	128	176	128	65	32	LES
1790	40	128	256	128	65	32	LES
1790	70	128	376	128	65	32	LES
3460	5	192	96	192	65	32	LES
3460	10	192	144	192	65	32	LES
3460	25	192	304	192	65	32	LES
3460	40	192	480	192	65	32	LES
3460	70	192	640	192	65	32	LES

2.5.3. Exchange flow configuration: regime transitions

Similarly to oscillatory flows, density-driven exchange flows have also been investigated previously. This research has mainly focused on the formation of fronts in transient currents, also called gravity currents (e.g. Benjamin (1968); Shin, Dalziel, and Linden (2004); Ottolenghi, Adduce, Inghilesi, Roman, and Armenio (2016); Ottolenghi, Adduce, Inghilesi, Armenio, and Roman (2016); Ottolenghi, Adduce, Roman, and Armenio (2017); Lefauve et al. (2019b)). Two reasons might explain this fact: (i) the difficulty to sustain a steady state density-driven flow for a significant

time, and (ii) the variation of the density in the streamwise direction of the flow. The first difficulty is associated with experiments. The second difficulty is associated with numerical simulations and the apparent incompatibility between density-driven flows and the horizontal periodic boundary conditions characteristic of most DNS simulations.

However, Meyer and Linden (2014); Lefauve et al. (2018, 2019a); Lefauve and Linden (2020a) were able to investigate density-driven flows more recently, in an experimental set-up with large salt- and fresh-water reservoirs connected by a channel. They added another degree of freedom to the system by allowing the channel to be tilted. They were able to sustain a steady flow for a significant time and identified four different regimes based on the inclination of the duct and the gravitational Reynolds number. This Reynolds number is defined as

$$\text{Re}_g = \frac{\sqrt{gh^3}}{\nu} \sqrt{\frac{\Delta\rho}{\rho_{\text{ref}}}}, \quad (2.23)$$

with $\Delta\rho$ the initial density difference between the two fluids brought in contact.

Linden and co-authors (Meyer & Linden, 2014; Lefauve et al., 2018, 2019a; Lefauve & Linden, 2020a) observed that for low values of the Reynolds number the flow was laminar. This regime is called the laminar regime. By increasing the tilting angle of the duct or the Reynolds number, characteristic cusped waves would appear at the interface. This regime is called the Holmboe wave regime. By increasing the tilting angle or the Reynolds number even further, the waves break down generating turbulence and mixing. The regime in which this break down is intermittent is called the intermittent regime, while the regime in which this break down is sustained is called the turbulent regime.

2.5.4. Exchange flow configuration: numerical settings

The reproduction of the regimes of a sustained density driven flow with a DNS simulation was until now not possible. As mentioned earlier, the required computational domain would be too large. Often, the requirements for the use of large computational domain are bypassed in DNS/LES configuration by restricting the computational domain to a small section of the total domain, and by applying horizontal periodic boundary conditions. This approach is successfully used hereafter for the oscillatory flow. However, it turned out to be incompatible with the horizontal density gradient and strong stratification, and no reformulation of the problem circumventing the need for a large computational domain was available.

As a result, recent DNS studies of steady exchange flows either focused on very weakly stratified exchange flow (Li et al., 2008, 2010), or on simulations in which the velocity profile and the density profile are imposed (Salehipour, Caulfield, & Peltier, 2016; Salehipour, Peltier, & Caulfield, 2018; Salehipour, Peltier, & Mashayek, 2015). However, using a new mathematical formulation developed during this PhD project, we were able for the first time to simulate a strongly stratified exchange flow with periodic boundary conditions. Hereafter, we briefly describe the mathematical formulation allowing these type of simulations. For more detail, and for a derivation of the mathematical model, the reader is referred to Chapter 7.

In the exchange flow configuration, the flow is driven by a large-scale horizontal pressure gradient along the y -coordinate, generated by a horizontal density gradient. Density plays an active role. As a result, the body force F_i^b is expressed as

$$F_i^b = -\frac{g}{\rho_{\text{ref}}} \left(\int_z^h \frac{\partial \bar{\rho}}{\partial y} d\tilde{z} - \frac{1}{h} \int_0^h z \frac{\partial \bar{\rho}}{\partial z} dz \right) \delta_{i2} \quad (2.24)$$

where ρ_r is the ‘resolved’ density and $\bar{\rho}$ is the horizontally averaged density. For more information about these quantities, the reader is referred to Chapter 7.

For the density-driven flow, Eqs (2.4), can be made non-dimensional by scaling x_i with the vertical length-scale h , the velocity variables \tilde{u}_i with U_g , the time t with h/U_g , the pressure \tilde{p} with $\rho_{\text{ref}} U_g^2$ and the density with the density difference $\Delta\rho$. The gravitational (or buoyancy) velocity scale U_g is defined as

$$U_g = \sqrt{\frac{\Delta\rho}{\rho_{\text{ref}}} gh}. \quad (2.25)$$

The non-dimensional equations are

$$\frac{\partial u_i}{\partial x_i} = 0 \quad (2.26a)$$

$$\frac{\partial u_i}{\partial t} + \frac{\partial u_i u_j}{\partial x_j} = -\frac{\partial p}{\partial x_i} + \frac{1}{\text{Re}_g} \frac{\partial^2 u_i}{\partial x_j^2} - \rho_r \delta_{i3} - \left(\int_z^1 \frac{\partial \bar{\rho}}{\partial y} d\tilde{z} - \int_0^1 z \frac{\partial \bar{\rho}}{\partial y} dz \right) \delta_{i2}, \quad (2.26b)$$

$$\frac{\partial \rho_r}{\partial t} + \frac{\partial}{\partial x_j} (\rho_r u_j) = \frac{1}{\text{ScRe}_g} \frac{\partial^2 \rho_r}{\partial x_j^2} - \bar{v} \frac{\partial \bar{\rho}}{\partial y}, \quad (2.26c)$$

in which some new symbols are introduced: the resolved density ρ_r (derived in Chap. 7), the horizontally averaged velocity in the y -direction \bar{v} and the Schmidt number Sc . In this configuration, only DNS simulations have been carried out. As a result, no subgrid-scale terms nor filtered variables appear. In these equations, two sets of non-dimensional numbers emerge, the Reynolds number Re_g and the Schmidt number Sc . The expression of the non-dimensional numbers is

$$\text{Re}_g = \frac{U_g h}{\nu}, \quad (2.27a)$$

$$\text{Sc} = \frac{\nu}{\kappa}. \quad (2.27b)$$

In reality, a third non-dimensional number also plays a role: the ratio Γ between the water depth and the length of the duct linking the salt water reservoir and the fresh water-reservoir. More details about these non-dimensional numbers is given in Chapters 5-7.

As mentioned above, very few numerical simulations of strongly stratified exchange flow exist. Since the present set-up is innovative, no bench-mark data was available to estimate the numerical settings required to perform simulations in specific regimes.

Both the size of the computation domain, and the resolution were arbitrary chosen, and evaluated a posteriori. Only one set of parameter values was simulated: $\text{Re}_g = 4 \times 10^5$, $\Gamma = 1/60$ and $\text{Sc} = 50$. The computational domain was chosen with horizontal size of 4π in the streamwise (y) direction and 2π in the spanwise (x) direction. The grid comprised 256 cells in each direction, and the non-dimensional time step was 5×10^{-3} .

3

Effect of the water depth on oscillatory flows over a flat plate: from the intermittent towards the fully turbulent regime

3.1. Introduction

As discussed in Section 1.4.2, the flow driven by an oscillatory pressure gradient is studied in this thesis as a model for purely tidal flows. Flows driven by an oscillating pressure gradient were studied extensively in the past (e.g. Jensen et al. (1989); Salon et al. (2007); Costamagna et al. (2003)). However, the majority of these studies were performed in experimental set-ups or computational domains where the water depth h was much larger than the thickness of the turbulent boundary layer δ . To evaluate if this model is a good approximation of the Rhine-ROFI, it is necessary to estimate the thickness of the turbulent boundary layer in the Rhine ROFI and compare it to the average water-depth. The first step is to estimate the thickness of the boundary layer δ that would exist in an infinitely deep water column, i.e. if $h \gg \delta$. According to Jensen et al. (1989); Salon et al. (2007), δ is defined as the height at which the velocity is maximum for the phase $\omega t = \pi/2$, where ω is the angular frequency and t the time. This phase is defined relatively to the free-stream velocity $U_\infty = U_0 \sin(\omega t)$, with U_0 the amplitude of U_∞ . This definition is valid for both experiments (Jensen et al., 1989) and numerical simulations (Salon et al., 2007). Jensen et al. (1989) determined the values of δ as a function of the Reynolds number using experimental data. They plotted the non-dimensional boundary layer thickness $\delta\omega/U_0$ as a function of the Reynolds number based on the free-stream velocity, Re_s (see their Fig. 24).

Table 3.1: Recapitulation of the turbulent tidal boundary layer thickness in the Rhine estuary for spring tide and neap tide. The results are obtained for a tidal period $T_{M2} = 12.42$ h (Zimmerman, 1986), a tidal angular frequency $\omega = 1.41 \cdot 10^{-4} \text{ s}^{-1}$, a kinematic viscosity $\nu = 1.14 \cdot 10^{-6} \text{ m s}^{-1}$, a non-dimensional boundary layer thickness $\delta\omega/U_0 \sim 5 \cdot 10^{-3}$ (Jensen et al., 1989) a depth $h = 20$ m, and the velocity measurements of van der Giessen et al. (1990) to estimate U_0 .

	U_0 (m s ⁻¹)	Re_{fs}	δ (m)	h/δ
neap tide	0.7	$3.06 \cdot 10^9$	24.88	0.51
spring tide	1.1	$7.55 \cdot 10^9$	39.11	0.80

An example of tidal flow in which $\delta > h$ can be found along the Dutch coast, around the mouth of the river Rhine. In this region, the tidal flow takes the form of a Kelvin wave (Van Alphen, De Ruijter, & Borst, 1988), and the boundary layer extends over the entire water depth (de Boer, 2009). Under unstratified conditions, the tidal currents are therefore rectilinear along the coast (Visser et al., 1994; Simpson et al., 1993), making them a prototype of an environmental oscillatory flow. In this case, Re_{fs} can be estimated using measurements of the surface velocity (see Table 3.1) and according to the expression $\text{Re}_{fs} = U_0^2/(\omega\nu)$, where ν is the kinematic viscosity. The values of Table 3.1 combined with an extrapolation of the scaling graph by Jensen et al. (1989) give a non-dimensional boundary layer thickness $\delta\omega/U_0 \sim 5 \cdot 10^{-3}$. As a result, $0.51 \lesssim h/\delta \lesssim 0.80$, i.e. the theoretical boundary layer is larger than the water depth.

However, this scaling law is based on experiments and simulations in which the water depth was much larger than the thickness of the turbulent boundary layer, and this is not the case in the example of the Rhine estuary above. Previously, the influence of a reduced water depth on an oscillatory flow has only been briefly investigated by Li et al. (2005). He showed in a preliminary study that a reduced water depth greatly influences the momentum balance between the pressure gradient, the local acceleration of the flow, and the wall shear stress.

To obtain more insight into the effect of shallowness on oscillatory flows, we propose to study a simplified model in which the effect of the water-depth has been isolated. In particular, we focus on flows within the intermittent turbulent regime reaching the start of the fully turbulent regime. This choice has led to a simplified approach in which variations in the surface elevation and the bottom roughness have been neglected. These choices are further motivated in the discussion section. We performed a series of idealized simulations in which the tidal forcing is modeled by a horizontal uniform oscillating pressure gradient:

$$\frac{\partial P}{\partial x} = -\rho_{\text{ref}} U_0 \omega \cos(\omega t), \quad (3.1)$$

with P the pressure, ρ_{ref} the density, x the streamwise direction and U_0 the previously mentioned amplitude of the free-stream velocity. This approach has been used in Li et al. (2005); Radhakrishnan and Piomelli (2008); Salon et al. (2007), and the simplicity of such a numerical set-up allows easy comparisons with experiments in similar configurations (Carstensen et al., 2010; Jensen et al., 1989). We have simulated

the oscillatory flow for three different values of the Reynolds number

$$\text{Re}_\delta = \frac{U_0 \delta_s}{\nu} \quad (3.2)$$

based on the thickness of the Stokes boundary layer $\delta_s = \sqrt{2\nu/\omega}$. Note that this definition differs from that of δ which was previously defined as the depth of the velocity maximum at $\omega t = \pi/2$. In fact, this depth in the laminar case is given by $\delta = \frac{3}{4}\pi\delta_s$ (Carstensen et al., 2010). The chosen values for Re_δ ($\text{Re}_\delta=990, 1790$ and 3460) correspond to tests 6, 8 and 10 in the study of Jensen et al. (1989). For each value of Re_δ , we varied the ratio h/δ_s from 5 to 70.

In the remaining part of this manuscript, we first briefly present a laminar analytical solution. Afterwards, we describe the numerical model and the set-up. Finally, we expose our numerical results on the turbulent flow in shallow water environments through a study of mean velocity profiles, the mean wall shear stress, and the depth-integrated turbulent kinetic energy (TKE).

3.2. Laminar solution

In the laminar case, the flow is governed by the simplified Navier-Stokes equations,

$$\frac{\partial u}{\partial t} = \nu \frac{\partial^2 u}{\partial z^2} + U_0 \omega \cos(\omega t), \quad (3.3)$$

in which the streamwise velocity u depends on the vertical coordinate z (positive upwards) and on time. This equation can be rewritten as

$$\frac{\partial u}{\partial t} = -\frac{1}{\rho_{\text{ref}}} \frac{\partial P}{\partial x} + \frac{1}{\rho_{\text{ref}}} \frac{\partial \tau_s}{\partial z}, \quad (3.4)$$

where τ_s represents the shear stress defined as $\tau_s = \rho_{\text{ref}}\nu(\partial u/\partial z)$. In order to analyze the influence of the reduced water depth on the velocity profile, the analytical solutions to equation (3.3) can be studied via: (i) a phase difference Φ , and (ii) a change in the amplitude A . Both Φ and A are defined with respect to the free-stream velocity U_∞ , i.e. the time-signal of the velocity infinitely far away from the bottom wall. For more details about the analytical solutions, the reader is referred to Appendix B. Since the flow is investigated in terms of velocity profiles, water depth and wall shear stress, three different phase shifts and three different amplitudes are considered: Φ_∞ , $\Phi_{h,f}$ and Φ_τ , and A_∞ , $A_{h,f}$ and A_τ . The shift Φ_∞ and the amplitude A_∞ are not related to a reduced water depth. They simply denote the phase shift and amplitude of the infinite velocity profile as a function of the position z in the water column; the shift $\Phi_{h,f}$ and amplitude $A_{h,f}$ denote the phase shift and the amplitude of the surface velocity signal in a reduced water depth configuration as a function of the total water-depth h ; shift Φ_τ and amplitude A_τ denote the phase shift and the amplitude of the wall-shear stress signal in a reduced water depth configuration as a function of the total water-depth h .

As expected, the phases and amplitudes change with changing depth. Figure 3.1 shows these different phase shifts (i.e. positive phase differences Φ) defined with

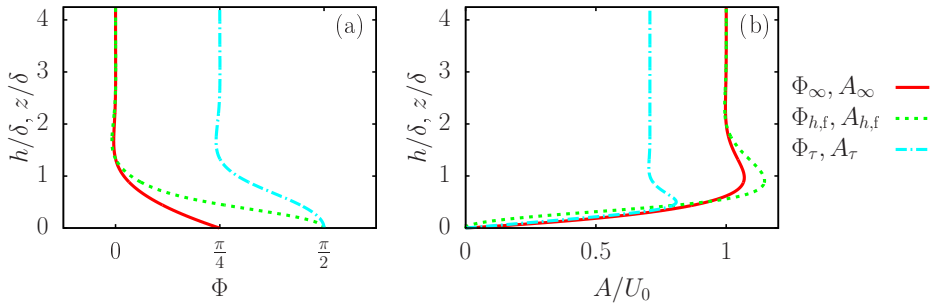


Figure 3.1: Phase shift (a) and the amplitude (b) of the surface velocities and the wall shear stress with respect to U_∞ . Note that Φ_∞ and A_∞ are function of z/δ while $\Phi_{h,f}$, Φ_τ , $A_{h,f}$ and A_τ are function of h/δ .

respect to U_∞ as a function of z/δ (for Φ_∞) or h/δ (for $\Phi_{h,f}$ and Φ_τ). This figure also shows of A_∞ , $A_{h,f}$ and A_τ . From Fig. 3.1, it can be seen that the influence of the water-depth on the velocity phase and amplitude becomes significant from $h \lesssim 2\delta$. For a general description, four different cases can be identified.

Case 1: $h \gtrsim 2\delta$. The wall shear stress leads the free-stream velocity by an angle $\Phi_\tau = \pi/4$. The momentum balance is mainly between the local acceleration and the pressure gradient. When h decreases, the phase shifts and amplitudes remain constant but the contribution of the wall shear stress to the momentum balance becomes increasingly more important

Case 2: $\delta \lesssim h \lesssim 2\delta$. When $h \sim 2\delta$, the velocity profile changes to accommodate to the no-stress boundary condition at the free-surface which results in slight adjustments of $\Phi_{h,f}$, Φ_τ and $A_{h,f}$. When h approaches δ , the amplitude of the free surface velocity $A_{h,f}$ reaches a maximum and the phases $\Phi_{h,f}$, Φ_τ increase significantly. This is due to the size reduction of the upper water layer lying in between the heights $z = \delta$ and $z = h$. As this upper layer is resisting via viscous forces the motion of the lower water layer, lying between $z \lesssim \delta$, its size reduction implies a reduction of its damping effect on the lower such that $A_{h,f}$ can reach a maximum.

Case 3: $h \lesssim \delta$. First, the increasing amplitude of the velocity generates higher gradients close to the wall resulting in an increase in the shear stress amplitude A_τ . Second, when h becomes too small, the oscillating boundary cannot fully develop anymore: $A_{h,f}$ and A_τ both decrease towards zero. At the same time, $\Phi_{h,f}$ and Φ_τ keep increasing until they converge to $\pi/2$.

The analytical laminar solutions give an overview of the influence of the water depth on the oscillating boundary layer in the laminar regime. It is also a model for turbulent flows if the eddy viscosity is considered constant. Nevertheless, a constant eddy viscosity is not realistic (see the plane averaged eddy viscosity calculations of Salon et al. (2007, 2009); Salon and Armenio (2011)). In order to investigate the

turbulent oscillatory flow accurately, we performed numerical simulations which we describe in the following sections.

3.3. Numerical set-up

In high resolution numerical simulations, the value of the Reynolds number that can be achieved is limited by computational requirements. In fact, the value for most tidal flows cannot be reached with the current day resources. This is also the case for the Rhine estuary: the characteristics of the Rhine estuary presented in the introduction (i.e. $\omega = 1.41 \cdot 10^{-4} \text{s}^{-1}$; $\nu = 1.14 \cdot 10^{-6} \text{m}^2 \text{s}^{-1}$ and $0.7 \text{m s}^{-1} \leq U_0 \leq 1.1 \text{m s}^{-1}$) suggest $\text{Re}_\delta \sim 10^5$. The highest Reynolds number that we can compute with the present day resources at a satisfactory resolution is $\text{Re}_\delta = 3460$, and this is also the highest value of Re_δ for which experimental data is available. A similar 'down-scaling' approach has already been used by Salon et al. (2009) to study turbulence in an oscillatory flow subjected to rotation. Simulations with $\text{Re}_\delta = 1790$ (using large eddy simulations, abbreviated 'LES') and $\text{Re}_\delta = 990$ (using direct numerical simulations, abbreviated 'DNS'), have also been performed to investigate the influence of this parameter on the flow, between the laminar and fully turbulent flow. For these values of the Reynolds number, either fully developed turbulence (for $\text{Re}_\delta = 1790$) or intermittent turbulence (for $\text{Re}_\delta = 990$) is present (Costamagna et al., 2003; Salon et al., 2007), although not throughout the full tidal cycle.

The equations governing the flow were given by Eqs (2.22) in Sec. 2.5.2. The simulations at $\text{Re}_\delta = 1790$ and $\text{Re}_\delta = 3460$ are performed with LES, while the simulations at $\text{Re}_\delta = 990$ are performed in DNS (i.e. with finer resolution and $\tau_{ij} = 0$). This is motivated by the fact that, although the dynamic Smagorinsky model proved to give excellent results for highly unsteady flows (Scotti & Piomelli, 2002), it is not able to reproduce well the relaminarization occurring at the lower Reynolds number of $\text{Re}_\delta = 990$ (Salon et al., 2007).

3.4. Results

3.4.1. Validation against experimental data

The data of Jensen et al. (1989) was used to validate several numerical simulation studies with similar set-ups to ours, including Costamagna et al. (2003) (for $\text{Re}_\delta = 990$), Salon et al. (2007) (for $\text{Re}_\delta = 3460$) and Radhakrishnan and Piomelli (2008) (for $\text{Re}_\delta = 3460$). Jensen et al. (1989) performed their experiments in a U-shaped water tunnel with a 10m long working section, a 0.39m width and a 0.28m depth. The velocities were measured with two laser-Doppler anemometers, and the wall shear stress with a hot film probe using a sample interval of 14 and 48ms within an oscillating cycle of 9.72s (i.e. 200 to 600 samples per cycle). For more details about the experimental set-up, the reader is referred to Jensen et al. (1989).

Among the several numerical studies, the one of Salon et al. (2007) used a previous version of our code. Salon and co-authors extensively compared their numerical results at $\text{Re}_\delta = 1790$ and $h/\delta_s = 40$ to the experimental results in terms of wall shear stress, velocity profiles, turbulence intensities and Reynolds shear stresses, and they claimed a very good agreement except for some discrepancies between some of the

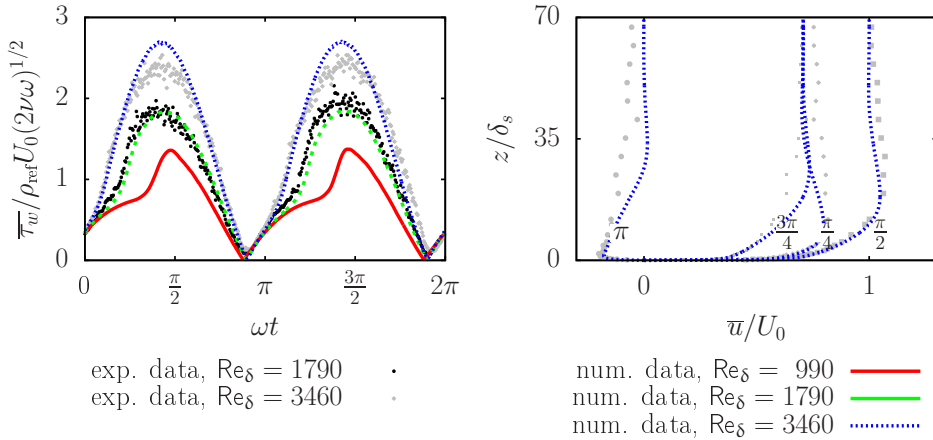


Figure 3.2: Comparison between the results of the numerical simulations and the data from the experimental results of Jensen et al. (Jensen et al., 1989). On the left hand side (a) the numerically computed, plane and phase averaged wall shear stress is displayed for the three values of the Reynolds numbers in the largest depth configuration (i.e. $h/\delta_s = 70$). On the right hand side (b), the plane and phase-averaged velocity profiles for $\text{Re}_\delta = 3460$ and $h/\delta_s = 70$ are shown for $\omega t = \{\pi/4, \pi/2, 3\pi/4, \pi\}$. Wall shear stress data for $\text{Re}_\delta = 990$ was not available.

numerical and experimental turbulent intensities. Since our simulations at $\text{Re}_\delta = 3460$ are the first simulations at this high Reynolds number value for which the wall layer is resolved (in Radhakrishnan and Piomelli (2008) a wall model was used), we display the wall shear stress and four velocity profiles in Fig. 3.2 together with the available data of Jensen et al. (1989). Note that $\bar{\tau}$ denotes a plane and phase-averaged quantity. The wall shear stress agreement is excellent for $\text{Re}_\delta = 1790$ and very good for $\text{Re}_\delta = 3460$ except that the maximum in the numerical signal is slightly higher than the maximum in the experimental signal. This feature was also observed by Radhakrishnan and Piomelli (2008) and the difference is consistent with the rounding performed by Jensen et al. (1989) (private communication) to compute the value of the Reynolds number.

The agreement of the velocity profiles is also excellent in the wall region but differs non-negligibly higher in the water column. We can however argue about the accuracy of the experimental data higher in the water-column. Indeed, far from the wall, the surface velocity evolves as $\sin(\omega t)$ and the velocity profiles at $\omega t = \pi/4$ and $\omega t = 3\pi/4$ should coincide. This concurrence is observed in the numerical profiles but not in the experimental data. Furthermore, the divergence between numerical and experimental results are also visible in the modelled wall simulations of Radhakrishnan and Piomelli. A possible explanation of these discrepancies is that the experimental set-up does not lead to a perfectly symmetric flow as suggested by the authors themselves in Sumer, Laursen, and Fredsøe (1993) and later pointed out by Salon et al. (2007).

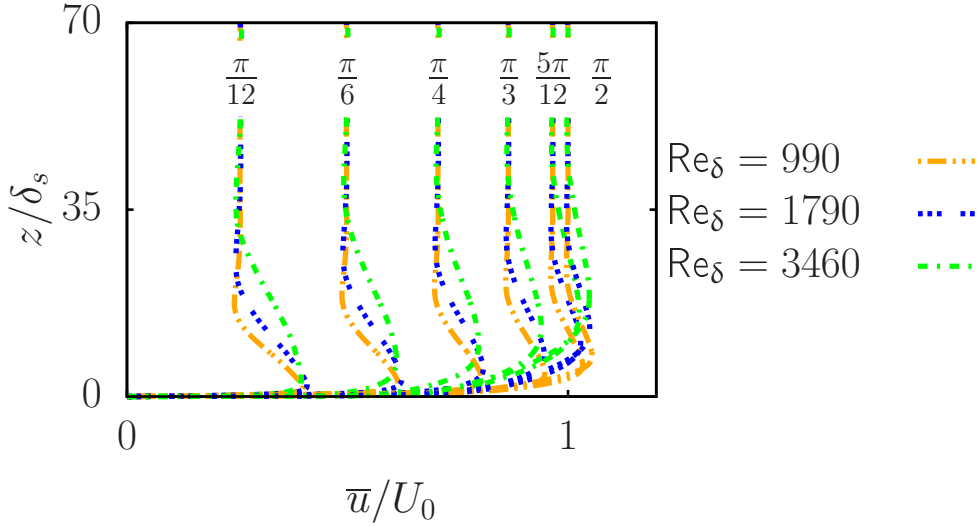


Figure 3.3: Velocity profiles for $h/\delta_s = 70$ every $\Delta\omega t = \pi/12$ in the acceleration phase and for three different Reynolds number values.

3.4.2. Velocity profiles and turbulent boundary layer thickness

The velocity profiles for the three values of Re_δ (i.e. 990, 1790 and 3460) and $h/\delta_s = 70$ are displayed in Fig. 3.3, and the turbulent boundary layer thickness δ can be estimated from the graph by determining, for each value of Re_δ , the height at which the velocity profile for the phase $\omega t = \pi/2$ is maximum.

Re_δ	δ/δ_s	δ/h	$\text{Re}_\delta, h/\delta_s$	5	10	25	40	70
990	7.76	0.11	990	0.64	1.29	3.22	5.15	9.02
1790	12.60	0.18	1790	0.40	0.79	1.98	3.17	5.56
3460	17.60	0.25	3460	0.28	0.57	1.42	2.27	3.98

Table 3.2: Turbulent boundary layer thickness for the three different Reynolds numbers in sufficiently large domains, i.e. $h/\delta_s = 70$, (left) and the corresponding h/δ ratio for the 15 different $(\text{Re}_\delta, h/\delta_s)$ couples. The cells colored in gray represent simulations for which the h/δ ratio is comparable with the h/δ ratio estimated for the Rhine estuary.

Table 3.2 shows that the turbulent boundary layer grows in size with Re_δ . As a result every simulation is characterized by a specific value of h/δ and the simulations cover a wide range of values for h/δ , including simulations that are not influenced and simulations strongly influenced by the finite water depth. Three simulations have a value for h/δ similar to those of the Rhine estuary.

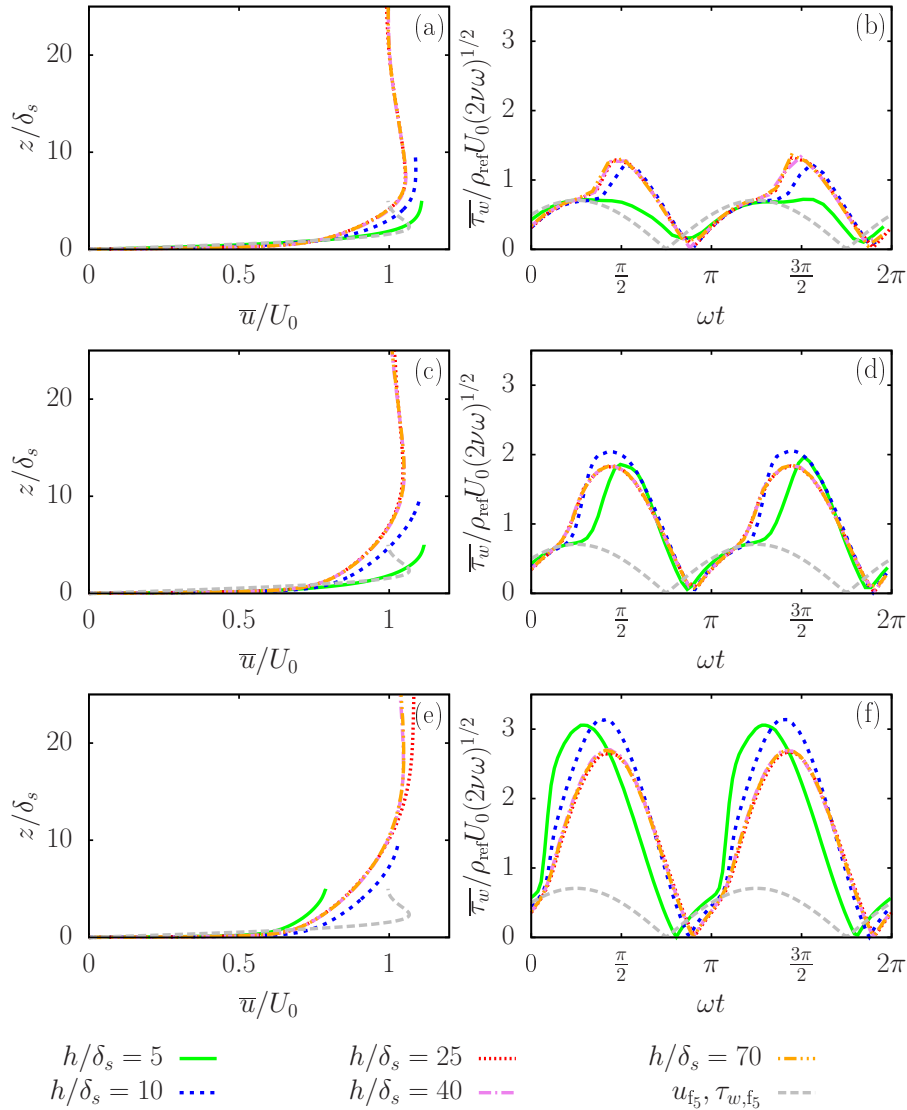


Figure 3.4: Plane and phase averaged velocity profiles at $\omega t = \pi/2$ (left column, i.e. (a), (c) and (e)) and wall shear stress series (right column, i.e. (b), (d) and (f)) for $\text{Re}_\delta = 990$ (top, i.e. (a) and (b)), $\text{Re}_\delta = 1790$ (middle, i.e. (c) and (d)) and $\text{Re}_\delta = 3460$ (bottom, i.e. (e) and (f)). The laminar analytical solutions are also displayed and the subscript 5 refers to $h/\delta_s = 5$.

3.4.3. Surface velocity and turbulent wall shear stress

The impact of a reduced water-depth on the flow properties is observable in Fig. 3.4. In this figure, the wall shear stress is shown as a function of time, and the velocity at $\omega t = \pi/2$ is shown as a function of depth, for all the combinations of values of Re_δ and h/δ_s . For simulations with $\text{Re}_\delta = 990$ and $\text{Re}_\delta = 1790$ and $h/\delta_s \geq 25$, the velocity

profiles are hardly affected by the water depth, but for simulations with $\text{Re}_\delta = 3460$, the profile is already affected when $h/\delta_s = 25$. According to Table 3.2, $h/\delta = 1.98$ for the simulation with $(\text{Re}_\delta = 1790; h/\delta_s = 25)$ and $h/\delta = 1.42$ for the simulation with $(\text{Re}_\delta = 3460; h/\delta_s = 25)$. This means that the effect of the water depth becomes clearly visible for $1.5 \lesssim h/\delta \lesssim 2.0$.

Similar to the velocity profiles, the wall shear stress is also affected by the water depth. For all the values of the Reynolds number simulated, the signals of the wall shear stress as a function of time are nearly equal as long as $h/\delta \geq 25$ but the signals react differently for each Re_δ -value if a smaller depth is considered, see Fig. 3.4. For $\text{Re}_\delta = 1790$ and for $\text{Re}_\delta = 3460$, the amplitude of the wall shear stress is the largest for $h/\delta_s = 10$, followed by $h/\delta_s = 5$ and finally by $h/\delta_s \geq 25$. This behavior suggests that for $0.50 \lesssim h/\delta \lesssim 2.00$, the amplitude of the wall shear stress is maximum. In contrast, for $\text{Re}_\delta = 990$ the magnitude of the wall shear stress decreases slightly for $h/\delta_s = 10$ compared to the cases with $h/\delta_s \geq 25$ and almost collapses on that of the laminar solution for $h/\delta_s = 5$. This drop is probably related to a complete relaminarization of the flow except for the deceleration phase where disturbances are still generated. Despite this complete relaminarization is not observed for the other simulations, some elements suggest that a strong decrease of turbulent activity occurs for these other simulations too, although during only part of the oscillation cycle. In fact, it is well known that the transition to turbulence is marked by a sudden increase in the slope of the wall shear stress time-series (Jensen et al., 1989; Costamagna et al., 2003; Salon et al., 2007). This phenomenon of sudden increase is observed in all the simulations but the wall shear stress follows the laminar solution for some part of the cycle only (i) for $\text{Re}_\delta = 990$ and $h/\delta_s \geq 10$, (ii) for $\text{Re}_\delta = 1790$ and $h/\delta_s \leq 10$ and (iii) for $\text{Re}_\delta = 3460$ and $h/\delta_s = 5$. This behaviour suggests that these latter simulations experience partial relaminarization, the simulation with $h/\delta_s = 5$ and $\text{Re}_\delta = 990$ experiences complete relaminarization while the other simulations just experience a reduction in turbulent activity.

Additionally, a more careful look at the velocity profiles for $\text{Re}_\delta = 990$, $\text{Re}_\delta = 1790$ and $h/\delta_s = 5$, indicated already relaminarization since the velocity profiles converge towards the analytical laminar solution. This tendency might be caused by the water depth becoming too small to contain the largest turbulence scales. Earlier studies of oscillating pipe flows have also shown that reducing the diameter of the pipe delays the transition to turbulence (Hino et al., 1976; Tuzi & Blondeaux, 2008). During this regime, the boundary layer thickness probably switches between its laminar and turbulent thickness. This process is further investigated by means of the TKE in the next section.

3.4.4. Turbulent kinetic energy

In order to estimate the amount of turbulence in the computational domain, we define the resolved plane averaged TKE, $\overline{E_k}^p$, by

$$\overline{E_k}^p = \frac{1}{2U_0^2} \left(\left(\overline{(u - \overline{u}^p)^2} \right) + \left(\overline{(v - \overline{v}^p)^2} \right) + \left(\overline{(w - \overline{w}^p)^2} \right) \right) \quad (3.5)$$

where $\overline{\cdot}^p$ refers to plane averaging only. The choice of not using a combined plane and phase averaged velocity for the computation of the plane and phase averaged TKE,

E_k , is motivated by the turbulence intermittency observed in some simulations. For example, for $h/\delta_s=5$ and $Re_\delta = 1790$, there is a certain randomness in the phase at which transition to turbulence occurs, and the flow at a specific phase can be either laminar during a certain cycle or turbulent during a different cycle. The mean velocity of the flow in laminar conditions is different from the mean velocity of the flow in turbulent conditions. As a result, computing $\overline{E_k}^p$ for each phase using the local mean velocity gives more reliable results than using the phase-averaged mean velocity. The mean resolved TKE E_k is defined as the phase average of the $\overline{E_k}^p$ over the number of cycles n_c :

$$E_k = \frac{1}{n_c} \sum_{i=1}^{n_c} \overline{E_{k_i}}^p. \quad (3.6)$$

where the cycle numbers 1 and n_c do not account for the discarded cycles in the transient regimes. To have a fair comparison between the different simulations, E_k is integrated between 0 and $5\delta_s$:

$$E_{k,5\delta_s}(t) = \int_0^{5\delta_s} E_k(z; t) dz. \quad (3.7)$$

This quantity is displayed as a function of time in Fig. 3.5. For $Re_\delta = 3460$, the

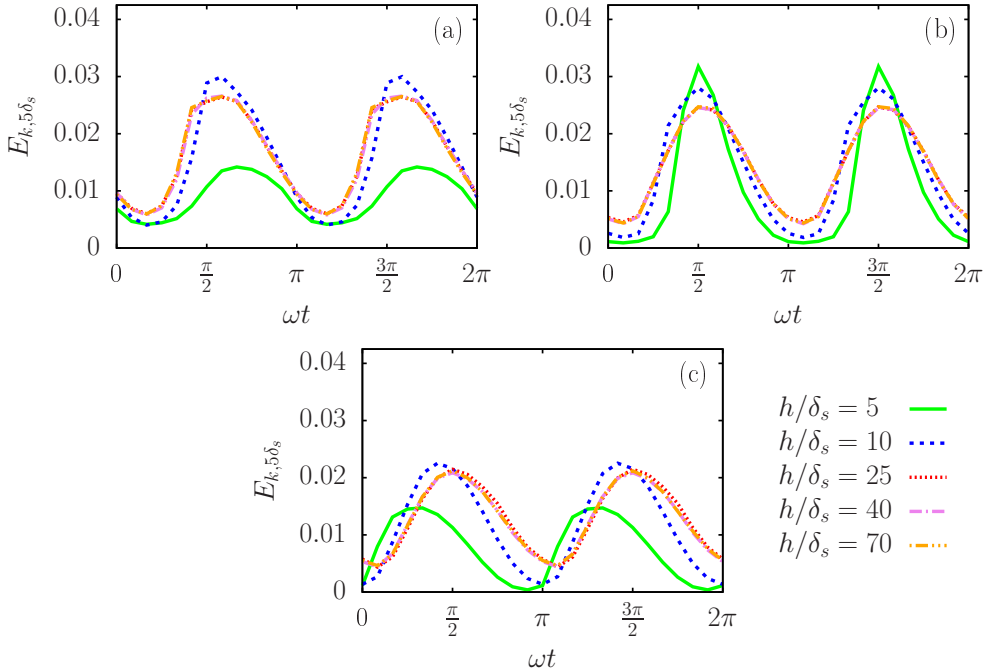


Figure 3.5: Resolved turbulent kinetic energy integrated over $0 \leq z \leq 5\delta_s$, $E_{k,5\delta_s}$ for $Re_\delta = 990$ (a), $Re_\delta = 1790$ (b) and $Re_\delta = 3460$ (c).

minimum value of $E_{k,5\delta_s}$ decreases with h/δ_s . Furthermore, the lowest values of $E_{k,5\delta_s}$

for $h/\delta_s = 5$, $\text{Re}_\delta = 3460$ occur slightly before $\omega t = \pi$, just before the increase in slope of the wall shear stress, a strong indication of relaminarization in the acceleration phase. This feature confirms that the sudden increase in slope of the wall shear stress signal is due to transition to turbulence after previous relaminarization. For the lower Re_δ values, the results are similar. The temporal minimum of $E_{k,5\delta_s}$ still decreases with h/δ_s , and the extent of the cycle for which $E_{k,5\delta_s}$ stays low increases, particularly for $h/\delta_s = 5$. Additionally, for all the values of Re_δ , $E_{k,5\delta_s}$ decreases during large parts of the cycle for $h/\delta_s = 10$ when compared to the simulations with higher h/δ_s ratios. The turbulent kinetic energy shows a maximum, which is actually the highest for $h/\delta_s = 10$. This could mean that there are higher levels of turbulence during the decelerating phases of the cycle even if the rest of the cycle relaminarizes. This finding was already suggested by the wall shear stress in Fig. 3.4: the evolution of the wall shear stress has a higher maximum but also suggests a longer period of turbulence activity reduction for $h/\delta_s = 10$ and $\text{Re}_\delta = 1790$ or $\text{Re}_\delta = 3460$ than for the large depth simulations.

An additional feature is the apparent decrease of $E_{k,5\delta_s}$ with increasing Re_δ values. This could have several origins: (i) at high Reynolds numbers, turbulent kinetic energy is faster transported away from the wall and does not remain in the region $0 \leq z \leq 5\delta_s$; (ii) the use of DNS for $\text{Re}_\delta = 990$ while LES is used for $\text{Re}_\delta = 1790$ and $\text{Re}_\delta = 3460$ resulting in a larger fraction of the resolved fluctuations (this only explains the increase in $E_{k,5\delta_s}$ between $\text{Re}_\delta = 990$ and $\text{Re}_\delta = 1790$). The exact cause of this increase in $E_{k,5\delta_s}$ remains however unclear and is of minor importance for our investigation.

3.4.5. Amplitude and phases of the velocities and wall shear stresses

Figs 3.4 and 3.5 have shown that both the value of Re_δ and the value of h/δ_s impact the the velocity, the wall-shear stress and TKE. Since the flow is periodic in time, the velocity and the wall shear-stress can be investigated by means of the phase and the amplitude of the periodic signal, in a similar way as for the laminar solution.

The results for Φ_∞ , $\Phi_{h,f}$, A_∞ and $A_{h,f}$ are shown in Fig. 3.6 for the turbulent results as well as for the analytical solution. The dependence of $A_{h,f}$ on h/δ and of A_∞ on z/δ are similar for the data from turbulent numerical simulations and the laminar analytical solutions. The amplitudes A_∞ and $A_{h,f}$ are maximum around $h = \delta$ and then decrease towards zero. The deviation of A_∞ curves near the bottom is due to the differences in vertical shear between a laminar bottom boundary and a turbulent bottom boundary. The agreement between the laminar and turbulent results for $\Phi_{h,f}$ and Φ_∞ is more qualitative: for the simulations as well as for the laminar theory, $\Phi_{h,f}$ increases with decreasing z/δ and Φ_∞ increases with decreasing h/δ . However, the rate of increase is faster and the limit values are different when the flow is laminar than when the flow is turbulent: Φ_∞ increases towards $\pi/4$ in the laminar case while it increases towards approximately $\pi/16$ in the turbulent case. Additionally, the data points from the simulations characterized by relaminarization of the flow are slightly out of trend. A last remarkable feature is that both the turbulent profiles of A_∞ and of Φ_∞ collapse on each other, for the three Reynolds numbers. This proves that δ is an excellent scaling parameter.

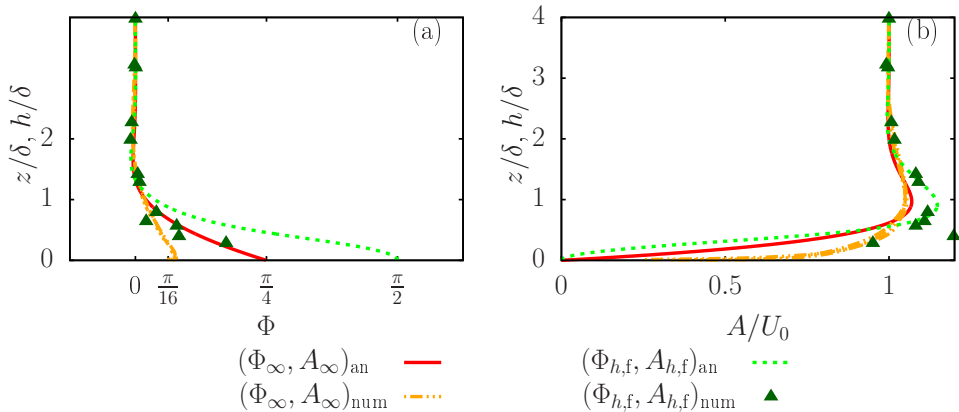


Figure 3.6: Phase shift (a) and the amplitude (b) of the surface velocity with respect to the free-stream velocity, for $Re_\delta = 990, Re_\delta = 1790$ or $Re_\delta = 3460$. Note that Φ_∞ and A_∞ are functions of z/δ while $\Phi_{h,f}$ and $A_{h,f}$ are functions of h/δ . For turbulent flows enough data points are available to present Φ_∞ and A_∞ as line but one point per simulation is available for $\Phi_{h,f}$ and $A_{h,f}$ and they are presented as symbols. The subscript 'an' refers to the laminar analytical solution while the subscript 'num' refers to the numerical solution.

The variation of the magnitude A_τ and phase-shift Φ_τ of the wall shear stress is also studied, but the analysis of this quantity is more delicate. Indeed Fig. 3.4 has shown that the temporal signal of the wall-shear stress is not sinusoidal for the turbulence simulations which makes the identification of the phase shift rather difficult. As a result, the phase lead of the wall shear stress with respect to the free-stream velocity is defined as the phase difference between the maximum wall shear stress and the maximum free stream velocity, in agreement with Jensen et al. (1989). Nevertheless, also this definition is difficult to handle. Previous studies have shown that turbulence was characterized by a reduction of the phase lead of the wall shear stress with respect to the free-stream velocity (Jensen et al., 1989; Carstensen et al., 2010), while the laminar theory suggests an increase of this phase lead with decreasing h/δ_s and thus with h/δ , see Fig. 3.1). We are, therefore, in the presence of two competing mechanisms: on one side, transition to turbulence decreases the phase lead of the wall shear stress while the interference between the boundary layer and the free surface increases this phase lead. Nevertheless, the amplitude and phase angles for the wall shear stress have been displayed in Fig. 3.7. In order to eliminate the influence of the Reynolds number, A_τ and Φ_τ have been scaled, so that for high values of h/δ , A_τ and Φ_τ are close to their laminar value, respectively $\pi/4$ and $\sqrt{2}/2$. The amplitude of the wall shear stress A_τ for the turbulence simulations shows a similar behaviour as in the laminar theory, as long as the flow stays turbulent. The data points lying slightly out of trend correspond to the lowest Reynolds number ($Re_\delta = 990$). For this value of Re_δ , there is no maximum in the wall shear stress and A_τ decreases with h/δ due to relaminarization.

The behavior of the turbulent phase shift Φ_τ is very different from the laminar case: it decreases instead of increasing for decreasing h/δ . It remains unclear if this

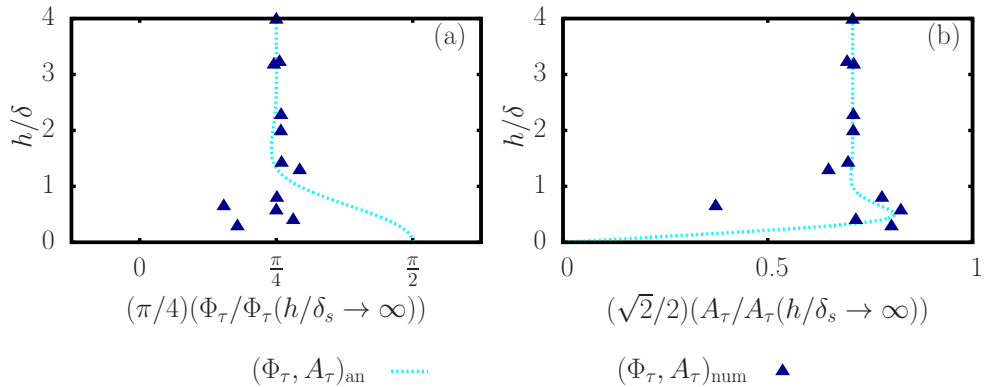


Figure 3.7: Phase shift Φ_τ (a) and the amplitude A_τ (b) of the wall shear stress, for $\text{Re}_s = 990$, $\text{Re}_s = 1790$ or $\text{Re}_s = 3460$. The subscript 'an' refers to the laminar analytical solution while the subscript 'num' refers to the numerical solution.

discrepancy is due to the relaminarization occurring for low values of h/δ , to the non-sinusoidal shape of the wall shear stress signal or to a combination of these two phenomena. The reason of this behavior could partly be clarified with simulations at a much higher Reynolds number, but they are not achievable with the current resources yet.

3.5. Discussion

Numerical simulations have shown that a reduction of the water depth strongly affects turbulent oscillatory flows by generating changes in the amplitude and in the phase of both the velocity signals and the wall shear stress signals. The evolution of the phases and the amplitudes with the water depth shows a similar trend to the analytical solution in which a constant (kinematic) viscosity has been used. In many environmental applications, turbulence is not resolved but modelled for cost efficiency purposes. In this regard, an analytical model of the turbulent flow using a constant eddy viscosity approach could give a quick first estimation of the velocity profiles and the wall-shear stress. However, for more accurate results, environmental flows often rely on somewhat more sophisticated turbulence models, such as the $k - \epsilon$ model. The $k - \epsilon$ model could be a time saving alternative to high resolution simulations, under the condition that it is able to reproduce the features observed in the present numerical simulations and in particular the relaminarization. In this regard, the results presented in this paper could be an interesting bench mark for $k - \epsilon$ based solvers (such as in the paper by Pu (2015)), so that more realistic oscillatory flows, incorporating free-surface, bottom roughness, rotation or just a higher value for the Reynolds number, can be simulated reliably at lower computational costs.

The role played by the ratio h/δ in the theoretical solution of the oscillating boundary layer flow is also relevant for applications in environmental flows. Our results confirm the finding of Li et al. (2005), that for small ratios of h/δ (such as tidal

flows along the Dutch coast), the momentum balance is between the local acceleration, the driving pressure gradient and the wall shear stress τ_w , whereas for large values of h/δ (tidal currents in deep oceans, wave boundary layers or seiches in lakes), the balance is mainly between the local acceleration and the driving pressure gradient. The claim by Lorke, Umlauf, Jonas, and Wüest (2002), that the momentum balance for seiches in an Alpine lake (lake Alpnach) is not comparable with the momentum balance of tidal oscillatory flows, is explained by the large h/δ ratio of the lake when compared to tidal flows. Note that the oscillatory flow in this Lake is generated by a diurnal wind forcing. As a result, free surface effects do not play an important role and due to the absence of the Coriolis force (because of the small size of the lake), Lake Alpnach can be considered as a prototype example of our deep-water simulations.

Additionally, the present results could play a role in estimating the free-stream velocity or the friction parameter f_w of oscillating tidal flows such as for example in the North Sea, the main channel of Skagit Bay (studied for example in Gross and Nowell (1983)) or the tidal channel in Three Mile Slough (studied for example in Stacey, Monismith, and Bureau (1999)). The results even suggest that the tidal free-stream velocity along the Dutch coast, presented in the introduction, could be overestimated by 10% to 20% since it does not coincide, as implicitly assumed, with the surface velocity. However, it is necessary to evaluate how accurate the oscillating boundary layer model is for actual tidal flows. As mentioned in the introduction, four simplifying assumptions have been used: (i) the absence of the Coriolis force, (ii) the presence of a flat bottom, (iii) a rigid-lid assumption and a (iv) a relatively low Reynolds number. The first assumption, the absence of the Coriolis force can be justified because the purely oscillating motion of the flow is a direct result from the Earth's rotation, via the Kelvin wave. The incorporation of the Coriolis force would generate a Stokes-Ekman boundary layer (Salon et al., 2009; Salon & Armenio, 2011) and generate tidal ellipses that are only observed near the Rhine mouth under stratified conditions, or far away from the coast (Visser et al., 1994). For the current study, it seems less relevant. The second assumption, ignoring of bottom roughness, is clearly a disadvantage of the model. However, roughness is known to facilitate transition to turbulence (Jensen et al., 1989), so that it can be expected that oscillatory flows with rough bottoms are less affected by relaminarization, maintaining the similar trends for laminar and turbulent oscillating flow at lower value of the Reynolds number. The third assumption, the rigid lid assumption is probably the most challenging one. Near the Rhine mouth, the tidal amplitude varies roughly between 1m during neap tide to 2m during spring tide on a water depth of approximately 20m (*Rijkswaterstaat Waterinfo*, n.d.), so that the free surface might play an important role. these first three assumptions could be investigated in the future with a DNS or LES approach providing tailor-made models. However, the fourth assumption, increasing the Reynolds number value significantly is not realistic in the near future. Therefore, although we do believe that the reduction of the water-depth has a non-negligible impact on oscillating tidal flows, we recommend to quantify this impact with Reynolds-Averaged Navier-Stokes simulations. The present results are then very useful as a reference case and including understanding of the basic phenomena a calibration for the Reynolds-Averaged Navier-Stokes simulations.

3.6. Conclusion

The influence of a reduced water depth on turbulent oscillatory flows has been investigated using a high resolution numerical approach (direct numerical simulations and wall-resolving large eddy simulations) and compared to a laminar analytical solution. In this study the water depth h was compared to the thickness of the boundary layer δ . It was found that turbulent, oscillatory flows are characterized by an increase of the phase lead of the surface velocity and the wall shear stress on the free-stream velocity, if the water-depth is decreased. The evolution of the phase and the amplitude of the turbulent velocity time-signals shows similar trends to the analytical laminar solution. However, if the water-depth is decreased too much, the flow relaminarizes. We would expect that for very high Reynolds numbers this relaminarization will only take place for very low values of h/δ_s (i.e. $h/\delta_s < 5$), but we cannot currently confirm or validate this statement due to the high computational costs such simulations require.

The results of our study may have implications for applications of oscillatory flows such as tidal flows. For example, the tidal currents along the Dutch coast are in the shallow water regime. However, the influence of other physical actors such as free-surface or bottom-roughness have been neglected in the present study and they might be responsible for additional effects on these tidal flows. Therefore, we believe that the present findings constitute an excellent benchmark for typical environmental fluid mechanics configurations and their associated numerical solvers with which the impact of a reduced water depth on environmental flows can be further investigated.

A point of attention is that the majority of the large-scale, RANS-type, numerical solvers do not usually resolve the entire boundary layer. As seen in this chapter, the large gradients in this region require a significant number of grid points in the wall normal direction. In most RANS models, the resolution in the vertical is low enough to require to accurately model the velocity at the wall. The most common of these models relies on the assumption of a logarithmic dependence of the velocity on the depth for some section of the velocity profile. The validity of this assumption is the subject of the next chapter.

4

Existence and properties of the logarithmic layer in oscillating flows

4.1. Introduction

Oscillatory flows, such as the one investigated in the previous chapter, are part of the wall-bounded flow category. The wall-bounded flow category also includes classical steady flow configurations, such as the plane channel flow (Afzal & Yajnik, 1973; Kim et al., 1987; Bernardini, Pirozzoli, & Orlandi, 2014; Hoyas & Jiménez, 2006) flow or the Couette flow (Pirozzoli, Bernardini, & Orlandi, 2014). Wall-bounded flows are extensively studied with high resolution numerical simulations (Hoyas & Jiménez, 2006; Kim et al., 1987; Jiménez & Moser, 2007) because they allow to gain insight in turbulent processes, but also because they are relatively simple models of geophysical flows. However, such flows are generally computationally expensive to fully resolve numerically (Piomelli & Balaras, 2002; Radhakrishnan & Piomelli, 2008). Sufficient resolution is required in the wall normal direction to resolve the boundary layer. Additionally, sufficient resolution is also important for resolving the separation of scales between the large-scale energy carrying eddies and the small-scale dissipative eddies. As a result, these difficulties are often bypassed using a so called wall-model, in which the wall velocities are parametrized (Piomelli & Balaras, 2002; Radhakrishnan & Piomelli, 2008). Although different wall models exist, the most commonly used is based on the ‘the law-of-the-wall’ (Piomelli & Balaras, 2002; Radhakrishnan & Piomelli, 2008; Marusic et al., 2010), a classical theory for wall bounded flows and described below.

In classical wall bounded flow theory, it is assumed that the velocity distribution in a wall-bounded flow can be categorized in four regions or layers (Nieuwstadt et al., 2016; Radhakrishnan & Piomelli, 2008). Starting at the wall, there is, first, the viscous sub-layer, where the flow is dominated by viscous forces and where the non-dimensional velocity $u^+ = \bar{u}/u_\tau$ varies linearly with the non-dimensional height

$z^+ = zu_\tau/\nu$ according to $u^+ = y^+$. In these formulae, \bar{u} is the ensemble averaged mean velocity in the stream-wise direction, $u_\tau = \sqrt{\tau_w/\rho_{\text{ref}}} = \sqrt{\nu(\partial\bar{u}/\partial z)_w}$ is the friction velocity, z is the height above the wall, τ_w is the wall shear stress, ρ_{ref} is the fluid density, and ν is the kinematic viscosity. Second, there is the buffer layer, where the viscous model is not valid anymore and no simple scaling for the velocity exists. The buffer layer is connecting the viscous sub-layer to the the third layer, the logarithmic layer. In the logarithmic layer (in this manuscript also referred to as log-layer or log-region), the velocity is logarithmically dependent on z^+ according to

$$u^+ = \frac{1}{k} \ln(z^+) + B, \quad (4.1)$$

with k the von Kármán constant and B the logarithmic layer intercept. Finally, there is the outer layer, for which a theoretical expression depending on the type of flow is also possible, but will not be considered here (e.g. Kundu and Cohen (2002)).

In most models relying on the law-of-the-wall, the first computational point is assumed to be located within the log-layer (Piomelli & Balaras, 2002). The suitability of these models is now widely accepted. First, it is possible to derive the log-layer analytically, based on scaling arguments (Nieuwstadt et al., 2016), and second, the existence of the log-layer has been observed for steady flows in many studies, including numerical simulations (Hoyas & Jiménez, 2006; Kim et al., 1987; Jiménez & Moser, 2007), experiments (Marusic, Monty, Hultmark, & Smits, 2013; Perry & Li, 1990; Mckeen, Li, Jiang, Morrison, & Smits, 2004) and field measurements (Andreas et al., 2006; Frenzen & Vogel, 1995). Moreover, a log-region has also been detected in streamwise oscillating flows (Akhavan et al., 1991; Tuzi & Blondeaux, 2008; Hsu, Lu, & Kwan, 2000; Jensen et al., 1989; Salon et al., 2007; Jonsson & Carlsen, 1976; Scandura, Faraci, & Foti, 2016) even if its theoretical derivation ignores the mean local acceleration (Nieuwstadt et al., 2016; Piomelli & Balaras, 2002). It is important to note that the log layer was also studied in spanwise oscillating flows. Under spanwise wall oscillations, the transient behaviour of the boundary layer when adjusting itself to a lower drag state has implications for the log-region (Skote, 2014).

In an early study, Jonsson (1980) developed a phase dependent expression linking the velocity to the logarithm of the depth. However, this model was already assuming the existence of a logarithmic layer. Although Sleath (1987) found that this theoretical expression agreed well with his measurements, he also admitted that equally good agreement could be obtained for several different values of the von Kármán constant. Additionally, the expression was based on rough wall flows, and Mujal-Colilles, Christensen, Bateman, and Garcia (2016) showed that rough walls generated different coherent structures than smooth walls, at least in the transition to turbulence. Radhakrishnan and Piomelli (2008) obtained good agreement between numerical simulations of a streamwise oscillating flow and experimental data at high Reynolds numbers, while using a law-of-the-wall as boundary condition. They used a hybrid wall model composed of a viscous sub-layer part (in which the velocity scales linearly with the depth), and a log-layer part, in order to take into account low Reynolds number effects when the wall shear stress changes sign. Indeed, several studies have shown that a log-region does not necessarily exist at all times in flows for which the mean properties are highly time dependent (Hino et al., 1983; Jensen

et al., 1989; Salon et al., 2007). For example, Jensen et al. (1989) found that for a streamwise oscillating flow there can be large parts of the oscillation cycle where no logarithmic layer is detected, with its presence interval depending strongly on the value of the Reynolds number. As a result, the existence of the log layer and its properties need to be thoroughly investigated. Using these properties, the conditions for which it is justified to use a wall model in turbulent non-steady flows can be defined.

In this manuscript, we present the results of an analysis of the existence and the properties of the logarithmic layer in a canonical unsteady flow: the turbulent oscillating boundary layer. Besides being a classical example of a statistically time-dependent flow, the turbulent oscillating boundary layer has many applications, for example, in biology (e.g. pulmonary flows; see Tuzi and Blondeaux (2008)) and in coastal engineering (e.g. tidal channel flows; see Li et al. (2005); Gross and Nowell (1983)). Additionally, the existence and properties of the log-region are crucial in many computer model applications where the boundary layer cannot be resolved. These properties need to be known, and this is the purpose of the present study. Our study is based on results of direct numerical simulations (DNS) and large eddy simulations (LES) of an open channel flow driven by a homogeneous, uniform, streamwise, oscillating pressure gradient,

$$-\frac{1}{\rho_{\text{ref}}}\frac{\partial P}{\partial x} = U_0\omega \cos(\omega t) \quad (4.2)$$

with P the pressure, x the coordinate in the streamwise direction, U_0 the amplitude of the free-stream velocity, ω the angular frequency and t the time. The flow is characterized by two non-dimensional parameters: the Reynolds number based on the thickness of the Stokes boundary layer $\text{Re}_\delta = U_0\delta_s/\nu$, characterizing the transition to turbulence (Jensen et al., 1989; Salon et al., 2007), and the ratio between the water depth h and the Stokes boundary layer thickness δ_s (for definitions, see Section 4.2). Different configurations are simulated, covering different applications, e.g. high value of Re_δ and a relatively-low value of h/δ_s for simulations of tidal-like boundary layers, or low value of Re_δ and large value of h/δ_s for simulations of wave-like boundary layers. As a result, for the first time, the logarithmic layer is characterized as a function of Re_δ , h/δ_s and the phase of the oscillating pressure gradient.

4.2. Problem formulation

If h/δ_s is large enough, Re_δ is the only parameter governing the transition to turbulence (Jensen et al., 1989; Salon et al., 2007; Kaptein et al., 2019). Here, large enough means that the turbulent boundary layer is not influenced by the water-depth, which is the case for $h/\delta_s \geq 25$ for $\text{Re}_\delta \leq 1790$ or $h/\delta_s \geq 40$ for $1790 \leq \text{Re}_\delta \leq 3460$ (Kaptein et al., 2019). Previous studies (Kaptein et al., 2019; Jensen et al., 1989) show that the flow is in the intermittent turbulent regime for $\text{Re}_\delta = 990$ and in the fully turbulent regime for $\text{Re}_\delta = 1790$ and $\text{Re}_\delta = 3460$, although fully developed turbulence is not observed through the entire oscillation cycle. Additionally, damping of turbulence is observed during part of the cycle for $h/\delta_s \leq 10$ and throughout the entire cycle for $h/\delta_s \leq 5$, for these three values of the Reynolds number (Kaptein et al., 2019). The domain size is overall in agreement with the size of the turbulent struc-

tures (Costamagna et al., 2003; Jiménez & Moin, 1991), and the horizontal boundary conditions are periodic, see Sec. 2.5.2 for more details.

The value of z^+ used for grid considerations is defined with respect to the maximum of τ_w over the oscillation cycle, implying $z^+ = 1$ is a ‘worst case scenario’. For most of the oscillation cycle, the first grid point is located at $z^+ < 1$. In both DNS and LES configuration, there are at least five points (without counting the bottom boundary itself) located in the viscous sub-layer and part of the buffer layer, i.e. $z^+ \leq 11$. Additionally, for two of the simulations with $h/\delta_s \leq 10$ and $\text{Re}_\delta \leq 1790$, grid convergence was checked and obtained by doubling the vertical or the horizontal resolution. For the particular case with h/δ_s and $\text{Re}_\delta = 1790$, convergence was only obtained after reducing the value of the Courant number from 0.6 to 0.3. For h/δ_s and $\text{Re}_\delta = 990$, grid convergence could not be obtained.

4.3. Results

4.3.1. Identification of the logarithmic layer

The determination of the existence and the extent of the logarithmic layer is a well known challenge in the study of turbulent flows (Hoyas & Jiménez, 2006; Marusic et al., 2013). The logarithmic depth dependence of the streamwise velocity is based on the assumption that the turbulence eddies scale with the distance from the wall (Townsend, 1961); a hypothesis that has been frequently debated and that seems only satisfied at very high values of the Reynolds number (Perry & Li, 1990). As a result, the velocity profile slightly deviates from the logarithmic asymptote, even in the so-called logarithmic region (Bernardini et al., 2014). This is the log-layer defect and makes the log-layer more challenging to detect (Marusic et al., 2013).

An additional challenge is that some of the present simulations are characterized by intermittent turbulence. The intermittent character of the flow is visualized for two simulations in Fig. 4.1, by means of the resolved turbulent kinetic energy (TKE), integrated over a $5\delta_s$ thick layer close to the wall. Identical phases are marked by a symbol and the position of these symbols demonstrates that the TKE is nearly constant from cycle to cycle for $\text{Re}_\delta = 1790$, $h/\delta_s = 70$ and $\omega t = \pi/12$ (low value of the TKE) and $\omega t = 2\pi/3$ (high value of the TKE). However for $\text{Re}_\delta = 990$, $h/\delta_s = 10$ and $\omega t = \pi/2$ the TKE strongly varies from cycle to cycle indicating intermittency for these parameter settings.

The impact of this intermittency on the velocity profiles can be seen in Fig. 4.2, in which the plane-averaged velocity profiles have been plotted for three different value combinations of Re_δ , h/δ_s and the phase of the surface velocity (denoted ωt). The profiles have not yet been phase-averaged, which means that each value combination leads to about 20 profiles, each of them corresponding to a distinct oscillation cycle. The sub-figures of Fig. 4.2 clearly show three different regimes. In Fig. 4.2a, none of the profiles for the parameter values $\text{Re}_\delta = 1790$, $h/\delta_s = 70$ and $\omega t = \pi/12$ approaches the theoretical log-law curve given by Eq. (4.1): this is the non-logarithmic regime. In Fig. 4.2b, some of the profiles for $\text{Re}_\delta = 990$, $h/\delta_s = 10$ and $\omega t = \pi/2$ do approach this log-law while others are still a long way from it: this is the intermittent regime. Finally, in Fig. 4.2c all the profiles for $\text{Re}_\delta = 1790$, $h/\delta_s = 70$ and $\omega t = 2\pi/3$ collapse on the log law: this is the logarithmic regime. The results of Fig. 4.2

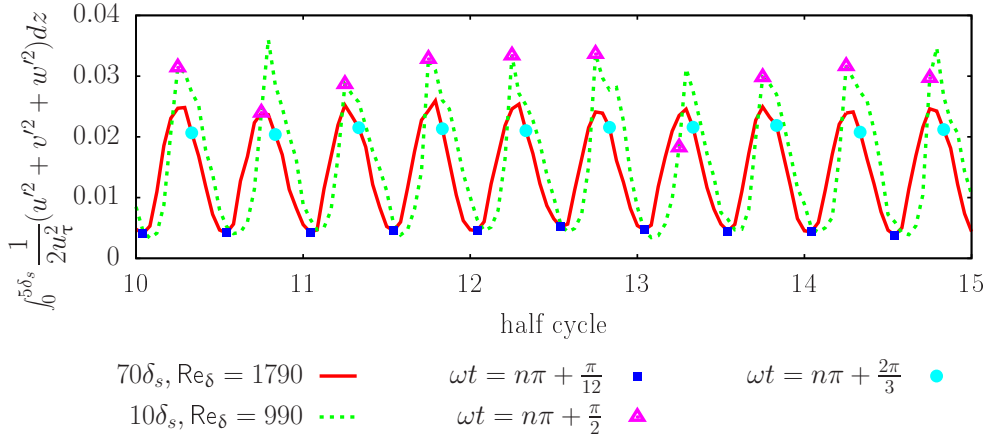


Figure 4.1: Resolved TKE within a $5\delta_s$ thick layer adjacent to the bottom boundary layer for ten successive half cycles. The two curves represent simulations with different values of the Reynolds number and the h/δ_s ratio. The symbols mark the TKE values at specific phases.

reveal two important findings. First, the log-layer is not necessarily present for all values of ωt , at given Re_δ and h/δ_s . Second, still at given Re_δ and h/δ_s , there might be some phases where the presence of the log-layer for a certain ωt also depends on the specific oscillation cycle. This latter finding is particularly important when computing the values of k and B . The accuracy of these values is related to the size of statistical sample from which they are computed, such that phase-averaging is needed for improved precision. However, it only makes sense to average profiles that have a log-layer. As a result, conditional averaging will be performed, and phases with no well-defined log-layer will be excluded. Under the assumption that a log-layer is a signature of the turbulent character of a flow, the conditional averaging can be regarded as averaging exclusively over the turbulent flow fields.

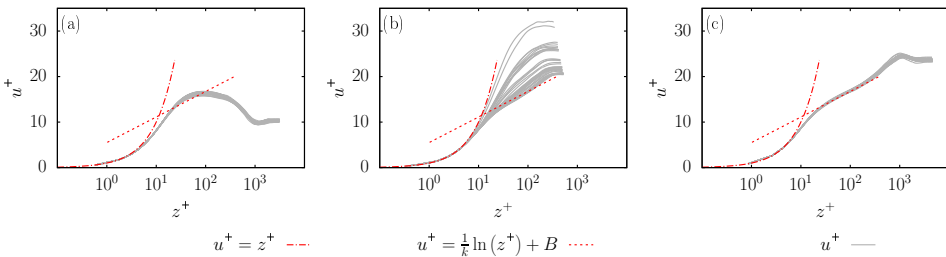


Figure 4.2: Profiles of the plane-averaged, streamwise non-dimensional velocity u^+ in semi-logarithmic scale for three different value combination of Re_δ , h/δ_s and ωt . (a) $\text{Re}_\delta = 1790$, $h/\delta_s = 70$ and $\omega t = \pi/12$, (b) $\text{Re}_\delta = 990$, $h/\delta_s = 10$ and $\omega t = \pi/2$, and (c) $\text{Re}_\delta = 1790$, $h/\delta_s = 70$ and $\omega t = 2\pi/3$. The theoretical solution has been obtained for $k = 0.41$ and $B = 5.5$.

As a result, the plane-averaged velocity profiles with a logarithmic layer had to be

identified by eye for all values of the parameters Re_δ , h/δ_s and ωt . This identification is obviously quite subjective, and had to be performed for about $12 \times 2 \times 20 \times 5 \times 3 = 7200$ profiles. The number 12 refers to the number of phases considered, 2 to the symmetry of the oscillation cycle, 20 to the number of oscillation cycles, 3 to the number of different values for Re_δ and 5 to the number of different values for h/δ_s .

To gain more confidence and objectivity in our estimations, but also to avoid to repeat the subjective identification procedure in the future, we want to find a robust signature of the log-layer in the simulation data. It has been suggested in previous work (Pirozzoli et al., 2014; Bernardini et al., 2014; Jiménez & Moser, 2007; Afzal & Yajnik, 1973) that a good method to analyze velocity profiles could be done through the log-law diagnostic function Ξ defined as

$$\Xi = \frac{du^+}{d \ln(z^+)} = z^+ \frac{du^+}{dz^+}. \quad (4.3)$$

This quantity is supposed to reach a plateau equal to $1/k$ (the inverse of the von Kármán constant) in the log-region but several studies (Hoyas & Jiménez, 2006; Jiménez & Moser, 2007) report that such a flat region is never reached. This finding suggest that the log-law diagnostic function is not more suitable for detecting the log-layer than the velocity profile. However, Fig. 4.3 shows that Ξ still gives valuable information. In Fig. 4.3a, the velocity profiles of Fig. 4.2b (in the intermittent regime) are reproduced, while differentiating the profiles that are logarithmic (red-dashed), the profiles that are not logarithmic (gray-solid), and the profiles for which the presence of the log-layer is uncertain (black-solid). These three profile categories are then investigated in terms of Ξ (see Fig. 4.3b), and one specific feature emerges concerning the height in wall units at which Ξ is locally maximum. This height is larger than the thickness of the viscous sub-layer (located at $z^+ = 5$) but smaller than the center of the buffer layer (located at $z^+ = 17$). As a result, we will call this height the ‘thickness of the viscosity dominated layer’: a layer where the molecular viscosity is dominant but turbulent fluctuation are not necessarily negligible. The advantage of this definition is that it can be used for laminar, turbulent and intermittent flows. The thickness of the viscosity dominated layer seems to be constant and approximately equal to $z^+ = 10$, when the profile approaches the log-layer, but it increases significantly up to values of approximately $z^+ = 22$, when the flow does not have a log-layer. This evolution in the location of the local maximum has been earlier observed by Hino et al. (1983).

Taking advantage of this trend, two maps of points defined by the coordinates $(\ln(z_{vs}^+); u(z_{vs}^+)/U_0)$ are displayed in Fig. 4.4, with z_{vs}^+ the height of the first local maximum of Ξ and $u(z_{vs}^+)/U_0$ the value of the velocity at that height. Figure 4.4a contains points from all the simulations with $\text{Re}_\delta = 990$ while Fig. 4.4b contains points from all the simulations with $\text{Re}_\delta = 3460$. Each point represents $(\ln(z_{vs}^+); u(z_{vs}^+)/U_0)$ for a given phase ωt in an oscillation cycle for one of the simulations. The points in each panel form a distinct shape with three branches: (i) a first branch drawing a convex path from the bottom left corner to the top right corner of the figure, (ii) a second branch going from the top right corner to the center of the figure and (iii) a third branch going from the center of the figure towards the bottom. The first and second branches coincide with points from the laminar analytical solution of Stokes’

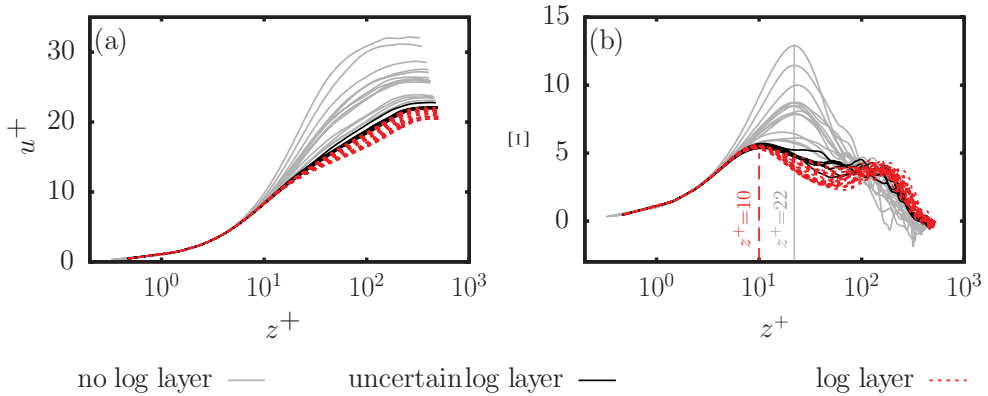


Figure 4.3: (a) Reproduction of the profiles of Fig. 4.2 while differentiating the profiles having a log-layer (red-dashed) from the ones that did not have a log-layer (gray-solid) and the ones for which the presence of the log-layer is uncertain (black-solid) and (b) their associated log-layer diagnostic function Ξ for $\text{Re}_\delta = 990$, $h/\delta_s = 10$ and $\omega t = \pi/2$. The absence of a plateau at $1/k$ for Ξ might be difficult to detect in logarithmic scale. Therefore, this figure has been reproduced in normal scaling in the Appendix, Fig. C.1.

second problem displayed in blue (see e.g. Kaptein et al. (2019) or Chapter 3), while the third branch approaches the theoretical line $z_{vs}^+ = 11$ displayed with a black dashed line. This line results from the assumption that the thickness of the viscosity dominated layer can be obtained by equating the scaling function in the viscous sub-layer, i.e. $u^+ = z^+$, and the scaling function in the logarithmic layer, i.e. Eq. (4.1). Forcing the intersection of these two lines at $z^+ = 11$ gives $B = 5.2$ for $k = 0.41$.

The symbols in Figs 4.4a and 4.4b follow the same trend. At the beginning of the oscillation cycle (denoted by the blue circle), the light gray diamonds are distributed close to the curve of the laminar solution. The profiles are in the non-logarithmic regime. As the oscillation cycle progresses, the gray diamonds follow the blue curve towards the top-right until they reach the phase at which transition to turbulence occurs. This phase is highly dependent on the value of Re_δ (Jensen et al., 1989). When the flow transitions to turbulence, the gray diamonds leave the laminar curve and migrate towards the line defined by $z_{vs}^+ = 11$. When approaching this line, the profiles enter the logarithmic regime, marked by the red points. In the logarithmic regime, the red points follow approximately the line $z_{vs}^+ = 11$, until they reach again the blue line of the laminar solution. This joining happens at the end of the deceleration phase, just before a new boundary layer builds up in the other direction, and might indicate that the presence of the log-layer at these phases is due to a history effect rather than equilibrium turbulence.

Although the symbols in Figs 4.4a and 4.4b describe similar paths, there are also discrepancies. First, it can be seen that the logarithmic branch in Fig. 4.4b is closer to the theoretical line $z_{vs}^+ = 11$ than the logarithmic branch in panel 4.4a, but it still deviates from it. These differences already suggest that the constants k and B probably depend on both Re_δ and the phase ωt . Second, some of the light

gray diamonds in Fig. 4.4a are located outside the branches, on the right of the non-logarithmic branch; these points are from the shallowest simulations, i.e. with $h/\delta_s = 5$ and $h/\delta_s = 10$. These simulations are characterized by such a high level of intermittency that the symmetry in the oscillation cycle is broken leading to a net flow in one direction over an oscillation cycle. This phenomenon is not explicitly shown or discussed here but has also been observed by Tuzi and Blondeaux (2008) and might explain the out-of-trend location of these points, particularly because for higher Reynolds number values, all points collapse into the curves (see Fig. 4.4b).

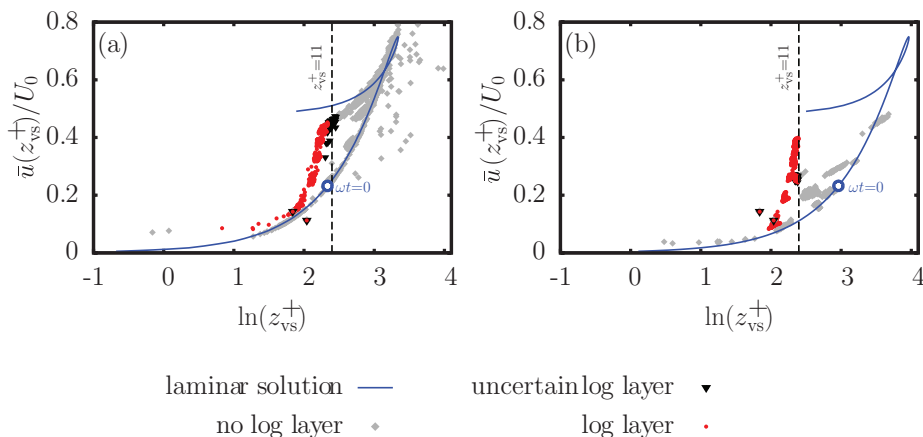


Figure 4.4: Points of coordinates $(\ln(z_{vs}^+); \overline{u(z_{vs}^+)}/U_0)$, i.e. the height of the viscous sub-layer and its associated velocity. Each point corresponds to a specific value of the phase ωt , a specific period and a specific value of h/δ_s . (a) $Re_\delta = 990$ and (b) $Re_\delta = 3460$. The plane-averaged velocity \bar{u} has been made non-dimensional with the outer scale U_0 instead of the inner scale u_τ because in this way the difference between the laminar points and the turbulent points is emphasized. The points of the laminar solution are obtained by taking the first maximum of $z^+ \partial u_\infty / \partial z$, where u_∞ is the analytical solution under infinite depth assumption (Kaptein et al., 2019). The start of the oscillating cycle $\omega t = 0$ is marked by the blue circle.

The free-stream phases particularly characterized by intermittency are summarized in Table 4.1. Intermittent turbulence is restricted to a few phases in simulations with either a low value of Re_δ or a low value of h/δ_s . The intermittency will be taken into account while computing the ensemble-averaged statistics, i.e. we are considering in these cases conditional phase-averaged vertical profiles of streamwise velocity. From now on, these profiles will be both plane and phase averaged. For the phases characterized by intermittency, only the velocity fields in which the presence of the logarithmic layer is confirmed by diagrams as shown in Fig. 4.4 are used in the phase averaging. As mentioned previously, discarding flow fields with no log-layer comes down to using only turbulent flow fields for computing the properties of the log layer.

Table 4.1: Overview of the phases characterized by intermittency. These phases are defined as the profiles for which, at identical value of Re_δ , h/δ_s and ωt , the $(\ln(z_{vs}^+); \overline{u(z_{vs}^+)}/U_0)$ points are located simultaneously on the logarithmic branch and significantly off the logarithmic edge.

Re_δ	h/δ_s	ωt
990	5	$\frac{7}{12}\pi, \frac{2}{3}\pi, \frac{3}{4}\pi, \frac{5}{6}\pi$
990	10	$\frac{1}{2}\pi, \frac{7}{12}\pi$
990	25, 40, 70	$\frac{5}{12}\pi$
1790	5	$\frac{5}{12}\pi, \frac{1}{2}\pi, \frac{7}{12}\pi$
3460	5	$\frac{1}{12}\pi$

4.3.2. Von Kármán constant and intercept

Even if the velocity profile is characterized by the presence of a logarithmic region, we anticipated that the characteristics of this region will depend on the value of the governing parameters and on the phase. Here, we obtain the values of the von Kármán constant k and the intercept B used in the logarithmic fit given by Eq. (4.1). Although it is possible to find k and B by fitting Eq. (4.1) through the log region, we prefer determining the constant and the intercept in a different way. In fact, the fitting procedure requires to initially determine subjectively the extent of the log region and this should be done for all the plane- and phase-averaged velocity profiles (up to 180 profiles). Instead, we propose a simpler procedure that is easier to reproduce. We first assume the necessary but not sufficient condition that the logarithmic region can only exist for $z_{\min}^+ < z^+ < z_{\max}^+$. The depth z_{\min}^+ is then defined as the thickness of the viscosity dominated layer, (which was computed in the previous section), i.e. $z_{\min}^+ = z_{vs}^+$. The depth z_{\max}^+ is in turn defined as the depth z^+ at which \bar{u} reaches its first local maximum. In this way, z_{\max}^+ can be interpreted as the thickness of the boundary layer, depending on the phase ωt . For $z_{\min}^+ < z^+ < z_{\max}^+$, we then determine the depth z_c^+ at which Ξ is minimum and call this depth z_c^+ the center of the logarithmic layer. The introduced z_{\min}^+ and z_c^+ are sketched in Fig. 4.5a while z_{\max}^+ is sketched in Fig. 4.5b. The value of the von Kármán constant is then $k = 1/\Xi(z_c^+)$, and the value of the intercept is $B = u^+(z_c^+) - \ln(z_c^+)/k$.

Figure 4.6 displays k and B as a function of the phase for each value of Re_δ and h/δ_s . It can be seen, that the average values of k and B depend strongly on the value of Re_δ . The mean von Kármán constant k increases from 0.37 at $\text{Re}_\delta = 990$ to 0.46 at $\text{Re}_\delta = 3460$, which is slightly different from the values obtained by Tuzi and Blondeaux (2008) in a pipe flow simulation. For $\text{Re}_\delta = 8000$ and $R/\delta_s = 4$ (with R the radius of their pipe), they found a von Kármán constant of 0.4 and an intercept at 5.5. Note that R/δ_s is similar to h/δ_s except that R is also a measure of the curvature of the bottom boundary, while the bottom boundary in the open channel configuration is flat. Similarly, the mean value of B increases from 4.2 at $\text{Re}_\delta = 990$ to 8.0 at $\text{Re}_\delta = 3460$. The dependence of k on the Reynolds number was already observed by Frenzen and Vogel (1995) and Nagib and Chauhan (2008) for steady

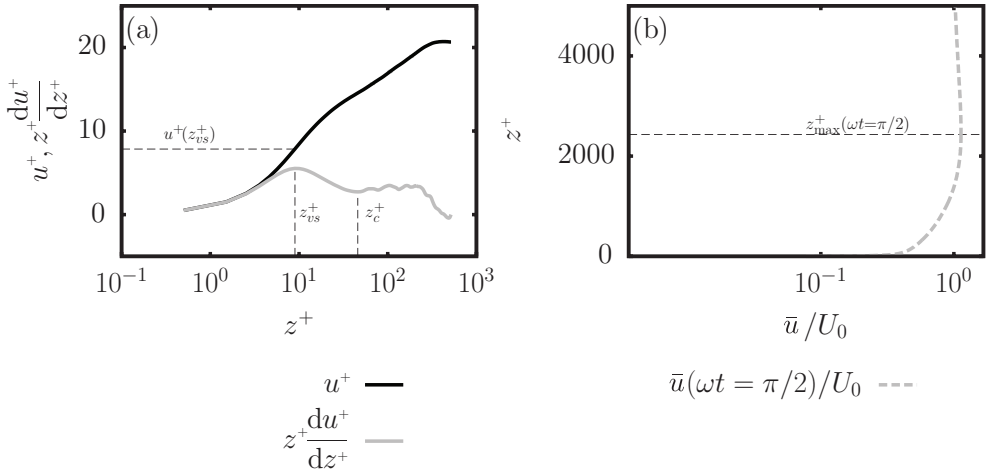


Figure 4.5: Sketch of (a) a velocity profile in logarithmic scale with its corresponding log-layer diagnostic function for $\text{Re}_\delta = 990$, $h/\delta_s = 10$ and $\omega t = \pi/2$ and (b) a velocity profile for $\text{Re}_\delta = 3460$, $h/\delta_s = 70$ and $\omega t = \pi/2$. The thickness of the viscous sub-layer $z_{\min} \equiv z_{vs}^+$ and z_c are sketched on (a) while z_{\max}^+ is sketched on (b).

flows. However, in those cases, k decreases with increasing value of the Reynolds number. Additionally, Marusic et al. (2010) stated that the value of k depends on the type of wall-bounded flow (e.g. pipe flow or channel flow), which might explain the small discrepancies between our results and the results from Tuzi and Blondeaux (2008). A last feature is the decrease of both k and B at the end of the deceleration phase (around $\omega t = \pi$), with a much stronger decrease for B than for k . This decrease is remarkable as it is not observed at the beginning of the acceleration phase (i.e. in the presence of a favorable pressure gradient), suggesting an asymmetry between the acceleration and the deceleration phases (i.e. in the presence of an adverse pressure gradient). The asymmetry reinforces an assumption mentioned earlier: the observed log-layer is not related to the turbulence conditions at this particular phase, but to the remainder of a log-layer that had been generated in an earlier stage of the flow. Finally, similarly to the points in Fig. 4.4, some points are out-of-trend and these points again correspond to simulations with $h/\delta_s = 5$ making the presence of a true logarithmic region at these values of h/δ_s questionable.

The established values and observed trends for k and B are critically based on their definitions, i.e. $k = 1/\Xi(z_c^+)$ and $B = u^+(z_c^+) - \ln(z_c^+)/k$. To test the sensitivity of the results to these definitions, k and B have also been estimated via a linear fit in Fig. 4.7. The fitting interval was chosen such that the relative error Err satisfies

$$\text{Err}(z^+) = \left| \frac{\frac{1}{k} \ln(z^+) + B - u^+(z^+)}{u^+(z^+)} \right| \leq \epsilon, \quad (4.4)$$

with ϵ maximum value of the error. The new values of k and B for $\text{Re}_\delta = 3460$ and $h/\delta_s = 40$ are displayed in Figs 4.7a and 4.7b, respectively. On one side, it is obvious from this figure that the previously mentioned discrepancies between the

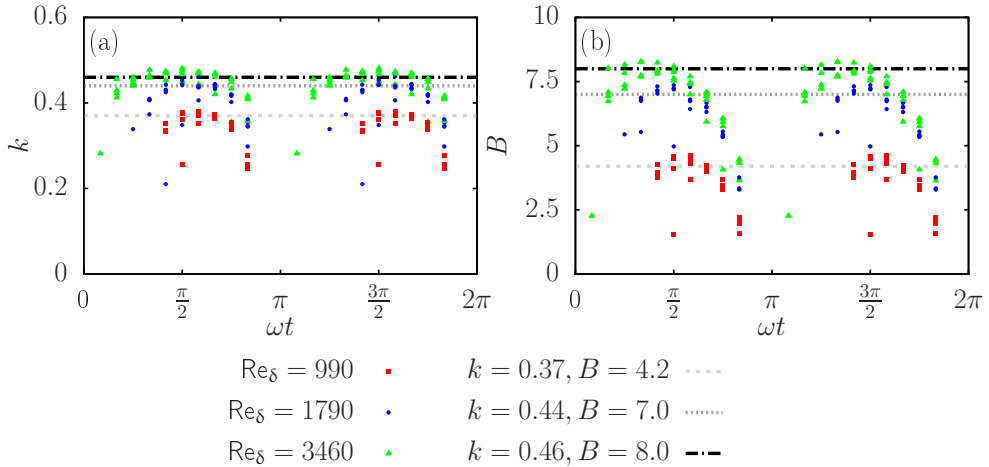


Figure 4.6: Evolution of the von Kármán constant (a) and the intercept B (b) as a function of the phase ωt . The influence of the Reynolds number has been highlighted by using different coloured symbols for the data points corresponding to simulations with different values of Re_δ . All values of h/δ_s are considered. Different dotted lines are also displayed in order to indicate specific values of k and B .

observed values of k and B in the present study, and the values in the literature, can be attributed to the way of computing them. In fact, when the fitting method is used, the von Kármán constant becomes extremely close to 0.41 for $\epsilon = 0.065$. Similarly, the value of B is then also lower with respect to the method using $k = 1/\Xi(z_c^+)$ and $B = u^+(z_c^+) - \ln(z_c^+)/k$. For higher value of $\epsilon = 0.115$, k and B decrease further. This result proves that the method used to determine these constants is crucial for the accuracy of the results.

On the other side the general trend in the phase-evolution of k and B is observed throughout the oscillation cycle, except for the earlier phases. The reduction in k and B at the end of the deceleration phases is still observed and supports once more that the log-layer presence at these phases is due to a history effect. In contrast, the different behaviour of k and B at $\omega t = \pi/6$ and $\pi/4$ could imply that the formation process of the log-layer is not yet completed at these phases.

4.3.3. Spatial and temporal extent of the logarithmic layer

The determination of the spatial extent of the log-layer is something quite subjective too (Hoyas & Jiménez, 2006; Marusic et al., 2013). In Section 4.3.2 we mentioned the necessary condition that the log-layer could only exist for $z_{\min}^+ < z^+ < z_{\max}^+$. However, the spatial extent could also be smaller than $[z_{\min}^+ : z_{\max}^+]$, such that this condition is not sufficient. Here, we assume that the spatial extent of the log-layer is the space-interval at which the relative error, Err , defined in Eq. (4.4) is smaller than $\epsilon = 5 \cdot 10^{-3}$. The coefficients used in Eq. (4.4) are computed using the method proposed in this paper, $k = 1/\Xi(z_c^+)$ and $B = u^+(z_c^+) - \ln(z_c^+)/k$. The start and the

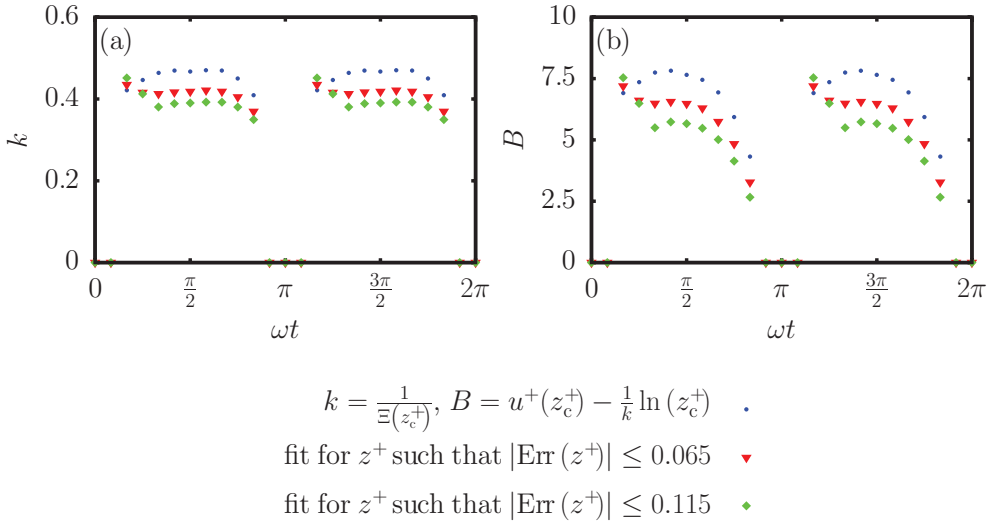


Figure 4.7: Value of the von Kármán constant (a) and the intercept B (b) as a function of the phase ωt , for $\text{Re}_\delta = 3460$ and $h/\delta_s = 40$. Two different ways of computing k and B are tested. One is based on the minimum of the log-layer diagnostic function Ξ (blue dots) and the other is based on fitting a function through an interval depending on the relative error Err of the velocity profile with respect to the log-law (red triangles and green diamonds).

end of the log-layer for each ratio h/δ_s and each Re_δ according to this definition are plotted as a function of the phase in Fig. 4.8. For all the simulations, the log-layer

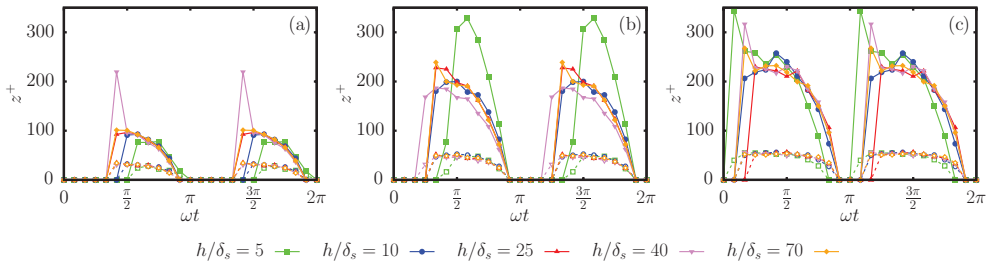


Figure 4.8: Spatial extent and existence interval of the log-layer, depending on Re_δ and h/δ_s : $\text{Re}_\delta = 990$ (a), $\text{Re}_\delta = 1790$ (b) and $\text{Re}_\delta = 3460$ (c). The open symbols and dashed line mark the start for the logarithmic region and the filled symbols and solid line mark its end.

starts around $25 < z^+ < 50$ (in agreement with the literature results of Tennekes and Lumley (1972)) but extends over different lengths, mainly depending on the value of Re_δ . Clearly, the spatial extent of the log-layer increases with the value of the Reynolds number, although these increments are less significant between $\text{Re}_\delta = 1790$ and $\text{Re}_\delta = 3460$ than between $\text{Re}_\delta = 990$ and $\text{Re}_\delta = 1790$. In general, the water depth does not seem to affect the spatial extent except for $\text{Re}_\delta = 1790$ and $h/\delta_s = 5$ where

it drastically increases when compared to the other values of h/δ_s . At $\omega t = \pi/2$, the log-region extends up to $z^+ = 300$ while the surface is located at $z^+ = 414$. This difference is relatively small, particularly considering the small value of ϵ that is used to define the spatial extent. The proximity of the end of the log-layer and the surface could suggest an interaction between the logarithmic layer and the top boundary. The choice of the boundary condition plays an important role in this situation. In a lot of environmental applications, a free-surface boundary conditions is more realistic. The free-surface would probably lead to more complex interactions with the log layer. However, it also introduces an additional parameter, the Froude number. The incorporation of a free-surface would make the isolation of the Reynolds number effects or reduced water-depth effect more difficult and is not in the scope of the present study. Finally, peaks in the spatial extent of the log-layer are observed at the earliest phases where the log-layer is detected. These peaks might be related to the formation process of the log-layer already discussed earlier, still ongoing at these phases, making its detection and extent more sensitive to the setting of ϵ or to the evaluation of the characteristic point defined by $(\ln(z_{vs}^+), \overline{u(z_{vs}^+)}/U_0)$. This phenomenon also explains why a log-layer is detected at $\omega t = \pi/5$ for $\text{Re}_\delta = 1790$ and $h/\delta_s = 40$ but not for the other values of h/δ_s at $\text{Re}_\delta = 1790$.

Similarly to the spatial extent, the phase interval during which the log-layer is present (the presence interval) also increases with the value of the Reynolds number. The size of the presence interval also appears to be related to the ratio h/δ_s . For $\text{Re}_\delta = 3460$ and $h/\delta_s = 5$, the presence interval of the log-layer is shifted by a phase $\Delta\omega t = \pi/12$ towards the earlier phases, but the size of the presence interval remains approximately the same compared to the higher h/δ_s values. For lower Re_δ values, the influence of the reduction of the water-depth is more significant as the size of the presence interval reduces. For $\text{Re}_\delta = 990$, the presence interval reduces with decreasing h/δ_s from $\pi/3 \leq \omega t \leq 11\pi/12$ at $h/\delta_s = 10$ to $5\pi/12 \leq \omega t \leq \pi$ at $h/\delta_s = 5$. For $\text{Re}_\delta = 1790$, the size of presence interval reduces from $\pi/4 \leq \omega t \leq 11\pi/12$ at $h/\delta_s = 10$ to $\pi/3 \leq \omega t \leq 5\pi/12$ implying that this size reduction increases with decreasing value of Re_δ .

The findings about the spatial-extent and time-interval presence of the log-layer have been obtained for a specific value of ϵ . To understand how the spatial-extent changes for a different value of ϵ , the start and the end of the log-layer are plotted as function of ϵ in Fig. 4.9, for $\text{Re}_\delta = 3460$, $h/\delta_s = 40$. Each line represents the start (or end) of the log-layer at different phase ωt . For $\omega t \in \{\pi/6; \pi/4; \pi/3\}$, the end of the log-layer reaches a plateau for a certain value of ϵ . This plateau is equal to z_{\max}^+ and implies that the log-layer has reached its maximum extent. For the other values of ωt , the end of the log-layer increases and the start of the log-layer decreases uniformly with ϵ , conserving the relative extent observed for $\epsilon = 5 \cdot 10^{-3}$.

4.3.4. Reynolds number based on the friction velocity

So far, this study shows that the presence of the logarithmic layer in turbulent oscillating flows depends on three different parameters Re_δ , h/δ_s and ωt . Nevertheless, previous research demonstrates that, when fully developed turbulence is observed in the oscillating flow, the behaviour of the flow is nearly identical to that of a steady wall-bounded flow (Salon et al., 2007; Jensen et al., 1989). In these steady boundary

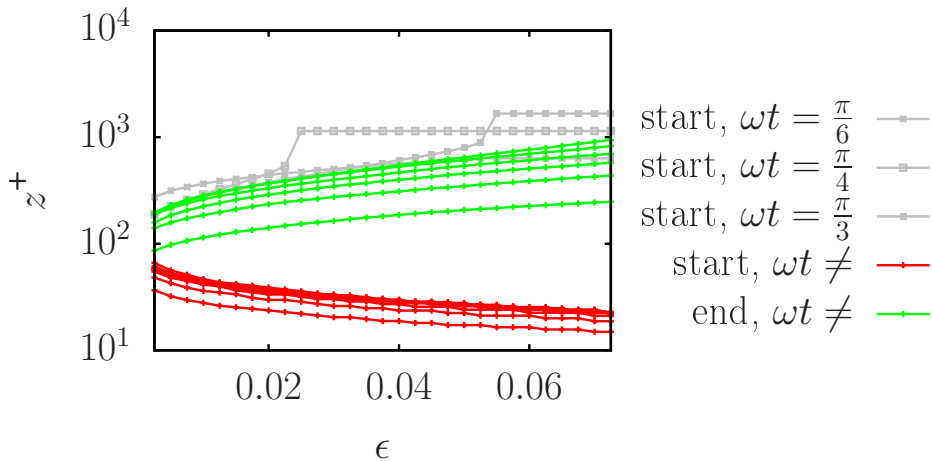


Figure 4.9: Start and end of the log-layer depending on the maximum error ϵ for $\text{Re}_\delta = 3460$, $h/\delta_s = 40$. Each green line or red line marks a different value of the phase ωt .

layer flows, the existence and properties of the log-layer are usually investigated in term of one single parameter: R_τ , the Reynolds number based on the friction velocity u_τ ,

$$\text{R}_\tau = \frac{u_\tau d}{\nu}. \quad (4.5)$$

where d is the channel half depth. As an example, Kim et al. (1987) detected a log-layer in their velocity profile for $\text{R}_\tau = 180$ in their pioneering DNS study of a steady plane channel flow. The definition of a characteristic parameter for unsteady turbulent flows was already discussed for pulsating flows (Ramaprian & Tu, 1983; Scotti & Piomelli, 2001). It was propose to use the eddy viscosity to define a turbulent Stokes layer thickness as a characteristic length scale rather than δ_s . However, although the eddy viscosity could be computed directly from the simulations, its depth dependence implies that a unique value of the eddy viscosity per phase does not exist.

Instead of using the turbulent Stokes layer thickness, we investigate the possibility of extending the use of R_τ to an oscillating flow, to analyze the standard approach used to study logarithmic layers in steady flows, and to test its validity of for non-steady flows. This extension makes use of a different interpretation of d . In a turbulent plane channel flow, d is also the largest distance that a fluid parcel can be separated from the closest wall, such that d is a measure of the thickness of the wall dominated layer. As a result, the velocity at a distance d of the wall is the maximum velocity in the water column. The analogy with the turbulent oscillating boundary layer is then quickly made: d should be defined as the height at which the velocity profile has its (first) maximum. In fact, $u_\tau d/\nu = z_{\max}^+$, such that $u_\tau d/\nu$ has already been sketched in Fig. 4.5b for $\text{R}_\tau = 3460$ and $h/\delta_s = 70$.

A first advantage of using R_τ is that d and u_τ , and therefore R_τ , depend on ωt . Additionally, a previous study on the same data set (Kaptein et al., 2019) determined

that Re_δ is the only parameter governing the flow as long as $d < h$ throughout the oscillation cycle, but that h/δ_s has to be taken into account if $d = h$ during at least part of cycle. A second advantage of using R_τ is that it takes into account this specific h/δ_s dependence. In Fig. 4.10a, $h > d$, and it can be seen that both d and u_τ are identical for $h/\delta_s = 40$ and $h/\delta_s = 70$ at fixed phase ωt , and for $\text{Re}_\delta = 3460$. This similarity implies that Re_δ is also identical for $h/\delta_s = 40$ and $h/\delta_s = 70$ at this specific Reynolds number. In Fig. 4.10b, $h \not> d$ for some part of the oscillation cycle, such that d and eventually u_τ are different between $h/\delta_s = 25$ and $h/\delta_s = 70$ for $\text{Re}_\delta = 3460$. These differences result in divergent R_τ for these two cases.

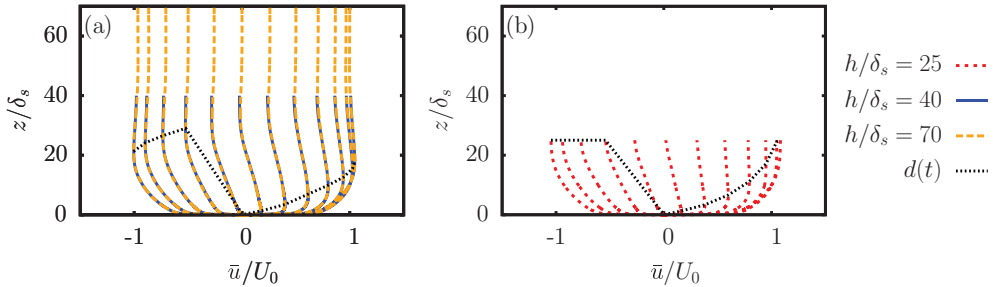


Figure 4.10: Velocity profiles every $\Delta\omega t = \pi/12$ starting at $\omega t = -5\pi/12$ (most left profile) ending at $\omega t = \pi/2$ (most right profile) for $\text{Re}_\delta = 3460$. The thickness of the wall-dominated layer d , defined as the height above the bottom at which the velocity profile has its first maximum is depicted by the black dotted line. A distinction is made between the deep water solution (a) and the shallow water solution (b).

In summary, R_τ depends on the phase ωt , the Reynolds number Re_δ and on the ratio h/δ_s . From these dependences, it might be expected that the existence of the log-layer is only governed by R_τ . However, this claim appears to be refuted by Fig. 4.11, in which the presence of the logarithmic layer is displayed as a function of R_τ and ωt . At $\omega t = \pi/3$, no log-layer is detected for $\text{R}_\tau < 180$, while a log-layer was already detected at this value of the Reynolds number in a plane-channel flow (Kim et al., 1987). In the region where the log-layer is present due to the local turbulence properties and not due to a history effect (i.e. from the start of the existence interval up to $\omega t < 5\pi/12$), a threshold of about $\text{R}_\tau = 400$ seems appropriate. However, for $\omega t = 2\pi/3$ a log-layer is detected for $\text{R}_\tau < 180$. These results suggest that once the log-layer enters the late deceleration phases, the threshold $\text{R}_\tau = 400$ is not valid any more. In addition, at $\omega t = \pi/3$ and $\omega t = 7\pi/12$, the log-layer is sometimes detected for lower values of R_τ than the values of R_τ for which the log-layer is not detected. These findings imply that it is not possible to reduce the number of parameters on which the presence of the log-layer depends, using R_τ . As result, the log-layer in a turbulent oscillating flow cannot be analyzed in a similar way as the log-layer in a steady turbulent flow, despite the similarities between the flows. To our current knowledge the three parameters Re_δ , h/δ_s and ωt are necessary for this analysis.

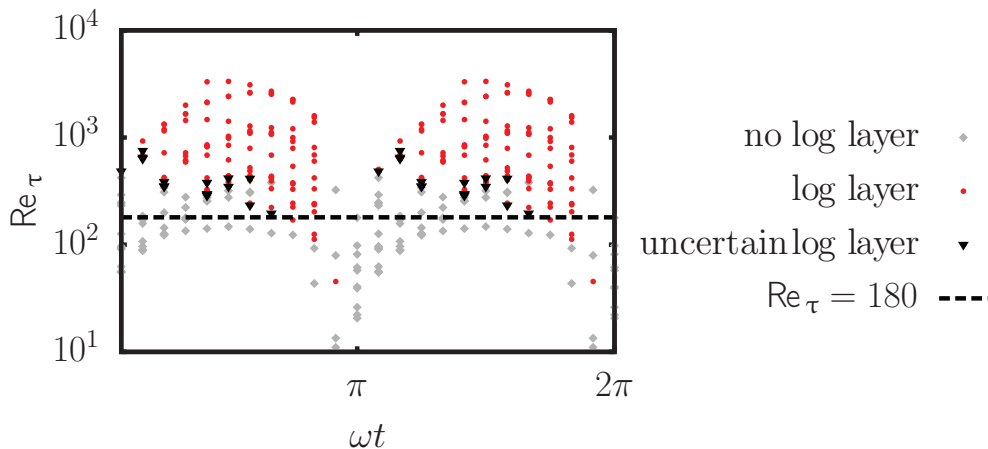


Figure 4.11: Link between the log-layer existence and the plane and phase averaged value of R_τ . The threshold for which the log-layer has been identified in the plane channel flow of Kim et al. (1987), i.e. $R_\tau = 180$, is also displayed.

4.4. Discussion and conclusions

The present study confirms that a logarithmic region in the velocity profiles is present for oscillating flows, with a phase interval and a spatial extent that increases with the Reynolds number. A new identification method, the map of points of coordinates $(\ln(z_{vs}^+); \overline{u}(z_{vs}^+)/U_0)$, where z_{vs}^+ is the thickness of the viscous viscosity dominated layer, demonstrates that the points of logarithmic velocity profiles collapse onto a single curve. This collapse makes the coordinates $(\ln(z_{vs}^+); \overline{u}(z_{vs}^+)/U_0)$ a distinct signature of the logarithmic layer and can help to identify its presence.

This study also shows that the logarithmic layer is never present throughout the whole cycle at the values of the Reynolds number simulated in this investigation, in agreement with previous studies (Salon et al., 2007; Jensen et al., 1989). Nevertheless, the simulation results show that with increasing value of the Reynolds number, the log-layer appears earlier in the oscillation cycle and grows in spatial extent. Furthermore, the values of the von Kármán constant k and the intercept B are found to be phase and Reynolds number dependent and to deviate by an order of 10% with respect to the classical values of $k = 0.41$ and $B = 5.5$. This is particularly remarkable because previous studies (Akhavan et al., 1991; Tuzi & Blondeaux, 2008; Scandura et al., 2016; Pedocchi, Cantero, & García, 2011) reported a value of the von Kármán constant much closer to the classical value. However, these studies were carried out in pipe flows, and a study by Marusic et al. (2010) stated that the universality of the von Kármán constant depends on the type of flow (pressure driven flow, plane channel flow or pipe flow). Nevertheless, deviation of order 10% for k and a decrease of B towards the end of the cycle was also reported by Salon et al. (2007). They attributed the decreasing value of B at the end of the deceleration phase, in the presence of an adverse pressure gradient, to a low-Reynolds number effect, but we believe that the presence of the log-layer at the end of the deceleration phase is just due to a history effect.

Additionally, two other sources of discrepancies between different values of the log-layer constants might be considered. First, the mechanism of turbulence generation is not exclusively similar to that of steady wall-bounded flows, for low Reynolds number values: during the acceleration phase small disturbances are damped (Vittori & Verzicco, 1998) while turbulence at the end of the deceleration phase is generated by the collapse of the wall shear stress, due to the adverse pressure gradient, and not by the rigid wall itself (Jensen et al., 1989). This is only true for lower values of the Reynolds numbers. For high Reynolds number values, turbulence appears already during the acceleration phase (Jensen et al., 1989). Second, the method with which the von Kármán constant was determined (i.e. by taking the local minimum of the log-layer diagnostic function Ξ) might lead to a slight overestimation when compared to fitting a log-layer through the velocity profile (Pirozzoli et al., 2014; Jiménez & Moser, 2007). In fact, the present investigation demonstrates that when the fitting procedure was applied, the obtained values of k and B could be much closer to the values reported in literature. However, the new values are then dependent on the size of the fitting interval. Therefore, the main result is that the values for k and B strongly depend on three distinct parameters: Re_δ , h/δ_s and the phase ωt . To our current understanding, it is not possible to reduce the number of parameter on which the properties of the logarithmic layer depend, like a Reynolds number based on the friction velocity u_τ .

Finally, the reduction of the ratio h/δ_s is found to (i) increase the phase interval for which intermittent turbulence is observed and (ii) shifts the existence interval of the log-layer to earlier phases. For these simulations characterized by intermittency, the presence of the logarithmic layer also depends on the oscillation cycle. Nevertheless, the values of the Reynolds numbers for the simulations presented here are relatively low for some applications. In tidal flows for example, Reynolds number values might be one order of magnitude higher (Kaptein et al., 2019), and we would expect the logarithmic layer to be present for a longer phase interval and the properties of the log-layer to be more constant.

Overall, we believe that the logarithmic assumption in wall models as formulated by Piomelli and Balaras (2002) is (i) a good approximation for oscillating flows at very high Reynolds number and (ii) an acceptable approximation at moderate Reynolds numbers. Nevertheless, if more accurate results need to be obtained, or for oscillating flows characterized by a strong reduction in turbulence activity or intermittent turbulence during (at least part of) the oscillation cycle, more sophisticated wall models are needed. These models should taking into account the phase and Reynolds number dependence of (i) the existence of the log-layer and (ii) the values of the von Kármán constant and the intercept. Also, if a wall model is used the height above the bottom in wall units of the first computational point is crucial. Depending on the phase within the oscillation cycle it can either be in the viscous sub-layer or in the logarithmic region. Therefore, an accurate wall model would have to incorporate the entire law-of-the-wall, i.e. $u^+ = z^+$ in the viscous sub-layer, $u^+ = 1/k \ln(z^+) + B$ in the log layer, as well as an adequate parametrization of the buffer layer.

This last statement closes the study of the pure oscillatory flow. Some remarks regarding this flow are given in the conclusion of this thesis. In the next three chapters, the attention moves towards the flow driven by a horizontal density gradient.

5

Analysis of one-dimensional models for exchange flows under strong stratification

5.1. Introduction

As discussed in Section 1.4.2, the flow driven by a horizontal density gradient is studied in this thesis as a model for the horizontal density structure in the coastal sea, particularly in the vicinity of a ROFI (see Sec 1.3.1 for a definition). In fact, gravity driven exchange flows due to horizontal density differences occur in many natural environmental situations, at the junction between two water-bodies with different densities. A gravity driven exchange flow or gravitational current, broadly defined, is a flow in which denser water flows over the bottom from the dense water body towards the less dense water body, and lighter water flows at the surface in the opposite direction. This type of exchange flows can take various forms, such as lock-exchange type of gravity currents with an initial horizontal density step (Benjamin, 1968; Shin et al., 2004), the gravitational circulation in estuaries (Hansen & Rattray Jr, 1965; MacCready, 2004; Burchard & Hetland, 2010; Burchard, Hetland, Schulz, & Schuttelaars, 2011; Geyer & MacCready, 2014), natural convection in a closed cavity with heated end walls (Cormack, Leal, & Imberger, 1974), exchange flows in straits (Gregg, Ozsoy, & Latif, 1999; Gu & Lawrence, 2005) or exchange that are not confined to channels, in coastal areas close to river plumes, such as described in this thesis (Simpson et al., 1990).

Very often, these exchange flows strongly impact the hydrodynamics of a large surrounding area due to the density stratification they generate. Additionally, strong (vertical) stratification limits vertical mixing in the water column and these exchange flows are known for driving disproportionately large horizontal transport of different substances such as pollutants, sediment, and micro-organisms (Geyer & MacCready, 2014). These properties make the understanding of exchange flows of the utmost importance in coastal oceanography.

As a result, models have been developed to estimate their properties, ranging from one-dimensional (1D) water-column models (Hansen & Rattray Jr, 1965; Blaise & Deleersnijder, 2008; Burchard & Hetland, 2010), to two-layer models (Gu & Lawrence, 2005; Shin et al., 2004) or idealized three-dimensional models with periodic horizontal forcing (Li et al., 2008, 2010), called from now on *three-dimensional horizontally-periodic* models, abbreviated as *3D-HP* models. A common challenge of all these models is to parametrize the driving force due to the horizontal difference in density. In 1D or 3D-HP models, the horizontal density differences are often parametrized using an imposed, constant horizontal density gradient. This choice allows to reformulate the governing equations (i.e., those for momentum and transport of salinity or density) in such a way that the mean velocity variable and the mean density variable are independent of the horizontal coordinate (an example of a reformulation is given in Appendix D.1). This feature is crucial, particularly in the 3D-HP models, for the consistency with periodic boundary conditions and needs to be upheld throughout a simulation. However, an inconvenience of imposing a constant horizontal density gradient is that the steady state is determined by the equilibrium between the imposed gradient and diffusion of both momentum and density. This equilibrium causes the stratification to grow out of bounds, a phenomenon usually called ‘runaway-stratification’.

The extent to which 1D models and 3D-HP models are affected by runaway-stratification differs. For example, in early 1D models of the gravitational circulation (Hansen & Rattray Jr, 1965; Chatwin, 1976), the stratification generated by the density gradients was limited by turbulent mixing due to tides, via the eddy viscosity and eddy diffusivity constants. The magnitude of the exchange flow was assumed to be proportional to the horizontal density gradient and the mean eddy viscosity. The eddy viscosity coefficient was then tuned to fit the measurements (Hansen & Rattray Jr, 1965; Chatwin, 1976; MacCready & Geyer, 2010) if chosen sufficiently high, it was able to counterbalance the increasing stratification. However, in estuaries characterized by very weak tides, the magnitude of the required eddy viscosity turned out to become unrealistically large (Simpson et al., 1990). In 3D-HP models, adjusting the eddy viscosity is not an option, since (a large part of) it is directly resolved in the numerical computations (e.g., in an LES) and can, therefore, not be imposed. Accordingly, the value of the horizontal density gradient should be kept low to avoid runaway-stratification. This constraint implies that only exchange flows driven by very weak density gradients can be investigated with existing 3D-HP models. An improved parametrization of the horizontal density gradient is required to allow application of 3D-HP models, and even 1D models, to zones of the parameter space currently out of reach due to runaway-stratification. Application of new and improved parametrizations in these 3D-HP models requires conservation of the linearity of the horizontal density gradient to properly satisfy the periodic boundary conditions in the horizontal direction.

In the present study, we isolated the ingredients generating environmental exchange flows (i.e., an initial horizontal density gradient and a quasi-infinite source of potential energy), and analyzed and modelled the resulting flow. We first propose a two-dimensional (2D) numerical set-up to simulate idealized exchange flows inside a channel for both the transient and the steady-state flow. This setup is similar to

those used in previous numerical and experimental studies on idealized gravity driven exchange flow (see e.g. Anati, Assaf, and Thompson (1977); Maderich, Konstantinov, Kulik, and Oleksiuk (1998); Hogg, Ivey, and Winters (2001)). Subsequently, numerical simulations using this set-up are performed to characterize the stratification process associated with horizontal density gradients as a function of the parameters of the problem. The results of the 2D model are then used to develop improved 1D models for the cross-sectional velocity profile along the channel and for the density profile at the center of the channel (with respect to the inlet and outlet). The performance of the models is discussed as a function of their suitability to be incorporated in water-column models and their suitability as homogeneous forcing in 3D-HP models.

5.2. Two-dimensional asymptotic model for exchange flows

5.2.1. Numerical set-up

The numerical set-up for the 2D simulations is displayed in Fig. 5.1. The flow is described in a Cartesian reference frame (y, z) , in which y represents the along-channel direction and z represents the vertical direction, with velocity vector $\mathbf{v} = (v, w)$. Gravity acts in the negative z -direction. The set-up, which is inspired by different experimental configurations (see, for example Simpson and Linden (1989); Meyer and Linden (2014); Lefauve et al. (2018)), consists of two reservoirs connected by a channel of height h and length L , with $L \gg h$ (implicitly assuming that end effects at $y = \pm L/2$ can be ignored). Each reservoir contains water with a different initial salt concentration, denoted by the salinities s_1 and s_2 in the left and right reservoirs, respectively. Initially, the salinity $s(y, z)$ in the channel is uniform in the vertical, and the salinity gradient in the along-channel direction is constant: $\partial s / \partial y = (s_2 - s_1) / L$. The salt concentration is the only physical quantity altering the fluid density in the present set-up. The inhomogeneous initial horizontal salt distribution leads to an unstable horizontal density gradient driving an exchange flow and generating vertical stratification. The steady state is reached once the driving mechanism (due to the density difference between the two reservoirs) is balanced by diffusion of both momentum and salt. Since this set-up represents environmental situations where the availability of the fresher and saltier water can be considered infinite, the reservoirs are much larger than the channel. In this way, the salinity of each reservoir can be considered constant and will not be influenced by the inflow of water from the other reservoir. In our 2D computational model, the size of a reservoir is equal to $6400h^2$, which is basically a trade-off between available computational resources and keeping the salinity in both reservoirs within an accepted margin of their initial values.

The 2D numerical set-up is implemented in COMSOL, using the ‘laminar flow’ and the ‘transport of diluted species’ modules. For details, see “COMSOL Multiphysics Reference Manual” (n.d.). The flow is governed by the 2D continuity and Navier-

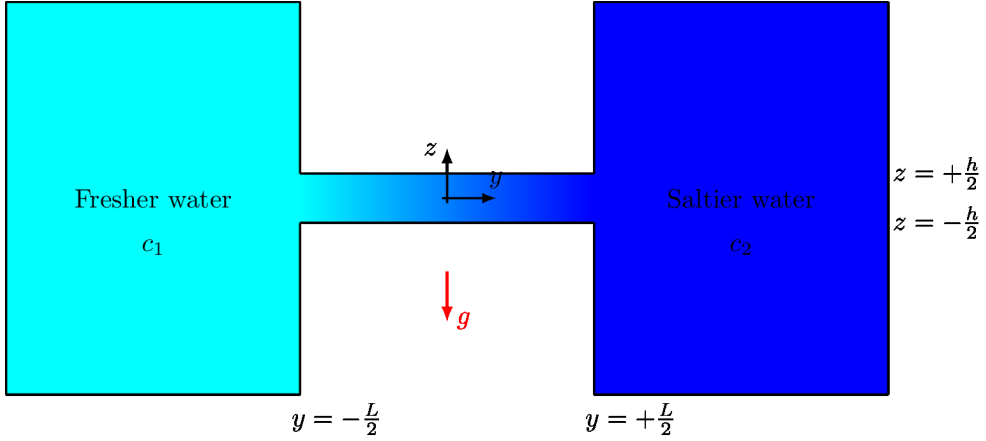


Figure 5.1: Side-view of the 2D computational domain, with the initial distribution of salt. This sketch is not to scale as $L \gg h$ and we assume very large salt reservoirs. The salt concentration in the left reservoir is denoted by the salinity s_1 and will be kept constant (as we assume an infinitely large reservoir). Similarly, the salt concentration in the right reservoir is denoted $s_2 > s_1$ (and also kept constant). The acceleration of the gravity g is in the negative z -direction. Note that this configuration is mirrored with respect to the ROFI configuration of Chapter 1 and the configuration of Chapter 6.

Stokes equations in Boussinesq approximation for an incompressible fluid:

$$\frac{\partial v}{\partial y} + \frac{\partial w}{\partial z} = 0, \quad (5.1)$$

$$\frac{\partial v}{\partial t} + v \frac{\partial v}{\partial y} + w \frac{\partial v}{\partial z} = -\frac{1}{\rho_{\text{ref}}} \frac{\partial p}{\partial y} + \nu \left(\frac{\partial^2 v}{\partial y^2} + \frac{\partial^2 v}{\partial z^2} \right), \quad (5.2)$$

$$\frac{\partial w}{\partial t} + v \frac{\partial w}{\partial y} + w \frac{\partial w}{\partial z} = -\frac{1}{\rho_{\text{ref}}} \frac{\partial p}{\partial z} + \nu \left(\frac{\partial^2 w}{\partial y^2} + \frac{\partial^2 w}{\partial z^2} \right) - \frac{1}{\rho_{\text{ref}}} \rho_{\text{var}} g, \quad (5.3)$$

where p denotes the pressure, and ρ_{var} denotes the variable part of the total density. The constant ν represents the kinematic viscosity of the fluid (which is assumed to be independent of the salinity). The density ρ_{ref} is a reference density, related to the total density ρ and to ρ_{var} by $\rho = \rho_{\text{ref}} + \rho_{\text{var}}$, with $\rho_{\text{ref}} \gg \rho_{\text{var}}$. The salinity s is governed by the advection-diffusion equation:

$$\frac{\partial s}{\partial t} + v \frac{\partial s}{\partial y} + w \frac{\partial s}{\partial z} = \kappa \left(\frac{\partial^2 s}{\partial y^2} + \frac{\partial^2 s}{\partial z^2} \right), \quad (5.4)$$

in which κ is the diffusivity of salt. The density ρ depends on the salinity s , via the equation of state $\rho = \rho_0 (1 + \beta s)$, in which ρ_0 is the density of fresh water and $\beta \cong 7.7 \times 10^{-4}$ (MacCready, 2004; Geyer & MacCready, 2014). The salinity is expressed in the practical salinity scale (PSS). The reference density is defined as $\rho_{\text{ref}} = \rho_0 [1 + \frac{1}{2} \beta (s_1 + s_2)] = \rho_0 (1 + \beta s_{\text{av}})$, with $s_{\text{av}} = \frac{1}{2} (s_1 + s_2)$ the average salinity

of both reservoirs. The equation of state for the variable part of the density is then

$$\rho_{\text{var}} = \rho_0 \beta [s - \frac{1}{2}(s_1 + s_2)] = \rho_0 \beta (s - s_{\text{av}}) . \quad (5.5)$$

For simplicity, only exchange flows with constant viscosity ν and salt diffusivity κ are considered, i.e. no turbulence model is used. Furthermore, simulations are stopped and results rejected for further analysis, once shear instabilities start to develop at the quasi-horizontal density interface that emerge during the flow evolution for simulations for high Reynolds number values. This justifies the use of a 2D numerical set-up instead of a 3D one, saving computational time and allowing for a thorough exploration of the parameter space. The use of a constant kinematic viscosity and salt diffusivity for application to coastal flows can be regarded as considering a constant effective turbulent (or eddy) viscosity and diffusivity. This simplification is common in classical studies of exchange flows (see e.g. Geyer and MacCready (2014)), and it is used here because it allows for analytical solutions that further our understanding of the system.

Initially, the fluid is at rest and the salinity in each reservoir is uniform. In the channel, the salinity at initial time t_0 is given by

$$s(y, z; t_0) = \frac{\Delta s}{L} y + s_{\text{av}} \quad \text{for} \quad -\frac{1}{2}L \leq y \leq \frac{1}{2}L , \quad (5.6)$$

where the initial salinity difference $\Delta s = s_2 - s_1$ has been introduced. As a result, the isopycnals at $t = t_0$ are vertical and equidistant. The horizontal density gradient in the center of the channel ($y = 0$) is given by

$$\frac{\partial \rho_{\text{var}}}{\partial y}(y = 0, z; t_0) = \frac{\Delta \rho}{L} , \quad (5.7)$$

with $\Delta \rho = \rho_0 \beta \Delta s$ the initial density difference. Subsequently, ρ_{var} at $y = 0$ is equal to zero at $t = t_0$ over the whole depth.

At the solid walls of both reservoirs and the channel, no-slip boundary conditions are applied for the fluid velocity and no-flux boundary conditions for the salinity. This choice of boundary conditions in the channel results in an antisymmetric horizontal velocity profile with respect to $z = 0$ at $y = 0$. Additionally, the profile of the variable density ρ_{var} and salinity s_{var} are also antisymmetric with respect to $z = 0$ at $y = 0$. The case with a no-slip boundary condition for the fluid velocity at the bottom and a no-stress boundary condition at the top of the channel is discussed in Sec 5.3.4.

The equations are solved in their non-dimensional form. To make them dimensionless, the buoyancy velocity scale U_g is introduced and linked to the previously defined Δs :

$$U_g = \sqrt{\frac{\rho_0 \beta \Delta s}{\rho_{\text{ref}}} gh} = \sqrt{\frac{\beta \Delta s}{1 + \beta s_{\text{av}}} gh} . \quad (5.8)$$

The spatial coordinates are scaled with h , time with a buoyancy time scale h/U_g , the fluid velocities with U_g , the pressure with $\rho_{\text{ref}} U_g^2$, the density with $\Delta \rho$, and the

salinity with Δs . By eliminating the density in Eq. (5.3) using Eq. (5.5), the set of Eqs. (5.1)-(5.4) are rewritten in non-dimensional form yielding

$$\frac{\partial v^*}{\partial y^*} + \frac{\partial w^*}{\partial z^*} = 0, \quad (5.9)$$

$$\frac{\partial v^*}{\partial t^*} + v^* \frac{\partial v^*}{\partial y^*} + w^* \frac{\partial v^*}{\partial z^*} = -\frac{\partial \tilde{p}^*}{\partial y^*} + \frac{1}{\text{Re}_g} \left(\frac{\partial^2 v^*}{\partial y^{*2}} + \frac{\partial^2 v^*}{\partial z^{*2}} \right), \quad (5.10)$$

$$\frac{\partial w^*}{\partial t^*} + v^* \frac{\partial w^*}{\partial y^*} + w^* \frac{\partial w^*}{\partial z^*} = -\frac{\partial \tilde{p}^*}{\partial z^*} + \frac{1}{\text{Re}_g} \left(\frac{\partial^2 w^*}{\partial y^{*2}} + \frac{\partial^2 w^*}{\partial z^{*2}} \right) - \left(s^* - \frac{1}{2} s_{\text{av}}^* \right) \quad (5.11)$$

$$\frac{\partial s^*}{\partial t^*} + v^* \frac{\partial s^*}{\partial y^*} + w^* \frac{\partial s^*}{\partial z^*} = \frac{1}{\text{Re}_g \text{Sc}} \left(\frac{\partial^2 s^*}{\partial y^{*2}} + \frac{\partial^2 s^*}{\partial z^{*2}} \right), \quad (5.12)$$

where the asterisk (*) denotes a non-dimensional variable. In the case that the left tank contains fresh water, thus with $s_1 = 0$, $s_{\text{av}}^* = s_2/2$ and $U_g = \sqrt{\beta g h s_2 / (1 + \frac{1}{2} \beta s_2)}$. In these equations, there are two non-dimensional parameters: the gravitational Reynolds number $\text{Re}_g = U_g h / \nu$ and the Schmidt number $\text{Sc} = \nu / \kappa$. The last non-dimensional number we need to introduce is the aspect ratio $\Gamma = h/L$, that does not appear explicitly in Eqs. (5.9)-(5.12) but plays a role via the computational domain. Note that the Grashof number Gr , which quantifies the ratio of the buoyancy to viscous force, is related to the Reynolds number such that $\text{Gr} = \text{Re}_g^2$. Both Gr and Re_g are commonly used to characterize density driven flows governed by Eq. (5.12) (See e.g. Ottolenghi, Adduce, Inghilesi, Armenio, and Roman (2016); Härtel, Meiburg, and Necker (2000)). Here, we will use the Reynolds number throughout.

The momentum equations are discretized using a first-order finite-element method for the pressure and the velocity. The equation for the transport of salt is discretized using a quadratic method. The computational domain is meshed with a triangular grid, using 62 elements over the depth of the channel. The time-integration is performed with an implicit backward-difference scheme. More details about spatial discretization, grids and time integration can be found in ‘‘COMSOL Multiphysics Reference Manual’’ (n.d.). The grid in the reservoirs is coarser since these reservoirs act just as a supply of water and salt, and the details of the hydrodynamics in these reservoirs are not of interest to us in the present investigation.

5.2.2. Salinity distribution in the channel: flow regime identification

Depending on the values of the parameters Re_g , Sc and Γ , the initial situation evolves towards a steady state governed by the competition between diffusive and advective processes. In this section, we describe the steady-state conditions of four distinct flow regimes: the diffusion-dominated regime, the transition regime, the high-advection/high-diffusion regime, and the high-advection/low-diffusion regime. We show results for three simulations with $\text{Sc} = 300$ and $\Gamma = 1/60$ for which we varied the value of the gravitational Reynolds number, and one simulation with $\text{Sc} = 1$, $\Gamma = 1/60$ and $\text{Re}_g = 5000$. For these four simulations in the steady state, Fig. 5.2 shows the density field and the isopycnals, and Fig. 5.3 shows the vertical profiles of density, of the horizontal density gradient, and of the mean horizontal velocity for

$y = 0$. The results of a thorough exploration of the parameter space are presented in Sec. 5.3.3.

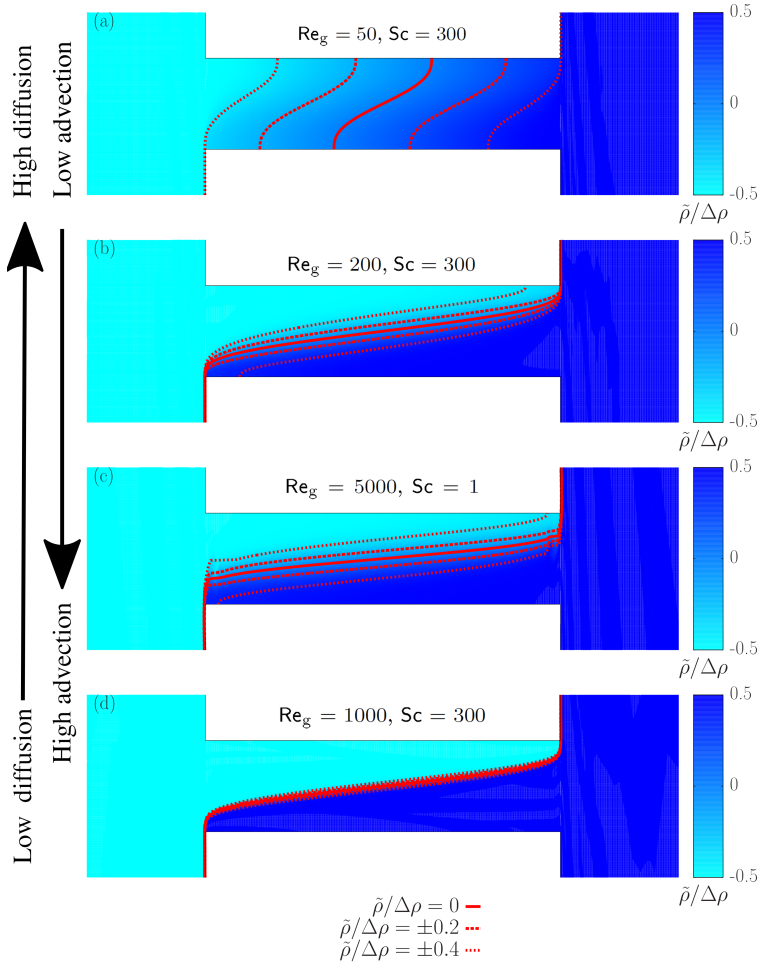


Figure 5.2: The density distribution in the channel (not to scale as $h \ll L$) for four simulations in the four different regimes: (a) the diffusion-dominated regime (here with $\text{Re}_g = 50$, $\text{Sc} = 300$ and $\Gamma = 1/60$), (b) the transition regime ($\text{Re}_g = 200$, $\text{Sc} = 300$ and $\Gamma = 1/60$), (c) the high-advection/high-diffusion regime ($\text{Re}_g = 5000$, $\text{Sc} = 1$ and $\Gamma = 1/60$) and (d) the high-advection/low-diffusion regime ($\text{Re}_g = 1000$, $\text{Sc} = 300$ and $\Gamma = 1/60$). Note that $\rho_{\text{var}}/\Delta\rho = s^* - s_{\text{av}}^*$. With $s_1 = 0$ this implies $s_{\text{av}}^* = \frac{1}{2}$ and $0 \leq s^* \leq 1$ and thus $-0.5 \leq \rho_{\text{var}}/\Delta\rho \leq 0.5$.

In the diffusion-dominated regime, a steady state is reached once the mechanism driving the exchange flow due to the horizontal density gradient is balanced by momentum diffusion, and when the vertical stratification process is balanced by salt diffusion. Effectively, the advective transport of salt from the saltier to the fresher reservoir is fully counteracted. The isopycnals in the steady state of the diffusion-

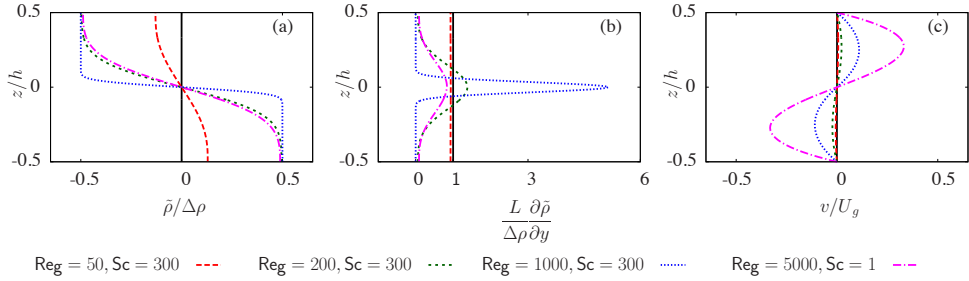


Figure 5.3: The profiles at $y = 0$ of (a) the resolved density, (b) the horizontal density gradient, and (c) the mean horizontal velocity in the steady state for the same four simulations used to describe the four regimes in Fig.5.2. The solid black line represents the initial condition.

dominated regime are no longer vertical but are sigmoid functions of the depth and resemble the typical lines of equal density observed in some estuaries (MacCready & Geyer, 2010), as can be seen in Fig. 5.2a. The isopycnals are still equidistant close to the center of the channel (around $y = 0$), suggesting a conservation of the linearity of the initial horizontal density gradient. Additionally, ρ_{var} at $y = 0$ is no longer constant and equal to zero over the height of the channel, as seen in Fig. 5.3a. The water column is now stratified close to $z = 0$, and very weakly stratified close to the top and bottom boundaries due to the no-flux boundary condition applied there. Finally, the value of the horizontal density gradient at $y = 0$ has slightly decreased with respect to its original value, but remains in good approximation constant over the depth of the channel, as seen in Fig. 5.3b.

In the transition regime, momentum and salt diffusion are no longer strong enough to balance the force driving the exchange flow and the formation of the stratification. This means that net transport of salt from the saltier to the fresher reservoir will occur. In the steady state, water with salinity s_1 , flowing along the top wall of the channel, reaches the saltier water reservoir, and water with salinity s_2 , flowing over the bottom of the channel, reaches the fresh water reservoir. This process can be observed in Fig.5.2b, where the lines of equal density for $\rho_{\text{var}}/\Delta\rho = 0$ and $\rho_{\text{var}}/\Delta\rho = \pm 0.2$ span over the entire channel in the horizontal direction between $-L/2 \leq y \leq L/2$. The lines of equal density for $\rho_{\text{var}}/\Delta\rho = \pm 0.4$ do not span the whole channel, suggesting that diffusion of momentum and salt still plays a role in the steady-state balance. The vertical density profile $\rho_{\text{var}}/\Delta\rho$ at $y = 0$ in the transition regime has a similar shape to the density profile in the diffusion-dominated regime, but clearly, with a larger amplitude (Fig. 5.3a). A clear stratification is present close to $z = 0$, and a very weak stratification close to the top and bottom boundaries. In comparison with the diffusion-dominated regime, the amplitude of the density profile has increased and $\rho_{\text{var}}/\Delta\rho$ at $z = \pm h/2$ has reached its possible extreme values: $\pm 1/2$ at $z = \mp h/2$.

In practice, this steady state is achieved already in a finite time denoted by t_s . The profiles of the horizontal density gradient at $y = 0$ in the steady state (i.e. for $t > t_s$) are significantly different to those of the diffusion-dominated regime, as seen in Fig. 5.3b. The horizontal density gradient is no longer constant over the depth.

Instead, it has decreased towards zero at the top and bottom boundaries, and it has increased around $z = 0$, taking the shape of a Gaussian function.

In the high-advection/high-diffusion regime, the density distribution in the steady state is similar to the distribution in the transition regime (see Fig. 5.2). In both cases, fluid from each reservoir reaches the opposing reservoir, but there is a diffuse interface separating them. Some differences between these two regimes are mainly observed at the ends of the channel. In fact, Fig. 5.3a shows that the density profile at $y = 0$ for the simulations in these two regimes are almost indistinguishable. However, the flow velocity (Fig. 5.3c) is clearly much stronger for the simulation within the high-advection/high-diffusion regime. This implies that in spite of the strong advection by the flow, the interface is spread out due to the high diffusion.

In the high-advection/low-diffusion regime, the steady state is characterized by water from each reservoir being able to reach unmixed the opposite reservoir. Diffusion of both momentum and salt play hardly a role in balancing the force driving the exchange flow and the stratification. This can be seen in Fig. 5.2d, where all the isopycnals span over the entire channel length from $y = -L/2$ to $y = L/2$ and nearly collapse onto each other: diffusion is too small to smoothen the sharp interface generated by the exchange flow, an advective process. In Fig. 5.3a, it can be seen that the thickness of the pycnocline decreases drastically and that any vertical stratification is absent close to the channel boundaries. The density in the upper layer is equal to $-\Delta\rho/2$ while the density in the lower layer is equal to $\Delta\rho/2$. The horizontal density gradient still takes the shape of a Gaussian function but with a much narrower and much higher peak (Fig. 5.3b). This observation suggest that as advection becomes increasingly important while diffusion is weak, the steady-state system converges towards a two-layer system. At $y = 0$, each layer has a constant density equal to $\Delta\rho/2$ for $z < 0$ and $-\Delta\rho/2$ for $z > 0$. As a result, the density at the top and bottom boundaries in the steady state is given by

$$\rho_{\text{var}} \left(y = 0, z = \mp \frac{1}{2}h; t \rightarrow \infty \right) = \pm \frac{1}{2}\Delta\rho. \quad (5.13)$$

It is relevant to mention that, although this relationship must be satisfied in the high-advection/low-diffusion regime, it already emerges in the transition regime, and might also occur in the high-advection/high-diffusion regime. Similarly, the horizontal density gradient at those boundaries is given by

$$\frac{\partial \rho_{\text{var}}}{\partial y} \left(y = 0, z = \mp \frac{1}{2}h; t > t_s \right) = 0. \quad (5.14)$$

5.3. Proposals for one-dimensional models

Based on the characteristics of the different regimes and the initial condition, it is possible to develop a parametrization of the horizontal density gradient at the center of the channel, $y = 0$. In this way, the time evolution of the horizontal velocity profile at $y = 0$ is governed by a 1D diffusion equation supplemented with a specific source term containing information on the horizontal density gradient, and the time evolution of the density profile at this location is governed by a classical 1D advection-diffusion equation.

5.3.1. Mathematical formulation

The equations governing the 1D model at $y = 0$ are

$$\frac{\partial v}{\partial t} = \nu \frac{\partial^2 v}{\partial z^2} + \frac{g}{\rho_{\text{ref}}} \int_0^z \frac{\partial \rho_{\text{var}}}{\partial y} d\tilde{z}, \quad (5.15)$$

$$\frac{\partial \rho_{\text{var}}}{\partial t} = \kappa \frac{\partial^2 \rho_{\text{var}}}{\partial z^2} - v \frac{\partial \rho_{\text{var}}}{\partial y}, \quad (5.16)$$

in which $\partial \rho_{\text{var}}/\partial y$ is the term that needs to be parametrized. For a derivation of the momentum equation, the reader is referred to Appendix D.1. Based on the steady-state horizontal density gradient profiles obtained in Sec. 5.2.2, the parametrized horizontal density gradient needs to satisfy three conditions. First, it should be constant over the vertical in the absence of stratification. Second, it should decrease at the boundaries with the onset of stratification. Third, it should increase in the center of the channel once the flow converges towards a two-layer system. We expect then that the parametrized horizontal density gradient $\partial \rho_{\text{var}}/\partial y$ depends on both ρ_{var} and $\partial \rho_{\text{var}}/\partial z$. A parametrization satisfying these conditions is

$$\frac{\partial \rho_{\text{var}}}{\partial y} = a_0 + a_1 |\rho_{\text{var}}| + a_2 \left| \frac{\partial \rho_{\text{var}}}{\partial z} \right|, \quad (5.17)$$

where a_0 , a_1 and a_2 are constants to be determined. Note that, in the case $a_2 = 0$, the parametrization resembles the one proposed by Blaise and Deleersnijder (2008), while in the case $a_1 = 0$ and $a_2 = 0$, the classical constant horizontal density gradient parametrization is recovered.

To find a_0 , the initial condition at $t = t_0$ in the channel is used: $\rho_{\text{var}} = 0$, $\partial \rho_{\text{var}}/\partial z = 0$ and $\partial \rho_{\text{var}}/\partial y$ is given by Eq. (5.7). Substituting these values in the density parametrization given by Eq. (5.17), yields

$$a_0 = \frac{\Delta \rho}{L}. \quad (5.18)$$

To find a_1 , Eqs. (5.13)–(5.14), which are valid from the transition regime are used combined with the no-flux boundary condition at the top boundary of the channel, i.e. $\partial \rho_{\text{var}}/\partial z = 0$ at $z = h/2$ to obtain

$$a_1 = -\frac{2}{L}. \quad (5.19)$$

Finding a_2 is more challenging and, to our current knowledge, it cannot be obtained from the steady-state conditions in the advection-dominated regime (Sec. 5.2.2). We will see in Sec. 5.3.2 that its value can be chosen equal to $\Gamma/3$ for high Sc values, but we leave a_2 for now.

Equations (5.15)–(5.17) are scaled as in Sec. 5.2, i.e with h for the spatial coordinates, h/U_g for the time, U_g for the velocities, $\rho_{\text{ref}} U_g^2$ for the pressure, and $\Delta \rho$ for

the density. This scaling results in

$$\frac{\partial v^*}{\partial t^*} = \frac{1}{\text{Re}_g} \frac{\partial^2 v^*}{\partial z^{*2}} + \int_0^{z^*} \frac{\partial \rho_{\text{var}}^*}{\partial y^*} dz^*, \quad (5.20)$$

$$\frac{\partial \rho_{\text{var}}^*}{\partial t^*} = \frac{1}{\text{Re}_g \text{Sc}} \frac{\partial^2 \rho_{\text{var}}^*}{\partial z^{*2}} - v^* \frac{\partial \rho_{\text{var}}^*}{\partial y^*}, \quad (5.21)$$

$$\frac{\partial \rho_{\text{var}}^*}{\partial x^*} = \Gamma(1 - 2|\rho_{\text{var}}^*|) + a_2 \left| \frac{\partial \rho_{\text{var}}^*}{\partial z^*} \right|, \quad (5.22)$$

where the asterisk (*) denotes a non-dimensional variable. The aspect ratio Γ was previously a parameter tunable through the computational domain, but in the present 1D model, it appears directly in the equations.

5.3.2. Limiting cases

The set of Eqs. (5.20)–(5.22) is a priori not integrable analytically. However, by simplifying the equations, it is possible to have an exact solution of the approximated problem, which can in turn provide some scaling properties for the amplitudes of the exchange flow and the stratification.

In the diffusion-dominated regime, the horizontal density gradient is in good approximation constant over the depth, i.e. $\partial \rho_{\text{var}}^* / \partial y^* = \Gamma$, such that the equations governing the flow and the density distribution in a steady state become

$$0 = \frac{1}{\text{Re}_g} \frac{\partial^2 v^*}{\partial z^{*2}} + \Gamma z^*, \quad (5.23a)$$

$$0 = \frac{1}{\text{Re}_g \text{Sc}} \frac{\partial^2 \rho_{\text{var}}^*}{\partial z^{*2}} - \Gamma v^*. \quad (5.23b)$$

Using no-slip boundary conditions for the velocity and no-flux boundary conditions for the density at the top and at the bottom wall of the channel, we obtain $v^{d,\infty}$ and $\rho_{\text{var}}^{d,\infty}$, the steady-state solutions for the velocity and the density in the diffusion-dominated regime

$$\frac{v^{d,\infty}(z)}{U_g} = \frac{\text{Re}_g \Gamma}{24} \left(\frac{z}{h} - 4 \left(\frac{z}{h} \right)^3 \right), \quad (5.24a)$$

$$\frac{\rho_{\text{var}}^{d,\infty}(z)}{\Delta \rho} = \frac{\text{Re}_g^2 \Gamma^2 \text{Sc}}{24} \left(-\frac{1}{16} \left(\frac{z}{h} \right) + \frac{1}{6} \left(\frac{z}{h} \right)^3 - \frac{1}{5} \left(\frac{z}{h} \right)^5 \right). \quad (5.24b)$$

It is clear that $v^{d,\infty}$ depends on $\text{Re}_g \Gamma$ (this combination of parameters is also known as the Simpson number) while $\rho_{\text{var}}^{d,\infty}$ depends on $\text{Re}_g^2 \Gamma^2 \text{Sc}$ so that only two parameters govern the steady-state solutions. This solution is commonly known as the viscous advective diffusive solution (VAD) (Cormack et al., 1974; Hogg et al., 2001). Notice, however, that it is valid for both low and high Sc values.

As the value of $\text{Re}_g \Gamma$ increases two distinct possibilities emerge. For small Sc values, the flow will tend towards the hydraulic limit (Hogg et al., 2001). In this regime, mixing, viscosity, and friction are neglected, and the density and velocity both tend towards a two layer configuration. In each of these layers, the density and

velocity can be considered as uniform, and the non-dimensional volume flux becomes independent of $\text{Re}_g \Gamma$.

For large Sc values, the flow tends towards the high-advection/low-diffusion regime, the exchange flow in the channel also converges towards a two-layer system. In this case, the horizontal density gradient reduces to $\partial \rho_{\text{var}}^* / \partial y^* = a_2 |\partial \rho_{\text{var}}^* / \partial z^*| = -a_2 \partial \rho_{\text{var}}^* / \partial z^*$ (as $\partial \rho_{\text{var}}^* / \partial z^* \leq 0$ for $-\frac{1}{2} \leq z^* \leq \frac{1}{2}$) such that the equations governing the flow and the density distribution become

$$0 = \frac{1}{\text{Re}_g} \frac{\partial^2 v^*}{\partial z^{*2}} - a_2 \int_0^{z^*} \frac{\partial \rho_{\text{var}}^*}{\partial z^*} dz^*, \quad (5.25a)$$

$$0 = \frac{1}{\text{Re}_g \text{Sc}} \frac{\partial^2 \rho_{\text{var}}^*}{\partial z^{*2}} + a_2 v^* \frac{\partial \rho_{\text{var}}^*}{\partial z^*}. \quad (5.25b)$$

The last term in the first equation can be integrated, and in the limit $\text{Sc} \rightarrow \infty$, the system of Eqs. (5.25) can be rewritten as

$$\frac{\partial^2 v^*}{\partial z^{*2}} = \text{Re}_g a_2 \rho_{\text{var}}^*, \quad (5.26a)$$

$$a_2 v^* \frac{\partial \rho_{\text{var}}^*}{\partial z^*} = 0. \quad (5.26b)$$

The non-trivial solution (i.e. with $v^* \neq 0$) for Eq. (5.26b) is the steady-state solution for the density in the high-advection/low-diffusion regime where ρ_{var}^* is a constant. However, this solution can have a jump at $z = 0$ since $v^*(z = 0) = 0$ due to symmetry. This can be seen by integrating Eq. (5.26b) from $z = -\epsilon$ to $z = +\epsilon$ (with ϵ a positive real number) yielding

$$\lim_{\epsilon \rightarrow 0} v^*(z = 0) [\rho_{\text{var}}^*(z = +\epsilon) - \rho_{\text{var}}^*(z = -\epsilon)] = 0.$$

Since $v^*(z = 0) = 0$, $[\rho_{\text{var}}^*(z = +\epsilon) - \rho_{\text{var}}^*(z = -\epsilon)]$ can take any value. This means that the solution to Eq. (5.26b) is a piecewise constant function, and in agreement with Eq. (5.13), we take

$$\frac{\rho_{\text{var}}^{a, \infty}(z)}{\Delta \rho} = \frac{1}{2} - H(z), \quad (5.27)$$

where $H(z)$ is the Heavyside function which is defined as: $H(z > 0) = 1$, $H(z < 0) = 0$, and $H(z = 0) = 1/2$. Moreover, $dH(z)/dz = \delta_D(z)$ with $\delta_D(z)$ the Dirac delta function (which also satisfies $\int_{-\infty}^{+\infty} \delta_D(z) dz = 1$ and $\int_0^z \delta_D(z) dz = \frac{1}{2}$). The steady-state solution for the velocity in the high-advection/low-diffusion regime, $v^{a, \infty}$, follows:

$$\frac{v^{a, \infty}(z)}{U_g} = \begin{cases} \text{Re}_g a_2 \left[\frac{1}{8} \frac{z}{h} + \frac{1}{4} \left(\frac{z}{h} \right)^2 \right] & \text{for } z \leq 0, \\ \text{Re}_g a_2 \left[\frac{1}{8} \frac{z}{h} - \frac{1}{4} \left(\frac{z}{h} \right)^2 \right] & \text{for } z \geq 0. \end{cases} \quad (5.28)$$

From this solution, the constant a_2 can be determined by assuming that the shear at $z = 0$ is conserved from the diffusion-dominated (obtained from Eq. (5.24a)) regime

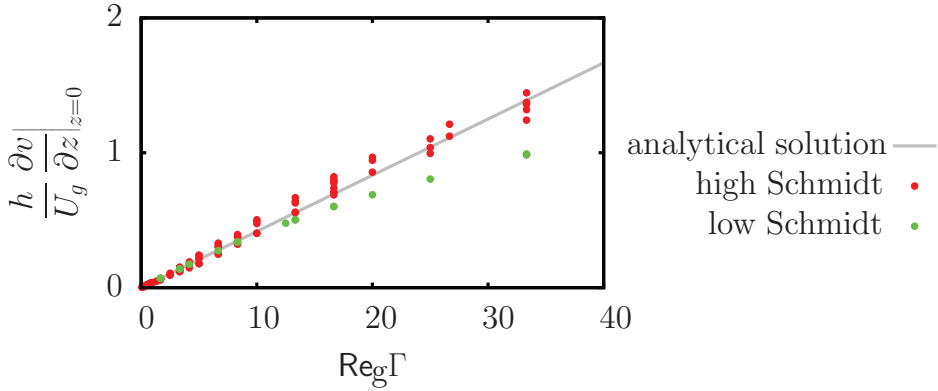


Figure 5.4: Shear at mid-depth as a function of $\text{Re}_g \Gamma$ spanning all different flow regimes, from the diffusion dominated to the high-advection/low-diffusion. Low Schmidt number values correspond to $\text{Sc} = 1$, and high Schmidt number values correspond to $\text{Sc} = 50, 300, 1000$.

to the advection-dominated regime, which gives

$$a_2 = \frac{1}{3} \Gamma . \quad (5.29)$$

This also means that the magnitude of the velocity and the volume flux still depend exclusively on $\text{Re}_g \Gamma$ as long as the Sc value is large. We use the 2D simulations to test this assumption. The resulting shear at $z = 0$ is displayed as a function of $\text{Re}_g \Gamma$ in Fig. 5.4. Despite some small deviations, there is a good agreement between our assumption and the 2D numerical data for high Schmidt number values where the flow is dominated by the shear at the interface. Clearly, this agreement is not as good for low Schmidt number values and large values of $\text{Re}_g \Gamma$ (i.e. towards the high-advection/high-diffusion regime and the hydraulic limit). The difference between these two limiting cases is that in the high-advection/low-diffusion regime, viscosity and friction play a role close to the top and bottom boundaries and at the interface so that the velocity is not uniform in each of the layers.

The ability of the 1D model to reproduce correctly the steady-state velocity profiles and density profiles in the different regimes determines its validity. This ability is investigated in the next section by comparing the results of the new 1D model to results of the 2D model, and to results from 1D models using more classical parametrizations of the horizontal density gradient.

5.3.3. Numerical results: model comparison

The 1D set of non-dimensional Eqs. (5.20)-(5.22) is integrated numerically using a centred finite-difference scheme for the spatial derivatives, a trapezoidal numerical method for the integral and an explicit upwind time integration scheme. The numerical algorithm is, therefore, globally first order accurate in time and second order accurate in space. The steady-state results of the 1D model are compared to the steady-state results (evaluated for $t > t_s$, with t_s the time at which the steady state

is reached) of the 2D model in terms of four different quantities: (i) the amplitude of the stratification $\Delta\rho_{\text{var}} = \rho_{\text{var}}(-\frac{1}{2}h) - \rho_{\text{var}}(\frac{1}{2}h)$, (ii) the integral over the channel cross section of the absolute value of the density, (iii) the amplitude of the exchange flow $\Delta v_{\text{max}} = v_{\text{max}} - v_{\text{min}}$, and (iv) the integral of the absolute value of the velocity profile over the channel cross section.

We consider three versions of the 1D model: the 1D0 model, where $a_0 = \Delta\rho/L$ and $a_1 = a_2 = 0$, which corresponds to the classical parametrization with a constant, uniform horizontal density gradient; the 1D1 model, where $a_0 = \Delta\rho/L$, $a_1 = -2/L$ and $a_2 = 0$, which is similar to the parametrization suggested by Blaise and Deleersnijder (2008); and the new 1D2 model, where $a_0 = \Delta\rho/L$, $a_1 = -2/L$, and $a_2 = \Gamma/3$. In the present study, four different values of the Schmidt number Sc are considered: 1, 50, 300 and 1000, and three different values of the aspect ratio, $\Gamma = 1/30, 1/60$, and $1/120$. The value of the Reynolds number Re_g is varied between 2 and 4000. For certain combinations of Re_g , Γ and Sc , the simulations show the emergence of shear instabilities, such as the appearance of Kelvin-Helmholtz billows. These simulations are not considered in the analysis as they are outside the scope of the present investigation.

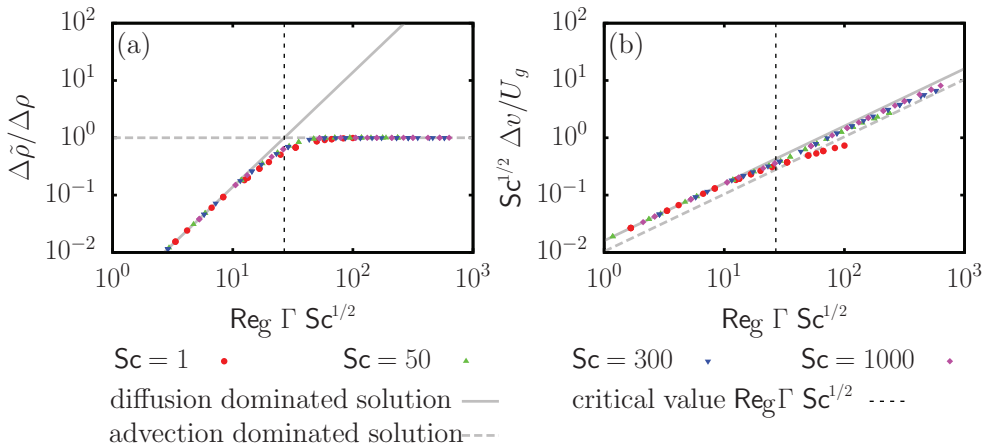


Figure 5.5: Magnitude of the steady-state stratification (a) and the steady-state exchange flow scaled with $Sc^{1/2}$ (b) as a function of $Re_g \Gamma Sc^{1/2}$ as obtained from the 2D simulations. Different Schmidt number values are displayed with different colors. The gray solid line represents the analytical solution in the diffusion-dominated regime [i.e. the solution to Eqs. (5.24b)–(5.24a)], and the gray dashed line represents the analytical solution for the high-advection/low-diffusion regime [i.e. the solution to Eqs. (5.27)–(5.28)]. Both of these solutions are derived in Appendix D.2. The black vertical dashed line at $Re_g \Gamma Sc^{1/2} = 12\sqrt{5}$ represents the transition at which the two analytical solutions for $\Delta\rho_{\text{var}}/\Delta\rho$ intersect.

In Fig. 5.5, the magnitude of the steady-state stratification $\Delta\rho_{\text{var}}/\Delta\rho$ and the steady state exchange flow are first analyzed only for the 2D model. The main objective of this figure is to provide a first impression of the different trends that the 1D

models should be able to reproduce. When plotting the magnitude of the steady-state stratification $\Delta\rho_{\text{var}}/\Delta\rho$ as a function of $\text{Re}_g\Gamma\text{Sc}^{1/2}$ (Fig. 5.5a), there is a clear collapse of the data. This collapse indicates that $\text{Re}_g\Gamma\text{Sc}^{1/2}$ is the governing parameter for the stratification. For small values of $\text{Re}_g\Gamma\text{Sc}^{1/2}$, $\Delta\rho_{\text{var}}/\Delta\rho$ follows the theoretical curve of the diffusion-dominated regime. For intermediate values of $\text{Re}_g\Gamma\text{Sc}^{1/2}$, $\Delta\rho_{\text{var}}/\Delta\rho$ deviates from this theoretical curve as the increase in stratification slows down. In this transition, the data points for $\text{Sc} = 1$ lie slightly under the data points for other Sc values. For high values of $\text{Re}_g\Gamma\text{Sc}^{1/2}$, $\Delta\rho_{\text{var}}/\Delta\rho$ reaches its maximum possible value when $\Delta\rho_{\text{var}} = \Delta\rho$. This value corresponds to the initial density difference between the reservoirs. It is possible to define a transition point indicating the intersection between the theoretical line of the diffusion-dominated regime and the line given by $\Delta\rho_{\text{var}}/\Delta\rho = 1$. This transition occurs at $\text{Re}_g\Gamma\text{Sc}^{1/2} = 12\sqrt{5} \approx 26.8$.

The magnitude of the exchange flow obtained from the reference 2D model shows a clearly distinct behaviour between high and low Schmidt number values (Fig. 5.5b). This magnitude follows the theoretical line of the diffusion-dominated regime for relatively small values of $\text{Re}_g\Gamma$ for both low and high values of the Schmidt number. However, slightly before the transition point at $\text{Re}_g\Gamma\text{Sc}^{1/2} = 12\sqrt{5}$, it deviates (in a rather subtle way) towards the theoretical prediction for the high-advection/low-diffusion regime (high Schmidt number values). However, for low Schmidt number values, the deviation is more pronounced since the solution tends towards the hydraulic limit, where the velocity becomes independent of $\text{Re}_g\Gamma$. Note, however, that our simulations do not reach this limit since the simulations with $\text{Sc} = 1$ go up to a value of $\text{Re}_g\Gamma \approx 10^2$, while the hydraulic limit is reached for $\text{Re}_g\Gamma \approx 10^3$ (Hogg et al., 2001).

The performance of the 1D models is tested through an analysis of the magnitude of the steady-state stratification in Fig. 5.6. A distinction is made between the results for high Schmidt number values, $\text{Sc} = 50, 300, 1000$, shown in Fig. 5.6a-b, and for low Schmidt number value, $\text{Sc} = 1$, shown in Fig. 5.6c-d. The different 1D models reproduce the results from the 2D model with different levels of accuracy. The stratification predicted by the 1D0 model grows linearly with $(\text{Re}_g\Gamma\text{Sc}^{1/2})^2$, as given by Eq. (5.24b), even beyond the transition point between the diffusion regime and the high-advection regimes. This is a perfect illustration of runaway stratification. Naturally, $\text{Re}_g\Gamma\text{Sc}^{1/2} = 12\sqrt{5}$ is the limit of applicability of the 1D0 model. In contrast, the 1D1 model and the 1D2 model reproduce the trend of the 2D model for all the values of $\text{Re}_g\Gamma\text{Sc}^{1/2}$ that were investigated, with the data points of the 1D2 model being almost superimposed on the data points of the 2D model. The relative errors shown in Figs. 5.6b,d quantify the performances previously observed. The relative error of the 1D0 model grows indefinitely beyond the transition point, while the error of the 1D1 model and the 1D2 model is maximum around this transition point, before decreasing again. Globally, the 1D2 model performs better than the 1D1 model: their respective maximum relative errors are approximately 10% and 30% for high Schmidt number values and approximately 10% and 20% for low Schmidt number values.

We have also evaluated the integral of $|\rho_{\text{var}}/\Delta\rho|$ over the channel height, which is a measure of the stratification in the channel. The dependence of this integral quantity

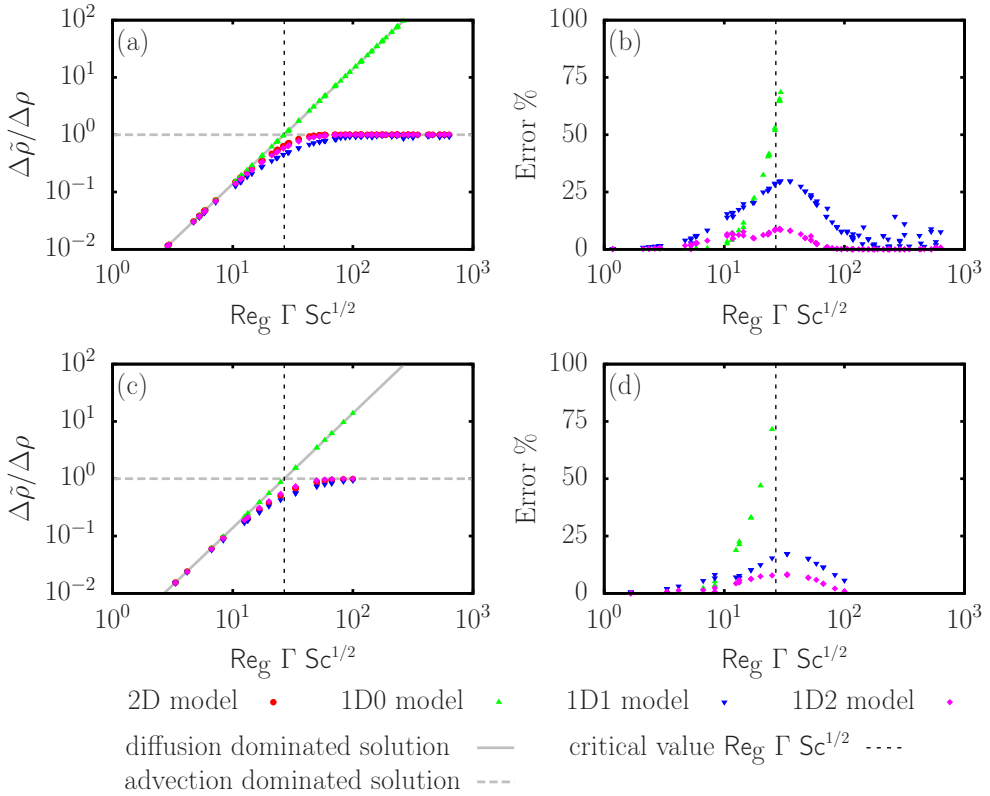


Figure 5.6: The magnitude of the steady-state stratification for the different Sc models for high Sc values (a) and for $\text{Sc} = 1$ (c), and the corresponding errors between the 2D model and the 1D models for high Sc values (b) and for $\text{Sc} = 1$ (d). The gray solid line represents the analytical solution in the diffusion-dominated regime [i.e. the solution to Eqs. (5.24b)-(5.24a)], and the gray dashed line represents the analytical solution for the high-advection/low-diffusion regime [i.e. the solution to Eqs. (5.27)-(5.28)]. Both of these solutions are derived in Appendix D.2. The black vertical dashed line at $\text{Re}_g \Gamma \text{Sc}^{1/2} = 12\sqrt{5}$ represents the transition at which the two analytical solutions intersect; see panels (a) and (c).

on the value of $\text{Re}_g \Gamma \text{Sc}^{1/2}$ (not shown) is similar to that of $\Delta\rho_{\text{var}}/\Delta\rho$. In addition, the comparisons between the 2D model and the three 1D models give similar results, with the trends in the errors being comparable with those shown in Fig. 5.6. This proves that not only the steady-state stratification is well predicted, but that the entire density profile is well approximated over the channel height (around $y = 0$) by the 1D1 and the 1D2 models.

The magnitude of the velocity in the exchange flow from the 1D models and the 2D model are displayed in Fig. 5.7. For this quantity, there is a strong Schmidt number dependence that contrasts with the weak Schmidt-number dependence of the reference

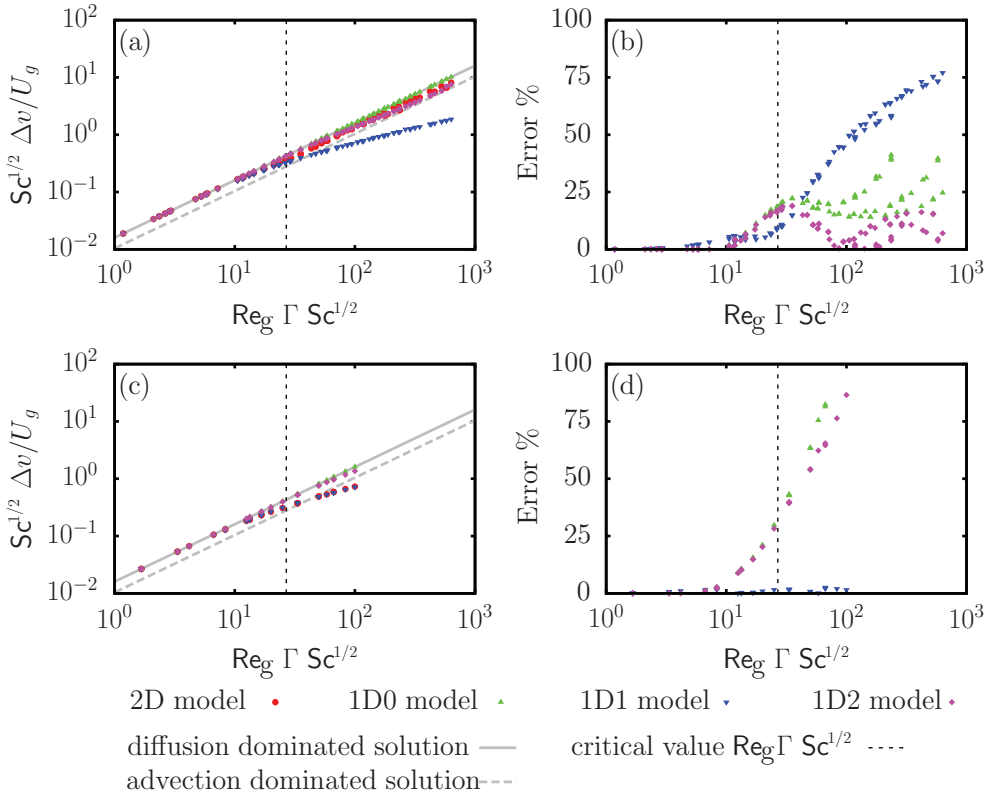


Figure 5.7: Magnitude of the steady-state exchange flow for the different models for high Sc in (a) and $\text{Sc} = 1$ in (c), and the corresponding errors between the 2D model and the 1D models in (b) for high Sc and in (d) for $\text{Sc} = 1$. The gray solid and dashed lines display the trends resulting from the analytical solutions for $\Delta v/U_g$, based on Eqs. (5.24a) and (5.28), and explicitly written in Appendix D.2. The black vertical dashed line represents the transition point at $\text{Re}_g \Gamma \text{Sc}^{1/2} = 12\sqrt{5}$.

stratification, discussed in the previous paragraphs. This has a significant impact on the accuracy of the 1D models in modeling the flow velocity. As expected from the analytical derivation in Sec. 5.3.2, all 1D models agree well with the theoretical prediction and the 2D model within the diffusion-dominated regime independently of the Schmidt number value. Also independently of the Schmidt number values, the relative error of the 1D0 model increases drastically as the value of $\text{Re}_g \Gamma \text{Sc}^{1/2}$ approaches the transition value of $12\sqrt{5}$ and the runaway stratification appears. The 1D1 and 1D2 models perform significantly differently for high Schmidt number values and low Schmidt number values. For high Schmidt number values, the relative error of the 1D2 model peaks approximately at a value of 25% around the transition point $\text{Re}_g \Gamma \text{Sc}^{1/2} = 12\sqrt{5}$ and decreases for larger values of $\text{Re}_g \Gamma \text{Sc}^{1/2}$. The relative error

in the 1D1 model continues increasing with increasing values of $\text{Re}_g \Gamma \text{Sc}^{1/2}$. Clearly, the 1D2 model gives the closest results to the 2D model in terms of exchange flow magnitude for high Schmidt numbers. For low Schmidt number values, the trend in the magnitude of the exchange flow predicted by the 2D model is, in contrast, very well reproduced by the 1D1 model (Fig. 5.7c) resulting in almost no relative error (Fig. 5.7d). On the other hand, the 1D2 model strongly deviates from the results of the 2D model as $\text{Re}_g \Gamma \text{Sc}^{1/2}$ approaches the transition values (Fig. 5.7c,d). The error of the 1D2 model is, in fact, comparable to the error of the 1D0 model (Fig. 5.7d). The 1D1 model outperforms the 1D2 models in predicting the exchange flow magnitude, for the high- advection/high-diffusion regime, because the 1D2 results in a large horizontal density gradient at the interface that is not present in that regime.

In analogy with the height-integrated density, the results for the integral over the channel height of $|v/U_g|$ and the associated relative error are almost identical to the results for $\Delta v/U_g$ (not shown). The ability to reproduce the magnitude of the exchange flow from the 2D model – or the incapability to reproduce it – extends to the entire velocity profile.

5.3.4. Extension to flows with a no-stress top boundary condition

The previous results correspond to an exchange flow in the plane channel flow configuration. This configuration, with a no-slip boundary condition for the velocity at the lower and upper walls of the channel, preserves the symmetry of the flow. Although this symmetry was convenient for estimating steady-state conditions, it is not realistic for environmental exchange flows. An open-channel flow configuration, with a no-stress boundary condition at the top wall of the channel (or a free surface), would be a better approximation. In such a case, the non-dimensional momentum equation for the horizontal velocity Eq. (5.20) is slightly modified yielding

$$\frac{\partial v^*}{\partial t^*} = \frac{1}{\text{Re}_g} \frac{\partial^2 v^*}{\partial z^{*2}} + \tau_w^* - \int_{z^*}^{\frac{1}{2}} \frac{\partial \rho_{\text{var}}^*}{\partial y^*} dz^* + \int_{-\frac{1}{2}}^{\frac{1}{2}} \left(\zeta^* + \frac{1}{2} \right) \frac{\partial \rho_{\text{var}}^*}{\partial y^*} dz^*, \quad (5.30)$$

with the appearance of a new term:

$$\tau_w^* = \frac{1}{\text{Re}_g} \frac{\partial v^*}{\partial z^*} \Big|_{z^*=-\frac{1}{2}}, \quad (5.31)$$

which represents the non-dimensional wall-shear stress.

Results for the stratification in the open-channel flow configuration are similar to those in the plane-channel flow configuration. The magnitude of the stratification $\Delta \rho_{\text{var}}/\Delta \rho$ in the 2D model follows the theoretical solution in the diffusion-dominated regime before the stratification saturates at $\Delta \rho_{\text{var}}/\Delta \rho = 1$ (Figs. 5.8a,c). The 1D0-model reproduces the 2D results within the diffusion-dominated regime, but the error increases drastically towards the transition to the advection-dominated regimes (Figs. 5.8b,d). The 1D1 model and the 1D2 model reproduce the stratification very well, with a maximum error near the transition point of around 25% and 10% for the models 1D1 and 1D2, respectively. The results of the integral over the channel height

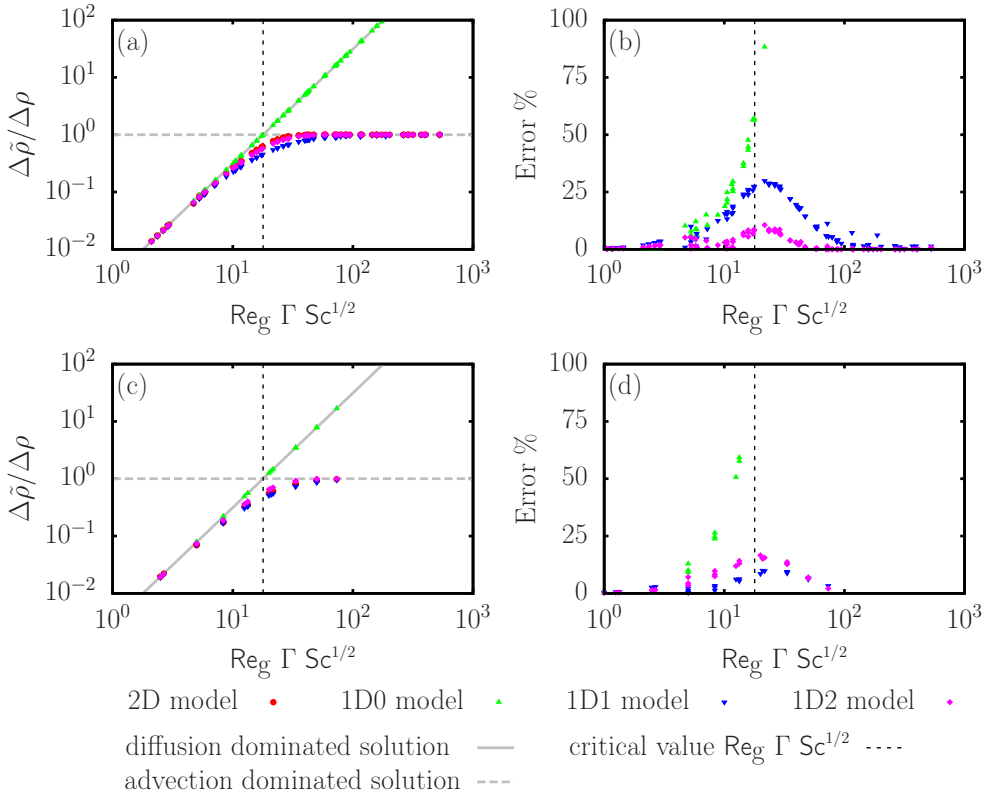


Figure 5.8: Magnitude of the steady-state stratification for the different models in the open-channel configuration for high Sc values (a) and $\text{Sc} = 1$ (c). The corresponding errors between the 2D model and the 1D models are also shown for high Sc values (b) and for $\text{Sc} = 1$ (d). The gray solid and dashed lines display the trends resulting from the analytical solutions for $\Delta\rho_{\text{var}}/\Delta\rho$, based on Eqs. (D.18) and (5.27) for the diffusion dominated and high-advection/low-diffusion flows, respectively, and explicitly written in Appendix D.3. The black vertical dashed line represents the transition where the two analytical solutions intersect at $\text{Re}_g \Gamma \text{Sc}^{1/2} = 8\sqrt{5}$.

of $|\rho_{\text{var}}/\Delta\rho|$ confirm that the trends observed in $\Delta\rho_{\text{var}}/\Delta\rho$ are representative for the entire profile. However, a major difference with respect to the plane-channel configuration is the increase of the magnitude of stratification as a function of $\text{Re}_g^2 \Gamma^2 \text{Sc}$. For the plane-channel configuration it increases as $\text{Re}_g^2 \Gamma^2 \text{Sc}/720$ while for the open channel configuration it increases much faster as $\text{Re}_g^2 \Gamma^2 \text{Sc}/320$ due to the absence of friction at the top boundary. As a result the transition $\text{Re}_g \Gamma \text{Sc}^{1/2} = 8\sqrt{5} \approx 17.9$ occurs sooner in the open-channel configuration.

Again, the results of the 2D model show a clear difference in the magnitude of the velocities between the high Schmidt number values (Fig. 5.9a), where $\Delta v/U_g$ deviates

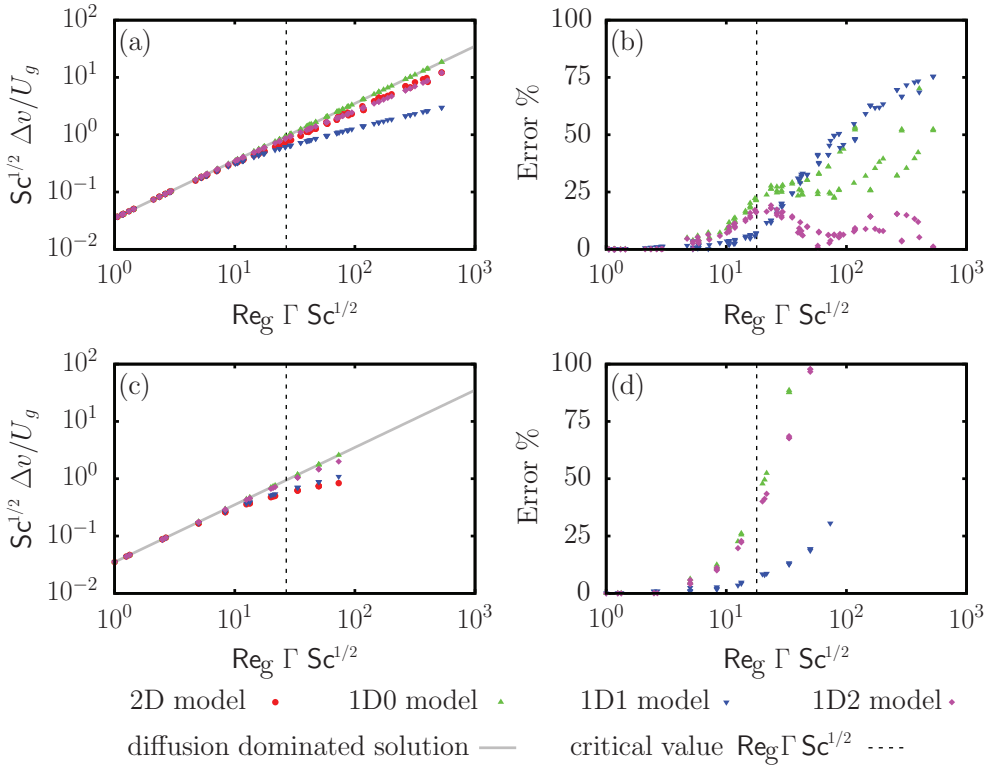


Figure 5.9: Magnitude of the steady-state exchange flow velocities for the different models in the open-channel configuration for high Sc values (a) and for $Sc = 1$ (c). The corresponding errors between the 2D model and the 1D models are given for high Sc values (b) and for $Sc = 1$ (d). The gray solid lines in panels (a) and (c) represent the trend resulting from the analytical solution for $\Delta v/U_g$, based on Eq. (D.15) for the diffusion-dominated flows and derived in Appendix D.3. The black vertical dashed line represents the critical value $Re_g \Gamma Sc^{1/2} = 8\sqrt{5}$ for transition between the diffusion and advection-dominated regimes.

only slightly from the theoretical line, and the low Schmidt number value (Fig. 5.9c), where this deviation is much more pronounced as it tends towards the hydraulic limit. The 1D2 reproduces the 2D results better in the high Schmidt number regime, while the 1D1 model performs better for low Schmidt number values. The analysis of the integral over the channel height of $|v/U_g|$ confirms that the trend observed for $\Delta v/U_g$ is representative for the entire profile.

5.4. Discussion

In laminar flows, the diffusion of salt is governed at a molecular level with the Schmidt number of order 700. In turbulent flows, the diffusion of salt at large scales is governed

by turbulent diffusion that can be represented using a turbulent Schmidt number, which is usually of order 1. The results presented in the current paper imply then that the choice of 1D model should be based on the regime of the flow, i.e. the 1D2 model for laminar flows and the 1D1 for turbulent flows. In addition, if 3D-HP models are used using direct numerical simulation (DNS) or large-eddy simulation (LES) techniques, turbulent diffusion is solved for rather than imposed or parametrized. From a numerical point of view, such flows have high Schmidt number values, but from a physical point of view, such flows are governed by low Schmidt number values at the large scales. These differences in Schmidt number values can lead to inconsistencies when a 1D model is used as a body force in 3D-HP models, such that the choice will have to be carefully motivated.

Up to now, the results show that the new parametrization of the density gradient leads to a significant improvement in the ability of 1D models to reproduce the density profiles obtained from numerical simulations of a 2D reference model. However, despite this agreement, there are still discrepancies between the 1D models in their ability to reproduce the velocity profiles. To better analyze the differences between the 1D1 and 1D2 models, the steady-state vertical profiles of the horizontal density gradient are displayed in Fig. 5.10 for different parameter values covering the four distinct regimes (i.e., diffusion-dominated, transition, high-advection/high-diffusion and high-advection/low-diffusion). Globally, the 1D models reproduce the general evolution of the horizontal density gradient of the 2D model quite well. For example, it is seen that for the diffusion-dominated regime (Figs. 5.10a), the nearly constant profile of the horizontal density gradients is reproduced by all the models.

However, some features are not well reproduced by the 1D models. For all cases, the horizontal density gradient resulting from the 1D1 model is limited to a maximum values of unity, while the horizontal density gradient resulting from the 2D simulation can reach values higher than unity (see e.g. Figs.5.10a,b,d). On the other hand, the 1D2 model tends to overestimate the value of the horizontal density gradient around mid-depth. This is mostly observed in the high-advection/high-diffusion regime (Fig. 5.10c), which explains the large discrepancies between the 1D2 model and the 2D model for low Sc values. Nonetheless, in the high-advection/low-diffusion regime, where the density profile tends towards a two-layer configuration but the velocity profile does not, there is a good agreement between the 2D and the 1D2 model, as expected from the analytical solution in this limit (see Sec 5.3.2).

The results of this study have implications for the range of applicability of 1D water-column models in environmental exchange flows with external turbulent mixing. In the case of the gravitational circulation, for example, the traditional version of the 1D model (i.e., with the constant density gradient or 1D0 model) can still be used for well-mixed estuaries, in which the tidal turbulence is strong enough to (partly) destroy the stratification in agreement with Hansen and Rattray Jr (1965) and Chatwin (1976). However, with the new parametrization of the horizontal density gradient, the estuarine circulation can also be simulated in cases of weak tidal flows, for which runaway stratification would occur (Burchard et al., 2011) or for which the eddy-viscosity was set too high (Simpson et al., 1990). However, knowledge about the turbulent nature of the flow is crucial to justify the choice between the 1D1 and 1D2 model. In turbulent estuaries the flow is likely to be governed by the turbulent

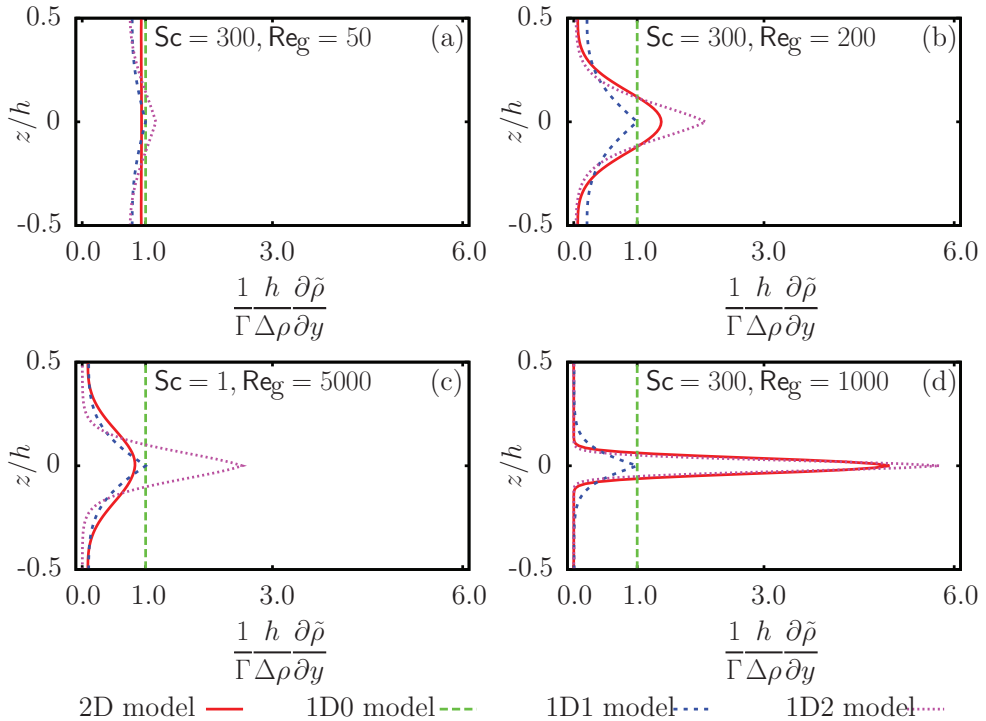


Figure 5.10: Vertical profiles of the horizontal density gradient for the four cases representative of the four regimes. The cases correspond to the those in Fig. 5.2. (a) Diffusion-dominated regime ($Re_g = 50$, $Sc = 300$), (b) Transition regime ($Re_g = 200$, $Sc = 300$), (c) high-advection/high-diffusion regime ($Re_g = 5000$, $Sc = 1$), and (d) high-advection/low-diffusion regime ($Re_g = 1000$, $Sc = 300$). $\Gamma = 60$ for all four cases.

Schmidt number rather than the molecular Schmidt number such that the use of the 1D1 model should be preferred, see Figs. 5.7c,d. On the other hand, high-resolution numerical simulations of the mixing processes in an exchange flow subjected to instabilities (e.g. Salehipour et al. (2016)) or relatively small-scale experiments of exchange flows (e.g. Lefauve et al. (2018)) have to be performed in three-dimensional domains. Note, however, that in earlier experimental work on exchange flows through straits (Anati et al., 1977; Maderich et al., 1998), temperature was used to generate the density differences. In such a case, the Prandtl number (the equivalent to the Schmidt number for heat) is approximately equal to 7, which facilitated reaching the hydraulic limit.

Considering the turbulent viscosity and diffusivity as constant and homogeneous is only a first approximation for the exchange flows in estuaries. However, spatial and temporal variability of the eddy viscosity can give rise to more complex dynamics, for example, in the case of the *eddy viscosity-shear covariance circulation* (ESCO

circulation) that produces a more complex vertical structure in strongly stratified situations (Cheng, De Swart, & Valle-Levinson, 2013; Dijkstra, Schuttelaars, & Burchar, 2017). However, these dynamics should emerge naturally when an appropriate one-dimensional model for the horizontal density gradient is used to force the flow.

5.5. Conclusion

In the present study, we introduce two new parametrizations for the horizontal density gradient driving environmental exchange flows that can be incorporated in 1DV models. These 1DV models incorporate a feedback of the stratification on the driving horizontal density gradient to limit the effect of runaway stratification. The parametrizations have been extensively tested by comparing their results of the 1DV models with the results of 2D numerical simulations of laminar exchange flows, and with those of previous parametrizations. Depending on the parameter values, four different regimes are identified: (i) diffusion dominated, (ii) transition, (iii) high-advection/high-diffusion, and (iv) high-advection/low-diffusion. The classical model, which considers a constant horizontal density gradient, only performs well in the diffusion dominated regime, where the stratification is weak. The new 1D models outperform the classical model in all other regimes, but they perform differently depending on the Schmidt number. For low Schmidt number values the so-called 1D1 model should be preferred, for example for models of turbulent gravitational flows in estuaries. For high Schmidt number values, the so-called 1D2 model should be preferred, for example for the simulation of laminar exchange flows at laboratory scale. Both the 1D1 model and the 1D2 model predict the steady-state stratification very well. The new parametrizations were able to reproduce the density profiles obtained with the 2D model within 10% of accuracy, resolving the problem of runaway stratification. They are also able to predict a reduction of the magnitude of the exchange flow velocities observed in strongly stratified situations.

The improvements in 1D models of exchange flow can have a significant impact in the future research of these type of flows. For example, it unlocks the possibility to explore regions of the estuarine-circulation parameter space characterized by strong stratification. Additionally, the formulation of the model, which is independent of the horizontal coordinates, also opens the traditional direct numerical simulation set-ups with horizontally periodic domains to the simulation of density-driven exchange flows. The simulation of turbulent flows with lateral induced stratification are now possible. This option is investigated in the next chapter.

6

Regime transitions in stratified shear flows: the link between horizontal and inclined ducts

6.1. Introduction

The analytical velocity profiles derived in the previous chapter can help to understand the pre-eminent experimental set-up for stationary exchange flows: the stratified inclined duct (SID) experiment (Macagno & Rouse, 1961; Meyer & Linden, 2014; Lefauve et al., 2019a; Lefauve & Linden, 2020a). In the SID experiment, two large tanks with fluid with different densities are linked by an inclined, long duct (see Fig. 6.1). In recent years, there has been vast progress in the understanding of the flow in SID experiments driven by improved measurement capabilities that allow for simultaneous detailed measurements of the three-dimensional density and velocity fields (Partridge, Lefauve, & Dalziel, 2019). A key question that has been addressed is the transitions between flow regimes: from laminar to the emergence of interfacial waves, to intermittently turbulent, and to fully turbulent (Macagno & Rouse, 1961; Meyer & Linden, 2014; Lefauve et al., 2019a; Lefauve & Linden, 2020a). Although these different regimes have been observed for 60 years, explaining them over a wide range of parameter values remains a challenge. In fact, one of the unanswered questions is “How to explain flow regime transitions in horizontal ducts or ducts inclined at a slightly negative angle?” (Lefauve et al., 2019a).

Lefauve et al. (2019a) distinguished between two situations: *lazy* and *forced* flows. To explain this distinction, it is necessary to define the internal angle of the duct $\alpha = \arctan(h/L)$, where h is the height of the duct and L its length. *Lazy* flows are defined as those occurring when the inclination angle θ of the duct satisfies $\alpha \gg \theta > -\alpha$, and *forced* flows as those occurring when $\theta > \alpha$. The term *forced* refers to the

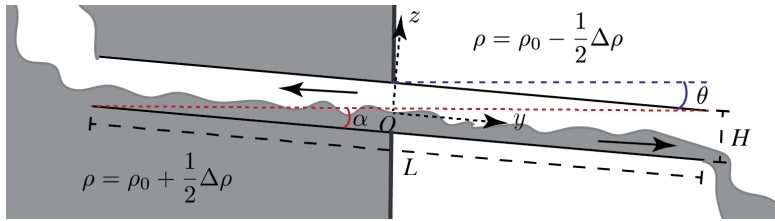


Figure 6.1: Schematic representation of the side view of a stratified inclined duct (SID) experimental setup. In the center: the duct of length L and height h inclined an angle θ with respect to the horizontal. The duct connects two large tanks: one with water with density $\rho = \rho_{\text{ref}} + \Delta\rho/2$ and the other with density $\rho = \rho_{\text{ref}} - \Delta\rho/2$. The internal angle of the duct is $\alpha = \arctan(h/L)$. The along-duct coordinate is y_θ and the coordinate perpendicular to the bottom and the top of the duct is z_θ . The origin O of the coordinate system is located at the center of the duct. Note that this set-up is mirrored with respect to Chapter 5 and Chapter 7, but in agreement with the Rhine ROFI of Chapter 1.

increased importance of the gravitational forcing due to the tilt. Meyer and Linden (2014) and Lefauve et al. (2019a) have proposed two different conditions for the regime transitions in *forced* flows showing good agreement with experimental data. However, these conditions are unreliable for *lazy* flows in general, and unsuitable for flows in horizontal ducts ($\theta = 0$) and ducts with slightly negative angles ($\theta < 0$).

The current chapter proposes an explanation for the regime transitions in SID experiments with large Schmidt number values that spans both *lazy* and *forced* flows, i.e. encompassing slightly negative inclinations, horizontal ducts, and positive inclinations. This explanation is based on the numerical and analytical study of the previous chapter, particularly the high-advection/low-diffusion regime. In this regime, advection can be neglected from the momentum equation but not from the density transport equation. The one-dimensional (1D) model and the associated analytical solution in the limit of zero mass diffusion, are extended to inclined ducts; we discuss the implications for the regime transitions, and we make a comparison with experimental results. The proposed link between horizontal and inclined ducts should allow to further exploit the results of SID experiments for the understanding of large scale environmental exchange flows.

6.2. Description of the system and background

The SID setup, mentioned earlier and sketched in Fig. 6.1, consists of two tanks with fluid at densities $\rho_{\text{ref}} \pm \Delta\rho/2$ (due to differences in, for example, salt concentration or temperature), joined by a duct. The duct with length L and height h is inclined at an angle θ with respect to the horizontal. In fact, there are only two differences with respect to the two-dimensional set-up of Chapter 5, the inclination angle and the initial condition (i.e. constant horizontal density gradient in Chapter 5 versus sharp interface in the SID setup). As a result, the same assumptions apply. The fluid is considered to have uniform and constant viscosity ν . It is still convenient to define the typical velocity scale $U_g \equiv \sqrt{g'h}$, where $g' \equiv g\Delta\rho/\rho_{\text{ref}}$ with g the gravitational acceleration. Besides the angle of the duct θ , the system can be described by three non-dimensional parameters: the aspect ratio of the duct $\Gamma \equiv h/L$, the gravitational

Reynolds number and the Schmidt number $Sc \equiv \nu/\kappa$ with κ the diffusivity of salt (or heat, in which case the Schmidt number is referred to as the Prandtl number). However, for comparison purposes, it is more convenient to adopt the Reynolds number formulation from Lefauve and Linden (2020a),

$$Re \equiv \frac{hU_g}{2\nu} = \frac{h\sqrt{g'h}}{2\nu}, \quad (6.1)$$

which differs with a factor 1/2 with respect to Re_g . This difference is due to the typical length scale, which is here chosen to be $h/2$ instead of h in the previous chapter. We consider long ducts: $\Gamma \ll 1$. For ducts with different widths W , we must introduce an additional parameter $B = W/h$.

Meyer and Linden (2014) proposed an empirical condition for the transition between different regimes by defining the Grashof number $Gr = 2 \sin \theta Re^2 / \Gamma$ which quantifies the ratio of the buoyancy force to the viscous force. They proposed the critical value $Gr = 4 \times 10^7$ for the transition between the intermittently turbulent and the turbulent regimes showing good agreement with experimental results. Lefauve et al. (2019a) proposed that the transitions between different regimes for a SID setup with a given Γ -value occur at constant θRe -values. Lefauve and Linden (2020a) compared their proposed transitions against several experimental data sets including those of Meyer and Linden (2014). They remarked particularly good agreement with experiments for *forced* flows (i.e. $\theta > \alpha$) when, in addition, $\Gamma Re \lesssim 50$. However, the comparison was inconclusive when considering the full parameter space explored. Independently of this, the conditions proposed by both Meyer and Linden (2014) and Lefauve et al. (2019a) are clearly not valid for $\theta \leq 0$. Furthermore, the definition of Gr proposed by Meyer and Linden (2014) is not consistent with its common definition for horizontal systems: $Gr = Re^2$ (Härtel et al., 2000; Hogg et al., 2001).

In horizontal ducts, the flow is dominated by diffusion for $Re\Gamma \ll (180/Sc)^{1/2}$, as found in the previous chapter (this limit is equivalent to $Re\Gamma \ll 12(5/Sc)^{1/2}$ using their definitions). This regime is known as the viscous advective-diffusive (VAD) solution (Cormack et al., 1974; Hogg et al., 2001), the *hydrostatic-viscous balance* (Lefauve & Linden, 2020a) or the diffusion-dominated regime (previous chapter). In this regime, the flow is characterized by the linear growth of the magnitude of the streamwise velocity (made dimensionless with U_g) with $Re\Gamma Sc^{1/2}$. For $Re\Gamma \gg (180/Sc)^{1/2}$, two distinct flow regimes arise depending on the Sc -value. For $Sc \sim 1$, the flow tends to the hydraulic limit, in which the velocity reaches the maximum peak value U_g and becomes independent of Re (Hogg et al., 2001). However, for large Sc -values, the velocity keeps increasing linearly with $Re\Gamma$, like in the VAD solution, in what we called the high-advection/low-diffusion regime in the previous chapter. This continuous growth is, most probably, only possible because a transition to a turbulent flow is not considered. This suggests that the high-advection/low-diffusion regime resides between the VAD regime and the emergence of waves, and eventually, turbulence. In other words, the upper bound for the high-advection/low-diffusion regime should be determined by the regime transition from laminar to the emergence of interfacial waves.

6.3. Analytical model

6.3.1. Horizontal ducts

Since a different length scale is used in this chapter with respect to Chap. 5, it adds clarity to repeat the governing equations and the analytical solution with regards to the present scaling. If the governing equations are made dimensionless by scaling the spatial coordinates with $h/2$, time with $h/(2U_g)$, the velocity with U_g , the pressure with $\rho_{\text{ref}}U_g^2$, and the density with $\Delta\rho$, the non-dimensional equations are

$$0 = \frac{1}{2} \int_0^{z^*} \frac{\partial \rho'^*}{\partial y^*} dz^* + \frac{1}{\text{Re}} \frac{\partial^2 v^*}{\partial z^{*2}}, \quad (6.2)$$

$$v^* \frac{\partial \rho'^*}{\partial y^*} = \frac{1}{\text{ReSc}} \frac{\partial^2 \rho'^*}{\partial z^{*2}} \quad (6.3)$$

with the asterisk denoting a non-dimensional variable. For simplicity, the asterisk is omitted from here on. For consistency with Lefauve and Linden (2020a), there are two differences in the definition of the problem with respect to Chapter 5. The typical length scale of the problem is $h/2$ instead of h , and the tank with the higher density is on the $y < 0$ side.

As a reminder, advection of momentum is neglected with respect to viscous diffusion, but advection in the density transport equation is not, in the high-advection/low-diffusion regime. This is substantiated by considering the relative magnitude of along-channel derivatives of the density and the velocity. The magnitude (denoted by $[\dots]$) of $\partial \rho' / \partial y$ is imposed by the density difference between the two tanks so that $[\partial \rho' / \partial y] \sim \Gamma/2$. However, $[\partial v / \partial y]$ depends on the flow dynamics. It can be easily shown using mass conservation that the local value of $[\partial v / \partial y]$ is proportional to the local slope of the pycnocline with respect to the channel. Thus neglecting advection of momentum compared to diffusion means that the slope of the pycnocline must be small. In addition, we make use of the fact that the duct is long to neglect diffusion in the y -direction and advection in the z -direction.

In the VAD solution ($\text{Re} \rightarrow 0$), advection in the transport equation (6.3) is neglected, and the slope of the pycnocline and $\partial v / \partial y$ are equal to zero. As the value of Re increases, the slope and $[\partial v / \partial y]$ increase. However, the simplifications leading to (6.2)–(6.3) mean that we consider the possibility that $[v \partial \rho' / \partial y] \gtrsim [(\text{Re}, \text{Sc})^{-1} \partial^2 \rho' / \partial z^2]$ while still $[\text{Re}^{-1} \partial^2 v / \partial z^2] \gg [v \partial v / \partial y]$ at least in some region of the parameter space. This region was shown to exist for horizontal ducts using 2D numerical simulations (see Chapter 5), and we show, in the current paper, that it is also observed experimentally in inclined ducts.

A limitation of the transformation to a 1D problem is that the horizontal density gradient $\partial \rho' / \partial y$ needs to be parametrized. For large Sc -values, the parametrization

$$\frac{\partial \rho'}{\partial y} = \Gamma \left(-\frac{1}{2} + |\rho'| \right) - \frac{\Gamma}{3} \left| \frac{\partial \rho'}{\partial z} \right|. \quad (6.4)$$

was proposed in Chapter 5.

This parametrization has the advantage that every term has a simple physical interpretation. The first term represents the large-scale density gradient due to the

density difference between the two tanks. The second term represents the reduction of the horizontal density gradient for a given height z due to vertical stratification. In the limit of a two-layer stratification, $|\rho'| = 1/2$ everywhere except at $z = 0$ where $\rho' = 0$. In this limit, the first two terms cancel each other.

The last term in (6.4) accounts for having a sharp pycnocline inclined with a slope related to Γ (for a detailed discussion on the shape of the pycnocline, see Gu and Lawrence (2005)). It could be tempting to neglect this term since $\Gamma \ll 1$, but when a two-layer stratification develops, $|\partial\rho'/\partial z|$ at $z = 0$ can become large enough so that this term cannot be neglected. The factor $1/3$ is obtained by assuming that the shear at the interface is the same as in the VAD solution independently of the value of $\text{Re}\Gamma$. This assumption was shown to be valid for large Sc -values using 2D simulations (see Chapter 5). Furthermore, notice that, if stratification is weak (i.e. $|\rho'|, |\partial\rho'/\partial z| \ll 1$), the parametrization (6.4) simplifies to $\partial\rho'/\partial y = -\Gamma/2$, and the VAD solution is recovered.

In the limit where the Péclet number $\text{Pe} = \text{ReSc} \rightarrow \infty$, while Re remains finite, diffusion can be neglected in the transport equation (6.3). In this case, the density gets organized into two layers with an infinitely sharp interface such that

$$\rho'(z) = \frac{1}{2} - \mathcal{H}(z). \quad (6.5)$$

where $\mathcal{H}(z)$ is the Heavyside function defined as: $\mathcal{H}(z > 0) = 1$, $\mathcal{H}(z < 0) = 0$, and $\mathcal{H}(z = 0) = 1/2$ (see Chapter 5). Notice that, by substituting (6.5) into (6.4), the transport equation (6.3) is satisfied in the limit of zero mass diffusion. In addition, only the last term in (6.4) remains, and (6.2) can be written as

$$\frac{\partial^2 v}{\partial z^2} = -\frac{\text{Re}\Gamma}{6}\rho'. \quad (6.6)$$

Finally, the velocity profile is

$$v(z) = \frac{\text{Re}\Gamma}{24}z(|z| - 1). \quad (6.7)$$

The mass flux per unit width Q_m is commonly used to characterize the flow with $Q_m = 1/2$ in the hydraulic limit (Hogg et al., 2001; Lefaue et al., 2019a). In the limit $\text{Pe} \rightarrow \infty$,

$$Q_m = \int_{-1}^1 |\rho'(z)v(z)|dz = \frac{\text{Re}\Gamma}{144}. \quad (6.8)$$

This suggests that the hydraulic limit is reached when $\text{Re}\Gamma = 72$ if Pe is sufficiently large. Furthermore, it advocates for the use of the parameter

$$\Psi = \frac{\text{Re}\Gamma}{144}. \quad (6.9)$$

to characterize the flow.

The flow in the high-advection/low-diffusion regime is described by (6.5), (6.7), and (6.8). In this regime, the density is not affected by diffusion and is arranged into two layers. On the other hand, flow velocity is affected by friction with the upper

and lower channel boundaries, and equation (6.7) indicates that momentum diffusion is also not negligible in the interior. In other words, this flow is not hydraulically controlled. Values for the mass flux Q_m smaller than 1/2 have been measured in experiments (see e.g. Fig. 6 by (Lefauve & Linden, 2020a)) implying that those flows are also not hydraulically controlled. Hence, we hypothesize that some of the laminar experiments fall within the the high-advection/low-diffusion regime.

On the other hand, Q_m does tend to 1/2 for turbulent experimental flows, suggesting that they are hydraulically controlled (Lefauve & Linden, 2020a). In such flows, momentum and mass diffusion are due to turbulence, and the ratio between momentum and mass diffusion is characterized by a turbulent Schmidt number value of order unity (Hogg et al., 2001).

In the previous chapter, we have shown that, for small Sc-values ($Sc \sim 1$), it is better to parameterize the horizontal density gradient as

$$\frac{\partial \rho'}{\partial y} = \Gamma \left(-\frac{1}{2} + |\rho'| \right) \quad (6.10)$$

because the interface is thick, and hence, the last term in (6.4) can be neglected. In this case, the first term in the r.h.s. of (6.2) is equal to zero, meaning that diffusive transport of momentum can be neglected (except in the boundary layers close to the bottom and top). In this case, the hydraulic limit is easier to reach like in the experiments by Anati et al. (1977) and Maderich et al. (1998), where temperature is used to generate the density differences. This suggests that, when $Sc \gg 1$, the hydraulic limit might be reached once the flow becomes turbulent and the ratio between momentum and mass diffusion is characterized by the turbulent Schmidt number value of order unity.

6.3.2. Extension to inclined ducts

To extend the previous analysis to inclined ducts, we must consider the two distinct situations of *lazy* and *forced* flows in the parametrization of the horizontal density gradient (6.4). In other words, the parametrization must account for the inclined interface only in the case of *lazy* flows since the interface becomes parallel to the top and bottom walls of the duct in the case of *forced* flows (Lefauve & Linden, 2020a). Hence, for a tilted duct, the horizontal density gradient is parametrized as

$$\frac{\partial \rho'}{\partial y} = \Gamma \left(-\frac{1}{2} + |\rho'| \right) - \frac{1}{3} \mathcal{H}(\alpha - \theta) \tan(\alpha - \theta) \left| \frac{\partial \rho'}{\partial z} \right|. \quad (6.11)$$

Since $\alpha = \arctan \Gamma$, we recover the parametrization for horizontal ducts (6.4) when $\theta = 0$. In the border between lazy and forced flows (when $\alpha = \theta$), the interface becomes parallel to the bottom, and the last term in (6.11) is equal to zero. For $\theta > \alpha$, the last term remains equal to zero since the angle of the interface cannot be inverted (Lefauve et al., 2019a).

In an inclined duct, (5.2) has an additional gravity term $\rho' g \sin \theta / \rho_{\text{ref}}$, and the gravity term in (5.3) becomes $-\rho' g \cos \theta / \rho_{\text{ref}}$ (Macagno & Rouse, 1961). When the density tends to get organized in a two-layer configuration for $Sc \gg 1$ and large-

enough Re-values, and the equation for the velocity (6.2) becomes

$$\frac{\partial^2 v}{\partial z^2} = -\frac{\Gamma}{6} \left[\frac{1}{\Gamma} \mathcal{H}(\alpha - \theta) \tan(\alpha - \theta) \cos \theta + \frac{3}{\Gamma} \sin \theta \right] \text{Re} \rho'. \quad (6.12)$$

Equations (6.6) and (6.12) become identical if we define the generalized Reynolds number for an inclined duct:

$$\text{Re}_\theta = \left[\frac{1}{\Gamma} \mathcal{H}(\alpha - \theta) \tan(\alpha - \theta) \cos \theta + \frac{3}{\Gamma} \sin \theta \right] \text{Re}, \quad (6.13)$$

which can be further simplified in the case $\theta \ll 1$ and $\alpha \ll 1$ to

$$\text{Re}_\theta = \left[\mathcal{H}(\alpha - \theta) \left(1 - \frac{\theta}{\alpha} \right) + 3 \frac{\theta}{\alpha} \right] \text{Re}. \quad (6.14)$$

It can be seen that for $\theta = 0$, $\text{Re}_\theta = \text{Re}$, and for $\theta \geq \alpha$, $\text{Re}_\theta = 3\theta \text{Re}/\alpha$. It is also possible to define a generalized Grashof number $\text{Gr}_\theta = \text{Re}_\theta^2$, which is consistent with the Grashof number for horizontal gravity currents: $\text{Gr}_\theta = \text{Re}^2$ for $\theta = 0$, but not with the one proposed by Meyer and Linden (2014).

The solution to (6.12) is similar to that for the horizontal duct (6.7) where only the Reynolds number Re has to be replaced by Re_θ . Consequently, the mass flux is $Q_m = \text{Re}_\theta \Gamma / 144$ so that we define the governing parameter for tilted ducts

$$\Psi_\theta = \frac{\text{Re}_\theta \Gamma}{144}. \quad (6.15)$$

Notice that $\text{Re}_\theta < 0$ for $\theta < -\alpha/2$. However, this theory does not account for this possibility since it is only valid for $\text{Re}_\theta \Gamma \gg (180/\text{Sc})^{1/2}$. For negative angles, the flow is slowed down (i.e. $\text{Re}_\theta \rightarrow 0$) as $\theta \rightarrow -\alpha/2$ so that it is eventually described by the VAD solution (Cormack et al., 1974; Hogg et al., 2001).

6.4. Experimental data

To validate our theory, we use the experimental data sets by Meyer and Linden (2014), Lefaue et al. (2019a) and Lefaue and Linden (2020a). These data sets have been jointly discussed and made available online (<https://doi.org/10.17863/CAM.48821>) by Lefaue and Linden (2020a, 2020b). Four experimental setups, differing in their dimensions, were used. We will refer to them as mSID, tSID, LSID and HSID in accordance with Lefaue and Linden (2020a). Table 6.1 summarizes the characteristics of all the setups. For each setup, the inclination angle of the duct θ and Re were varied independently. The fluid used was a salt (NaCl) solution ($\text{Sc} = 700$), and the value of Re was varied by changing the salt concentration in each of the tanks. In total, we use 738 data points.

Meyer and Linden (2014) distinguished four different regimes: laminar (L), Holmboe waves (H), intermittently turbulent (I), and turbulent (T). Lefaue and Linden (2020a) introduced a ‘waves’ (W) regime where waves other than Holmboe waves were observed. The different regimes were mostly identified by shadowgraph observations over a subsection of the duct, following the qualitative description of each regime by





name	h (mm)	Cross-section	Γ^{-1}	B	Sc	θ (deg.)	Re
mSID	45		30	1	700	[-1,6]	[300, 6 000]
tSID	90		15	1/4	700	[-1,3]	[3 000, 15 000]
LSID	100		30	1	700	[-1,4]	[2 000, 20 000]
HSID	100		15	1	700	[0,4]	[1 000, 20 000]

Table 6.1: Characteristics of the experiments used in this paper. Four duct geometries [abbreviated mSID (m for mini), tSID (t for tall), LSID (L for large), HSID (H for half)] are used (Lefauve & Linden, 2020a). We list the values of the dimensionless numbers describing each duct geometry (Γ and B), the value of Sc for salt in water, and the ranges of θ and Re explored.

Meyer and Linden (2014). A schematic of the shadowgraph set-up was presented by Lefauve et al. (2018). A complication for the comparison with the experimental data is that, as pointed out by Lefauve and Linden (2020a), there is a surprising difference between the results from the LSID and the mSID setups: the regions in the (θ, Re) -plane where the different regimes occur do not coincide even if the values of all the dimensionless parameters are the same.

6.5. Comparison with experiments

Figure 6.2 shows the location of the different regimes in the parameter space (θ, Re) for all experimental setups together with curves of constant Ψ_θ . It can be clearly seen that curves of constant Ψ_θ correspond with the transitions between the different regimes through all values of θ .

For the mSID setup the emergence of waves is given by $\Psi_\theta \approx 1/2$. This is an intuitive transition since the laminar analytical solution presented Section 6.3 becomes invalid, and hence, the flow must adapt to remain statistically steady by maintaining the balance between increased forcing and momentum diffusion. For the tSID setup, waves also emerge when $\Psi_\theta \approx 1/2$ if the Reynolds number is re-scaled by a factor $B = 1/4$. This might be because the relevant length scale for viscous diffusion is the width of the channel since $B < 1$. No sufficient data (LSID) and no data (HSID) are available to test if the emergence of waves also occurs at $\Psi_\theta \approx 1/2$ for these setups.

Although curves of constant Ψ_θ match the transitions for all setups, the particular values of Ψ_θ associated with the transitions differ. For the mSID and tSID setups, they coincide if the Reynolds number for the tSID setup is scaled. The value $\Psi_\theta \sim 1$ marks the transition to the intermittently turbulent regime and $\Psi_\theta \sim 2$ to the fully turbulent regime. For the LSID and HSID setups, it would seem that the Re-values have to be divided by a factor 2 and a factor 3, respectively, to match the values for the mSID setup. This difference between the experimental data sets and the factor 2 between the LSID and mSID setups was already pointed out by Lefauve and Linden (2020a). The reason for this cannot be explained using the laminar model derived in this paper. However, the observation by Lefauve and Linden (2020a) that the flow is hydraulically controlled ($Q_m \approx 1/2$) only when it is turbulent suggests that the

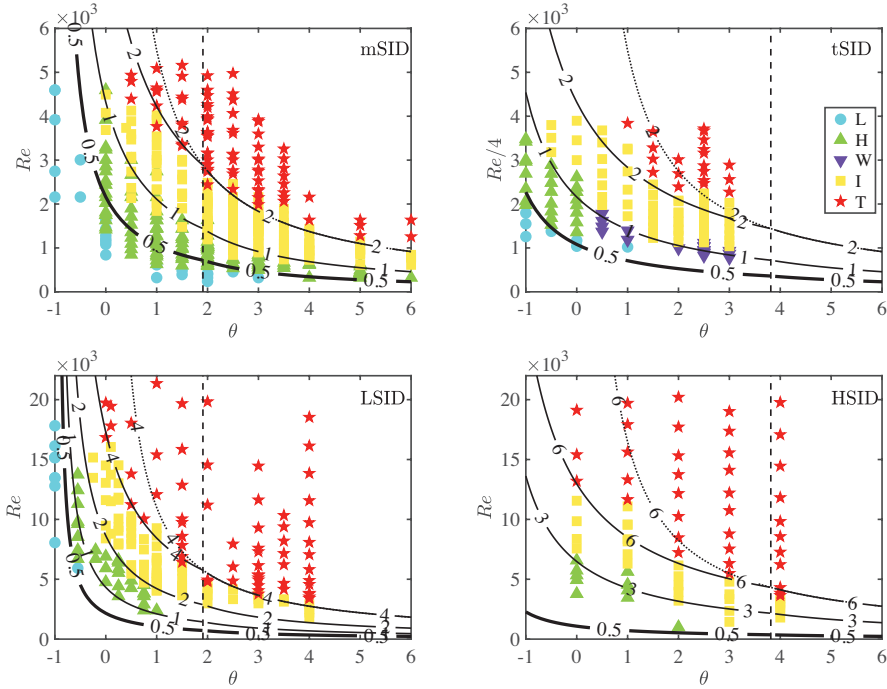


Figure 6.2: Location of the different regimes in the $(Re-\theta)$ plane for the four different setups: mSID, tSID, LSID, and HSID. The different symbols represent the different regimes laminar (L), Holmboe waves (H), other waves (W), intermittently turbulent (I) and turbulent (T). The solid lines represent curves of constant Ψ_θ with the value indicated along the line. The dashed line represents $\theta = \alpha$. The dotted line represents the continuation of the transition between the intermittently turbulent and fully turbulent regimes for *forced* flows given by θRe equal to a constant as proposed by Lefaue et al. (2019a). For the tSID setup Re is multiplied by the aspect ratio $B = 1/4$ to account for the increased momentum diffusion in the across-channel direction.

transition to turbulence is due to the flow and the geometry at the ends of the channel where differences between the setups might play a role.

In the case of *forced* flows (i.e. $1 \gg \theta \geq \alpha$), $\Psi_\theta = \sin \theta Re / 48 \approx \theta Re / 48$. This means that the transitions given by a constant value of Ψ_θ are equivalent to a constant value of θRe for a given setup. This is in agreement with the transitions proposed by Lefaue et al. (2019a) and that Lefaue and Linden (2020b) derived using a two-layer frictional hydraulics model. However, curves of constant Ψ_θ -value without simplification show a much better agreement for *lazy* flows ($\theta < \alpha$), as can be seen in Figure 6.2 when comparing the solid and dotted lines.

6.6. Conclusions

In the current paper, we propose an analytical model that provides the transition curves between different regimes of stratified shear flows with a large Sc -value in both horizontal and inclined ducts. This explanation is made possible by extending to inclined ducts the analytical solution for the high-advection/low-diffusion regime

introduced in the previous chapter in the limit of $\text{Pe} = \text{ReSc} \rightarrow \infty$. In this regime, advection is negligible in the momentum equations but dominates in the transport equation. The self-consistent explanation spanning from small negative duct inclination angles to small positive inclination angles provides the definition of a generalized Reynolds number for inclined ducts: Re_θ . Furthermore, the critical value $\text{Re}_\theta \Gamma = 72$ for the emergence of waves is obtained from physical principles. In general, curves with constant values of $\Psi_\theta \propto \text{Re}_\theta \Gamma$ correspond to all regime transitions observed experimentally. Nonetheless, it is still an open question why the results from laminar flow theory extend to the transitions of turbulent flows.

7

Turbulent flow driven by a horizontal density gradient

7.1. Introduction

The two-dimensional set-up of Chapter 5 allowed to gain insight into steady, laminar density driven exchange flows. However, the exchange flows in the Rhine ROFI are turbulent and therefore highly three-dimensional. As a result, a model set-up for simulating these type of flows in three dimensions with high resolution is imperative to catch the turbulent structures.

A significant challenge in expanding the entire two-dimensional domain of Chapter 5 into three dimensions is that it is computationally too expensive. A three-dimensional computational set-up with horizontal periodic boundary conditions (since Chapter 5 referred to as 3D-HP) would significantly reduce the computational costs by drastically diminishing the domain size. Up to now, simulations using the 3D-HP type of set-up have been limited to very weak horizontal density gradients in Li et al. (2008, 2010). A reason for this limitation was that the stratification would grow without bounds for large horizontal density gradients, a phenomenon called 'runaway-stratification' (Blaise & Deleersnijder, 2008).

The problem of runaway-stratification was circumvented by Salehipour et al. (2016, 2015, 2018) by directly imposing the steady state velocity and density profiles instead of the horizontal density gradient, and only solving for the deviations of the density. However, this method removed the feedback between stratification, velocity and horizontal density gradient. As a result, while this approach is suitable for studying specific physical phenomena such as Kelvin-Helmholtz instabilities or Holmboe waves (Salehipour et al., 2016, 2015, 2018), it is not appropriate for the simulation of transient or intermittent processes.

In this regard, simulating strongly stratified exchange flows with a 3D-HP model using a driving force rather than imposed velocity and density profiles would be a significant step forward in this field of research. It would enable the possibility of re-laminarisation under stratification, and subsequently the possibility of periodic strat-

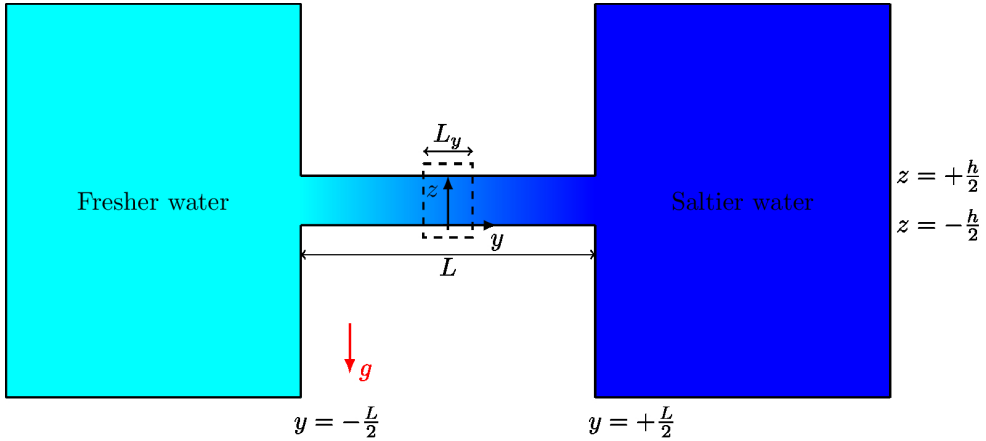


Figure 7.1: Sketch of the two dimensional numerical simulation set-up used in Chapter 5 (not to scale). Two reservoirs containing water at a different salinity are connected by a horizontal channel of length L . A section of the channel with length L_y that could be simulated with a direct numerical simulation set-up is depicted by a dashed square. Note that this configuration is mirrored with respect to the ROFI configuration of Chapter 1 and the configuration of Chapter 6. It is in agreement with the configuration of Chapter 5.

ification. Furthermore, it would allow to directly compare the results of numerical simulations with the results from laboratory experiments such as those in stratified inclined ducts (Lefaue et al., 2018, 2019a; Lefaue & Linden, 2020a). Additionally, it would allow to analyze very specifically certain turbulence characteristics such as turbulent kinetic energy budgets and eddy viscosity profiles, something which experimental set-ups cannot achieve with the same level of detail. Finally, it would bridge the gap between experiments and earlier numerical investigations of Salehipour et al. (2016, 2015, 2018).

As proven in Chapter 5, the new one-dimensional models help overcome the issue of runaway stratification. However, if these models are directly implemented in the three dimensional domain, compatibility issues occur between the horizontal density gradient and the horizontal periodicity. As a result this implementation requires some mathematical effort to adapt the one-dimensional models to higher dimensions. This mathematical formulation is extensively presented in the next section. The subsequent mathematical model is then applied to a strongly stratified, turbulent exchange flow, as an illustration of its capabilities. Finally, the obtained results are analyzed and compared to the state-of-the-art literature on laboratory experiments Lefaue et al. (2018, 2019a); Lefaue and Linden (2020a) and numerical simulations (Salehipour et al., 2015, 2016, 2018).

7.2. Numerical model

7.2.1. Computational domain

The expansion of the one-dimensional models of Chapter 5 into three dimensions first requires a specific definition of the three-dimensional computational domain. The one-

dimensional models were validated by comparing them to a two-dimensional model displayed in Fig. 7.1, by specifically defining them at the center of the channel. The objective of the three-dimensional set-up is also to reproduce the flow in the central region of the channel. Accordingly, the computational domain should be located far enough from the edges, such that their influence on the mean velocity profile in the computational domain is reduced as much as possible, thus end effects can be considered negligible. Simultaneously, its horizontal, streamwise dimension L_y should be small with respect to the length of the duct L , such that the average, large scale horizontal density gradient in the domain can be considered constant along y at any time. A domain satisfying these conditions is displayed with dashed lines in Fig. 7.1. To make the domain three-dimensional, a spanwise dimension x , pointing towards the reader, added (see Fig. 7.2).

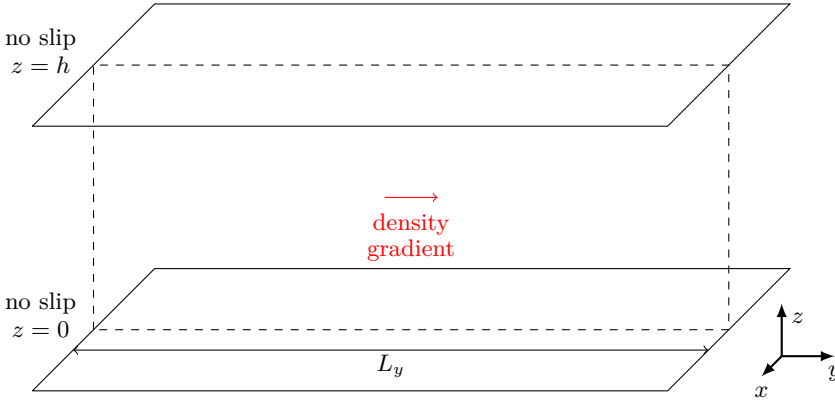


Figure 7.2: Computational domain, and coordinate system. The horizontal density gradient is in the y direction, and the z direction represents the vertical coordinate.

7.2.2. Modification of the governing equations

The derivation of the equations governing a flow driven by a horizontal density gradient in a periodic domain is an exercise that needs to be undertaken with caution. It requires the definition of several intermediate variables as well as some specific variable decompositions. The full process is described below.

The starting point is the continuity equation, the full Navier-Stokes equations and the equation of transport for the density:

$$\frac{\partial u_j}{\partial x_j} = 0, \quad (7.1a)$$

$$\rho \frac{\partial u_i}{\partial t} + \rho \frac{\partial u_i u_j}{\partial x_j} = -\frac{\partial p}{\partial x_i} + \mu \frac{\partial^2 u_i}{\partial x_j^2} - \rho g \delta_{i3}, \quad (7.1b)$$

$$\frac{\partial \rho}{\partial t} + \frac{\partial \rho u_j}{\partial x_j} = \kappa \frac{\partial^2 \rho}{\partial x_j^2}. \quad (7.1c)$$

As a reminder, u_i is the velocity in the x_i direction, t is time, ρ is the density, p the pressure, μ the dynamic viscosity, ρ the density, g the gravitational acceleration, δ_{ij} (with $(i, j) \in [1 : 3]^2$) the Kronecker delta, and κ the diffusivity. Implicit summation is applied for a repeating j index.

Boussinesq approximation

We also define p_{ref} and ρ_{ref} , the reference pressure and density for a fluid at rest, i.e. $u_i = 0$. The Navier-Stokes equations then become

$$\frac{\partial p_{\text{ref}}}{\partial x} = \frac{\partial p_{\text{ref}}}{\partial y} = 0, \quad (7.2a)$$

$$-\frac{\partial p_{\text{ref}}}{\partial z} = \rho_{\text{ref}} g, \quad (7.2b)$$

in which Eq. (7.2b) is the hydrostatic equation. Accordingly, the reference pressure p_{ref} is independent on x and y , but still depends on the vertical z . The reference density ρ_{ref} could also depend on the vertical, in case of stratification. However, for convenience, we chose an unstratified reference situation, such that ρ_{ref} is constant in both time and space.

It is possible to assume that the density and pressure variables can be decomposed into the sum of a 'static' reference fraction and a dynamic fraction according to:

$$\rho(x, y, z, t) = \rho_{\text{ref}} + \rho_{\text{dyn}}(x, y, z, t), \quad (7.3a)$$

$$p(x, y, z, t) = p_{\text{ref}}(z) + p_{\text{dyn}}(x, y, z, t), \quad (7.3b)$$

with

$$\rho_{\text{ref}} \gg \rho_{\text{dyn}}, \quad (7.4a)$$

$$p_{\text{ref}} \gg p_{\text{dyn}}. \quad (7.4b)$$

As a result, subtracting Eq. (7.2b) from Eq. (7.1b), dividing the result by ρ_{ref} and applying Eqs (7.4) yields the Navier-Stokes equations under the Boussinesq approximation. Applying decomposition (7.3a) to Eq. (7.1c) transforms the latter equation from a transport equation for ρ to a transport equation for ρ_{dyn} . The new equations are

$$\frac{\partial u_i}{\partial t} + \frac{\partial u_i u_j}{\partial x_j} = -\frac{1}{\rho_{\text{ref}}} \frac{\partial p_{\text{dyn}}}{\partial x_i} + \nu \frac{\partial^2 u_i}{\partial x_j^2} - \frac{\rho_{\text{dyn}}}{\rho_{\text{ref}}} g \delta_{i3}, \quad (7.5a)$$

$$\frac{\partial \rho_{\text{dyn}}}{\partial t} + \frac{\partial \rho_{\text{dyn}} u_j}{\partial x_j} = \kappa \frac{\partial^2 \rho_{\text{dyn}}}{\partial x_j^2}, \quad (7.5b)$$

with the continuity equation not shown again for conciseness. In these equations, the kinematic viscosity $\nu = \mu/\rho_{\text{ref}}$ was introduced. In the new equation set, the dynamic pressure and density variables have replaced the total pressure and density variables. Additionally, the equations are simplified since the density now only appears in the gravitational term. It is possible, to return to a set of equations for the original variables, while keeping the simplification. It only requires to sum Eqs (7.5a) and (7.2b), and to remark that Eqs (7.5b) and (7.1c) are equivalent (since ρ_{ref} is constant in time and space). Nevertheless, it is convenient for the following steps, to maintain p_{dyn} and ρ_{dyn} as the variables of the equations.

Decomposition of the density

The new density variable ρ_{dyn} is still incompatible with horizontal periodic boundary conditions. Therefore, we assume an additional decomposition:

$$\rho_{\text{dyn}} = A(z, t) \left(y - \frac{L_y}{2} \right) + \overline{\rho_{\text{dyn}}^p} + \rho', \quad (7.6)$$

where $A(z, t)$ is the horizontal density gradient, L_y is the size of the computational domain in the y direction, $\overline{\rho_{\text{dyn}}^p}$ is the plane averaged density fraction, and ρ' is the density fraction fluctuating due to turbulence. The plane averaging operator applied to ρ_{dyn} is defined as

$$\overline{\rho_{\text{dyn}}^p} = \frac{1}{L_x L_y} \int_0^{L_x} \int_0^{L_y} \rho_{\text{dyn}} dy dx, \quad (7.7)$$

where L_x is the size of the computational domain in the lateral x direction. This definition is a Reynolds operator since, for two quantities ϕ and ψ , and a constant λ , it verifies

- i) $\overline{\phi + \psi^p} = \overline{\phi}^p + \overline{\psi}^p$,
- ii) $\overline{\lambda \phi^p} = \lambda \overline{\phi}^p$,
- iii) $\frac{\partial \overline{\phi}^p}{\partial s} = \overline{\frac{\partial \phi^p}{\partial s}}$,
- iv) $\overline{\phi^p \psi^p} = \overline{\phi}^p \overline{\psi}^p$.

The verification of assertions i) and ii) is trivial due to the linearity of the integral. The verification of assertion iii) can be obtained by applying Leibniz integral rule and using the fact that the borders of the computational domain are fixed in time and space. For the particular cases of $s = x$ or $s = y$, one can remark that x and y should be directions of homogeneity. In fact, obtaining this homogeneity is the main purpose of the variable modifications proposed and discussed in this section. As a result, average gradients in the x and y direction should be zero. Assertion iv) is usually the assertion upon which integral-based averages fail to be regarded as Reynolds operators. However, most often these type of averages assume that the volume over which the integral is performed does not span the entire domain, and is local. Subsequently, the averages still depend on x and y . In our case, due to the conditions of homogeneity, we can average over the entire computational domain and the resulting average is independent of x and y . Additionally, taking the plane average of Eq. (7.6) satisfies the definition, i.e. Eq. (7.7).

Modification of the momentum equations

Inserting the decomposition of the density, Eq. (7.6), into the momentum equation gives

$$\begin{aligned} \frac{\partial u_i}{\partial t} + \frac{\partial u_i u_j}{\partial x_j} = & - \frac{1}{\rho_{\text{ref}}} \frac{\partial p_{\text{dyn}}}{\partial x_i} + \nu \frac{\partial^2 u_i}{\partial x_j^2} \\ & - \frac{1}{\rho_{\text{ref}}} \left[A(z, t) \left(y - \frac{L_y}{2} \right) + \overline{\rho_{\text{dyn}}^p} + \rho' \right] g \delta_{i3}. \end{aligned} \quad (7.8)$$

This formulation clearly highlights a y dependency of the flow, incompatible with horizontal periodic boundary condition. To circumvent this issue, we first assume that the pressure p_{dyn} is the sum of an ensemble averaged $\langle p_{\text{dyn}} \rangle_e$ and a fluctuating quantity p'' , verifying $\langle p'' \rangle_e = 0$. The choice for a decomposition using an ensemble average instead of a plane average is deliberate. We will see below that the mathematical formulation below requires that averages of p_{dyn} explicitly depend on y , which would by definition not be the case for a plane average. Additionally, none of the ensemble averaged variables survives until the final equations; they are only intermediate variables used for the construction of these equations. As a result of this average, the fluctuating quantity p_{dyn}'' is also different from the quantity p_{dyn}' . Additionally, we define a new plane-averaged pressure variable $\langle p^* \rangle_e$, as

$$\langle p^* \rangle_e(x, y, z, t) = \langle p_{\text{dyn}} \rangle_e(x, y, z, t) - \langle p_{\text{dyn}} \rangle_e(x, y, h, t) - \left(y - \frac{L_y}{2} \right) \int_z^h gA(\tilde{z}, t) d\tilde{z}. \quad (7.9)$$

This formulation is inspired by the expression for the pressure in a laminar flow, which can be obtained by integration of the momentum equation along z . Subsequently, this formulation leads to the expression of the pressure gradients in each direction

$$\frac{\partial \langle p^* \rangle_e}{\partial x} = \frac{\partial \langle p_{\text{dyn}} \rangle_e}{\partial x} - \frac{\partial \langle p_h \rangle_e}{\partial x}, \quad (7.10a)$$

$$\frac{\partial \langle p^* \rangle_e}{\partial y} = \frac{\partial \langle p_{\text{dyn}} \rangle_e}{\partial y} - \frac{\partial \langle p_h \rangle_e}{\partial y} - \int_z^h gA(\tilde{z}, t) d\tilde{z}, \quad (7.10b)$$

$$\frac{\partial \langle p^* \rangle_e}{\partial z} = \frac{\partial \langle p_{\text{dyn}} \rangle_e}{\partial z} + \left(y - \frac{L_y}{2} \right) gA(\tilde{z}, t). \quad (7.10c)$$

In the formulation above, we have introduced $\langle p_h \rangle_e(x, y, t) = \langle p_{\text{dyn}} \rangle_e(x, y, z, t)$ for simplicity. We will assume that there is no mean pressure gradient at the surface in the x direction. However, we still allow the possibility of having a mean pressure gradient at the surface in the y direction, to reproduce the effect of a gently sloping surface in that direction. Inserting Eqs. (7.10) into Eq. (7.8) leads to

$$\begin{aligned} \frac{\partial u_i}{\partial t} + \frac{\partial u_i u_j}{\partial x_j} = & - \frac{1}{\rho_{\text{ref}}} \frac{\partial \langle p^* \rangle_e}{\partial x_i} - \frac{1}{\rho_{\text{ref}}} \frac{\partial p_{\text{dyn}}''}{\partial x_i} + \nu \frac{\partial^2 u_i}{\partial x_j^2} \\ & - \frac{1}{\rho_{\text{ref}}} \left(\frac{\partial \langle p_h \rangle_e}{\partial y} + \int_z^h A(\tilde{z}, t) g d\tilde{z} \right) \delta_{i2} \\ & - \frac{1}{\rho_{\text{ref}}} (\overline{\rho_{\text{dyn}}^p} + \rho') g \delta_{i3} \end{aligned} \quad (7.11)$$

In these equations, $\partial \langle p_h \rangle_e / \partial y$ is still unknown but can be resolved by assuming that the depth average of the ensemble averaged velocity is zero. i.e.

$$\int_0^z \langle v \rangle_e dz = 0 \quad (7.12)$$

Performing ensemble-averaging of Eq. (7.11) and the continuity equation, i.e. Eq. (7.1a) yields

$$\frac{\partial \langle u_i \rangle_e}{\partial x_i} = 0, \quad (7.13)$$

$$\begin{aligned} \frac{\partial \langle u_i \rangle_e}{\partial t} + \frac{\partial \langle u_i \rangle_e \langle u_j \rangle_e}{\partial x_j} &= -\frac{1}{\rho_{\text{ref}}} \frac{\partial \langle p^* \rangle_e}{\partial x_i} + \nu \frac{\partial^2 \langle u_i \rangle_e}{\partial x_j^2} - \frac{\partial \langle u_i'' u_j'' \rangle_e}{\partial x_j} \\ &\quad - \frac{1}{\rho_{\text{ref}}} \left(\frac{\partial \langle p_h \rangle_e}{\partial y} + \int_z^h A(z, t) g dz \right) \delta_{i2} \\ &\quad - \frac{1}{\rho_{\text{ref}}} (\langle \overline{\rho_{\text{dyn}}^p} \rangle_e + \langle \rho' \rangle_e) g \delta_{i3}. \end{aligned} \quad (7.14)$$

We assume a homogeneous flow in the x and y direction, Eq. (7.13) implies $\langle w \rangle_e$ is independent of z . Since the channel has rigid and impermeable walls,

$$\langle w \rangle_e = 0. \quad (7.15)$$

As a result, Eq. (7.14) along y can be simplified to

$$\frac{\partial \langle v \rangle_e}{\partial t} = \nu \frac{\partial^2 \langle v \rangle_e}{\partial z^2} - \frac{1}{\rho_{\text{ref}}} \left(\frac{\partial \langle p_h \rangle_e}{\partial y} + \int_z^h A(\tilde{z}, t) g d\tilde{z} \right) - \frac{\partial \langle v'' w'' \rangle_e}{\partial z} \quad (7.16)$$

by assuming that there is no large scale pressure gradient in the y direction other than the one at the surface. Integrating Eq. (7.16) over the depth and using Eq. (7.12) yields

$$0 = \nu \left(\frac{\partial \langle v \rangle_e}{\partial z} \Big|_{z=h} - \frac{\partial \langle v \rangle_e}{\partial z} \Big|_{z=0} \right) - \frac{1}{\rho_{\text{ref}}} \left(\frac{\partial \langle p_h \rangle_e}{\partial y} h + \int_0^h \int_z^h A(\tilde{z}, t) g d\tilde{z} dz \right). \quad (7.17)$$

In a symmetric configuration, for example a channel with a no-slip boundary condition at both the bottom and the top wall, the wall shear-stress at the top wall equal the wall shear stress at the bottom wall, such that

$$\frac{\partial \langle p_h \rangle_e}{\partial y} = -\frac{1}{h} \int_0^h \int_z^h A(\tilde{z}, t) g d\tilde{z} dz \quad (7.18)$$

Inserting Eq. (7.18) into Eq. (7.11), and applying an integration by parts gives

$$\begin{aligned} \frac{\partial u_i}{\partial t} + \frac{\partial u_i u_j}{\partial x_j} &= -\frac{1}{\rho_{\text{ref}}} \frac{\partial}{\partial x_i} (\langle p^* \rangle_e + p_{\text{dyn}}'') + \nu \frac{\partial^2 u_i}{\partial x_j^2} \\ &\quad - \frac{g}{\rho_{\text{ref}}} \left(\int_z^h A(\tilde{z}, t) d\tilde{z} - \frac{1}{h} \int_0^h z A(z, t) dz \right) \delta_{i2} \\ &\quad - \frac{1}{\rho_{\text{ref}}} (\langle \overline{\rho_{\text{dyn}}^p} \rangle_e + \rho') g \delta_{i3} \end{aligned} \quad (7.19)$$

Modification of the transport equation

The density decomposition [Eq. (7.6)] is inserted into the transport equation [Eq. (7.5b)]. Using the continuity equation (7.1a), this gives

$$\begin{aligned} \frac{\partial}{\partial t} \left(\overline{\rho_{\text{dyn}}^p} + \rho' + A(z, t) \left(y - \frac{L_y}{2} \right) \right) \\ = \frac{\partial}{\partial x_j} \left(\left(\overline{\rho_{\text{dyn}}^p} + \rho' + A(z, t) \left(y - \frac{L_y}{2} \right) \right) u_j \right) \\ + \frac{\partial^2}{\partial x_i^2} \left(\overline{\rho_{\text{dyn}}^p} + \rho' + A(z, t) \left(y - \frac{L_y}{2} \right) \right) \end{aligned} \quad (7.20)$$

To make, the equations compatible with periodic boundary conditions, while maintaining the forcing term, a scaling argument is imperative. First, we can assume that the density fluctuations scale with $\Delta\rho$. Additionally, $|y| \leq L_y$, with L_y the size of the computational domain. The scaling of $A(z, t)$ is more delicate. Nevertheless, when simulating an exchange flow with periodic boundary conditions, the average interface between two currents has to be flat, since a sloping interface would introduce a discontinuity at the horizontal boundaries, due to the periodicity. Such a flat interface was observed for 'forced flows' by Lefauve and Linden (2020a). In this case, we can assume that $A(z, t)$ scales with $\Delta\rho/L$. As a result,

$$\left(y - \frac{L_y}{2} \right) A(z, t) \sim \frac{L_y}{L} \Delta\rho. \quad (7.21)$$

Since L_y/L is small (see Sec. 7.2.1), the horizontal density gradient fraction can be neglected in front of the turbulent fluctuation fraction.

Subsequently, the velocity variable components are manipulated to demonstrate that the scaling argument allows to neglect specific terms only. First, the velocity is decomposed according to $u_i = \overline{u}_i^p + u'_i$. Second, the mean velocity component are made explicit, according to $\overline{u}_i^p = (\overline{u}^p, \overline{v}^p, \overline{w}^p)$. Note that, in contrast with the modification of the momentum equations, a plane-averaging decomposition is chosen here. This choice is inevitable, since the average v component of the velocity remains in the final equations, in contrast to the ensemble averaged components in the momentum, which disappear once the modification of the equation is finalized. Therefore, the average of v has to be computed during the simulation, and plane averaging seems to be the most natural method for it. After decomposing the velocity variables and pulling

apart the velocity components, Eq. 7.20 becomes

$$\begin{aligned}
& \frac{\partial}{\partial t} \left[\overline{\rho_{\text{dyn}}^p} + \rho' + \left(y - \frac{L_y}{2} \right) A(z, t) \right] \\
& + \frac{\partial}{\partial x} \left[\left(\overline{\rho_{\text{dyn}}^p} + \rho' + \left(y - \frac{L_y}{2} \right) A(z, t) \right) \bar{w}^p \right] \\
& + \frac{\partial}{\partial y} \left[\left(\overline{\rho_{\text{dyn}}^p} + \rho' \right) \bar{v}^p \right] \\
& + \frac{\partial}{\partial z} \left\{ \left[\overline{\rho_{\text{dyn}}^p} + \rho' + \left(y - \frac{L_y}{2} \right) A(z, t) \right] \bar{w}^p \right\} \\
& + \frac{\partial}{\partial x_j} \left[\left(\overline{\rho_{\text{dyn}}^p} + \rho' + \left(y - \frac{L_y}{2} \right) A(z, t) \right) u_j' \right] \\
& = \kappa \frac{\partial^2}{\partial x_i^2} \left[\overline{\rho_{\text{dyn}}^p} + \rho' + \left(y - \frac{L_y}{2} \right) A(z, t) \right] - A(z, t) \bar{v}^p
\end{aligned} \tag{7.22}$$

where the striped terms can be neglected according to Eq. 7.21. By summing the mean and fluctuating fractions of the velocity components, the transport equation finally becomes:

$$\frac{\partial}{\partial t} (\overline{\rho_{\text{dyn}}^p} + \rho') + u_j \frac{\partial}{\partial x_j} (\overline{\rho_{\text{dyn}}^p} + \rho') = \kappa \frac{\partial^2}{\partial x_j^2} (\overline{\rho_{\text{dyn}}^p} + \rho') - A(z, t) \bar{v}^p. \tag{7.23}$$

Resolved equations

After the variable transformations in the previous sections, two new sums of variables appear $\overline{\rho_{\text{dyn}}^p} + \rho'$ and $\bar{p}^{*p} + p'_{\text{dyn}}$. Accordingly, by defining the 'resolved' variables as

$$\rho_r = \overline{\rho_{\text{dyn}}^p} + \rho' \tag{7.24}$$

$$p^* = \langle p^* \rangle_e + p_{\text{dyn}}'', \tag{7.25}$$

the transformed equations of the associated variables are obtained

$$\frac{\partial u_i}{\partial x_i} = 0 \tag{7.26a}$$

$$\begin{aligned}
\frac{\partial u_i}{\partial t} + \frac{\partial u_i u_j}{\partial x_j} = & - \frac{1}{\rho_{\text{ref}}} \frac{\partial p^*}{\partial x_i} + \nu \frac{\partial^2 u_i}{\partial x_j^2} - \frac{1}{\rho_{\text{ref}}} \rho_r g \delta_{i3} \\
& - \frac{g}{\rho_{\text{ref}}} \left(\int_z^h A(\tilde{z}, t) d\tilde{z} + \frac{1}{h} \int_0^h z A(z, t) dz \right) \delta_{i2}.
\end{aligned} \tag{7.26b}$$

$$\frac{\partial \rho_r}{\partial t} + u_j \frac{\partial \rho_r}{\partial x_j} = \kappa \frac{\partial^2 \rho_r}{\partial x_j^2} - A(z, t) \bar{v}^p \tag{7.26c}$$

7.2.3. Parametrization of the horizontal density gradient

In the previous section, the equations governing a density current were made compatible with the use of the flow configuration shown in Fig. 7.2. Nevertheless, the equations are not ready for use yet. The mean horizontal density gradient, $A(z, t)$, is

unknown and needs to be parametrized. The parametrization of the horizontal density gradient as a constant is common practice in many oceanography studies in which the effect of a river outflow is incorporated (e.g. Li et al. (2008, 2010); Simpson et al. (1990)). It is well known that this parametrization performs well for weakly stratified conditions but fails for strongly stratified conditions (Blaise & Deleersnijder, 2008).

In Chapter 5, two different parametrizations for the horizontal density gradient were proposed (Kaptein et al., 2020). In the first parametrization, $A(z, t)$ only depends on the resolved density ρ_r

$$A(z, t) = \frac{\Delta\rho}{L} - \frac{2}{L} |\rho_r|. \quad (7.27)$$

In the second parametrization, $A(z, t)$ also depended on the vertical gradient $\partial\rho_r/\partial z$,

$$A(z, t) = \frac{\Delta\rho}{L} - \frac{2}{L} |\rho_r| + \frac{1}{3} \frac{h}{L} \left| \frac{\partial\rho_r}{\partial z} \right|. \quad (7.28)$$

Since these parametrizations were for one-dimensional models, the density ρ only depended on the vertical coordinate z , and not on the horizontal coordinates x and y . Both parametrizations gave very good results even in the strongly stratified case.

Nevertheless, there were also some differences between the two models. The incorporation of the vertical density gradient in the parametrization was beneficial in case of low vertical diffusion, but disadvantageous in case of high vertical diffusion (Kaptein et al., 2020). The parametrizations offered by Eqs (7.27) and (7.28) can potentially be used in a three-dimensional model. However, we decided to only analyze results of a simulation in which the parametrization given by Eq. (7.28) was used. The motivation is twofold. First, the main aim is to study a turbulent density driven flow, which implies that the effective viscosity of the flow after transition to turbulence is the eddy-viscosity. The eddy-viscosity is much larger than the kinematic viscosity, making the parametrization given by Eq. (7.28) more appropriate. Additionally, to derive Eq. (7.21), $A(z, t)$ was scaled with $\Delta\rho/L$, a scaling that does not hold if the $A(z, t)$ is given by Eq. (7.28). By extension to two-dimensional flows, the parametrization was slightly adjusted to

$$A(z, t) = \frac{\Delta\rho}{L} - \frac{2}{L} \overline{|\rho_r|}^p. \quad (7.29)$$

7.2.4. Non-dimensionalisation

Equations (7.26a-7.26c), can be written in non-dimensional form, by scaling the velocity with the buoyancy velocity scale U_g , the spatial coordinates with h , the time with $t_g = h/U_g$, the pressure with $\rho_{\text{ref}} U_g^2$, the density with $\Delta\rho$. In these equations, the buoyancy velocity scale is defined as

$$U_g = \sqrt{\frac{\Delta\rho}{\rho_{\text{ref}}} gh}. \quad (7.30)$$

The non-dimensional equations are

$$\frac{\partial u_i}{\partial x_i} = 0 \quad (7.31a)$$

$$\frac{\partial u_i}{\partial t} + \frac{\partial u_i u_j}{\partial x_j} = -\frac{\partial \bar{p}}{\partial x_i} + \frac{1}{\text{Re}_g} \frac{\partial^2 u_i}{\partial x_j^2} - \rho_r \delta_{i3} - \underbrace{\left(\int_z^1 A(z, t)(\hat{z}, t) d\hat{z} - \int_0^1 z A(z, t)(z, t) dz \right)}_{\text{Driving force due to the horizontal density gradient driving force}} \delta_{i2}, \quad (7.31b)$$

$$\frac{\partial \rho_r}{\partial t} + \frac{\partial}{\partial x_j} (\rho_r u_j) = \frac{1}{\text{ScRe}_g} \frac{\partial^2 \rho_r}{\partial x_j^2} \underbrace{-\bar{v}^p A(z, t)}_{\text{Source term}}, \quad (7.31c)$$

$$\frac{\partial \bar{p}}{\partial y} = \Gamma \left(1 - 2|\bar{\rho}_r|^p \right). \quad (7.31d)$$

Three non-dimensional parameters appear: the gravitational Reynolds number Re_g , the Schmidt number Sc and the aspect ratio Γ . They are defined as

$$\text{Re}_g = \frac{U_g h}{\nu}, \quad (7.32a)$$

$$\text{Sc} = \frac{\nu}{\kappa}, \quad (7.32b)$$

$$\Gamma = \frac{h}{L}. \quad (7.32c)$$

7.3. Application: illustration the stage transitions in a density driven flow initially at rest.

We consider sustained turbulent, stratified shear flows forced by a horizontal density gradient. Our simulation is based on the models derived in the previous section with the horizontal density gradient as given by Eq. (7.31d). We qualitatively explore the different stages of the flow from a fluid initially at rest towards the statistically quasi-steady turbulent state. Our emphasis is on the reproduction of the most relevant flow features as already reported in the literature without going into an in-depth analysis of the (turbulent) flow which we consider at the moment beyond the scope of the present study. Throughout the evolution of the flow, observation of its behavior indicates that the flow undergoes several transitions starting from an initial state at which the flow is at rest.

7.3.1. Temporal, evolution of the density distribution and mean velocity profiles

The stage transitions of the flow are described below for one set of parameters, mainly using visual representations of the density field as shown in Fig. 7.3. The value of the Reynolds number has to be sufficiently large such that the flow becomes turbulent. For

this analysis, the values of the non-dimensional numbers were set to $\text{Re}_g = 400,000$, $\Gamma = 1/60$ and $\text{Sc} = 50$. The value of the Reynolds number is much larger than the values used in the laminar simulations discussed in 5, but comparable to the experimental values described by (Simpson & Linden, 1989).

After the start of the simulation, the fluid initially at rest is set in motion due to the horizontal density gradient. This horizontal density gradient generates a pressure gradient that drives a typical exchange flow in which dense water is flowing at the bottom in the negative y -direction (i.e. towards the left in the different figures) and less dense water flows at the top in the positive y -direction (i.e. towards the right in the different figures). Under the action of the induced velocity field driven by the horizontal density gradient, the water-column slowly stratifies.

In Fig. 7.3a-d, snapshots from the density field are displayed for four different moments. The mean velocity profiles (Fig. 7.3e) and the mean density profiles (Fig. 7.3f) corresponding to these snapshots are also shown. The profiles are accompanied by the analytical solutions for a laminar, two-layered exchange flow, derived in Chapter 5. The analytical velocity profile is given by

$$\frac{\bar{v}^p}{U_g} = \begin{cases} \frac{\text{Re}_g \Gamma}{3} \left(\frac{1}{8} \frac{z}{h} + \frac{1}{4} \left(\frac{z}{h} \right)^2 \right) & \text{if } z < 0 \\ \frac{\text{Re}_g \Gamma}{3} \left(\frac{1}{8} \frac{z}{h} - \frac{1}{4} \left(\frac{z}{h} \right)^2 \right) & \text{if } z > 0, \end{cases} \quad (7.33)$$

and is anti-symmetric with respect to the channel half-depth ($z = h/2$) but symmetric with respect to the ‘layer’ half depth ($z = \{h/4; 3h/4\}$). The minimum of analytical solution of the velocity profile naturally occurs at $z = h/4$ while the maximum of the velocity profile naturally occurs at $z = 3h/4$. The analytical density profile is given by

$$\frac{\bar{\rho}^p}{\Delta \rho} = \frac{1}{2} - H(z) \quad (7.34)$$

with $H(z)$ the Heavyside function, defined according to: $H(z > 0) = 1$, $H(z < 0) = 0$, and $H(z = 0) = 1/2$.

In Fig. 7.3a, at $t/t_g = 75.0$ (with $t_g = h/U_g$), the density seems to be homogeneously distributed in the horizontal direction except near the top boundary where patches of heavier fluid ($\rho_r \sim 0$) coexist at the same height with patches of lighter fluid ($\rho_r < 0$). The mean velocity profile is linear over a significant portion of the water depth but two boundary layers have formed next to each wall (Fig. 7.3e). The mean density profile is mirrored with respect to the velocity profile (Fig. 7.3f). This feature implies that the water column is unstably stratified near the top and bottom boundaries.

In Fig. 7.3b, at $t/t_g = 200.0$, the density is now homogeneously distributed in the horizontal over the entire water column, even near the boundaries. The mean velocity profile exhibits a typical exchange flow, although its shape is different from the shape of the analytical solution (Fig. 7.3e). The profile is still anti-symmetric with respect to the channel half depth, but not symmetric with respect to the layer

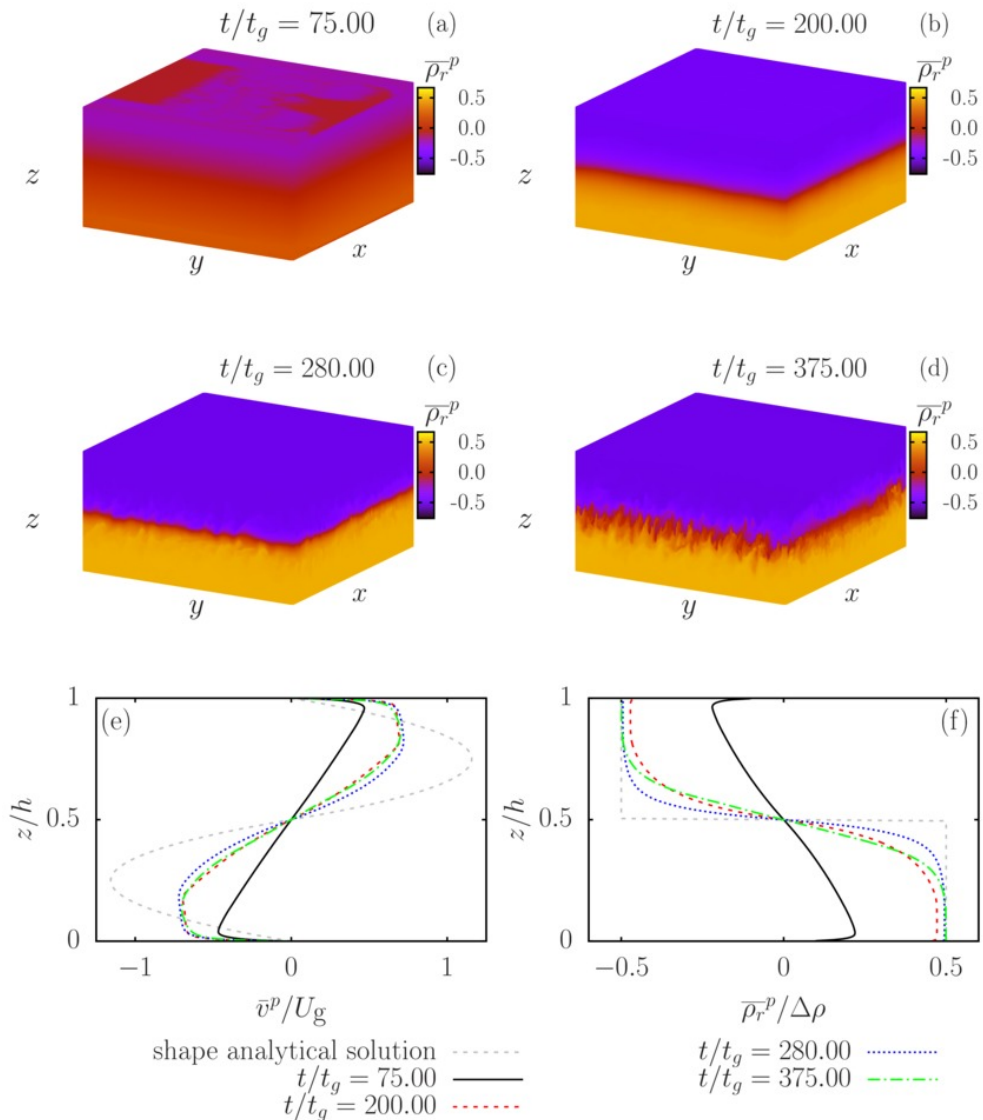


Figure 7.3: (a-d): Density field at different stages of the transient regime (respectively convective overturning and undisturbed interface, wavy interface, turbulent interface). (e): Corresponding velocity profiles and (f) corresponding density profiles. The analytical solutions, given by Eqs (7.33), (7.34) are also displayed. The analytical velocity profile was rescaled in order to fit on the graph.

half-depth. This lack in symmetry is related to a much thinner boundary layer in the simulations compared to the theoretical profile. The mean density profile shows

the water-column is fully stably stratified (Fig. 7.3f). The profile clearly highlights the presence of an interface between light and heavy fluid, but the density difference between the top and the bottom of the channel is not yet equal to $\Delta\rho$.

In Fig. 7.3c, at $t/t_g = 280.0$, waves are now visible at channel half-depth. The density gradient at $z = h/2$ has further sharpened and a pycnocline has now formed. The mean velocity profile at $t/t_g = 280.0$ does not differ much from the velocity profile at $t/t_g = 200.0$ (Fig. 7.3e), which suggests the mean velocity has reached its final shape. The magnitude of this velocity profile is much smaller than the magnitude of the theoretical laminar profile. Note, that this difference in amplitude between the two profiles is much larger than explicitly appears on Fig. 7.3e, because the former profile was divided by 30 in order to fit the graph. In general, the magnitude of a velocity profile results from an equilibrium between the horizontal density gradient forcing and dissipation. Since the forcing is the same between the theoretical profile and the simulation profile, the differences in these profiles suggest that there is much more dissipation in the simulation. The mean density difference between the top and the bottom is now $\Delta\rho$ (Fig. 7.3f).

In Fig. 7.3d, at $t/t_g = 375.0$, large structures are now visible at the interface between the light and the heavy fluid. As a result, the interface is much thicker. The shape of velocity profile is still relatively similar to the shape of the velocity profile at $t/t_g = 280.0$ (Fig. 7.3e) but the gradient steepness in the mean density profile at $z = h/2$ is now lower than at $t/t_g = 280.0$ and at $t/t_g = 200.0$ (Fig. 7.3f).

7.3.2. The path to turbulence

It is possible to reconstruct the different stages that the flow undergoes based on the observations in the previous sections, and backed by contour plots of the density in a (y, z) slice of the computational domain (see Fig. 7.4). As already discussed, the flow and density fields are anti-symmetric with respect to the channel axis. For the description and discussion, we consider the flow behavior near the top boundary (as the flow dynamics near the bottom wall can easily be inferred from this discussion).

Immediately after the start of the simulation, the fluid is set in motion and the water-column stratifies. We refer to the very first stage of the flow as the laminar stage (L). Shortly after this stage is established, the first instability appears. This instability is a consequence of an important feature at these early stages of the flow evolution. Close to the top boundary, a mean velocity profile $\bar{v}^p(y)$ develops which matches the no-slip condition at the top wall (with $\bar{v}^p(y = h) = 0$) and a high velocity amplitude below the wall at $z \approx 0.8h$ (before becoming zero at the channel axis). This means that lighter fluid is advected faster from left to right at a certain distance below the top wall underneath heavier fluid close to the top wall. This generates an unstable density stratification just beneath the top boundary. A similar phenomenon occurs near the bottom boundary of the channel. Depending on the flow characteristics one can expect two different processes to occur to counteract the unstable stratification nearby the top and bottom walls. When the flow remains laminar, diffusion processes are dominant to counteract unstable density gradients and the density field will quickly adapt while satisfying the no-flux boundary condition for the density field at the horizontal walls during this process. Basically, diffusive time scales are much smaller than the relevant advective time scales and emerging

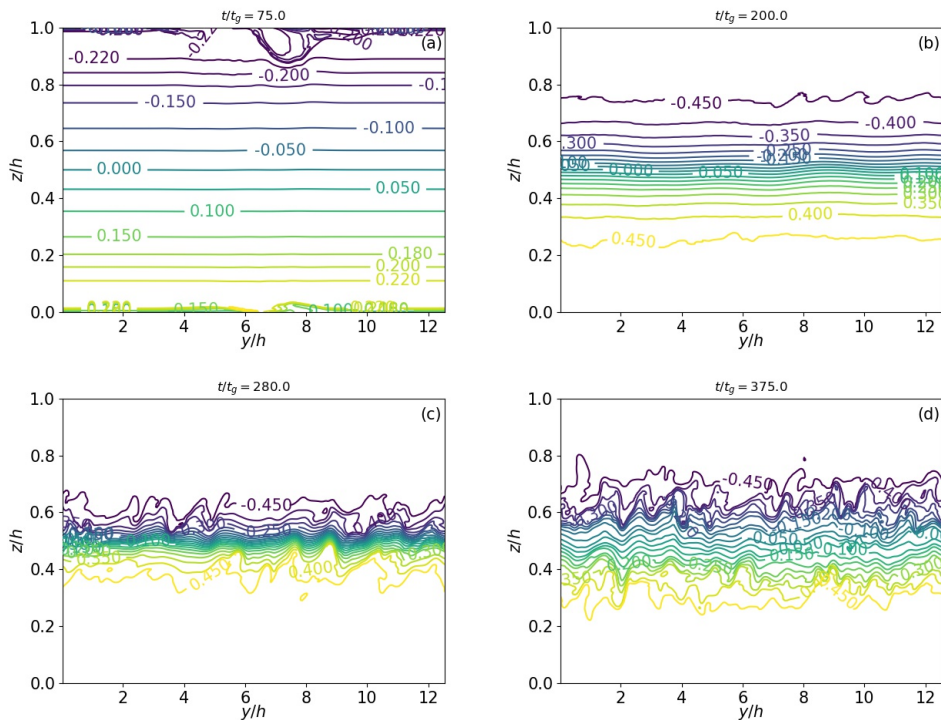


Figure 7.4: Contours of the density in a (y, z) slice of the computational domain at four different times.

instabilities are suppressed. It is, of course, also possible that these diffusive time scales are large compared to advection time scales, thus at higher Reynolds number flows. Instabilities can then grow and suddenly the unstable stratification is destroyed due to vigorous convective overturning (CO).

For the present set of parameters, the unstable stratification is destroyed by convective overturning. The phenomenon was the subject of the observations in Fig. 7.3a in which fluid patches of different density coexisted at the same vertical position. This coexistence is explained by the fact that not all the patches sink or rise at the same moment, but form plumes. Figure 7.4a displays, in two dimensions, a plume of heavier fluid detaching from the region close to the upper wall and sinking into an otherwise stably stratified and undisturbed fluid. The process, which is ongoing at $t/t_g = 75.0$ but already started earlier, is referred to as the convective overturning stage.

After the event of convective overturning, the water column is completely stably stratified. At $t/t_g = 200.0$, the pycnocline is still mostly flat, with the planes of equal density being strictly horizontal. However, significant disturbances in the isolines $\rho_r/\Delta\rho = \pm 0.450$ are visible (Fig. 7.4b). We can claim that these disturbances are due to wall turbulence rather than internal waves based on three arguments. First, the water-column is almost non-stratified at that location. Second, the velocity

profile showed in Fig. 7.3e displays a very thin boundary layer characteristic of wall turbulence. Third, the magnitude of the velocity profile is much smaller than its laminar theoretical counterpart, which suggest strong dissipation. We refer to this stage as flat-interface turbulent (FIT) stage.

The flow continues to evolve and, at $t/t_g = 280.0$, characteristic cusped waves appear (see Fig. 7.3c). These waves are the result of an inviscid instability and occur with strong stratification. As a result, these waves are likely to be Holmboe, as elaborated in the discussion section of this chapter, Sec. 7.4. These waves have been extensively described in literature (Salehipour et al., 2016; Lefauve et al., 2018). In contrast, another typical instability of stratified flows, the Kelvin Helmholtz instability is limited to stratified flows with a relative small density gradient with respect to the velocity gradient. On both sides of the pycnocline, structures are distinguishable (see Fig. 7.4c), with an ejection, departing from the crests of the wavy interface in the lower layer. We call this stage the Holmboe wave stage.

The magnitude of the Holmboe waves increases and the waves start to interact, maybe fed by the turbulent kinetic energy of the layers above and below the pycnocline. This speculation is further clarified below. Eventually the Holmboe waves break which leads to turbulence and a subsequent mixing layer seen in Fig. 7.3d). This phenomenon is in agreement with previous studies (Salehipour et al., 2016; Lefauve et al., 2018). The much thicker interface resulting from the mixing is clearly visible in Fig. 7.4d.

Further evolution of the flow generates alternated periods of more mixing and less mixing in the interface (not shown), in agreement with the intermittent stage observed in (Meyer & Linden, 2014; Lefauve et al., 2018). The analyses of the density field and the velocity profiles indicate that for $\text{Re}_g = 400,000$, the flow undergoes different stages going from a flow initially at rest, to a turbulent flow in which an apparent competition between stratification and turbulence leading to intermittent levels of mixing of the interface. During this transition, the flow is subjected to convective overturning and Holmboe wave with signs of stratified turbulence.

After having identified visually the different phases undergone by the modeled exchange flow, it is useful to determine the signatures of these phases. Indeed, these signatures can highlight stage transitions so that the flow stage can be identified quickly and robustly without having to proceed to visual techniques. To do so, several different physical quantities are analyzed. We start by investigating the temporal evolution of three different quantities: the volume averaged fluctuating kinetic energy, the thickness of the density interface or pycnocline, and the spatial distribution of the gradient Richardson number.

First, the depth-integrated, horizontally-averaged kinetic energy of the fluctuating part of the velocity field is defined as

$$\text{FKE} = \frac{1}{h} \int_0^h \frac{1}{2} \sum_i (u_i - \bar{u}_i^p)^2 dz. \quad (7.35)$$

Accordingly, it comprises contributions from wave-like behavior of the flow field as well as from turbulent velocity fluctuations. Significant variation in FKE can indicate the onset of turbulence, the presence of waves, the breaking of these waves, or the damping of turbulence due to (re)stratification.

Second, the interface thickness d_{int} , can be defined in two different ways. Based on the plane-averaged density, we can define the non-dimensional interface thickness of the horizontally averaged density, $\Delta z_{\bar{\rho}_r}$, as

$$\Delta z_{\bar{\rho}_r} = \frac{1}{h} \left(z|_{\bar{\rho}_r^p(z)=-0.25} - z|_{\bar{\rho}_r^p(z)=+0.25} \right). \quad (7.36)$$

Based on the contour lines of the local density shown in Fig. 7.4, we can define the average thickness of the local density interface, $\Delta \bar{z}_{\rho_r}$, as

$$\Delta \bar{z}_{\rho_r} = \frac{1}{h} \left(\bar{z}^p|_{\rho_r(x,y,z)=-0.25} - \bar{z}^p|_{\rho_r(x,y,z)=+0.25} \right). \quad (7.37)$$

The accuracy of this method naturally depends on the number of points used for the averaging procedure. In the case of $\Delta z_{\bar{\rho}_r}$, the number of points used for averaging is equal to the number of points in a horizontal plane. In the case of $\Delta \bar{z}_{\rho_r}$, the number of points for averaging is equal to the number of points used to define the contour lines, and can, therefore, vary slightly from line to line. As long as the flow is laminar, the quantities $\Delta z_{\bar{\rho}_r}$ en $\Delta \bar{z}_{\rho_r}$ should give the same result. With the onset of waves, the local fluctuations of the interface position will lead to an artificial smoothing of the vertical density gradients and subsequent thickening of the interface as defined by $\Delta z_{\bar{\rho}_r}$, which would be further pronounced with the breaking of the waves. In contrast, the thickness of the interface defined by $\Delta \bar{z}_{\rho_r}$ would still decrease with the onset of waves, and only start to increase with mixing across the interface due to the breaking of these waves. Accordingly the difference between $\Delta z_{\bar{\rho}_r}$ and $\Delta \bar{z}_{\rho_r}$ highlights the onset of interfacial waves.

Finally, the gradient Richardson number is defined as

$$\text{Ri} = -\frac{g}{\rho_{\text{ref}}} \frac{\frac{\partial \bar{\rho}_r^p}{\partial z}}{\left(\frac{\partial \bar{u}^p}{\partial z} \right)^2}. \quad (7.38)$$

This gradient Richardson number provides useful information about the linear instability of a two-dimensional exchange flow, and therefore, its ability to mix. Indeed $\text{Ri} < 0.25$ is a necessary condition for linear instability of a two-dimensional inviscid and stably stratified non-turbulent shear flow.

The three quantities, FKE, $\Delta z_{\bar{\rho}_r} - \Delta \bar{z}_{\rho_r}$ and Ri, are displayed in Fig. 7.5. The event of convective overturning is marked by a small bump in the FKE at $t/t_g = 75.0$ (see Fig. 7.5a) and some small differences between $\Delta \bar{z}_{\rho_r}$ and $\Delta z_{\bar{\rho}_r}$. These differences are marked by a short peak in relative difference between the two quantities (see 7.5b). Interestingly, the FKE starts to increase with the convective overturning event, and continues to increase relatively steadily afterwards. Since the interface is undisturbed before and after the event, the increase in FKE cannot be related to waves. As a result, the steady increase suggests that turbulence develops in each layer. At the beginning of the simulation, only a region in the vicinity of the wall satisfies $\text{Ri} < 0.25$ and is potentially subject to turbulent mixing (see 7.5c). As the flow progresses, two new regions appear where $\text{Ri} < 0.25$, roughly around $z \approx h/4$ and $z \approx 3h/4$. The

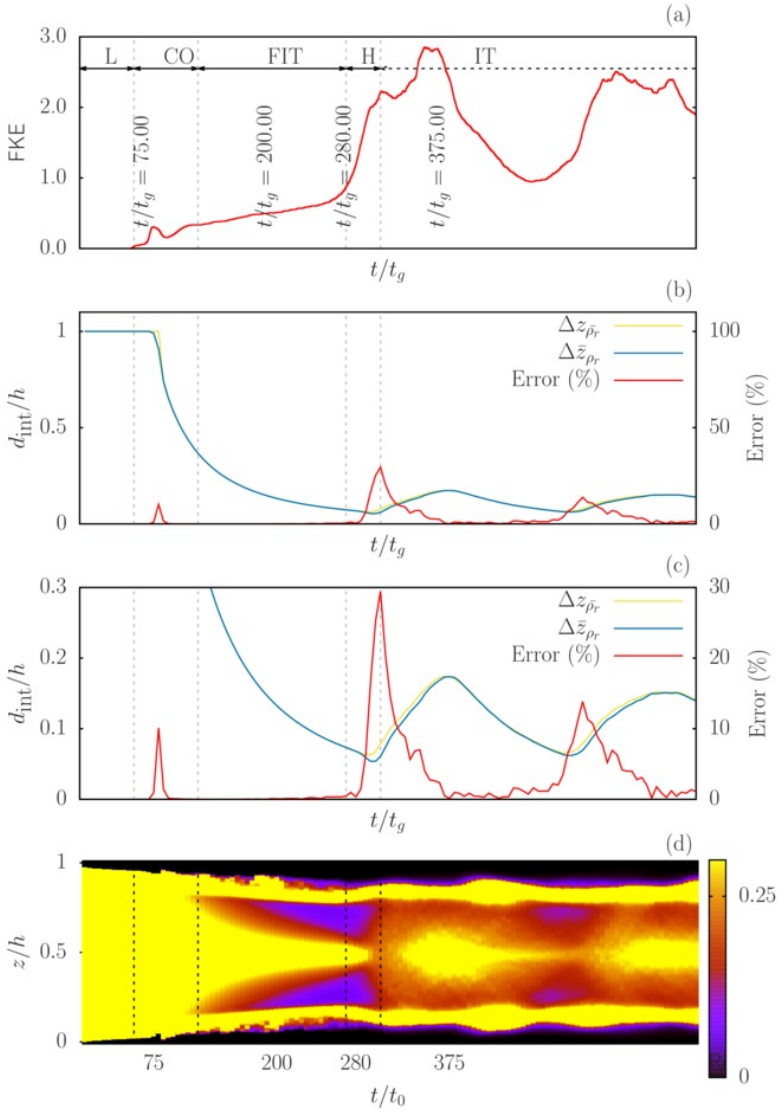


Figure 7.5: Temporal evolution of (a) the fluctuating kinetic energy, (b) the interface thickness, (c) the interface thickness with focus on the thin-interface stage, and (d) the gradient Richardson number. The different stages: laminar (L), convective overturning (CO), flat-interface turbulent (FIT), Holmboe (H), and intermittent turbulence (IT) are indicated on the graph, as well as the moments in time displayed in the previous figures.

vertical extent of these regions grows over time, but they are separated from each other and from the wall by regions where $Ri > 0.25$. These regions correspond to the region of the strong pycnocline (half channel depth) and to the regions of no shear (below the walls).

Some waves are already perceptible in the three-dimensional density field and the density contours (not shown) before the sudden increase of FKE. However, this event could mark the growth in magnitude of the Holmboe waves at the interface due to the contribution of vertical fluctuation to the FKE. This is further confirmed by the relative difference between $\Delta\bar{z}_{\rho_r}$ and $\Delta z_{\bar{\rho}_r}$. The instant that the relative difference between $\Delta\bar{z}_{\rho_r}$ and $\Delta z_{\bar{\rho}_r}$ is maximum coincides with the Richardson number dropping below $Ri < 0.25$, marking the breaking of the waves and a period of mixing.

The time-span after the breaking of the Holmboe waves is marked by a period of relaxation, during which the FKE decreases, the thickness of the interface increases (and the difference between $\Delta\bar{z}_{\rho_r}$ and $\Delta z_{\bar{\rho}_r}$ decreases), and the value of Ri rises beyond 0.25 again. Again a little later, the whole process starts again, with the onset, growing and breaking of interface waves or other instabilities, followed by turbulent mixing and a relaxation of the interface.

So far, the results demonstrate an intermittent character of the turbulence in the flow, a stage also identified as a regime by (Meyer & Linden, 2014; Lefauve et al., 2019a) in the experiments. However, based on the deformation of the contour lines, there are suggestions that wall turbulence is already present much earlier in the flow. In order to identify the regions of larger fluctuating activity, the root mean square (rms) velocities $u_i^{\text{rms}} = \sqrt{u_i'^2}$ are displayed in Fig. 7.6. In this figure, the rms velocities are non-dimensionalised with the wall friction velocity $u_\tau = \sqrt{\tau_w/\rho_{\text{ref}}} = \sqrt{\nu \partial \bar{v}^p / \partial z|_{z=0}}$.

During the period of convective overturning (Fig. 7.6a), the fluctuating activity is confined to the regions very close to the wall. The fluctuations of the vertical velocity are one order of magnitude smaller than the fluctuations in the streamwise direction. This result indicates that an important part of the FKE is generated by wall bounded turbulence and not by the convective overturning. Once the fluid column is fully stably stratified (7.6b), the region of significant values of v^{rms} is broader and not anymore strictly confined to the wall region. The streamwise fluctuations are also much larger than the vertical and spanwise fluctuations, in analogy with the results from the turbulent plane channel flow simulated in (Kim et al., 1987). During the Holmboe wave event, significant fluctuating activity is present over the entire fluid column. Three local minima in v^{rms} (streamwise) and u^{rms} (spanwise) are discernible, the middle one corresponding to the pycnocline, and the other two to the regions of minimum shear. The vertical fluctuations (w^{rms}) are now also significant, but the profile is almost flat, in contrast with the profiles for the other two components. These results picture a flow with considerable wave activity in the pycnocline and strong turbulent activity on both sides of the pycnocline and in the wall regions. After the breaking of the waves, the local minimum of the rms profiles in the pycnocline has almost disappeared. In fact, v^{rms} still has a smaller values in this region, while u^{rms} and w^{rms} are clearly maximum in what is now a mixing region. These result confirm the presence of a region of vigorous mixing and strong turbulent activity.

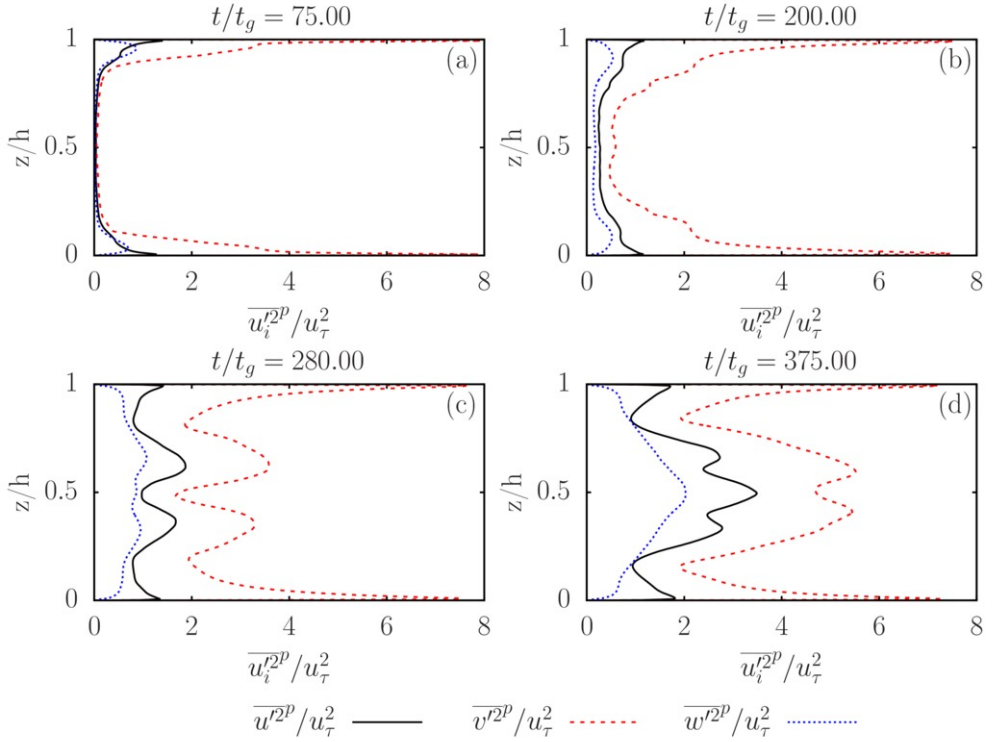


Figure 7.6: Root mean square velocities during (a) the event of convective overturning; (b) undisturbed interface; (c) Holmboe waves; (d) turbulent interface.

7.4. Discussion

7.4.1. Results in perspective of previous results

A question that emerged from the results is why wall turbulence is not reported in previous studies, particularly in the study of Lefaue et al. (Lefaue et al., 2019a). The answer might lie in the parameter values, and it is therefore necessary to compare these values. In Chapter 6, it is shown that it is possible to define a unique Reynolds number for inclined and horizontal ducts. This Reynolds number depends on the inclination angle of the duct and is equal to Re_g for a horizontal duct. Based on this definition, the highest value of the Reynolds number in the inclined duct experiment is 21,355 (Lefaue & Linden, 2020a), which is more than an order of magnitude less than the value used in this simulation: $\text{Re}_g = 400,000$.

Overall, it is difficult to compare directly the present numerical set-up with the inclined duct experimental set-up of (Lefaue & Linden, 2020a) when it comes to regime transitions. Coarse grid simulations with lower Reynolds number values (not shown) suggest that transition to a wavy regime or to turbulence occurs at much

higher Reynolds number values than in the SID experiment. This reinforces the previously mentioned intuition that the geometry of the experiment, and particularly the edges of the duct might play a crucial role in regime transitions. The absence of these edges, as well as the absence of side walls are the main difference between the SID experiment and the present simulation.

To put the present results further into perspective, it can be helpful to compare our simulation results to the results by Salehipour et al. (2016). They used a similar set-up to the one used in this study. However, they imposed the mean velocity profile and the mean density profile instead of imposing a horizontal gradient and letting the velocity and density evolve freely. This choice was motivated by the purpose of the study: the investigation of Holmboe waves, their generation mechanisms and their ability to generate sustained turbulence. If we adjust to our problem formulation the functions used in their imposed velocity and density profiles, we find that they evolve as $\bar{v}^p(z) = \frac{1}{2}\Delta\bar{v}^p \tanh(z/d)$, and, $\bar{\rho}_r^p(z) = -\frac{1}{2}\Delta\rho \tanh(z/\delta)$. In this formulation, d and δ are parameters that are determined by requiring the vertical derivatives of \bar{v}^p and ρ_r , to be equal between the simulation profile and the analytical profile. Additionally, in our case, $\Delta\bar{v}^p$ is the difference between the maximum and the minimum of the velocity profile. The output profiles of the present simulation are compared with the imposed profiles by (Salehipour et al., 2016) in Fig. 7.7, at $t/t_g = 200.00$, which is before the onset of Holmboe waves.

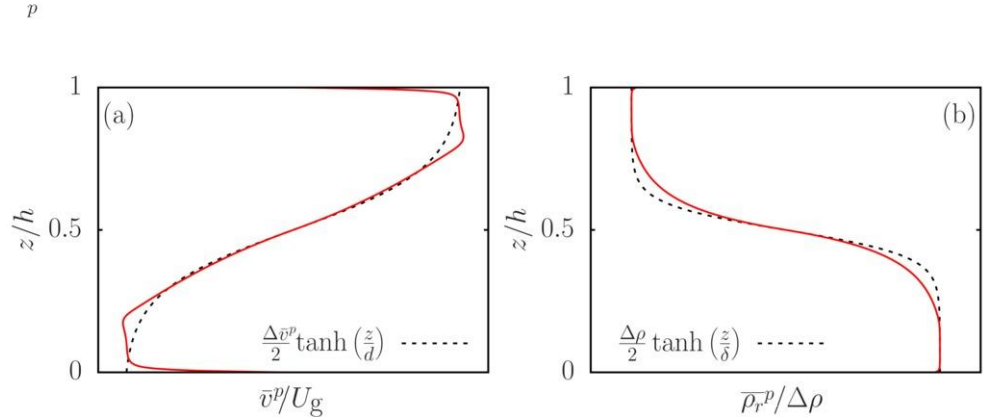


Figure 7.7: Simulation and analytical profiles of (a): the velocity and (b): the density.

It is evident that the agreement for the density profiles is very good over the entire depth, while the agreement for the velocity profiles is good except near the top and bottom boundaries. This result implies that the conditions at the interface are potentially similar between the two simulation set-ups. As discussed previously, there are no boundary layers in Salehipour's set-up, due to the choice for the velocity profile. This choice has no influence regarding the objective to simulate Holmboe waves, provided that a mechanisms triggering the waves is present in the set-up. The generation of Holmboe waves rather than Kelvin-Helmholtz instabilities is (partly) controlled by the parameter $R_\rho = d/\delta$.

Based on previous studies, $R_\rho = d/\delta$ close to unity is the identified condition

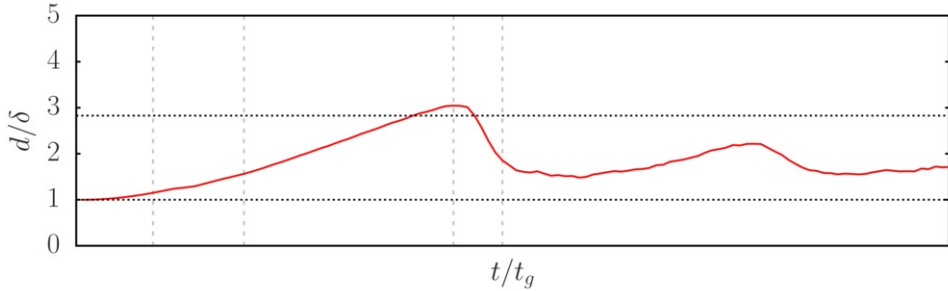


Figure 7.8: Ratio between the vertical density gradient and the velocity shear at the center of the channel and over time. The black dotted lines represent critical values of $R_\rho = 1$ and $R_\rho = \sqrt{8}$

for the exchange flow to be primarily susceptible to the Kelvin-Helmholtz instability, while for $R_\rho \gg 1$ is the condition for the flow to be primarily susceptible to Holmboe wave instability. In their simulations, R_ρ is scaled according to $R_\rho = \sqrt{\text{Pr}}$, with $\text{Pr} = 8$ the Prantl number, base upon (Smyth, Klaassen, & Peltier, 1988). In our simulation, we clearly observed Holmboe waves. However, the velocity and density profiles are not imposed here and R_ρ is an output parameter of the model and not an input parameter. In this regard, it is interesting to evaluate R_ρ to see if it matches the above mentioned condition for appearance of Holmboe waves. To do so, it is necessary to estimate the value of the ratio

$$-\frac{\Delta \bar{v}^p}{\Delta \bar{\rho}^p} \frac{\left. \frac{\partial \bar{\rho}_r^p}{\partial z} \right|_{z=1/2}}{\left. \frac{\partial \bar{v}^p}{\partial z} \right|_{z=1/2}}.$$

Indeed, this quantity is equal d/δ to a first order approximation. This statement can be proven by applying a Taylor series development to the functions describing the imposed velocity and density profile.

The evolution of R_ρ over time is displayed in Fig. 7.8, together with the lines $R_\rho = 1$ and $R_\rho = \sqrt{8}$. Three features of this evolution deserve a specific mention. First, the value of R_ρ is indeed much larger than 1 and of the order of $\sqrt{8}$ just before the onset of the Holmboe waves. Second, the value of R_ρ varies quite significantly in time. It does not seem to reach again the magnitude it attained just before the onset of the Holmboe waves, after they have broken for the first time. However, it has to be mentioned that the simulation has not been ran for a sufficient long time to completely rule out the possibility that R_ρ reaches this high values again. Third, R_ρ is not equal to $\sqrt{\text{Pr}}$ in our simulation. Indeed, in our model it is the Schmidt number that plays the role of Pr , and accordingly, R_ρ is expected to be of order $\sqrt{50} = 5\sqrt{2}$. Several factors can explain this difference. It is possible that, due to the coarseness of

the grid, the effective Prantl number is much lower. It also might that the instability and turbulence kick in way before R_ρ can reach its maximum value. Nevertheless, Fig. 7.3e and 7.3f showed that the velocity and density profiles did not evolve much between the flat-interface turbulent stage and the turbulent interface stage. As a result, it might be more probable that the turbulent Prandtl number (or in our case the turbulent Schmidt number) should be used as a measure for R_ρ , rather than the molecular Prandtl number. It would be meaningful to compute this number from the flow, but higher resolution is required to come up with a reliable result.

7.5. Conclusion

In this study, we simulated a strongly stratified shear flow driven by a horizontal density gradient, with three dimensional coarse direct numerical simulations. We use a new parametrization for the horizontal density gradient, that is inspired by the one dimensional models presented by 5. This parametrization permits to simulate density driven exchange flows with periodic boundary conditions without being troubled by the phenomenon known as runaway stratification, in which the stratification grows without bounds. The only input parameters are (i) a measure for the strength of the initial density gradient (an aspect ratio Γ), (ii) a measure for the viscous processes (a Reynolds number Re_g), and (iii) a measure for the diffusive processes Sc . Therefore, the mean velocity and mean density profiles were not prescribed but evolved freely depending on these input parameters. As a result, it is now possible to simulate with DNS/LES an exchange flow in which the mixing affects the mean profiles. This feature unlocks possibilities of further research in which the exchange flow that are modulated by oscillatory flows, such as in estuaries.

The results show a flow that undergoes several stage transitions from an fluid initially at rest towards quasi-steady turbulent flows. During this transition, several phenomena are observed such as convective overturning, Holmboe waves and mixing of the interface due to turbulence. Particularly these last two phenomena are in agreement with previous experiments and numerical simulations. The present set-up stands out from previous numerical set-ups by its ability to reproduce time-periodic stratification. Overall the study shows that the new parametrization produces reliable results and opens the path for a whole new series of studies of turbulent exchange flow that were unfeasible with the already existing techniques.

8

Conclusion

During this thesis a DNS/LES model was built to investigate specific physical processes occurring in regions of freshwater influence. More specifically, two physical processes were isolated and studied separately: the influence of the water-depth on the structure of the turbulent oscillating boundary layer, and strongly stratified turbulent exchange flows. The first physical process is used as a model for the tidal boundary layer in shallow seas, whereas the second physical process is used as a model for the exchange flows occurring in estuaries or river plumes.

8.1. Summary of results

The results of the simulation of the oscillating flow first identified the thickness of the turbulent boundary layer in a sufficiently deep computational domain. Subsequently, the height of the computational domain was reduced to be smaller than the previously defined boundary layer thickness. This configuration acted as model for the tidal flow in the Rhine region, where the boundary layer spans the entire water-depth. It was found that in such a configuration, the structure of the boundary layer changes significantly in three ways: (i) an increase of the phase lead of the surface velocity and the wall shear stress on the free-stream velocity, (ii) a change in the amplitude of the surface velocity (iii) a possible relaminarisation if the depth is decreased too much.

In shallow seas, the Reynolds number values are larger than the ones used for the simulations discussed in this thesis. As a result, the changes in phase lead and amplitude are likely to be reinforced and could impact the modeling of shallow seas using Reynolds-Averaged Navier-Stokes equations. In this type of numerical simulations, the grid is too coarse to fully resolve the wall layer, such that a wall model is used. These wall models generally assume the presence of a logarithmic layer and that the first grid point is located within this layer. The results of Chapter 4 show that, although a logarithmic layer is present in oscillatory flows, it is never present throughout the entire oscillation cycle at the Reynolds values considered. Particularly for shallow flows (i.e. the Rhine ROFI configuration), the intermittent turbulence also

leads to an intermittent presence of the logarithmic layer. Nevertheless, the Reynolds number cases reported in the present thesis are lower than the typical Reynolds number value of the tidal flow in the Rhine ROFI. As a result, more research is required to investigate the accuracy of a logarithmic layer model for the Rhine ROFI.

The objective of simulating a strongly stratified exchange flow using a classical DNS/LES domain could not be accomplished without the development of the new one-dimensional models for exchange flow presented in Chapter 5. These new models play a crucial role in (i) extending the state of the art theory of one-dimensional models to strongly stratified flows and (ii) unlocking the possibility to simulate strongly stratified, turbulent exchange flows with the classical horizontally periodic computational domains used in fundamental DNS or LES simulations. Besides these two direct applications, the one-dimensional models also bridge the gap between large scale oceanography and fundamental fluid mechanics, since physical processes characteristic of river plumes can now be simulated with DNS or LES.

As an additional result, the one-dimensional models for strongly stratified exchange flows also permitted to derive a generalized Reynolds number for the inclined duct experiment. The analysis of this classical experimental set-up suffered from the lack of continuity and uniqueness between the theories developed for inclined ducts and horizontal ducts. The newly derived Reynolds number for inclined ducts has the advantage of converging to the velocity scale for horizontal ducts when the inclination angle of the duct tends to zero.

Finally, the one-dimensional model was used as a forcing mechanism in a three-dimensional numerical set-up with periodic boundary conditions. This approach allowed, for the first time to simulate strongly stratified exchange flows in such a set-up. The simulation results are in agreement with other reference studies on the same topic, including experiments and numerical simulations in a slightly different set-up. The model was able to reproduce the Holmboe waves and turbulence observed in the previous studies. Most importantly, it allows for interactions of the mean flow and the density profile.

8.2. Implications for the Rhine

The oscillatory boundary layer in shallow flows and the turbulent density driven stratified exchange flow are two processes occurring in the Rhine ROFI. However, they were studied in a more fundamental way in this thesis. Therefore, it is interesting to estimate which impact the present results have on the understanding of the Rhine ROFI.

8.2.1. Oscillatory boundary layer

As extensively discussed in Chapter 3, the Rhine ROFI is clearly shallow. This fact implies that the Rhine is certainly affected by the phase shift and surface amplitude changes reported in Chapter 3. The values of the ratio between the water-depth and the theoretical turbulent boundary layer are similar in the simulations and in the Rhine ROFI (see Tables 3.1). However, the flow is also governed by two other parameters, Re_δ and Re_h , with $Re_h = U_0 h / \nu = Re_\delta h / \delta_s$. In Chapter 3, it was suggested that relaminarization observed in flows with a reduced water-depth would take place for

Table 8.1: Tide related parameters for the Rhine ROFI and the relevant simulations

	h/δ	Re_δ	Re_h
Rhine ROFI (neap)	0.51	$7.82 \cdot 10^4$	$1.23 \cdot 10^7$
Rhine ROFI (spring)	0.80	$1.23 \cdot 10^5$	$1.93 \cdot 10^7$
simulation	0.64	$9.90 \cdot 10^2$	$4.95 \cdot 10^3$
simulation	0.79	$1.79 \cdot 10^3$	$1.79 \cdot 10^4$
simulation	0.57	$3.46 \cdot 10^3$	$3.46 \cdot 10^4$

smaller time-intervals with increasing Reynolds number value. In Chapter 4, it was found that the log layer was present for longer time intervals with increasing Reynolds number value.

The free-stream Reynolds number of the Rhine ROFI, Re_{fs} was estimated based on the kinematic viscosity, the oscillation period and the free-stream velocity. This Reynolds number is related to Re_δ via $Re_{fs} = Re_\delta^2/2$. For a Rhine ROFI depth of $h = 20\text{m}$, the estimated parameter values for the Rhine ROFI and the simulations are summarized in Table 8.1. The parameter values indicate that the values of the Reynolds number are still several orders of magnitude higher in the Rhine ROFI than in the simulation. Concretely, this fact probably implies that relaminarization effects are significantly reduced if not absent in the Rhine ROFI, and that the log layer is present for significantly larger time intervals. Nevertheless, the evolution of the phase shift and amplitude certainly remains similar to the simulations. The simulation with parameter values closer to the ones of the Rhine ROFI requires a significant increase in resolution, and accordingly, computation time.

8.2.2. Exchange flows

To estimate if the flow regimes observed for the turbulent exchange flow have applications to the Rhine ROFI, it is interesting to estimate if the simulated parameter values are realistic. The estimation of the physical parameters is based on numbers found in literature, e.g. scientific articles or technical reports. In their article about the Rhine Region of Freshwater Influence, de Boer and co-authors (de Boer et al., 2009) show through sea surface temperature images, that 15°C is a good estimation for the seawater temperature around the Rhine river mouth. Along a transect near Hoek van Holland (slightly north of the Rhine mouth) the salinity increases from 26 to 34 over a distance of roughly 50 km (Suijlen & Duin, 2002). For these values of the temperature and salinity, the Schmidt number for salinity Sc varies between 679 and 697 (Ramsing & Gundersen, 2011). The average depth of the North Sea close to the River Rhine mouth is assumed to be 20 m, in agreement with the idealized model by de Boer et al. (2006).

The reference experiment of a density current generated by a horizontal density gradient is described by Simpson and Linden (1989). They used a reservoir measuring $L = 3.6\text{m}$ long and $h = 150\text{mm}$ deep. In their experiment, they do not provide directly the used salinity gradient. However, they define the initial salinity distribution as (neglecting the stratification) $\rho = \rho_{\text{ref}}(1 - \alpha x)$, where α varies between $6.5 \times 10^{-3}\text{m}^{-1}$ and $30.0 \times 10^{-3}\text{m}^{-1}$, and x varies between $-L/2$ and $+L/2$. Ac-

cordingly, $\Delta\rho = \rho_{\text{ref}}\alpha L$ and $U_g = \sqrt{\alpha L g h}$. It is not clear if the definition of ρ_{ref} in Simpson and Linden (1989) is the same as in the current manuscript. However, in the former paper ρ_{ref} is expressed as averaged value, implicitly over the duct. This definition implies that the formulation $\rho_{\text{ref}} = \rho_0 [1 + \beta s_{\text{av}}]$ is consistent with both Simpson and Linden (1989) and Chapter 5. Additionally, the salinity can be reconstructed by recombining the relationships between the different density definitions leading to $\Delta s = (1 + \beta s_{\text{av}})\alpha L/\beta$. Assuming the minimum salinity in the experiments was 0, $s_{\text{av}} = \Delta s/2$, we have $\Delta s = 2\alpha L/(\beta(2 - \alpha L))$. Assuming the experiments took place at 20 °C gives a Schmidt number larger than 531 (Ramsing & Gundersen, 2011).

The values of the parameters for the different situations are summarized in Table 8.2, together with estimates of the dimensionless numbers characterizing the flows. In Chapter 5, it is shown that the magnitude of the exchange flow scales with ΓRe_g so that this quantity can be considered as a good measure for eventual transitions to turbulence. Clearly, the value of ΓRe_g occurring in the Rhine ROFI is higher than the maximum value of the experiments by Lefauve et al. (2019a). It is in fact of the same order of magnitude as in our simulations ($\Gamma\text{Re}_g = 6666$). Therefore, we can claim with a quite high level of confidence that geophysical density driven flows are susceptible to be subjected to Holmboe waves and a mixing of the interface. Nevertheless, the Schmidt number in the Rhine ROFI is still one order of magnitude higher than the Schmidt number in the simulation. Additionally, in Chapter 7 it is mentioned that the grid used in the simulation is too coarse. As a result, simulating ROFI physics with sufficient resolution requires significant grid refinements and, therefore, computation time.

Table 8.2: Overview of the estimation of parameter values and non-dimensional numbers for different exchange flows, for $g = 9.91 \text{ m s}^{-2}$, $\beta = 7.7 \times 10^{-4}$ (Geyer & MacCready, 2014) and $\nu = 1 \times 10^{-6} \text{ m}^2 \text{ s}^{-1}$.

Parameter values				
	h (m)	L (m)	Δs	U_g (m s^{-1})
Rhine ROFI	20	5×10^4	8	1.08
Non-dimensional numbers				
	Re_g	Sc	Γ	ΓRe_g
Rhine ROFI	2.17×10^7	679-697	4.00×10^{-4}	8.69×10^3
Simulation	4×10^5	50	1.66×10^{-2}	6.66×10^3

8.3. Outlook

Based on the previous paragraph, it is tempting to pursue the investigation by simulating parameter values that are closer to the Rhine ROFI. With a better scaling of the code (i.e. full parallelisation in the second and third direction), as well as sufficient computation time, significant progress could be made in this direction. The progress could be further emphasized by the expected increase in algorithm speed since the start of this research project.

However, what makes the Rhine ROFI interesting and unique is the combination and interplay of the different physical actors. Accordingly, the focus should not be on trying to match the same parameter values, but to increase step by step the complexity of the model. This approach, could also lay the foundation of more specific estuarine research, in which physical phenomena are not studied while isolated individually, but are studied in combination. Proceeding this way would further bridge the gap between fundamental research of classical fluid mechanics problems motivated by estuarine physics on one side, and the research of river plumes using approaches and techniques novel to the field on the other side. Several steps for including additional processes in the model are proposed below.

8.3.1. Estuarine circulation

In Chapter 7, a turbulent stratified exchange flow was simulated using a plane channel configuration. For simplicity purposes, this symmetric set-up was chosen. The symmetry simplified the verification of certain requirements, in particular that the integral of the velocity over the vertical should be zero. However, a more realistic set-up for a ROFI, and a set-up compatible with the oscillatory flow set-up, would require a no-stress surface boundary condition. This change in boundary condition would probably not affect the results and findings of Chapter 7, but it would make the one-dimensional forcing more complex since the set-up would no longer be symmetric.

8.3.2. Tidal Straining

As mentioned in the introduction, tidal straining is an important component of the Rhine ROFI hydrodynamics. However, tidal straining in the Rhine ROFI is a complex mechanism that mainly results from a redistribution of the main tidal current (along-shore) into the direction of the main horizontal density gradient (cross-shore) via the Coriolis force. Therefore, an accurate reproduction of the tidal straining mechanism would require the activation of the Coriolis force. Nevertheless, a simpler approach would be to simulate a configuration in which the tidal flow is strictly aligned with the horizontal density gradient, without activating the Coriolis force. This configuration allows for example to study convective overturning. It certainly also requires an adjustment of the one-dimensional forcing mechanism of Chapter 5 to cope with the addition of the oscillating forcing. Accordingly, a preliminary study with a laminar two-dimensional model is recommended, while taking care that the two-dimensional model does not enter in the convective overturning regime (i.e. tidal straining and de-straining only takes place via differential advection).

8.3.3. Tidal mixing and spring-neap tidal cycle

A key feature of the Rhine ROFI physics is the changes in average mixing rate of the water column over the the spring neap tidal cycle. In the laminar regime, an oscillatory flow and a perpendicular density driven flow are decoupled. However, in the turbulent regime, momentum is redistributed in the three directions and the two flows are expected to be strongly coupled. On the one hand, turbulence generated by the oscillatory boundary layer can (i) modulate the mean velocity in the density driven flow by a change in eddy viscosity and (ii) (partly) destroy eventual stratification.

On the other hand, the stratification induced by the density driven flow can damp turbulence generated by the oscillatory flow. To estimate to which level the density driven and the oscillatory flow are influencing each other, a combined simulation of an oscillatory flow and a perpendicular density driven flow can be undertaken. It is recommended to carry out first a simulation without density. The turbulence generated by the oscillatory flow alone could already modulate the magnitude of the density driven flow due to changes in eddy viscosity. Once the latter process is understood well, density can be turned on. In a later stage, the influence of the spring-neap tidal cycle could be investigated by (i) changing the Reynolds number values for the oscillatory flow or (ii) adding a second periodicity in the oscillatory flow forcing.

8.3.4. Free surface

A significant short-coming of the present DNS/LES set-up as Rhine ROFI model is the absence of a free-surface. In the Rhine ROFI, changes in the surface elevation related to the propagation of the tidal wave can lead to relative changes in the water-depth of about 10%. These changes impact the mean velocity profile, can modulate turbulence and generate residual flows such as the Stokes return flow or the flow generated by the velocity-depth asymmetry. However, a challenge while implementing a free-surface in a periodic domain is that the domain size should be a multiple of the tidal wave length applied at its surface. This factor severely constrains the possible domain size and/or the tidal wave lengths that can be simulated. A different strategy could be to assume a flat surface (implying the domain size is small with respect to the tidal wave length) that moves homogeneously up and down according to the tidal forcing. However, even such a simple free-surface model would require significant changes in the algorithm upon which the code is built. For example, it may require a dynamic adaptation of the grid to the varying vertical domain size.

8.3.5. Tidal ellipses

A last possibility of building a more realistic Rhine ROFI model is to attempt to reproduce the typical tidal ellipses observed in the Rhine ROFI. Tidal ellipses were reproduced by Salon et al. (2009), but in a case without a coast, without stratification and in a much larger water-column. Their configuration was very close to the Prandle (1982a) configuration. However, as discussed in the introduction, the proximity of the coast induces a zero net flow condition in the cross-shore direction. The coupling between the top and the bottom layer (via the eddy viscosity) then determines if the tidal currents are elliptic (weak coupling) or rectilinear (strong coupling). To reproduce this physical phenomenon, an oscillatory flow in shallow depth configuration is required. Additionally, a vertical side wall should be included to approximate the presence of a coast. The Coriolis force should be activated to enable the possibility of having tidal ellipses. Finally, stratification should be switched on and off to change the coupling between the top and the bottom layer in the computational domain. It is crucial to mention that the stratification does not need to come from a lateral source and it could be enforced directly as an imposed scalar field.

A

Analytical solution for the tidal ellipses

Prandle (1982a) derived an analytical expression for the tidal ellipses. Starting point are the two-dimensional Shallow-water equations for the velocity components (u, v) expressed in the horizontal plane (x, y) :

$$\frac{\partial u}{\partial t} - fv = -g \frac{\partial \zeta_s}{\partial x} + \frac{\partial}{\partial z} \left(\nu_T \frac{\partial u}{\partial z} \right), \quad (\text{A.1a})$$

$$\frac{\partial v}{\partial t} + fu = -g \frac{\partial \zeta_s}{\partial y} + \frac{\partial}{\partial z} \left(\nu_T \frac{\partial v}{\partial z} \right). \quad (\text{A.1b})$$

In these equations, f is the Coriolis parameter, g the gravitational acceleration, ζ_s the surface elevation and ν_T the eddy-viscosity. Summing Eqs (A.1a) + i(A.1b), and defining the complex velocity vector and the complex surface elevation gradient

$$\mathbf{R} = u + iv \quad (\text{A.2a})$$

$$\mathbf{G} = -g \left(\frac{\partial \zeta}{\partial x} + i \frac{\partial \zeta}{\partial y} \right) \quad (\text{A.2b})$$

gives

$$\frac{\partial \mathbf{R}}{\partial t} + i f \mathbf{R} = \mathbf{G} + \frac{\partial}{\partial z} \left(\nu_T \frac{\partial \mathbf{R}}{\partial z} \right). \quad (\text{A.3})$$

We can assume that the water motion is purely oscillatory, function of the tidal frequency ω . As a result, the solutions for u and v are of the form

$$u(z, t) = a(z) \cos(\omega t) + b(z) \sin(\omega t), \quad (\text{A.4a})$$

$$v(z, t) = c(z) \cos(\omega t) + d(z) \sin(\omega t), \quad (\text{A.4b})$$

where a , b , c and d are amplitude function associated to the velocity. It is possible to notice that $\cos(\omega t) = (e^{i\omega t} + e^{-i\omega t})/2$ and $\sin(\omega t) = (e^{i\omega t} - e^{-i\omega t})/2i$. Subsequently, it is possible to put \mathbf{R} and \mathbf{G} under the form

$$\mathbf{R} = \|\mathbf{R}_1\| (z) \exp(i\omega t) + \|\mathbf{R}_2\| (z) \exp(-i\omega t) \quad (\text{A.5a})$$

$$\mathbf{G} = \|\mathbf{G}_1\| \exp(i\omega t) + \|\mathbf{G}_2\| \exp(-i\omega t) \quad (\text{A.5b})$$

where $\|\mathbf{R}_1\|$ and $\|\mathbf{G}_1\|$ can be interpreted as the magnitude of a counterclockwise motion, while $\|\mathbf{R}_2\|$ and $\|\mathbf{G}_2\|$ can be interpreted as the magnitude of a clockwise motion. Inserting Eqs (A.5a), (A.5b) into Eq. (A.3) leads to an equation for the counterclockwise motion, and an equation for the clockwise motion

$$i(f + \omega) \|\mathbf{R}_1\| = \|\mathbf{G}_1\| + \frac{\partial}{\partial z} \left(\nu_T \frac{\partial \|\mathbf{R}_1\|}{\partial z} \right) \quad (\text{A.6a})$$

$$i(f - \omega) \|\mathbf{R}_2\| = \|\mathbf{G}_2\| + \frac{\partial}{\partial z} \left(\nu_T \frac{\partial \|\mathbf{R}_2\|}{\partial z} \right). \quad (\text{A.6b})$$

If the eddy-viscosity is assumed constant, it is possible to integrated these differential equations. The solutions are then

$$\|\mathbf{R}_1\| (z) = R_{11} \exp\left(- (i+1) \frac{z}{\delta_+}\right) + R_{12} \exp\left((i+1) \frac{z}{\delta_+}\right) - \frac{i \|\mathbf{G}_1\|}{f + \omega} \quad (\text{A.7a})$$

$$\|\mathbf{R}_2\| (z) = R_{21} \exp\left(- (i+1) \frac{z}{\delta_-}\right) + R_{22} \exp\left((i+1) \frac{z}{\delta_-}\right) - \frac{i \|\mathbf{G}_2\|}{f - \omega} \quad (\text{A.7b})$$

where R_{11} , R_{12} , R_{21} and R_{22} are integration constants that can be determined using the boundary conditions. In the above equations, two boundary layer thicknesses appear, δ_+ related to the anti-clockwise motion and δ_- related to the clockwise motion. Theses boundary layer thicknesses are expressed as

$$\delta_+ = \sqrt{\frac{2\nu_T}{f + \omega}}, \quad (\text{A.8a})$$

$$\delta_- = \sqrt{\frac{2\nu_T}{f - \omega}}. \quad (\text{A.8b})$$

B

Analytical solution for the finite depth Stokes boundary layer

Depending on the top boundary condition used, two different analytical solutions are possible for Eq. (3.3). If an infinite depth is assumed,

$$u_{\infty}(z; t) = -U_0 \exp\left(-\frac{z}{\delta_s}\right) \sin\left(\omega t - \frac{z}{\delta_s}\right) + U_0 \sin(\omega t), \quad (\text{B.1})$$

where the subscript ∞ refers to the infinite-depth case. In the case of a finite-depth, a no-stress boundary condition is applied at $y = h$. In this case, the solution is given by

$$\begin{aligned} u_f(z; t) = U_0 & \left(A_{11} \exp\left(\frac{z}{\delta_s}\right) \sin\left(\omega t + \frac{z}{\delta_s}\right) + A_{12} \exp\left(\frac{z}{\delta_s}\right) \cos\left(\omega t + \frac{z}{\delta_s}\right) \right. \\ & + A_{21} \exp\left(-\frac{z}{\delta_s}\right) \sin\left(\omega t - \frac{z}{\delta_s}\right) + A_{22} \exp\left(-\frac{z}{\delta_s}\right) \cos\left(\omega t - \frac{z}{\delta_s}\right) \left. \right) \\ & + U_0 \sin(\omega t), \end{aligned} \quad (\text{B.2})$$

and the subscript f refers to the finite-depth solution. The real constants A_{11} , A_{12} , A_{21} and A_{22} are given by

$$A_{11} = -\frac{1}{2} \frac{\exp(-2h/\delta_s) + \cos(2h/\delta_s)}{\cosh(2h/\delta_s) + \cos(2h/\delta_s)}, \quad (\text{B.3a})$$

$$A_{12} = \frac{1}{2} \frac{\sin(2h/\delta_s)}{\cosh(2h/\delta_s) + \cos(2h/\delta_s)}, \quad (\text{B.3b})$$

$$A_{21} = -\frac{1}{2} \frac{\exp(2h/\delta_s) + \cos(2h/\delta_s)}{\cosh(2h/\delta_s) + \cos(2h/\delta_s)}, \quad (\text{B.3c})$$

$$A_{22} = -A_{12}. \quad (\text{B.3d})$$

The two velocities u_∞ and u_f , and the wall-shear stress associated to the latter, $\tau_{w,f}$, can be put under the form

$$u_\infty(z; t) = A_\infty(z/\delta_s) \sin(\omega t + \Phi_\infty(z/\delta_s)) \quad (\text{B.4a})$$

$$u_f(z = h; t) = A_{h,f}(h/\delta_s) \sin(\omega t + \Phi_{h,f}(h/\delta_s)) \quad (\text{B.4b})$$

$$\tau_{w,f}(h; t) = A_\tau(h/\delta_s) \sin(\omega t + \Phi_\tau(h/\delta_s)), \quad (\text{B.4c})$$

where the amplitudes A_∞ , $A_{h,f}$ and A_τ read

$$A_\infty(z/\delta_s) = U_0 \sqrt{\exp(-2z/\delta_s) - 2 \exp(-z/\delta_s) \cos(z/\delta_s) + 1} \quad (\text{B.5a})$$

$$A_{h,f}(h/\delta_s) = \sqrt{2} U_0 \frac{\cosh(h/\delta_s) - \cos(h/\delta_s)}{\sqrt{\cosh(2h/\delta_s) + \cos(2h/\delta_s)}} \quad (\text{B.5b})$$

$$A_\tau(h/\delta_s) = \sqrt{2} \frac{\rho_0 \nu U_0}{\delta_s} \sqrt{\frac{\cosh(2h/\delta_s) - \cos(2h/\delta_s)}{\cosh(2h/\delta_s) + \cos(2h/\delta_s)}}, \quad (\text{B.5c})$$

and the phases Φ_∞ , $\Phi_{h,f}$ and Φ_τ read

$$\Phi_\infty(z/\delta_s) = \arctan \left(\frac{\exp(-z/\delta_s) \sin(z/\delta_s)}{1 - \exp(-z/\delta_s) \cos(z/\delta_s)} \right) \quad (\text{B.6a})$$

$$\Phi_{h,f}(h/\delta_s) = \arctan \left(\frac{2 \sin(h/\delta_s) \sinh(h/\delta_s)}{\cos(2h/\delta_s) - 2 \cosh(h/\delta_s) \cos(h/\delta_s) + \cosh(2h/\delta_s)} \right) \quad (\text{B.6b})$$

$$\Phi_\tau(h/\delta_s) = \arctan \left(\frac{\sinh(2h/\delta_s) + \sin(2h/\delta_s)}{\sinh(2h/\delta_s) - \sin(2h/\delta_s)} \right). \quad (\text{B.6c})$$

C

Log-layer diagnostic function in normal scaling

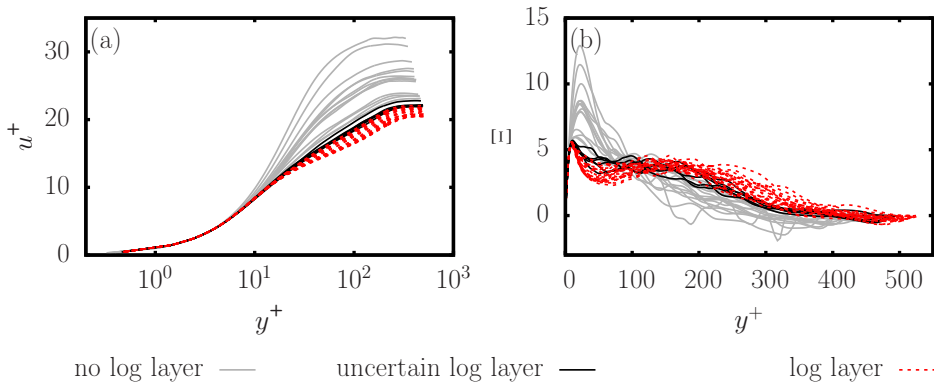


Figure C.1: Reproduction of the profiles of Fig. 4.3. (a) logarithmic layer and (b) their associated log-layer diagnostic Ξ function in normal scaling for $\text{Re}_s = 990$, $h/\delta_s = 10$ and $\omega t = \pi/2$.

D

One-dimensional models

D.1. Determination of the barotropic pressure gradient

The equations of motion for a 1D water-column model located at $y = 0$ are obtained by assuming $w(z) = 0$. Substitution of this assumption in Eq. (5.1) for mass conservation immediately implies $\partial v / \partial y = 0$. Using both expressions to simplify Eqs. (5.2) and (5.3) results in

$$\frac{\partial v}{\partial t} = -\frac{1}{\rho_{\text{ref}}} \frac{\partial \tilde{p}}{\partial x} + \nu \frac{\partial^2 v}{\partial z^2}, \quad (\text{D.1})$$

$$0 = -\frac{\partial \tilde{p}}{\partial z} - \rho_{\text{var}} g. \quad (\text{D.2})$$

To determine the barotropic pressure gradient, Eq. (D.2) is integrated between z and $\frac{1}{2}h$, which gives

$$\tilde{p}(z) = g \int_z^{\frac{1}{2}h} \rho_{\text{var}} d\tilde{z} + \tilde{P}_{\frac{1}{2}h}, \quad (\text{D.3})$$

where $\tilde{P}_{\frac{1}{2}h}$ is the pressure at $z = \frac{1}{2}h$. Then, Eq. (D.3) is substituted into in Eq. (D.1) which results in

$$\frac{\partial v}{\partial t} = \nu \frac{\partial^2 v}{\partial z^2} - \frac{g}{\rho_{\text{ref}}} \int_z^{\frac{1}{2}h} \frac{\partial \rho_{\text{var}}}{\partial y} d\tilde{z} - \frac{1}{\rho_{\text{ref}}} \frac{\partial \tilde{P}_{\frac{1}{2}h}}{\partial y}. \quad (\text{D.4})$$

The unknown quantity $\partial \tilde{P}_{\frac{1}{2}h} / \partial y$ can be evaluated by imposing the no net-flow condition over the vertical:

$$\int_{-\frac{1}{2}h}^{\frac{1}{2}h} v(z; t) dz = 0, \quad (\text{D.5})$$

such that integrating Eq. (D.4) over z between $-\frac{1}{2}h$ and $\frac{1}{2}h$ gives

$$h \frac{\partial \tilde{P}_{\frac{1}{2}h}}{\partial x} = \rho_{\text{ref}} \nu \left(\left. \frac{\partial v}{\partial z} \right|_{\frac{1}{2}h} - \left. \frac{\partial v}{\partial z} \right|_{-\frac{1}{2}h} \right) - g \int_{-\frac{1}{2}h}^{\frac{1}{2}h} \int_z^{\frac{1}{2}h} \frac{\partial \rho_{\text{var}}}{\partial y} d\tilde{z} dz. \quad (\text{D.6})$$

The pressure gradient $\partial\tilde{P}_{\frac{h}{2}}/\partial y$ then depends on the boundary conditions for the velocity. If a no-slip boundary condition is used both at the bottom wall and at the top wall, the solution for the horizontal velocity $v(z)$ is antisymmetric with respect to $z = 0$, and one can easily show that $\partial v/\partial z|_{-h/2} = \partial v/\partial z|_{+h/2}$. By partial integration and employing the fact that $\partial\rho_{\text{var}}/\partial y$ is an even function of z (at $y = 0$), see Fig. 5.3b, we finally obtain

$$h\frac{\partial\tilde{P}_{\frac{h}{2}}}{\partial y} = -g \int_{-\frac{1}{2}h}^{\frac{1}{2}h} \int_z^{\frac{1}{2}h} \frac{\partial\rho_{\text{var}}}{\partial y} d\check{z} dz = -gh \int_0^{\frac{1}{2}h} \frac{\partial\rho_{\text{var}}}{\partial y} d\check{z}. \quad (\text{D.7})$$

Substitution of this expression in Eq. (D.4) gives

$$\frac{\partial v}{\partial t} = \nu \frac{\partial^2 v}{\partial z^2} + \frac{g}{\rho_{\text{ref}}} \int_0^z \frac{\partial\rho_{\text{var}}}{\partial y} d\check{z}, \quad (\text{D.8})$$

which is the expression for the momentum equation (5.15).

D.2. Maximum velocities and density differences

In the diffusion-dominated regime, $|v^{d,\infty}/U_g|$ is maximum at $\frac{z}{h} = \pm\frac{1}{6}\sqrt{3}$ and

$$\frac{(\Delta v^{d,\infty})_{\text{max}}}{U_g} = \frac{\sqrt{3}}{108} \text{Re}_g \Gamma, \quad (\text{D.9a})$$

$$\frac{(\Delta\rho_{\text{var}}^{d,\infty})_{\text{max}}}{\Delta\rho} = \frac{1}{720} \text{Re}_g^2 \Gamma^2 \text{Sc}, \quad (\text{D.9b})$$

$$\int_{-\frac{1}{2}}^{\frac{1}{2}} \left| \frac{\Delta v^{d,\infty}}{U_g} \right| dz^* = \frac{\text{Re}_g \Gamma}{192}, \quad (\text{D.9c})$$

$$\int_{-\frac{1}{2}}^{\frac{1}{2}} \left| \frac{\Delta\rho_{\text{var}}^{d,\infty}}{\Delta\rho} \right| dz^* = \frac{11}{23040} \text{Re}_g^2 \Gamma^2 \text{Sc}. \quad (\text{D.9d})$$

In the high-advection/low-diffusion regime, $|v^{a,\infty}/U_g|$ is maximum for $\frac{z}{h} = \pm\frac{1}{4}$, and the magnitude of the velocity and density profiles is then

$$\frac{(\Delta v^{a,\infty})_{\text{max}}}{U_g} = \frac{1}{96} \text{Re}_g \Gamma, \quad (\text{D.10a})$$

$$\frac{(\Delta\rho_{\text{var}}^{a,\infty})_{\text{max}}}{\Delta\rho} = 1, \quad (\text{D.10b})$$

$$\int_{-\frac{1}{2}}^{\frac{1}{2}} \left| \frac{\Delta v^{a,\infty}}{U_g} \right| dz^* = \frac{\text{Re}_g \Gamma}{288}, \quad (\text{D.10c})$$

$$\int_{-\frac{1}{2}}^{\frac{1}{2}} \left| \frac{\Delta\rho_{\text{var}}^{a,\infty}}{\Delta\rho} \right| dz^* = \frac{1}{2}. \quad (\text{D.10d})$$

D.3. Open-channel flow in the diffusion-dominated regime

In environmental flows, the pressure at the upper boundary is obviously constant and equal to the atmospheric pressure. In addition, one key assumption for the exchange flow is that there is no net flow over the vertical. In other words, the integral of the velocity is zero over the vertical. However, the pressure induced by the horizontal density gradient varies linearly with distance from the surface, but does not change sign over the depth. Therefore, a small slope in the water surface is required, in order to generate a constant pressure gradient with opposite sign to the baroclinic pressure gradient. The sum of the two pressure gradients leads to a pressure gradient that depends linearly on the depth and changes sign, driving the typical exchange flow.

In our numerical set-up, this slope in the surface is not possible, since we have a rigid lid and just apply a no-stress condition. However, conservation of mass still implies and the integral of the velocity over the channel height should be zero. The only way to realize this is to have a non-constant pressure at the top boundary:

$$\frac{\partial \tilde{P}_{\frac{1}{2}h}}{\partial y} \neq 0. \quad (\text{D.11})$$

The derivation of Eq. (5.30) is similar as outlined in Appendix A but with a stress-free boundary condition for the flow at the top of the channel. Additionally, we need to take into account that for the open-channel flow $\partial \rho_{\text{var}} / \partial y$ is not an even function with respect to $z = 0$, in contrast to the derivation in Appendix A.

In the diffusion-dominated regime, Eq. (5.30) reduces to

$$\frac{\partial v^*}{\partial t^*} = \frac{1}{\text{Re}_g} \frac{\partial^2 v^*}{\partial z^{*2}} + \Gamma z + \tau_w^*. \quad (\text{D.12})$$

After integration, using a no-slip boundary condition at $z^* = -\frac{1}{2}$ and a no-stress condition at $z^* = \frac{1}{2}$, the steady-state solution $v^{d,\infty}$ is

$$\frac{v^{d,\infty}(z)}{U_g} = \frac{\text{Re}_g \Gamma}{24} \left[3 \frac{z}{h} - 4 \left(\frac{z}{h} \right)^3 + 1 \right] + \frac{\text{Re}_g \tau_w^*}{24} \left[12 \frac{z}{h} - 12 \left(\frac{z}{h} \right)^2 + 9 \right]. \quad (\text{D.13})$$

By setting the integral over the depth of Eq. (D.13) equal to zero, the unknown τ_w^* can be determined and is found to be equal to $-\frac{1}{8}\Gamma$. Thus, finally

$$\frac{v^{d,\infty}(z)}{U_g} = \frac{\text{Re}_g \Gamma}{192} \left[12 \frac{z}{h} + 12 \left(\frac{z}{h} \right)^2 - 32 \left(\frac{z}{h} \right)^3 - 1 \right]. \quad (\text{D.14})$$

In the diffusion-dominated regime, $v^{d,\infty}/U_g$ is maximum at $z/h = \frac{1}{2}$ and minimum $z/h = -\frac{1}{4}$, thus

$$\frac{(\Delta v^{d,\infty})_{\text{max}}}{U_g} = \frac{27}{768} \text{Re}_g \Gamma. \quad (\text{D.15})$$

In the diffusion-dominated regime, $v^{d,\infty}/U_g$ is negative for $-1/2 \leq z^* \leq (7 - \sqrt{33})/16$, and positive for $(7 - \sqrt{33})/16 \leq z^* \leq 1/2$ (with $(7 - \sqrt{33})/16 \approx 0.078$). As a result

the magnitude of the exchange flow is

$$\int_{-\frac{1}{2}}^{\frac{1}{2}} \left| \frac{\Delta v^{d,\infty}}{U_g} \right| dz^* = \frac{39 + 55\sqrt{33}}{32768} \text{Re}_g \Gamma \approx 0.011 \text{Re}_g \Gamma. \quad (\text{D.16})$$

The evolution of the density in the diffusion-dominated regime still satisfies

$$\frac{\partial \rho_{\text{var}}^*}{\partial t} = \frac{1}{\text{Re}_g \text{Sc}} \frac{\partial^2 \rho_{\text{var}}^*}{\partial z^{*2}} - \Gamma u^*. \quad (\text{D.17})$$

The steady-state solution of this equation, using to no-flux conditions at $z = \pm \frac{1}{2}h$,

$$\frac{\Delta \rho_{\text{var}}}{\Delta \rho} = \frac{\text{Re}_g^2 \Gamma^2 \text{Sc}}{1920} \left[-10 \frac{z}{h} - 5 \left(\frac{z}{h} \right)^2 + 20 \left(\frac{z}{h} \right)^3 + 10 \left(\frac{z}{h} \right)^4 - 16 \left(\frac{z}{h} \right)^5 + A_1 \right]. \quad (\text{D.18})$$

If one of the two no-flux boundary conditions is satisfied, the polynomial given by Eq. (D.18) automatically satisfies the other no-flux boundary condition, such that one integration constant, A_1 , remains undetermined. This constant can be found by integrating Eq. (D.17) between $z = -\frac{1}{2}h$ and $z = \frac{1}{2}h$ and using

$$\frac{\partial}{\partial t} \int_{-\frac{1}{2}}^{\frac{1}{2}} \rho_{\text{var}} dz^* = 0. \quad (\text{D.19})$$

Since initially $\rho_{\text{var}} = 0$, it follows that $A_1 = 7/24$. The steady-state stratification will become

$$\frac{(\Delta \rho_{\text{var}}^{d,\infty})_{\text{max}}}{\Delta \rho} = \frac{1}{320} \text{Re}_g^2 \Gamma^2 \text{Sc}. \quad (\text{D.20})$$

Since the solution $\Delta \rho_{\text{var}}/\Delta \rho$ is a fifth-order polynomial, there is no general solution to find its roots analytically. Numerically, it is found that the only root, $\Delta \rho_{\text{var}}/\Delta \rho = 0$, for $-0.5 \leq z \leq 0.5$ is $z = 2.88 \times 10^{-2}$, such that

$$\int_{-\frac{1}{2}}^{\frac{1}{2}} \left| \frac{\Delta \rho_{\text{var}}^{d,\infty}}{\Delta \rho} \right| dz^* \approx 1.02 \times 10^{-3} \text{Re}_g^2 \Gamma^2 \text{Sc}. \quad (\text{D.21})$$

References

- Afzal, N., & Yajnik, K. (1973). Analysis of turbulent pipe and channel flows at moderately large Reynolds number. *Journal of Fluid Mechanics*, *61*(1), 23–31.
- Akhavan, R., Kamm, R., & Shapiro, A. (1991). An investigation of transition to turbulence in bounded oscillatory Stokes flows part 1. experiments. *Journal of Fluid Mechanics*, *225*, 395–422.
- Anati, D. A., Assaf, G., & Thompson, R. O. (1977). Laboratory models of sea straits. *Journal of Fluid Mechanics*, *81*(2), 341–351.
- Andreas, E. L., Claffey, K. J., Jordan, R. E., Fairall, C. W., Guest, P. S., Persson, P. O. G., & Grachev, A. A. (2006). Evaluations of the von Kármán constant in the atmospheric surface layer. *Journal of Fluid Mechanics*, *559*, 117–149.
- Armenio, V., & Piomelli, U. (2000). A lagrangian mixed subgrid-scale model in generalized coordinates. *Flow, Turbulence and Combustion*, *65*(1), 51–81.
- Bardina, J., Ferziger, J., & Reynolds, W. (1980). Improved subgrid-scale models for large-eddy simulation. In *13th fluid and plasmadynamics conference* (p. 1357).
- Benjamin, T. B. (1968). Gravity currents and related phenomena. *Journal of Fluid Mechanics*, *31*(2), 209–248.
- Bernardini, M., Pirozzoli, S., & Orlandi, P. (2014). Velocity statistics in turbulent channel flow up to $Re_\tau = 4000$. *Journal of Fluid Mechanics*, *742*, 171–191.
- Blaise, S., & Deleersnijder, E. (2008). Improving the parameterisation of horizontal density gradient in one-dimensional water column models for estuarine circulation. *Ocean Science*, *4*(4), 239.
- Blondeaux, P., & Vittori, G. (1994). Wall imperfections as a triggering mechanism for stokes-layer transition. *Journal of Fluid Mechanics*, *264*, 107–135.
- Burchard, H., & Hetland, R. D. (2010). Quantifying the contributions of tidal straining and gravitational circulation to residual circulation in periodically stratified tidal estuaries. *Journal of Physical Oceanography*, *40*(6), 1243–1262.
- Burchard, H., Hetland, R. D., Schulz, E., & Schuttelaars, H. M. (2011). Drivers of residual estuarine circulation in tidally energetic estuaries: Straight and irrotational channels with parabolic cross section. *Journal of Physical Oceanography*, *41*(3), 548–570.
- Carstensen, S., Sumer, B. M., & Fredsøe, J. (2010). Coherent structures in wave boundary layers. part 1. oscillatory motion. *Journal of Fluid Mechanics*, *646*, 169–206.
- CBS. (2019a). *Goederendoorvoer per spoor opnieuw gestegen*. <https://www.cbs.nl/nl-nl/nieuws/2019/28/goederenvervoer-per-spoor-opnieuw-gestegen>. (accessed May 12, 2020)
- CBS. (2019b). *Hoeveel vracht gaat er via de nederlandse binnenwateren?* <https://www.cbs.nl/nl-nl/visualisaties/verkeer-en-vervoer/goederen/binnenvaart/vracht>. (accessed February 4, 2021)
- Centraal Bureau voor de statistiek (CBS). (2018). *What is the volume of cargo going through dutch airports?* <https://www.cbs.nl/en-gb/faq/luchtvaart/what-is-the-volume-of-cargo-going-through-dutch-airports->. (accessed May 7, 2020)
- Chatwin, P. (1976). Some remarks on the maintenance of the salinity distribution in estuaries. *Estuarine and Coastal Marine Science*, *4*(5), 555–566.

- Chen, D., Chen, C., Tang, F.-E., Stansby, P., & Li, M. (2007). Boundary layer structure of oscillatory open-channel shallow flows over smooth and rough beds. *Experiments in fluids*, 42(5), 719–736.
- Cheng, P., De Swart, H. E., & Valle-Levinson, A. (2013). Role of asymmetric tidal mixing in the subtidal dynamics of narrow estuaries. *J. Geophys. Res.-Ocean*, 118, 2623–2639.
- Choi, S. K., Nam, H. Y., & Cho, M. (1995). A comparison of higher-order bounded convection schemes. *Computer methods in applied mechanics and engineering*, 121(1-4), 281–301.
- Comsol multiphysics reference manual [Computer software manual]. (n.d.).
- Cormack, D., Leal, L., & Imberger, J. (1974). Natural convection in a shallow cavity with differentially heated end walls. part 1. asymptotic theory. *Journal of fluid Mechanics*, 65(2), 209–229.
- Costamagna, P., Vittori, G., & Blondeaux, P. (2003). Coherent structures in oscillatory boundary layers. *Journal of Fluid Mechanics*, 474, 1–33.
- de Boer, G. J. (2009). *On the interaction between tides and stratification in the Rhine Region of Freshwater Influence* (Unpublished doctoral dissertation).
- de Boer, G. J., Pietrzak, J. D., & Winterwerp, J. C. (2006). On the vertical structure of the Rhine region of freshwater influence. *Ocean dynamics*, 56(3-4), 198–216.
- de Boer, G. J., Pietrzak, J. D., & Winterwerp, J. C. (2009). SST observations of upwelling induced by tidal straining in the Rhine ROFI. *Continental Shelf Research*, 29(1), 263–277.
- de Kok, J. (1996). A two-layer model of the Rhine plume. *Journal of marine systems*, 8(3-4), 269–284.
- Delft3D-FLOW User Manual. (2003). W| delft hydraulics, pp. B28-B70.
- De Ruijter, W., Huber, K., & Backhaus, J. (1987). North sea circulation. In *Report of the oceanography subgroup. second international conference on the protection of the north sea, scientific and technical working group* (pp. 19–36).
- de Ruijter, W., van der Giessen, A., & Groenendijk, F. (1992). Current and density structure in the Netherlands coastal zone. *Dynamics and exchanges in estuaries and the coastal zone*, 40, 529–550.
- de Ruijter, W. P. (1983). Effects of velocity shear in advective mixed-layer models. *Journal of physical oceanography*, 13(9), 1589–1599.
- de Ruijter, W. P. M., Postma, L., & De Kok, J. (1987). *Transport atlas of the southern north sea*. Rijkswaterstaat tidal waters division, Delft Hydraulics.
- Dijkstra, Y. M., Schuttelaars, H. M., & Burchard, H. (2017). Generation of exchange flows in estuaries by tidal and gravitational eddy viscosity-shear covariance (esco). *J. Geophys. Res.-Ocean*, 122, 4217–4237.
- Eckmann, D. M., & Grotberg, J. B. (1991). Experiments on transition to turbulence in oscillatory pipe flow. *Journal of Fluid Mechanics*, 222, 329–350.
- Fischer, E., Burchard, H., & Hetland, R. D. (2009). Numerical investigations of the turbulent kinetic energy dissipation rate in the rhine region of freshwater influence. *Ocean Dynamics*, 59(5), 629–641.
- Fletcher, C. A. (1988). Computational techniques for fluid dynamics. Volume 1-Fundamental and general techniques. Volume 2-Specific techniques for different

- flow categories. In *Berlin and new york, springer-verlag, 1988, p. vol. 1, 418 p.; vol. 2, 493 p.* (Vol. 1).
- Flores, R. P., Rijnsburger, S., Horner-Devine, A. R., Kumar, N., Souza, A. J., & Pietrzak, J. D. (2020). The formation of turbidity maximum zones by minor axis tidal straining in regions of freshwater influence. *Journal of Physical Oceanography*(2020).
- Flores, R. P., Rijnsburger, S., Horner-Devine, A. R., Souza, A. J., & Pietrzak, J. D. (2017). The impact of storms and stratification on sediment transport in the Rhine region of freshwater influence. *Journal of Geophysical Research: Oceans*, *122*(5), 4456–4477.
- Flores, R. P., Rijnsburger, S., Meirelles, S., Horner-Devine, A. R., Souza, A. J., Pietrzak, J. D., ... Reniers, A. (2018). Wave generation of gravity-driven sediment flows on a predominantly sandy seabed. *Geophysical Research Letters*, *45*(15), 7634–7645.
- Frenzen, P., & Vogel, C. A. (1995). On the magnitude and apparent range of variation of the von Kármán constant in the atmospheric surface layer. *Boundary-Layer Meteorology*, *72*(4), 371–392.
- Galea, A., Grifoll, M., Roman, F., Mestres, M., Armenio, V., Sanchez-Arcilla, A., & Mangion, L. Z. (2014). Numerical simulation of water mixing and renewals in the barcelona harbour area: the winter season. *Environmental Fluid Mechanics*, *14*(6), 1405–1425.
- Gayen, B., Sarkar, S., & Taylor, J. R. (2010). Large eddy simulation of a stratified boundary layer under an oscillatory current. *Journal of fluid mechanics*, *643*, 233–266.
- Germano, M., Piomelli, U., Moin, P., & Cabot, W. H. (1991). A dynamic subgrid-scale eddy viscosity model. *Physics of Fluids A: Fluid Dynamics*, *3*(7), 1760–1765.
- Geurts, B. J. (2003). *Elements of direct and large eddy simulation*. RT Edwards, Inc.
- Geyer, W. R., & MacCready, P. (2014). The estuarine circulation. *Annual review of fluid mechanics*, *46*, 175–197.
- Gonella, J. (1972). A rotary-component method for analysing meteorological and oceanographic vector time series. In *Deep sea research and oceanographic abstracts* (Vol. 19, pp. 833–846).
- Gregg, M. C., Ozsoy, E., & Latif, M. (1999). Quasi-steady exchange flow in the bosphorus. *Geophysical Research Letters*, *26*(1), 83–86.
- Gross, T. F., & Nowell, A. R. (1983). Mean flow and turbulence scaling in a tidal boundary layer. *Continental Shelf Research*, *2*(2-3), 109–126.
- Gu, L., & Lawrence, G. A. (2005). Analytical solution for maximal frictional two-layer exchange flow. *Journal of Fluid Mechanics*, *543*, 1–17.
- Hansen, D. V., & Rattray Jr, M. (1965). Gravitational circulation in straits and estuaries. *Journal of Marine Research*, *23*, 104–122.
- Harlow, F. H., & Welch, J. E. (1965). Numerical calculation of time-dependent viscous incompressible flow of fluid with free surface. *The physics of fluids*, *8*(12), 2182–2189.
- Härtel, C., Meiburg, E., & Necker, F. (2000). Analysis and direct numerical simulation of the flow at a gravity-current head. part 1. flow topology and front speed for slip and no-slip boundaries. *Journal of Fluid Mechanics*, *418*, 189–212.

- Hino, M., Kashiwayanagi, M., Nakayama, A., & Hara, T. (1983). Experiments on the turbulence statistics and the structure of a reciprocating oscillatory flow. *Journal of Fluid Mechanics*, *131*, 363-400.
- Hino, M., Sawamoto, M., & Takasu, S. (1976). Experiments on transition to turbulence in an oscillatory pipe flow. *Journal of Fluid Mechanics*, *75*(2), 193-207.
- Hisgen, R. G. W., & Laane, R. W. P. M. (2008). *Geheimen van de kust: van zwin tot marsdiep*. Veen Magazines.
- Hogg, A. M., Ivey, G. N., & Winters, K. B. (2001). Hydraulics and mixing in controlled exchange flows. *Journal of Geophysical Research: Oceans*, *106*(C1), 959-972.
- Horner-Devine, A. R., Pietrzak, J. D., Souza, A. J., McKeon, M. A., Meirelles, S., Henriquez, M., . . . Rijnsburger, S. (2017). Cross-shore transport of nearshore sediment by river plume frontal pumping. *Geophysical Research Letters*, *44*(12), 6343-6351.
- Hoyas, S., & Jiménez, J. (2006). Scaling of the velocity fluctuations in turbulent channels up to $Re \tau = 2003$. *Physics of fluids*, *18*(1), 011702.
- Hsu, C.-T., Lu, X., & Kwan, M.-K. (2000). LES and RANS studies of oscillating flows over flat plate. *Journal of Engineering Mechanics*, *126*(2), 186-193.
- Jensen, B., Sumer, B., & Fredsøe, J. (1989). Turbulent oscillatory boundary layers at high reynolds numbers. *Journal of Fluid Mechanics*, *206*, 265-297.
- Jiménez, J., & Moin, P. (1991). The minimal flow unit in near-wall turbulence. *Journal of Fluid Mechanics*, *225*, 213-240.
- Jiménez, J., & Moser, R. D. (2007). What are we learning from simulating wall turbulence? *Philosophical Transactions of the Royal Society of London A: Mathematical, Physical and Engineering Sciences*, *365*(1852), 715-732.
- Jonsson, I. G. (1980). A new approach to oscillatory rough turbulent boundary layers. *Ocean Engineering*, *7*(1), 109-152.
- Jonsson, I. G., & Carlsen, N. A. (1976). Experimental and theoretical investigations in an oscillatory turbulent boundary layer. *Journal of Hydraulic Research*, *14*(1), 45-60.
- Kaptein, S. J., Duran-Matute, M., Roman, F., Armenio, V., & Clercx, H. J. (2019). Effect of the water depth on oscillatory flows over a flat plate: from the intermittent towards the fully turbulent regime. *Environmental Fluid Mechanics*, *19*(5), 1167-1184.
- Kaptein, S. J., van de Wal, K. J., Kamp, L. P., Armenio, V., Clercx, H. J., & Duran-Matute, M. (2020). Analysis of one-dimensional models for exchange flows under strong stratification. *Ocean Dynamics*, *70*(1), 41-56.
- Kim, J., & Moin, P. (1984). Application of a fractional-step method to incompressible navier-stokes equation.
- Kim, J., Moin, P., & Moser, R. (1987). Turbulence statistics in fully developed channel flow at low Reynolds number. *Journal of Fluid Mechanics*, *177*, 133-166.
- Könemann, L., Stefánik, M., Gurňák, D., Hartstein, M., & Hanula, M. (2016). *Historica grote atlas van de wereld geschiedenis (geupdate versie)*. Parragon.
- Kundu, P. K., & Cohen, I. M. (2002). *Fluid mechanics-second edition*. Elsevier.
- Lefauve, A., & Linden, P. (2020a). Buoyancy-driven exchange flows in inclined ducts. *Journal of Fluid Mechanics*, *893*.

- Lefaue, A., & Linden, P. F. (2020b). *Research data supporting "Buoyancy-driven exchange flows in inclined ducts"*. <https://doi.org/10.17863/CAM.48821>.
- Lefaue, A., Partridge, J., & Linden, P. (2019a). Regime transitions and energetics of sustained stratified shear flows. *Journal of Fluid Mechanics*, *875*, 657–698.
- Lefaue, A., Partridge, J., & Linden, P. (2019b). Regime transitions and energetics of sustained stratified shear flows. *Journal of Fluid Mechanics*, *875*, 657–698.
- Lefaue, A., Partridge, J. L., Zhou, Q., Dalziel, S., Caulfield, C.-c., & Linden, P. (2018). The structure and origin of confined holmboe waves. *Journal of Fluid Mechanics*, *848*, 508–544.
- Leonard, B. P. (1988). Simple high-accuracy resolution program for convective modelling of discontinuities. *International journal for numerical methods in fluids*, *8*(10), 1291–1318.
- Li, M., Radhakrishnan, S., Piomelli, U., & Geyer, R. W. (2010). Large-eddy simulation of the tidal-cycle variations of an estuarine boundary layer. *Journal of Geophysical Research: Oceans*, *115*(C8).
- Li, M., Sanford, L., & Chao, S.-Y. (2005). Effects of time dependence in unstratified tidal boundary layers: results from large eddy simulations. *Estuarine, Coastal and Shelf Science*, *62*(1-2), 193–204.
- Li, M., Trowbridge, J., & Geyer, R. (2008). Asymmetric tidal mixing due to the horizontal density gradient. *Journal of physical oceanography*, *38*(2), 418–434.
- Lilly, D. K. (1992). A proposed modification of the germano subgrid-scale closure method. *Physics of Fluids A: Fluid Dynamics*, *4*(3), 633–635.
- Linden, P., & Simpson, J. (1986). Gravity-driven flows in a turbulent fluid. *Journal of Fluid Mechanics*, *172*, 481–497.
- Linden, P., & Simpson, J. (1988). Modulated mixing and frontogenesis in shallow seas and estuaries. *Continental Shelf Research*, *8*(10), 1107–1127.
- Lodahl, C., Sumer, B. M., & Fredsøe, J. (1998). Turbulent combined oscillatory flow and current in a pipe. *Journal of Fluid Mechanics*, *373*, 313–348.
- Lorke, A., Umlauf, L., Jonas, T., & Wüest, A. (2002). Dynamics of turbulence in low-speed oscillating bottom-boundary layers of stratified basins. *Environmental Fluid Mechanics*, *2*(4), 291–313.
- Maas, L., & van Haren, J. (1987). Observations on the vertical structure of tidal and inertial currents in the central North Sea. *Journal of Marine Research*, *45*(2), 293–318.
- Macagno, E. O., & Rouse, H. (1961). Interfacial mixing in stratified flows. *J. Engng Mech. Div. Proc. Am. Soc. Civ. Engrs*, *87*(EM5), 55–81.
- MacCready, P. (2004). Toward a unified theory of tidally-averaged estuarine salinity structure. *Estuaries*, *27*(4), 561–570.
- MacCready, P., Banas, N. S., Hickey, B. M., Dever, E. P., & Liu, Y. (2009). A model study of tide-and wind-induced mixing in the columbia river estuary and plume. *Continental Shelf Research*, *29*(1), 278–291.
- MacCready, P., & Geyer, W. R. (2010). Advances in estuarine physics. *Annual Review of Marine Science*, *2*, 35–58.
- Maderich, V., Konstantinov, S., Kulik, A., & Oleksiuk, V. (1998). Laboratory modelling of the water exchange through the sea straits. *OKEANOLOGIYA*, *38*(5), 665–672.

- Marozzi, J. (2014). *Baghdad: City of peace, city of blood*. Penguin Books.
- Marusic, I., McKeon, B. J., Monkewitz, P. A., Nagib, H. M., Smits, A. J., & Sreenivasan, K. R. (2010). Wall-bounded turbulent flows at high reynolds numbers: recent advances and key issues. *Physics of Fluids*, *22*(6), 065103.
- Marusic, I., Monty, J. P., Hultmark, M., & Smits, A. J. (2013). On the logarithmic region in wall turbulence. *Journal of Fluid Mechanics*, *716*.
- McKeon, B. J., Li, J.-d., Jiang, W., Morrison, J. F., & Smits, A. J. (2004). Further observations on the mean velocity distribution in fully developed pipe flow. *Journal of Fluid Mechanics*, *501*, 135–147.
- Meyer, C. R., & Linden, P. (2014). Stratified shear flow: experiments in an inclined duct. *Journal of fluid mechanics*, *753*, 242–253.
- Momen, M., & Bou-Zeid, E. (2017). Mean and turbulence dynamics in unsteady ekman boundary layers. *Journal of Fluid Mechanics*, *816*, 209–242.
- Mujal-Colilles, A., Christensen, K. T., Bateman, A., & Garcia, M. H. (2016). Coherent structures in oscillatory flows within the laminar-to-turbulent transition regime for smooth and rough walls. *Journal of Hydraulic Research*, *54*(5), 502–515.
- Münchow, A., & Garvine, R. W. (1993). Dynamical properties of a buoyancy-driven coastal current. *Journal of Geophysical Research: Oceans*, *98*(C11), 20063–20077.
- Nagib, H. M., & Chauhan, K. A. (2008). Variations of von Kármán coefficient in canonical flows. *Physics of Fluids*, *20*(10), 101518.
- Nash, J. D., Kilcher, L. F., & Moum, J. N. (2009). Structure and composition of a strongly stratified, tidally pulsed river plume. *Journal of Geophysical Research: Oceans*, *114*(C2).
- Nash, J. D., & Moum, J. N. (2005). River plumes as a source of large-amplitude internal waves in the coastal ocean. *Nature*, *437*(7057), 400–403.
- Nieuwstadt, F. T., Westerweel, J., & Boersma, B. J. (2016). *Turbulence: introduction to theory and applications of turbulent flows*. Springer.
- Ottolenghi, L., Adduce, C., Inghilesi, R., Armenio, V., & Roman, F. (2016). Entrainment and mixing in unsteady gravity currents. *Journal of Hydraulic Research*, *54*(5), 541–557.
- Ottolenghi, L., Adduce, C., Inghilesi, R., Roman, F., & Armenio, V. (2016). Mixing in lock-release gravity currents propagating up a slope. *Physics of Fluids*, *28*(5), 056604.
- Ottolenghi, L., Adduce, C., Roman, F., & Armenio, V. (2017). Analysis of the flow in gravity currents propagating up a slope. *Ocean Modelling*, *115*, 1–13.
- Partridge, J. L., Lefauve, A., & Dalziel, S. B. (2019). A versatile scanning method for volumetric measurements of velocity and density fields. *Meas. Sci. Technol.*, *30*(5). Retrieved from <https://doi.org/10.1088/1361-6501/ab0bfd> doi: 10.1088/1361-6501/ab0bfd
- Pedocchi, F., Cantero, M. I., & García, M. H. (2011). Turbulent kinetic energy balance of an oscillatory boundary layer in the transition to the fully turbulent regime. *Journal of Turbulence*(12), N32.
- Perry, A., & Li, J. D. (1990). Experimental support for the attached-eddy hypothesis in zero-pressure-gradient turbulent boundary layers. *Journal of Fluid Mechanics*, *218*, 405–438.

- Piomelli, U., & Balaras, E. (2002). Wall-layer models for large-eddy simulations. *Annual review of fluid mechanics*, *34*(1), 349–374.
- Pirozzoli, S., Bernardini, M., & Orlandi, P. (2014). Turbulence statistics in Couette flow at high Reynolds number. *Journal of Fluid Mechanics*, *758*, 327–343.
- Pope, S. B. (2001). *Turbulent flows*. IOP Publishing.
- Port of Rotterdam-Press release. (2020). *Port of rotterdam throughput amounted to 469.4 million tonnes in 2019*. <https://www.portofrotterdam.com/en/news-and-press-releases/port-of-rotterdam-throughput-amounted-to-4694-million-tonnes-in-2019>. (accessed May 7, 2020)
- Prandle, D. (1982a). The vertical structure of tidal currents. *Geophysical & astrophysical fluid dynamics*, *22*(1-2), 29–49.
- Prandle, D. (1982b). The vertical structure of tidal currents and other oscillatory flows. *Continental shelf research*, *1*(2), 191–207.
- Pu, J. H. (2015). Turbulence modelling of shallow water flows using kolmogorov approach. *Computers & Fluids*, *115*, 66–74.
- Radhakrishnan, S., & Piomelli, U. (2008). Large-eddy simulation of oscillating boundary layers: model comparison and validation. *Journal of Geophysical Research: Oceans*, *113*(C2).
- Ramaprian, B., & Tu, S. (1983). Fully developed periodic turbulent pipe flow. part 2. the detailed structure of the flow. *Journal of Fluid Mechanics*, *137*, 59–81.
- Ramsing, N., & Gundersen, J. (2011). Seawater and gases. *Limnol. Oceanogr*, *37*, 1307–1312.
- Rekenhof. (2016). *Baggerwerken in vlaanderen*. www.rekenhof.be.
- Rhie, C., & Chow, W. L. (1983). Numerical study of the turbulent flow past an airfoil with trailing edge separation. *AIAA journal*, *21*(11), 1525–1532.
- Rijkswaterstaat waterinfo*. (n.d.). <https://waterinfo.rws.nl/{#}!/kaart/waterhoogte-t-o-v-nap/>. (Accessed: 2018-11-28)
- Rijnsburger, S., Flores, R. P., Pietrzak, J. D., Horner-Devine, A. R., & Souza, A. J. (2018). The influence of tide and wind on the propagation of fronts in a shallow river plume. *Journal of Geophysical Research: Oceans*, *123*(8), 5426–5442.
- Rijnsburger, S., van der Hout, C. M., van Tongeren, O., de Boer, G. J., van Prooijen, B. C., Borst, W. G., & Pietrzak, J. D. (2016). Simultaneous measurements of tidal straining and advection at two parallel transects far downstream in the rhine rofi. *Ocean Dynamics*, *66*(5), 719–736.
- Roman, F., Stipcich, G., Armenio, V., Inghilesi, R., & Corsini, S. (2010). Large eddy simulation of mixing in coastal areas. *International Journal of Heat and Fluid Flow*, *31*(3), 327–341.
- Rubin, S. G., & Harris, J. E. (1975). Incompressible viscous flow in a driven cavity. *NASA Special Publication*, *378*, 1.
- Sagaut, P. (2006). *Large eddy simulation for incompressible flows: an introduction*. Springer Science & Business Media.
- Sakamoto, K., & Akitomo, K. (2006). Instabilities of the tidally induced bottom boundary layer in the rotating frame and their mixing effect. *Dynamics of atmospheres and oceans*, *41*(3-4), 191–211.
- Sakamoto, K., & Akitomo, K. (2008). The tidally induced bottom boundary layer

- in a rotating frame: similarity of turbulence. *Journal of fluid mechanics*, 615, 1–25.
- Sakamoto, K., & Akitomo, K. (2009). The tidally induced bottom boundary layer in the rotating frame: development of the turbulent mixed layer under stratification. *Journal of fluid mechanics*, 619, 235–259.
- Salehipour, H., Caulfield, C.-c., & Peltier, W. (2016). Turbulent mixing due to the holmboe wave instability at high reynolds number. *Journal of Fluid Mechanics*, 803, 591–621.
- Salehipour, H., Peltier, W., & Caulfield, C. (2018). Self-organized criticality of turbulence in strongly stratified mixing layers. *Journal of Fluid Mechanics*, 856, 228–256.
- Salehipour, H., Peltier, W., & Mashayek, A. (2015). Turbulent diapycnal mixing in stratified shear flows: the influence of prandtl number on mixing efficiency and transition at high reynolds number. *Journal of Fluid Mechanics*, 773, 178–223.
- Salon, S., & Armenio, V. (2011). A numerical investigation of the turbulent stokes–ekman bottom boundary layer. *Journal of fluid mechanics*, 684, 316–352.
- Salon, S., Armenio, V., & Crise, A. (2007). A numerical investigation of the stokes boundary layer in the turbulent regime. *Journal of Fluid Mechanics*, 570, 253–296.
- Salon, S., Armenio, V., & Crise, A. (2009). A numerical (les) investigation of a shallow-water, mid-latitude, tidally-driven boundary layer. *Environmental fluid mechanics*, 9(5), 525–547.
- Santo, M. A., Toffolon, M., Zanier, G., Giovannini, L., & Armenio, V. (2017). Large eddy simulation (les) of wind-driven circulation in a peri-alpine lake: Detection of turbulent structures and implications of a complex surrounding orography. *Journal of Geophysical Research: Oceans*, 122(6), 4704–4722.
- Scandura, P., Faraci, C., & Foti, E. (2016). A numerical investigation of acceleration-skewed oscillatory flows. *Journal of Fluid Mechanics*, 808, 576–613.
- Scotti, A., & Piomelli, U. (2001). Numerical simulation of pulsating turbulent channel flow. *Physics of Fluids*, 13, 1367–1384.
- Scotti, A., & Piomelli, U. (2002). Turbulence models in pulsating flows. *AIAA journal*, 40(3), 537–544.
- Shin, J., Dalziel, S., & Linden, P. (2004). Gravity currents produced by lock exchange. *Journal of Fluid Mechanics*, 521, 1–34.
- Simpson, J. (1997). Physical processes in the ROFI regime. *Journal of marine systems*, 12(1-4), 3–15.
- Simpson, J., & Hunter, J. (1974). Fronts in the irish sea. *Nature*, 250(5465), 404–406.
- Simpson, J., & Linden, P. (1989). Frontogenesis in a fluid with horizontal density gradients. *Journal of Fluid Mechanics*, 202, 1–16.
- Simpson, J., & Souza, A. (1995). Semidiurnal switching of stratification in the region of freshwater influence of the Rhine. *Journal of Geophysical Research: Oceans*, 100(C4), 7037–7044.
- Simpson, J. H., Bos, W. G., Schirmer, F., Souza, A. J., Rippeth, T. P., Jones, S. E., & Hydes, D. (1993). Periodic stratification in the Rhine ROFI in the North Sea. *Oceanologica Acta*, 16(1), 23–32.
- Simpson, J. H., Brown, J., Matthews, J., & Allen, G. (1990). Tidal straining, density

- currents, and stirring in the control of estuarine stratification. *Estuaries*, 13(2), 125–132.
- Skote, M. (2014). Scaling of the velocity profile in strongly drag reduced turbulent flows over an oscillating wall. *International Journal of Heat and Fluid Flow*, 50, 352–358.
- Sleath, J. (1987). Turbulent oscillatory flow over rough beds. *Journal of Fluid Mechanics*, 182, 369–409.
- Smagorinsky, J. (1963). General circulation experiments with the primitive equations: I. the basic experiment. *Monthly weather review*, 91(3), 99–164.
- Smyth, W., Klaassen, G., & Peltier, W. (1988). Finite amplitude holmboe waves. *Geophysical & Astrophysical Fluid Dynamics*, 43(2), 181–222.
- Souza, A., & Simpson, J. (1996). The modification of tidal ellipses by stratification in the Rhine ROFI. *Continental Shelf Research*, 16(8), 997–1007.
- Spalart, P. R., & Baldwin, B. S. (1989). Direct simulation of a turbulent oscillating boundary layer. In *Turbulent shear flows 6* (pp. 417–440). Springer.
- Stacey, M. T., Monismith, S. G., & Burau, J. R. (1999). Measurements of reynolds stress profiles in unstratified tidal flow. *Journal of Geophysical Research: Oceans*, 104(C5), 10933–10949.
- Suijlen, J., & Duin, R. (2002). Atlas of near-surface total suspended matter concentrations in the Dutch coastal zone of the North Sea. *Rapportnr.: 2002.059*.
- Sumer, B., Laursen, T., & Fredsøe, J. (1993). Wave boundary layers in a convergent tunnel. *Coastal engineering*, 20(3-4), 317–342.
- Tennekes, H., & Lumley, J. L. (1972). *A first course in turbulence*. MIT press.
- Townsend, A. (1961). Equilibrium layers and wall turbulence. *Journal of Fluid Mechanics*, 11(1), 97–120.
- Tuzi, R., & Blondeaux, P. (2008). Intermittent turbulence in a pulsating pipe flow. *Journal of Fluid Mechanics*, 599, 51–79.
- Van Alphen, J., De Ruijter, W., & Borst, J. (1988). Outflow and three-dimensional spreading of rhine river water in the netherlands coastal zone. In *Physical processes in estuaries* (pp. 70–92). Springer.
- van der Giessen, A., de Ruijter, W., & Borst, J. (1990). Three-dimensional current structure in the Dutch coastal zone. *Netherlands Journal of Sea Research*, 25(1-2), 45–55.
- Verzicco, R., & Vittori, G. (1996). Direct simulation of transition in stokes boundary layers. *Physics of Fluids*, 8(6), 1341–1343.
- Visser, A., Souza, A., Hessner, K., & Simpson, J. (1994). The effect of stratification on tidal current profiles in a region of fresh-water influence. *Oceanologica acta*, 17(4), 369–381.
- Vittori, G., & Verzicco, R. (1998). Direct simulation of transition in an oscillatory boundary layer. *Journal of Fluid Mechanics*, 371, 207–232.
- Vlasenko, V., Stashchuk, N., & McEwan, R. (2013). High-resolution modelling of a large-scale river plume. *Ocean Dynamics*, 63(11-12), 1307–1320.
- Zang, Y., Street, R. L., & Koseff, J. R. (1994). A non-staggered grid, fractional step method for time-dependent incompressible navier-stokes equations in curvilinear coordinates. *Journal of Computational Physics*, 114(1), 18–33.
- Zhu, J. (1992). On the higher-order bounded discretization schemes for finite volume

- computations of incompressible flows. *Computer Methods in Applied Mechanics and Engineering*, 98(3), 345–360.
- Zimmerman, J. (1986). The tidal whirlpool: a review of horizontal dispersion by tidal and residual currents. *Netherlands Journal of Sea Research*, 20(2-3), 133–154.

Summary

Reproducing estuarine processes with direct numerical simulations in horizontally periodic domains

Turbulence plays a crucial role in estuarine flows, in general, and in region of fresh-water influence (ROFI) hydrodynamics in particular, due to its contribution in mixing processes and dispersion of particles. A method to study the role of turbulence is to isolate specific ROFI processes and to analyze them with direct numerical simulation (DNS) or large-eddy simulation (LES). In this thesis, two characteristic processes of the Rhine ROFI were chosen: the hydrodynamics of the oscillatory boundary layer, as a model for the tidal boundary layer, and the exchange flow driven by a horizontal density gradient, as a model for the estuarine density-driven flows.

The oscillatory flow was simulated in a shallow water configuration, in which the oscillatory boundary layer spans the entire water depth similar to the Rhine ROFI (Chap. 3). The structure of the boundary layer experiences an increase of the phase lead of the surface velocity and the wall-shear stress, and a change in amplitude of the surface velocity, both with respect to the free-stream velocity. In addition, a possible relaminarisation of the flow during part of the oscillatory cycle can occur. Subsequently, the existence of the logarithmic layer in the velocity profile of the oscillatory boundary layer was investigated (Chap. 4). For the simulated parameter values, the logarithmic layer is never present throughout the entire oscillation cycle, but its presence interval increases with the Reynolds number values and decreases with the water depth. Additionally, the results show that the value of the von Kármán constant and the intercept of the logarithmic layer are phase and Reynolds number dependent.

The simulation of density driven flows in domains with periodic horizontal boundary conditions required the development of improved one-dimensional (1D) models to account for strong stratification (Chap. 5). Additionally, these 1D models overcome several other challenges related to the simulation of density-driven flows. They are able to tackle runaway stratification and predict an accurate evolution of the velocity and density profiles when compared to two-dimensional simulations of such problems. Subsequently, the existing theoretical framework for 1D vertical models used for density and velocity profiles in estuaries can be extended to strongly stratified estuaries. Until now, this theory was limited to estuaries with weak stratification due to the 'well-mixed' assumption. The new 1D models also lead to the derivation of a new velocity scale for density currents over slopes (Chap. 6). This new velocity scale outperforms previous velocity scales since it has the advantage of converging properly to the velocity scale of density currents over horizontal bottoms in the limit of a very weak slope.

When used in horizontal periodic domains, the 1D models enable to simulate

sustained density currents using DNS and LES (Chap. 7). The 1D models were applied as forcing mechanisms and the flow behavior showed qualitative agreement with results from the existing literature. In particular, characteristic features of the flow, such as Holmboe waves and interface turbulence were successfully reproduced.

The results presented and methods developed in this thesis form a solid base for further research in environmental fluid mechanics, particularly in estuaries, and in several fundamental (and often classical) fluid mechanics problems. For estuarine research, the present models can be combined, or expanded with other physical mechanisms (e.g. the Coriolis force) to analyze the interaction and the competition of the different physical mechanisms in estuaries. For classical flows, the models can be used to further study turbulence processes in shallow oscillating flows or in stratified shear flows.

Samenvatting

Het reproduceren van estuariene processen met directe numerieke simulaties in horizontaal periodieke rekendomeinen

Turbulentie speelt een cruciale rol in estuariene stromingen in het algemeen, en in ROFI (Region of Freshwater Influence, ofwel regio van zoetwater invloed) hydrodynamica in het bijzonder. Turbulentie draagt namelijk bij aan de menging en de dispersie van deeltjes. Eén van de methodes om ROFI-turbulentie te bestuderen is om specifieke ROFI-processen te isoleren en ze vervolgens te reproduceren met directe numerieke simulaties (DNS), of large-eddy simulaties (LES). In dit proefschrift zijn twee kenmerkende ROFI processen uitgekozen die optreden in de Rijnmond: de hydrodynamica van de oscillerende grenslaag, en de stroming gedreven door een horizontale dichtheidsgradient. Hierbij dient de eerste stroming als een model voor de getijstroming en de tweede stroming als een model voor de de horizontale dichtheids-effecten die optreden in riviermondingen.

De oscillerende stroming werd bestudeerd aan de hand van simulaties waarbij de waterdiepte bewust klein is genomen, zodat de turbulente grenslaag de volledige waterdiepte in beslag neemt, vergelijkbaar met de situatie in de Rijn ROFI (Hfdst. 3). De resultaten tonen aan dat er een toename optreedt van de mate waarin de fase van de oppervlakte-snelheid en de fase van de wandschuifspanning voorlopen op de fase van de snelheid van de vrije stroom. Tevens vindt er een toename plaats van de amplitude van de oppervlakte-snelheid ten opzichte van de amplitude van de snelheid van de vrije stroom. Bovendien is het ook mogelijk dat de stroming weer laminariseert gedurende een deel van de oscillatie-cyclus. Als volgt van deze bevindingen werd de aanwezigheid van de logaritmische laag in het snelheidsprofiel van de oscillerende grenslaag onderzocht (Hfdst. 4). Voor de parameter-waardes die in de simulatie gebruikt werden, is de logaritmische laag nooit aanwezig gedurende de hele oscillatie-cyclus, maar groeit de aanwezigheidsinterval met het reynoldsgetal, terwijl het krimpt met de waterdiepte. In aanvulling hierop, tonen de resultaten dat de waardes van de von Kármán -constante en van het nulpunt van de logaritmische laag veranderen met zowel de fase als de waarde van het reynoldsgetal.

De simulatie van dichtheidsgedreven stromingen in typische DNS en LES domeinen vereiste het ontwikkelen van verbeterde één-dimensionale (1D) modellen. De horizontale randvoorwaardes in typische DNS en LES domeinen zijn namelijk periodiek, en daardoor moeilijk verenigbaar met de horizontale dichtheidsgradiënten. De bestaande modellen waren al in staat om dit probleem voor zeer zwakke stratificatie op te lossen, maar de nieuwe modellen breiden de oplossing uit voor zeer sterke stratificatie (Hfdst.Chap. 5). Verder bieden deze nieuwe 1D modellen ook oplossingen voor een aantal andere uitdagingen die gerelateerd zijn aan dichtheidsgedreven stromingen. Ten eerste zijn ze in staan om het probleem van 'runaway stratification' aan

te pakken, één quasi oneindige toename van de stratificatie. Ten tweede, zijn de modellen ook in staat om de ontwikkeling van snelheidsprofielen en dichtheidsprofielen accuraat te voorspellen, waarbij de resultaten van twee-dimensionale simulaties van dezelfde stromingen als referentie dienden. Door deze eigenschappen kan het theoretische kader van 1D verticale modellen voor estuaria opgerekt worden naar sterk gestratificeerde toestanden, terwijl dit kader tot nu toe beperkt was tot estuaria met zwakke stratificatie (de aanname van een goed gemengde waterkolom). De nieuwe 1D modellen hebben ook geleid tot het afleiden van een nieuwe snelheidsschaal voor dichtheidsstromingen over een helling (Hfdst. 6). Deze nieuwe snelheidsschaal overtreft de vorige snelheidsschalen aangezien deze netjes convergeert naar de snelheidsschaal voor dichtheidsstromingen over horizontale bodems zodra de helling naar nul gaat.

Als de 1D modellen gebruikt worden als forcering in DNS/LES simulaties met periodieke horizontale randvoorwaardes, leiden ze tot een realistische weergave van gestage dichtheidsstromingen (Hfdst. 7). Het gedrag van de stromingen toonde namelijk kwalitatieve overeenkomsten met resultaten uit de literatuur. In het bijzonder werden kenmerkende eigenschappen van de de stroming met succes gereproduceerd, zoals Holmboe-golven, inwendige golven langs de overgangslaag tussen zout en zoet water, en turbulentie rond de overgangslaag.

De getoonde resultaten en ontwikkelde methodes uit dit proefschrift vormen een stevig fundament voor verder onderzoek in de stromingsleer toegepast op estuaria, alsmede verschillende fundamentele (en vaak klassieke) vloeistof mechanica onderwerpen. Voor verder onderzoek naar estuaria kunnen de huidige twee modellen gecombineerd worden, of doorontwikkeld worden met behulp van andere fysische processen (bv. de Coriolis kracht) om de interactie en de competitie tussen de verschillende fysische mechanismes in estuaria te bestuderen. Voor klassieke stromingen kunnen de modellen gebruikt worden om turbulentie processen in ondiepe stromingen en gestratificeerde schuifspanning stromingen te bestuderen.

Acknowledgments

During the spring of 2014, I was working at Deltares when I started prospecting for a PhD position. One of my colleagues, my previous internship supervisor Rob Uittenbogaard, notified me about the possibility of doing research on river plumes with Prof. Julie Pietrzak at the Delft University of Technology. The first meeting with Julie made me enthusiastic when she informed me about the project and the two PhD positions, the one in Delft and one at the Eindhoven University of Technology. However, it became rapidly clear that my profile suited better the position in Eindhoven. After a meeting with the head of the group, Prof. Herman Clercx, I finally moved to Eindhoven to start my academic journey.

Naturally, my first acknowledgments go to the people who made this journey possible by placing their confidence in me: Dr. Rob Uittenbogaard from Deltares, Prof. Julie Pietrzak from the Delft University of Technology, Prof. Herman Clercx, Prof. Bas van de Wiel and Dr. Matias Duran Matute, all from the Eindhoven University of Technology. The project was funded by STW, now NOW-TTW, and made possible by the users committee, which included, among others, Wouter Kranenburg (Deltares), Will Borst (Port of Rotterdam), Ad Stolk (Rijkswaterstaat) and Onno van Tongeren. I thank them all. My next acknowledgments go Sabine Rijnsburger, my co-PhD student in Delft, who took the lead in organizing the user committee meetings and who turned a blind eye when I was (again) late with handing in the progress report. Finally, I also acknowledge the members of my PhD committee, who accepted to take a look at my dissertation.

During my time in Eindhoven, I was lucky to be part of the Vortex Dynamics group which later became the Fluid and Flows group. I therefore thank my former co-PhD students and post-docs, some of which became friends, for the scientific discussions (at the office) and the less scientific discussions (during lunches or after hour activities). I am grateful to Abhitee, Abhineet, Alessandro, Altug, Andrei, Andres, Bijan, Bojia, Cosimo, Dario, Dennis, Felix, Florian, Francesca, Gianluca, Gianmarco, Hadi, Haijing, Jonathan, Judith, Kim, Lorenzo, Maarten, Marjan, Marlies, Matteo L., Matteo M., Matias, Neehar, Ozge, Pinaki, Pranav, Rik, Saskia, Sebastian, Sudhir, Vignesh, Wolfram, Xiao, Vitor, Werner, and my office mates, Andrei, Geert, Giorgia, Ivo, Josje, Michel and Samuel. I also would like to thank the professors, visiting professors and the technical staff, i.e. Federico, GertJan, Hanneke, Rudi, Willem, Chung-min, Freek, Gerald and Ad. I would like to thank in particular Dr. Duran Matute, to have accepted to take over my supervision after Prof. van de Wiel moved to Delft, and Dr. Leon Kamp to enlighten me about analytical solutions for partial differential equations. Finally, I had the opportunity to supervise five students, Lieke, Jurriaan, Daniel, Koen and Thijs, whose work contributed to this thesis, and for whom my gratitude is also in place

As part of my PhD project, I was lucky to collaborate with the University degli studi di Trieste. I would like to express my gratitude to Dr. Federico Roman and Prof.

Armenio for their hospitality and their support. I can look back upon some wonderful summers in Italy with the other members of the lab, Ahmad, Andrea P., Andrea R., Anna, Anton, Carlo, Catalina, Chiara, Fotini, Francesca, Giulia, Laleh, Marco, Mahmoud, Marjan, Marta, Najmeh, Shayan and Santiago. Besides my colleagues from the university, I also had the chance to interact with Stefano Salon, who's work on the oscillatory boundary layer laid the foundations for Chapter 3 and 4. After spending the first to stays in Trieste at the University dorm, I had the luck to be a housemate of Santiago, Catalina and Najmeh. Catalina, thank you for loosing my kitchenware (and subsequently admitting that the best potatoes are from the Netherlands to make up for it). Santiago, thanks for letting me worry when you were absent from home for several days without notifying. Although never my housemate, I should not forget to express sincere gratitude to Fotini for calming my concerns when Santiago did not come home for three days in a row.

During the conferences and summer schools I came to meet, among others, Giordano, Yoeri and Felix. Giordano, thank you for sharing your experience as a self-employed. Felix, thank you for triggering my curiosity with internal waves. Yoeri thank you for introducing me (indirectly) to my current employer. I also would like to express my gratitude to John Donners (project PRACE), whose work on improving the performances of the code was extremely helpful.

Besides work, I had the chance to visit Ravenna, Lecce, Shiraz and Mashhad with local guides Gianluca, Marco, Najmeh and Hadi. Gianluca, thank you for portraying me Justiniano and Theodora; Marco, thank you for receiving me in Salento; Najmeh, thank for handling the taxi drivers for me in Shiraz; and Hadi, thank you for suggesting me Torshi Seer. I also had the privilege to be invited to a authentic Veneto wedding, thank you Francesca and Guglielmo. I had the possibility to play table tennis with Alessandro and Andres. I had the pleasure to learn Italian face expressions from Matteo L. and to taste real Chinese dumplings by Haijing. I had the opportunity to clear my heart with Marjan, philosophize about friendship with Kim, to try choco shiznit (or however you write it) with Josje, and to make political incorrect jokes with Ivo. In short, I have special thoughts for the friends that I made in Eindhoven, the people that I might have forgotten to thank in these acknowledgments, but also the friends that I lost contact with during my PhD years. The freedom I endured during my PhD was a blessing but also came at a high cost...

Tot slot will ik graag mijn familieleden bedanken voor jullie steun, jullie interesse en jullie begrip gedurende mijn hele promotietraject. Ik bedankt mijn ouders, pap en mam. Ik bedank mijn opa's en oma's, opa en oma Kaptein en opa en oma van den Berg, ook al heeft mijn tweede opa het niet meer mee kunnen maken. Ook bedank ik mijn zusjes Mariska en Mathilde.

Karen meu amor, obrigado por estar comigo e por compreender quando nossos encontros eram perturbados pelo meu trabalho de doutorado.

Curriculum Vitae

Steven J. Kaptein was born on 06-08-1990 in Haarlem (the Netherlands). After finishing his Baccalauréat in 2008 at the Lycée Marie Reynoard in Villard-Bonnot (France), he studied Mathematical and Mechanical Modelling at the Bordeaux Institute of Technology in Bordeaux (France). In 2013 he graduated within the School of Biological Sciences on Ecological modelling of the Coorong. From May 2014 he started a PhD project at Eindhoven University of Technology in Eindhoven (the Netherlands) of which the results are presented in this dissertation. Since 2019 he is employed at Flanders Hydraulics Research.

List of publications

Published journal papers

- **S.J. Kaptein**, M. Duran-Matute, F. Roman, V. Armenio and H.J.H. Clercx. *Effect of the water depth on oscillatory flows over a flat plate: from the intermittent towards the fully turbulent regime*. Environmental Fluid Mechanics (2019), 19(5), 1167-1184. DOI 10.1007/s10652-019-09671-3. Chapter 3 of this thesis.
- **S.J. Kaptein**, M. Duran-Matute, F. Roman, V. Armenio and H.J.H. Clercx. *Existence and properties of the logarithmic layer in oscillating flows*. Journal of Hydraulic Engineering (2019), 57, 1–14. DOI:10.1080/00221686.2019.1661293. Chapter 4 of this thesis.
- **S.J. Kaptein**, K.J. van de Wal, L.P.J. Kamp, H.J.H. Clercx, V. Armenio and M. Duran-Matute. *Analysis of one-dimensional models for exchange flows under strong stratification*. Ocean Dynamics (2020), 70(1), 41–56. DOI:10.1007/s10236-019-01320-z. Chapter 5 of this thesis.

Conference contributions

- **S.J. Kaptein**, M. Duran-Matute and H.J.H. Clercx. *Tide and river outflow interaction: a DNS/LES study*. Poster presentation. Physics@FOM, Veldhoven, 19-20 January 2016.
- **S.J. Kaptein**, M. Duran-Matute, F. Roman, V. Armenio and H.J.H. Clercx. *A numerical investigation of the interaction between a horizontal density gradient and an oscillating turbulent flow*. Oral presentation. 69th meeting APS/DFD, Portland, OR, 20-22 November 2016.
- **S.J. Kaptein**, M. Duran-Matute and H.J.H. Clercx. *Interaction between cross-shore estuarine currents and along-shore tidal currents*. Poster presentation. Physics@Veldhoven, Veldhoven, 17-18 January 2017.
- **S.J. Kaptein**, M. Duran-Matute, F. Roman, V. Armenio and H.J.H. Clercx. *Interaction between a gravitational circulation and a tidal flow: a study using large eddy simulation*. Oral presentation. 4th ISSF, Eindhoven, NL, 26-28 June 2017.
- **S.J. Kaptein**, M. Duran-Matute, F. Roman, V. Armenio and H.J.H. Clercx. *Quantifying turbulent mixing in an estuary using idealized direct numerical simulations*. Oral presentation. CERF 2017, Providence, RI 5-9 November 2017.

- **S.J. Kaptein**, M. Duran-Matute and H.J.H. Clercx. *Oscillating flow over a flat plate: the influence of the water depth*. Poster presentation. Physics@Veldhoven, Veldhoven, 22-23 January 2018.
- **S.J. Kaptein**, M. Duran-Matute, F. Roman, V. Armenio and H.J.H. Clercx. *Tidal currents in shallow seas: influence of the water-depth on the structure of the turbulent boundary layer*. Oral presentation. 8th international symposium on environmental hydraulics, University of Notre Dame (South-Bend), IN, 4-7 June 2018.